DEPARTMENT OF PHYSICS
UNIVERSITY OF JYVÄSKYLÄ
RESEARCH REPORT No. 6/2013

# STUDIES OF ELECTRON CYCLOTRON RESONANCE ION SOURCE BEAM FORMATION, TRANSPORT AND QUALITY

**BY**

**VILLE TOIVANEN**

Academic Dissertation
for the Degree of
Doctor of Philosophy

*To be presented, by permission of the*
*Faculty of Mathematics and Science*
*of the University of Jyväskylä,*
*for public examination in Auditorium FYS-1 of the*
*University of Jyväskylä on August 9, 2013*
*at 12 o'clock noon*

Jyväskylä, Finland
July 2013

# Preface

The work reported in this thesis has been carried out at the accelerator laboratory of the Department of Physics, University of Jyväskylä, during the years 2008–2013. I want to sincerely thank my supervisor Dr. Hannu Koivisto for all the guidance and insight into the world of ion source physics that I have been privileged to receive during the years working in the ion source group. I wish to extend my thanks also to Dr. Olli Tarvainen, who has not only been a constant source of information and valuable instructions, but whose enthusiasm for physics has also been a major source of inspiration to my work. I would like to thank Dr. Detlef Küchler and Dr. Liangting Sun for reviewing my thesis and providing me with comments and suggestions which helped to improve it.

I wish to thank Mr. Taneli Kalvas for the numerous discussions concerning computer simulations and his invaluable help with the ion optical code IBSimu, which played an irreplaceable role in this thesis work. Mr. Jaakko Julin and Ms. Mari Napari deserve my warm thanks for all the activities we have shared over the years, both at work and during free time. I would also like to thank all the past and current members of the ion source group that I have been privileged to work with, especially Dr. Juha Ärje, Dr. Tommi Ropponen, Mr. Janne Ropponen, Ms. Olga Steczkiewicz, Mr. Jani Komppula, Mr. Vesa Aho, Mr. Janne Laulainen, Mr. Risto Kronholm and Mr. Juha Suutari, for years of collaboration in an inspirational, eventful and enjoyable working environment.

I am grateful for all the help I have received from everybody at the mechanical and the electrical workshops, which has enabled me to perform the experimental work described in this thesis. The help of the cyclotron operators, Mr. Anssi Ikonen, Mr. Jani Hyvönen and Mr. Markus Liimatainen, which was crucial in the work including the JYFL K-130 cyclotron, and much more, is gratefully acknowledged. I wish to thank Mr. Veikko Nieminen and Mr. Kimmo Ranttila for their help in the mechanical design of the experimental apparatus related to this thesis work.

I would like to express my most sincere thanks to all my friends for the invaluable relationships we have shared over the years. They have provided me with an environment where I can be simply myself and take the occasional escape from the world of ion sources and ion beams, albeit often into a world of even greater wonder, bafflement and absurdity.

I owe the biggest debt of gratitude to my parents Seppo and Sirkka and my brothers

Olli and Jussi, who have always supported me in my activities. Without them this work would not have been possible.

The work presented in this thesis was supported by the Academy of Finland under the Finnish Centre of Excellence in Nuclear and Accelerator Based Physics Research Programmes 2006–2011 and 2012–2017, and the European Union 7$^{\text{th}}$ Framework Programme "Integrating Activities – Transnational Access", Project Number 262010 (ENSAR). The financial support of the Graduate School in Particle and Nuclear Physics (GRASPANP), Ellen and Artturi Nyyssönen Foundation and Magnus Ehrnrooth Foundation is also gratefully acknowledged.

Jyväskylä, July 2013

Ville Toivanen

# Abstract

Toivanen, Ville, 1984 –
Studies of electron cyclotron resonance ion source beam formation, transport and quality
Jyväskylä, University of Jyväskylä, 2013
Research Report 6/2013 / Department of Physics, University of Jyväskylä
ISBN paper copy: 978-951-39-5286-0
ISBN PDF: 978-951-39-5287-7
ISSN: 0075-465X

This thesis presents the results of a broad study investigating different possibilities to improve the performance of the JYFL 14 GHz Electron Cyclotron Resonance Ion Source (ECRIS). The experimental work includes studies of ECRIS plasma, ion beam formation and beam transport, all of which contribute to the properties of ion beams produced with ECR ion sources. In particular, it is shown that the degradation of beam quality due to the formation of hollow beam structure is influenced by phenomena originating from all of these categories.

The effects of fine tuning the frequency of the plasma heating microwaves of the JYFL 14 GHz ECRIS are presented, showing that the frequency tuning can influence the ion beam properties. It is demonstrated that the ion beams produced with the ion source are not completely space charge compensated during the first section of the beam transport, and the space charge effects in this region have significant impact on the beam properties. Also, it is shown that mitigating these effects can lead to substantial improvement in beam quality. The temporal stability of ion beams produced with ECR ion sources is discussed and it is shown that the beams exhibit fast beam current oscillations in the $10^2 - 10^3$ Hz region, characteristics of which depend on the ion source tuning. Experiments with the so-called collar structure are presented, providing new insight into the plasma conditions near the ion extraction. As a culmination of the thesis work, a new extraction system has been designed and constructed for the JYFL 14 GHz ECRIS. It is shown that the new system provides improved performance compared to the old one in terms of extracted beam currents, beam quality and transmission efficiency.

**Keywords:** Electron cyclotron resonance ion source, highly charged heavy ions, beam formation, beam transport, beam quality

**Author** Ville Toivanen
Department of Physics
University of Jyväskylä
Finland

**Supervisor** Dr. Hannu Koivisto
Department of Physics
University of Jyväskylä
Finland

**Reviewers** Dr. Detlef Küchler
Accelerators and Beams Department
The European Organization for Nuclear Research (CERN)
Switzerland

Dr. Liangting Sun
Institute of Modern Physics
Chinese Academy of Sciences
China

**Opponent** Dr. Richard Pardo
Physics Division
Argonne National Laboratory
USA

# List of publications

This thesis consists of the following publications and some results that have not yet been published.

**A.I** V. Toivanen, H. Koivisto, O. Steczkiewicz, L. Celona, O. Tarvainen, T. Ropponen, S. Gammino, D. Mascali and G. Ciavola, *Effect of electron cyclotron resonance ion source frequency tuning on ion beam intensity and quality at Department of Physics, University of Jyväskylä*, Rev. Sci. Instrum. **81** (2010) 02A319.

**A.II** V. Toivanen, H. Koivisto, O. Steczkiewicz, L. Celona, O. Tarvainen, T. Ropponen, S. Gammino, D. Mascali, and G. Ciavola, *Erratum: Effect of electron cyclotron resonance ion source frequency tuning on ion beam intensity and quality at Department of Physics, University of Jyväskylä [Rev. Sci. Instrum. 81, 02A319 (2010)]*, Rev. Sci. Instrum. **82** (2011) 019900.

**A.III** V. Toivanen, O. Tarvainen, C. Lyneis, J. Kauppinen, J. Komppula and H. Koivisto, *ECRIS plasma chamber studies using a network analyzer as a loaded cavity probe*, Rev. Sci. Instrum. **83** (2012) 02A306.

**A.IV** V. Toivanen, O. Steczkiewicz, O. Tarvainen, T. Ropponen, J. Ärje and H. Koivisto, *The effects of beam line pressure to the beam quality of an electron cyclotron resonance ion source*, Nucl. Instrum. Meth. B **268** (2010) 1508–1516.

**A.V** V. Toivanen, O. Tarvainen, J. Komppula and H. Koivisto, *Oscillations of ECR ion source beam current along the beam transport of the JYFL K-130 cyclotron*, J. Instrum. **8** (2013) T02005.

**A.VI** V. Toivanen, O. Tarvainen, J. Komppula and H. Koivisto, *The effect of plasma electrode collar structure on the performance of the JYFL 14 GHz electron cyclotron resonance ion source*, Nucl. Instrum. Meth. A **726** (2013) 41–46.

**A.VII** V. Toivanen, T. Kalvas, H. Koivisto, J. Komppula and O. Tarvainen, *Double einzel lens extraction for the JYFL 14 GHz ECR ion source designed with IBSimu*, J. Instrum. **8** (2013) P05003.

The author has performed most of the experimental work of publications A.II – A.VII, and has played an integral role in the experiments of publication A.I. The majority of the data analysis in all of the publications has been performed by the author. The publications listed above are included in the end of the thesis.

# Contents

# Chapter 1

# Introduction

Highly charged heavy ion beams provide an ideal tool for scientific research to probe the structure of matter, study particle interactions and investigate a wide range of natural and exotic phenomena in laboratory conditions. In addition to basic research, during the last decades a vast field of applications has formed around ion beams, ranging from medical uses like radiation therapy to industrial material processing and analysis, as well as radiation hardness testing of electronics [1–4].

The advancing scientific research and the development of the applications constantly increase the demands set for the ion beam properties. In many cases these properties are directly linked to the performance of the ion source which acts as an injector for the particle accelerator. Higher beam energies and new ion species are needed to expand the range of phenomena available for studies and higher beam currents are required to make the observation of rare, low cross section reactions feasible. In addition, a high degree of beam quality, both in the temporal and spatial domains, is essential in many cases. These requirements act as a strong driving force for continuous ion source development.

The most widely used type of ion source for the production of high intensity highly charged heavy ion beams is the *Electron Cyclotron Resonance Ion Source* (ECRIS) [5], a plasma ion source with its roots in the plasma fusion research of 1960's. The high reliability and lack of eroding parts like filaments has made these ion sources very popular during the last decades. Already in 2008 there existed over 70 operational second and third generation ECR ion sources around the world [6], underlining the importance of ECRIS in the field of ion beam production.

The accelerator laboratory of the Department of Physics, University of Jyväskylä (JYFL), has two ECR ion sources for the production of highly charged ions [7, 8]. In order to meet the increasing demands set for the ion beams, a thorough investigation of the beam transport from the JYFL 14 GHz ECR ion source through the JYFL K-130 cyclotron [9] was carried out in the laboratory during 2007 – 2008 [10]. The results indicated that the transmission efficiency was severely degraded due to poor ion beam quality. The clearest indication of this was the hollow beam structure observed with many ion beams. Furthermore, it was observed that the beam quality degraded

with increasing current extracted from the ion source, limiting the ion source operation and indicating problems in the beam formation and transport [11].

These results provided strong motivation to initiate a broad study to investigate different possibilities to improve the beam quality and performance of the JYFL 14 GHz ECRIS. The different phenomena which affect the beam quality can be divided into three categories: (1) the production of ions inside the ion source plasma chamber, (2) beam formation in the ion source extraction region and (3) beam transport from the ion source through the accelerator to the target. The work presented in this thesis consists of a series of experimental studies in all these categories.

The thesis is outlined as follows. Chapter 2 is devoted to the electron cyclotron resonance ion source, presenting its general structure, main features and operating principles. Special emphasis has been given to the ion source performance and the beam quality. Chapter 3 presents the experimental apparatus, set-ups and methods used in the measurements. The JYFL 14 GHz ECRIS, which is the ion source used in the work presented in this thesis, is introduced in this chapter. The experimental work related to this thesis is presented in chapter 4. The chapter has been divided into three main subsections, the first concentrating on the studies related to the ECRIS plasma, the second to the beam transport and the third to the beam formation. The ECRIS plasma studies concentrate on the effects of varying the frequency of the plasma heating microwaves on the properties of the extracted ion beams. The beam transport studies comprise of space charge and ion beam temporal stability related experiments, and the influence of these phenomena on the beam quality and transmission efficiency. The beam formation section also includes two distinct studies. The first probes the properties of the extracted ions and the plasma conditions in the immediate vicinity of the beam extraction with a cylindrical collar structure around the extraction aperture. The second study describes the upgrade of the JYFL 14 GHz ECRIS extraction system. The problems of the old system are discussed and the structure and performance of the new extraction system are presented. Finally, chapter 5 summarizes the presented work and discusses the obtained results and future prospects.

# Chapter 2

# ECR ion sources

Electron Cyclotron Resonance (ECR) ion sources are currently the main workhorses of high intensity highly charged heavy ion production in the world. The ions are produced inside a plasma confined with external magnetic field and sustained with microwave radiation. This frees the ion production from eroding parts like cathodes, significantly improving the ion source reliability in continuous long term operation. This, combined with the capability to produce continuous (cw) or pulsed ion beams with usable currents from virtually any element, forms a solid basis for the popularity of the ECR ion sources.

The next section gives a short introduction to the origins and development of ECR ion sources. This is followed by a description of the operational principles of ECRIS, divided into several sections: (1) electron heating with microwaves at electron cyclotron resonance, (2) production of highly charged ions, (3) the confinement of the plasma with magnetic fields, (4) the introduction of material to be ionized, (5) different aspects affecting the ECRIS performance and (6) the beam extraction. In addition, the quality of ion beams produced with ECR ion sources are discussed.

## 2.1 A brief history of ECR ion sources

The origins of the ECR ion source lie in the plasma fusion research of the 1960's. The first ion source using ECR plasma heating was born in 1965, when R. Geller installed a beam extraction system to the 3 GHz PLEIADE plasma generator [5]. The promising results obtained with the device led to fast development of subsequent devices during the late 1960's and early 1970's.

In 1970 H. Postma proposed ECR heating as an efficient process for the production of multiply charged ions [12]. This was successfully demonstrated in 1972 by R. Geller *et al.* with the MAFIOS ion source [13,14] and independently by K. Wiesemann *et al.* [15]. A few years later in 1974 the enormously successful SUPERMAFIOS was constructed, incorporating magnetic hexapole field for radial confinement and two-stage plasma, yielding huge improvement to the production of multiply charged ions [16]. This device

is usually considered as the first true high charge state ECRIS and came to be the basis for practically all subsequent ECR ion sources.

In 1981 ECR ion sources became production devices, when the PICOHISKA source became the first ECRIS to be linked to an particle accelerator, the Karlsruhe cyclotron [5]. This combination has proven to be hugely successful, thanks to the fact that the cyclotron output energy is quadratically proportional to the charge of the accelerated ion.

During the last few decades the performance of ECR ion sources has steadily increased. This is the result of increasing understanding of the phenomena taking place in the ECR heated plasma and the subsequent improvements in the source design. The technological development, especially in the field of superconductors, has also had a significant impact. The development of ECR ion source performance can be described with different source generations. As the ECRIS performance scales with the frequency of the heating microwave (see the following sections), it is the natural choice for the classification. The first generation includes ion sources developed mostly in the 1980's and is mainly populated by devices with two-stage plasma heated with microwaves up to 10 GHz. For example the 6.4 GHz LBL ECR [17] and the 6.4 GHz RT-ECRIS [18] represent this generation. The second generation uses microwaves up to about 14 GHz, and includes e.g. the CAPRICE [19] and the AECR type ion sources [20]. The most powerful ECR ion sources currently operational in the world, e.g. VENUS [21], SECRAL [22] and RIKEN SC-ECRIS [23], belong to the third generation operating with microwave frequencies up to 28 GHz. The transition from room temperature to fully superconducting devices occurs between the $2^{\text{nd}}$ and $3^{\text{rd}}$ generations. The most powerful room temperature ECR ion sources operate at 18 GHz, placing them in the transition between the generations. To push the ECRIS performance even further, the 4th generation sources are envisioned to function between 40 and 56 GHz [24, 25]. This poses many technical challenges, especially with the superconducting magnet design [26].

## 2.2 Electron cyclotron resonance

In ECR ion sources the plasma heating is based on the energy transfer from microwaves to electrons via *electron cyclotron resonance* in external magnetic field. The resonance occurs when the cyclotron frequency (i.e. gyrofrequency) of an electron traversing in the magnetic field matches the frequency of the heating microwaves. This condition is described with the relation

$$\omega_{\text{rf}} = \omega_{\text{c}} = \frac{eB_{\text{ECR}}}{\gamma m_e}, \tag{2.1}$$

where $\omega_{\text{rf}}$ is the microwave angular frequency, $\omega_{\text{c}}$ the electron gyrofrequency, $e$ the electron charge, $B_{\text{ECR}}$ the magnetic field at the resonance, $\gamma$ the relativistic gamma factor and $m_e$ the electron mass. At the resonance the electron gains (or loses) energy

from the electromagnetic wave based on the phase difference between the electron gyrovelocity and the electric field component of the microwave perpendicular to the magnetic field. As the electrons pass through the resonance multiple times, the stochastic nature of the process leads to a net gain in the energy of the electron population. As the ECR process heats the electrons selectively, the ions remain cold in the plasma. This is desirable, because the ion temperature contributes to the emittance and energy spread of the extracted ion beams, and consequently low temperature improves beam quality. In addition, the low ion temperature increases the time the ions remain in the plasma, enabling production of highly charged ions via stepwise ionization by consecutive electron impacts, as is discussed in the next section.

The energy gain of the electrons in the resonance is affected by the electric field amplitude, which increases with increasing microwave power injected into the plasma chamber. In addition, the gradient of the external magnetic field at the resonance influences the energy transfer. As will be discussed in the following chapters, the ECR condition is fulfilled in ECR ion sources on a closed surface inside the plasma chamber. Consequently, altering the field gradient at the resonance effectively decreases or increases the thickness of the resonance surface, varying the volume where the resonance occurs and consequently the effectiveness of the energy transfer from the microwaves to the electrons.

Some insight into the properties of the electric field at the resonance can be obtained by considering the ECRIS plasma chamber as a resonating cavity for the microwaves. When microwaves are introduced into the cavity, an electromagnetic standing wave structure can be excited depending on the microwave frequency and the cavity dimensions. The structure of the electromagnetic field is characterized by transverse electric (TE) and transverse magnetic (TM) modes, which can be calculated theoretically for a simple cylindrical system approximating the ECRIS plasma chamber [27]. Each of these modes represents an electromagnetic field distribution which can be excited inside the cavity. The mode quality factor, or $Q$ *value*, describes the resonance properties of the mode in terms of how much energy is stored to the system in relation to the energy dissipation required to sustain the mode. High $Q$ value corresponds to low rate of energy loss compared to the stored energy in the system. The $Q$ value can also be presented in terms of the center frequency $f_0$ and the bandwidth $\Delta f$ (full width at half maximum) of the mode, yielding expression

$$Q = \frac{f_0}{\Delta f}. \tag{2.2}$$

Calculations with the simplified cylindrical system in vacuum can be used to obtain rough ideas of the modes and mode density inside ECRIS plasma chamber. It is observed that the plasma chamber of modern ECR ion sources is highly overmoded with high density of modes around the primary microwave frequency. For example, the separation of modes around 14 GHz with typical ECRIS plasma chamber dimensions is in the order of some MHz [27]. As the modes occupy a finite bandwidth, as described

by Eq. (2.2), this leads to overlapping of the adjacent modes and due to this mode coupling the final electromagnetic field structure present in the cavity is defined as a superposition of the individual modes.

However, the real ECRIS plasma chamber is not an ideal cylindrical cavity, as it typically includes pumping ports, aperture for beam extraction, a biased disc, microwave input structures, perhaps even oven and sputtering equipment to introduce material for ion beam production. Advanced simulation tools (e.g. CST Microwave Studio [28]) are required to model the resonance behavior of such a complex system.

With plasma the situation becomes even more complex. The spatial distribution of the confined plasma with density variations yields anisotropic permittivity distribution inside the cavity. The locally varying permittivity and the power absorption by the plasma decreases the $Q$ value and leads to broadening and shifting of the modes, increasing the mode overlapping and thus influencing the electromagnetic field structure. The field distribution also has spatial variations, which in turn influence the plasma through electron heating. As such the electromagnetic field and plasma distributions are coupled and functions of each other. Theoretical or numerical modeling of such a system is a very challenging task and consequently it is very difficult to describe the structure of the electromagnetic fields inside the plasma chamber during ECRIS operation. Because the $Q$ value decreases with increasing plasma density and power absorption, leading to increased overlapping of the broadening modes, the discrete structure of modes present in the vacuum filled cavity should be effectively smeared out and damped. However, some experimental studies do exist which suggest that some narrow bandwidth frequency dependent phenomena can still exist with plasma and can influence the properties of the extracted beams [29].

Another important factor in the microwave – plasma interaction is the plasma acting as a high-pass filter for electromagnetic radiation [15]. The cutoff frequency is determined by the *plasma frequency*, which is defined as

$$\omega_p = \sqrt{\frac{n_e e^2}{\epsilon_0 m_e}}, \tag{2.3}$$

where $n_e$ is the plasma density, $e$ the electron charge, $\epsilon_0$ the permittivity of vacuum and $m_e$ the electron mass. Microwaves with frequencies higher than the plasma frequency can propagate in the plasma, whereas microwaves with lower frequencies are reflected back. The plasma frequency depends on the plasma density, which indicates that plasma heating with fixed microwave frequency $\omega_{\mathrm{RF}}$ sets an upper limit for the obtainable plasma density. This so-called *critical density* can be described as

$$n_{e,\mathrm{crit}} = \frac{\epsilon_0 m_e \omega_{\mathrm{RF}}^2}{e^2}. \tag{2.4}$$

As higher plasma density is one of the requirements to produce higher beam currents, the ECR ion source development has been characterized by the increase of the plasma heating microwave frequency.

## 2.3 Production of highly charged ions

The ion production in ECRIS plasma can be divided into three types of processes: ionization processes to produce ions of charge state $q$, recombination processes that decrease ion charge state and ion losses through diffusion and transport processes. *Electron impact ionization* is the main ionization process in the ECR plasma, and *charge exchange* in collisions between ions and neutral particles is the dominating process that decreases the ion charge state. The time evolution of density of ions $n_i^q$ of species $i$ with charge state $q$ can be described with the balance equation [30]

$$\frac{dn_i^q}{dt} = n_e\langle\sigma v\rangle_{q-1,q}^{\text{ion}} n_i^{q-1} - n_e\langle\sigma v\rangle_{q,q+1}^{\text{ion}} n_i^q + n_{0,i}\langle\sigma v\rangle_{q+1,q}^{\text{cx}} n_i^{q+1} - n_{0,i}\langle\sigma v\rangle_{q,q-1}^{\text{cx}} n_i^q - \frac{n_i^q}{\tau_i^q}, \quad (2.5)$$

where $n_e$ is the electron density, $n_{0,i}$ the density of neutral particles of species $i$ and $\tau_i^q$ the confinement time of ions of this species and charge state $q$. The terms $\langle\sigma v\rangle_{q_1,q_2}^{\text{ion}}$ and $\langle\sigma v\rangle_{q_1,q_2}^{\text{cx}}$ are the rate coefficients of ionization and charge exchange processes from charge state $q_1$ to $q_2$, with $\sigma$ and $v$ the corresponding cross sections and interaction velocities. The first term of the above equation corresponds to the production rate of ions with the charge state $q$ from lower charge state and the second term is the further ionization of these ions to higher charge state. The third and fourth terms represent the production of the studied ions through charge exchange processes from the higher charge state and losses to lower charge states. The last term represents the ion losses through diffusion and transport from the plasma. This term is also relevant in light of beam extraction, as the extracted ions constitute of favorable losses from the plasma towards the extraction aperture.

High charge states are reached by consecutive electron impacts in a stepwise process. Many theoretical and empirical models have been developed to estimate the electron impact ionization cross section $\sigma_{q-1,q}$ [31], among which the empirical formula proposed by Lotz [32–35] is still widely accepted and used, describing the cross section as

$$\sigma_{q-1,q} = \sum_{j=1}^{N} a_j n_j \frac{\ln(E/P_j)}{EP_j} \{1 - b_j \exp[-c_j(E/P_j - 1)]\} \quad \text{and} \quad E \geq P_j, \quad (2.6)$$

where $E$ is the energy of impacting electron, $P_j$ is the binding energy of electrons in the $j$-th subshell ($P_1$ being the ionization potential), $n_j$ is the number of electron in the $j$-th subshell and $a_j$, $b_j$, $c_j$ are empirically determined constants, which depend on the atom or ion species to be ionized. The electron energy constraint presented in the above equation ($E \geq P_j$) dictates that only those terms (subshells) in the sum are included for the cross section calculation for which the electron energy is sufficient to remove electrons. Thus the binding energy of the electrons in the first, outermost subshell sets an energy threshold for the impacting electron for the ionization to occur. For neutral particles this is the first ionization potential, for singly charged ions the second ionization potential, and so forth. At energies higher than this threshold the cross section has strong dependence on the impacting electron energy, reaching

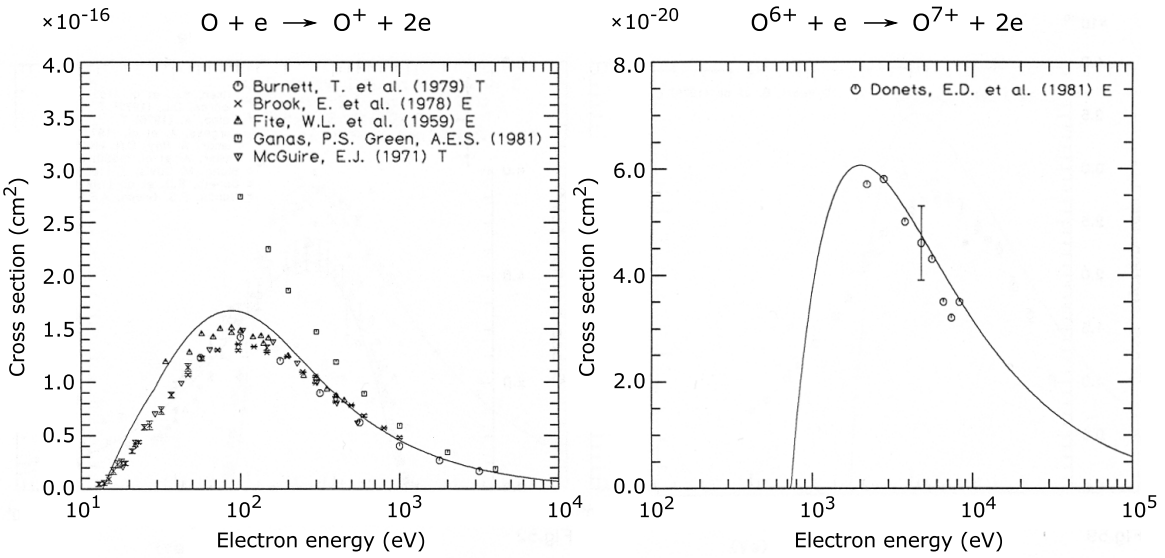


Figure 2.1: Electron impact ionization cross sections of $^{16}$O and $^{16}$O$^{6+}$ as a function of the impacting electron energy. Figure modified from Ref. [38], which includes references to the presented experimental data.

maximum at around 3 – 4 times the threshold value and decreasing with higher energies [15]. An example is presented in Fig. 2.1. Consequently, the production of highly charged ions requires electron energies up to tens or hundreds of keV. It has been demonstrated experimentally that the efficient ECR heating of electrons provides such energies [36, 37].

Charge exchange between ions and neutral atoms or molecules through collision processes is the main mechanism reducing the ion charge state in the plasma. The cross sections can be estimated with the empirical model presented by Müller and Salzborn [39, 40]. At low ion energies the charge exchange cross section depends only on the initial ion charge state $q$ and the first ionization potential $P_1$ of the neutral particle, and can be described as

$$\sigma_{q,q-k} = A_k \, q^{\alpha_k} \, P_1^{\beta_k}, \tag{2.7}$$

where $A_k$, $\alpha_k$ and $\beta_k$ are parameters acquired from fitting to experimental data and $k$ denotes the number of electrons transfered in the process. In general the single electron transfer is the dominant process and can be used to estimate the total charge exchange cross section [40]:

$$\sigma_{q,tot} \approx \sigma_{q,q-1} = 1.43 \cdot q^{1.17} \cdot P_1^{-2.76}, \tag{2.8}$$

where $\sigma_{q,tot}$ is in cm$^2$ when $P_1$ is given in eV.

As the above equation shows, the charge exchange cross section increases with increasing ion charge state. In addition, the charge exchange cross sections are significantly higher

than the electron impact ionization cross sections [15]. In order to compensate for this and produce highly charged ions, the electron density in the plasma must be significantly higher than the neutral density. These conditions are reached by operating the ECR ion source at low vacuum conditions reached with efficient pumping of the plasma chamber. The pumping is normally arranged from both axial and radial directions, if permitted by the ion source magnet structure around the plasma chamber (see section 2.4.1). As an example, the normal baseline vacuum (no material injection) measured for the JYFL 14 GHz ECRIS is in the $10^{-8}$ mbar region. During beam production with material injected into the plasma chamber the neutral pressure is normally varied from high $10^{-8}$ mbar to the $10^{-6}$ mbar region, depending on the ion species for which the ion source is optimized. High total extracted beam currents favoring the low charge state ions are produced when operating in the $10^{-6}$ mbar region, whereas the production of high charge state ions is optimized in the high $10^{-8}$ mbar or low $10^{-7}$ mbar regions, associated with low total extracted currents. Usually the pressure can not be measured directly from the plasma chamber due to technical constraints. This is also the case with the JYFL 14 GHz ECRIS, where the measurement is performed through one of the radial pumping ports of the plasma chamber. Consequently, the actual pressure inside the chamber is higher than the measured value.

## 2.4 Magnetic confinement of plasma

The external magnetic field of the ECRIS serves two purposes. Firstly, the field is necessary to form a region in the plasma chamber where the ECR condition is fulfilled. Secondly, the field provides magnetic confinement for the charged particles created through the ionization processes, leading to the formation of quasineutral plasma. This significantly increases the time the electrons and ions remain in the plasma volume. For electrons this allows multiple passes through the resonance and consequently enables them to reach the energies required for the production of highly charged ions. For ions the increased confinement time increases the probability to experience multiple consecutive electron impacts and thus reach higher charge states. The decreased particle losses from the plasma also decreases the required input energy to the system to produce and sustain a certain plasma density. Production of highly charged ion beams with high beam currents from the ion source plasma is obtained through a careful compromise between favored particle losses and confinement.

### 2.4.1 Minimum-$B$ configuration

The magnetic confinement in most ECR ion sources is based on the minimum-$B$ magnetic field structure. In this configuration the magnetic field minimum is located near the center of the plasma chamber and the field increases in every direction outwards from the minimum. In addition to providing efficient confinement, this

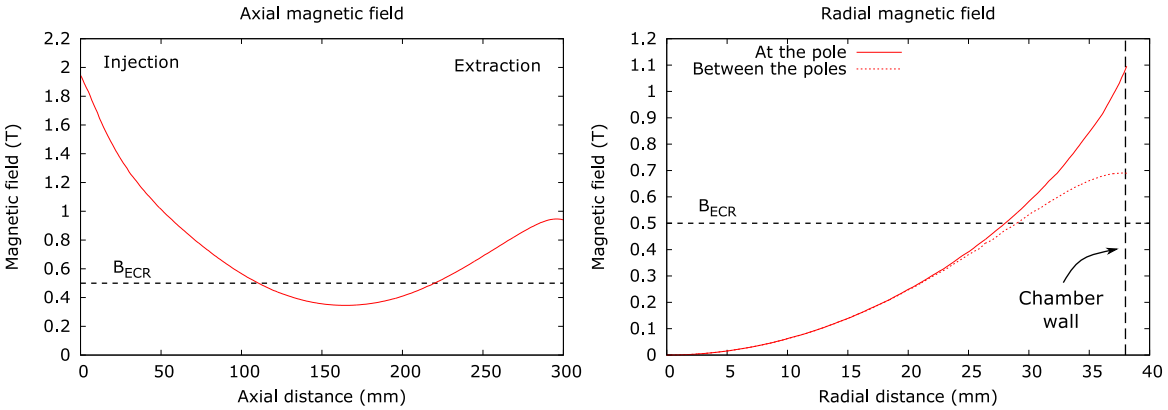


Figure 2.2: The axial and radial magnetic fields of the JYFL 14 GHz ECRIS. The radial field is presented at the pole and between the poles of the permanent magnet hexapole. The resonance field $B_{\mathrm{ECR}}$ is also indicated.

configuration also stabilizes the plasma against MHD instabilities [15]. Due to the minimum-$B$ structure, the ECR condition (Eq. (2.1)) is fulfilled on a closed magnetic equipotential surface, traditionally called the *ECR surface*.

The minimum-$B$ configuration is normally realized with a combination of solenoidal field providing the axial confinement and a multipole field providing the radial confinement. The solenoidal field is realized with coils at the ends of the plasma chamber producing axial mirror trap. In room temperature ion sources the multipole field is usually created with permanent magnets placed around the plasma chamber. In superconducting devices they are replaced with coils. Figure 2.2 presents as an example the axial and the radial magnetic fields of the JYFL 14 GHz ECRIS.

The choice of the multipole is a balance between the size and shape of the axial plasma flux towards the plasma chamber ends (and beam extraction) and the radial field strength [5]. The radial magnetic field of a multipole scales with the number of poles $n$ as $B_{\mathrm{r}} \propto r^{\frac{n}{2}-1}$. When the number of poles increases, the radial field close the plasma chamber axis decreases, which increases the area of the plasma flux coinciding with the plasma chamber ends. The number of poles also changes the shape of the flux pattern. For example, when combined with the solenoidal field, quadrupole yields a narrow line shaped pattern, hexapole a triangular pattern and octupole a square pattern. Hexapole offers a good compromise for a flux shape that is easy to extract through round extraction aperture, while still keeping the flux concentrated close to the chamber axis. Consequently, hexapole is used in virtually all ECR ion sources, though quadrupole and octupole configurations have also been studied experimentally [41, 42].

The hexapole can be constructed as a closed Halbach structure [43] or an open structure with spaces between the magnetic poles. The closed structure can provide higher magnetic fields as the full volume around the plasma chamber can be filled with magnet material. The advantage of the open structure is the radial access to the

plasma volume, allowing diagnostics, material introduction to plasma and enhanced vacuum pumping. Recently the use of additional iron tips at the magnetic poles has been demonstrated as a possible way to enhance the radial field produced with an open hexapole structure [44, 45].

The extracted ions, i.e. the ion beam, constitute of particle losses from the plasma. In order to favor particle losses through the extraction aperture and consequently enhance the extraction efficiency, the axial mirror field is asymmetric with lower peak magnetic field at the extraction end of the plasma chamber (see Fig. 2.2). The scaling of the ECRIS magnetic fields to achieve good performance is discussed further in section 2.6.1.

### 2.4.2 Magnetic mirror and loss cone

Charged particle confinement in minimum-$B$ field is based on the concept of *magnetic mirror*. Let us examine a particle with charge $q$, mass $m$ and velocity components $v_\perp$ and $v_\parallel$ with respect to the external magnetic field. The gyromotion of the charged particle produces circulating current $I = {}^{|q|\omega}/_{2\pi}$, where $\omega$ is the angular frequency. The current loop, encompassing an area $A = \pi r_\mathrm{L}^2$ with Larmor radius $r_\mathrm{L}$, produces magnetic moment $\vec{\mu}$, magnitude of which can be described as

$$\mu = IA = \frac{|q|\omega}{2\pi}\pi r_\mathrm{L}^2 = \frac{W_\perp}{B}, \tag{2.9}$$

where $\omega = {}^{v_\perp}/_{r_\mathrm{L}} = {}^{|q|B}/_{m}$ and $W_\perp$ the perpendicular kinetic energy of the particle with respect to the magnetic field. If the magnetic field variation during one particle revolution is small, the magnetic moment is conserved during the particle motion. Assuming no electric fields, the particle kinetic energy is also conserved. As the particle moves to increasing magnetic field, the perpendicular velocity component increases, as dictated by the conservation of magnetic moment in Eq. (2.9). As the total kinetic energy is conserved, this leads to decreasing parallel velocity, until the particle reaches the location where its parallel velocity reaches zero and is reflected back. This location is called the reflection or mirror point.

As the above description suggests, the ratio of the particle's perpendicular and parallel velocities determines whether or not it remains confined in the magnetic mirror field. This ratio can be related to the properties of the magnetic field with pitch angle $\theta$, defined in the velocity space ($v_\parallel$,$v_\perp$) as [5]

$$\tan\theta = \frac{v_\perp(s)}{v_\parallel(s)} = \sqrt{\frac{W_\perp(s)}{W_\parallel(s)}} \quad \text{and} \quad v_\perp = v\sin\theta \tag{2.10}$$

at location $s$. Using these definitions and Eq. (2.9) the magnetic moment of the particle can be written as

$$\mu = \frac{W_0 \sin^2\theta}{B(s)}. \tag{2.11}$$

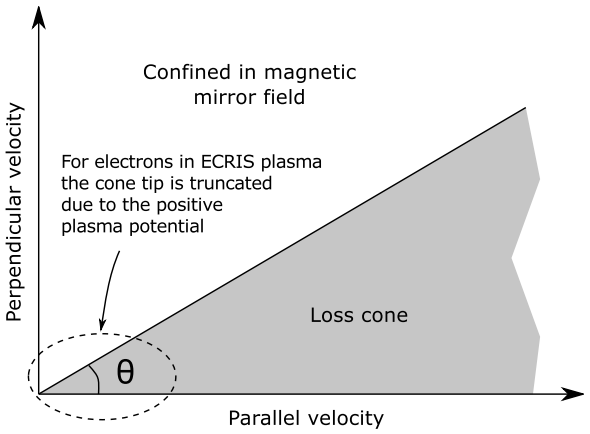


Figure 2.3: Loss cone of magnetic mirror field in velocity space. For electrons in ECRIS plasma the cone tip at low velocities is truncated due to the positive plasma potential.

At the reflection point $v_{\parallel} \to 0$ and consequently pitch angle $\theta \to \pi/2$. As the magnetic moment remains constant, writing the Eq. (2.11) for the particle at location $s$ and at the reflection point yields the definition of pitch angle using the external magnetic field

$$\sin\theta = \sqrt{\frac{B(s)}{B_{\mathrm{refl}}}}, \tag{2.12}$$

where $B_{\mathrm{refl}}$ is the magnetic field at the reflection point. The particle is trapped in the mirror field if $B_{\min} \leq B_{\mathrm{refl}} \leq B_{\max}$. Using this condition the confinement limit of the pitch angle can be written with Eq. (2.12) as

$$\sqrt{\frac{B(s)}{B_{\min}}} \geq \sin\theta \geq \sqrt{\frac{B(s)}{B_{\max}}}. \tag{2.13}$$

The left side of the equation is always fulfilled, imposing no limitation to the particle confinement. The right side of the equation thus describes the confinement condition in terms of velocity components relating them to the properties of the confining magnetic field. Particles which do not fulfill this requirement are in the region of velocity space called the *loss cone*, presented in Fig. 2.3, and escape from the magnetic mirror. The loss cone limit for particles starting from the magnetic minimum is

$$\sin\theta = \sqrt{\frac{B_{\min}}{B_{\max}}} = \frac{1}{\sqrt{R}}, \tag{2.14}$$

where $R = {}^{B_{\max}}/_{B_{\min}}$ is the *mirror ratio*, usually used to describe magnetic mirror systems. With ECR ion sources the $B_{\min}$ is usually replaced in the mirror ratio with $B_{\mathrm{ECR}}$, because crossing the resonance has a strong influence on the electron perpendicular velocity, which determines the electron confinement. Also, with ECR ion sources the loss cone for electrons is truncated at low velocities due to the attractive influence of the positive plasma potential, which is discussed in section 2.4.4.

### 2.4.3 Collisions in plasma

The collisions between electrons and ions leading to ionization and collisions between ions and neutral particles leading to charge exchange were discussed in section 2.3. In addition to this, the electrons and ions in plasma also experience collision processes between themselves. The average electron – electron collision frequency in the plasma can be estimated as [46]

$$\langle \nu_{ee} \rangle \approx \frac{10^6 \, n_e e^{5/2} \ln \Lambda}{\epsilon_0^2 m_e^{1/2} T_e^{3/2}}, \tag{2.15}$$

where $n_e$ is the electron density, $e$, $m_e$ and $T_e$ the electron charge, mass and temperature, $\epsilon_0$ the permittivity of vacuum and $\ln \Lambda$ is the Coulomb logarithm. For laboratory plasmas it can be estimated that $\ln \Lambda \approx 10$. [46]. The ion – ion collision frequency between ions of species $i$ and $j$ can be described as [30]

$$\nu_{ij} = \frac{6.8 \cdot 10^{-8} \, q^2 \ln \Lambda}{T_i^{3/2} A_i} \sum_j \sqrt{A_j} \sum_q n_j^q q^2, \tag{2.16}$$

where $q$ is the ion charge state, $T_i$ the ion temperature, $A_i$ and $A_j$ the mass number of ion species $i$ and $j$ and $n_j^q$ the density of ions of species $j$ and charge state $q$. Using the effective mean ion charge state in the plasma, $q_{\text{eff}}$, it can be estimated that $\sum_q n_j^q q^2 = n_e q_{\text{eff}}$. For both of the above equations the temperatures are in eV and densities in $\text{cm}^{-3}$, which yields the collision frequencies in units of $\text{s}^{-1}$ or Hz. Both of the equations assume that the particle energies follow Maxwell-Boltzmann distributions characterized by the the electron and ion temperatures $T_e$ and $T_i$.

Collisions between particles in plasma can alter the ratio of the particles' perpendicular and parallel velocities. Consequently, particles that exhibit high rate of collisions can be scattered into the loss cone. In addition, the collisions between charged particles randomize the particle motion in the confining magnetic field. The principle of the magnetic confinement presented in the previous sections assumes unperturbed particle motion which is dictated by the Lorentz force. If the particles are very collisional, they no longer strictly follow the external magnetic field. The degree of magnetization can be estimated by comparing the particle collision and gyrofrequencies (see Eq. 2.1). If the collision frequency is higher than the gyrofrequency, i.e. the particle experiences multiple collisions during the time required for one revolution around magnetic field line, the particle motion is no longer dictated by the magnetic field and the particles can not be considered magnetized.

The electrons in ECRIS plasma range from thermal electrons with $10^1$ eV energies up to hot electrons with energies in the order or excess of $10^5$ eV. Due to the ECR heating the electron population is characterized by accumulation of electrons at high energies. This distorts the energy distribution, making the assumption of Maxwell-Boltzmann energy distribution in Eq. 2.15 doubtful. However, the equation does allow evaluation of an upper limit for the electron collision frequency by assuming that

the whole electron population consists of the cold electrons, characterized by electron temperature $T_e = 10$ eV. Using the electron density of $5 \cdot 10^{11}$ cm$^{-3}$, obtained from ECRIS plasma experiments [30], this yields electron collision frequency of $10^7$ s$^{-1}$. With the magnetic field values associated with modern ECR ion sources the electron gyrofrequencies are still several orders of magnitude higher than this upper limit approximation, typically $\geq 10^{10}$ s$^{-1}$. As the hot electrons present in the ECRIS plasma are in reality even less collisional, it can be concluded that the electron population is well magnetized in the ECRIS plasma.

Due to the selective heating of electrons with the electron cyclotron resonance, the ions remain cold in the ECRIS plasma with energies around a few eV. Using reasonable assumption for argon plasma, $n_e = 5 \cdot 10^{11}$ cm$^{-3}$ and $T_e = 500$ eV, derived from experiments [30, 47], the collision frequencies of e.g. argon charge states 1+ and 12+ are $4.3 \cdot 10^5$ and $6.2 \cdot 10^7$ s$^{-1}$. With magnetic field variation between 0.5 and 1 T, the corresponding ion gyrofrequencies range from $1.9 \cdot 10^5$ to $3.8 \cdot 10^5$ s$^{-1}$ for 1+ and from $2.3 \cdot 10^6$ to $4.6 \cdot 10^6$ s$^{-1}$ for 12+. As the collision frequency scales with the square of the ion charge state while the gyrofrequency has linear dependency of the charge state, the difference between collision and gyrofrequencies increases with ion charge. For example, with 0.5 T magnetic field the collision frequency is more than an order of magnitude higher than the gyrofrequency with charge states $q \geq 5+$. For 1 T this occurs with $q \geq 9+$. As these examples indicate, the ions are not magnetized in the ECRIS plasma [30, 47].

The previous calculations are based on plasma density which is determined in the ECRIS core plasma. A rough order of magnitude approximation for the plasma density near the extraction aperture can be made based on the extracted ion current. If it is assumed that the ion velocity is Maxwell-Boltzmann distributed and the extracted current through the extraction aperture is governed by directional ion flux from the plasma, it can written

$$I_{\text{ext}} = \frac{1}{4}\langle q \rangle e n_i \langle v \rangle A, \tag{2.17}$$

where $\langle q \rangle$ is the mean ion charge state, $e$ the electron charge, $n_i$ the ion density, $\langle v \rangle$ the mean ion velocity and $A = \pi r^2$ the area of the round extraction aperture with radius $r$. It can be assumed that $n_e = \langle q \rangle n_i$ based on quasineutrality and the mean velocity can be expressed as $\langle v \rangle = \sqrt{8kT_i/\pi m_i}$, where $kT_i$ is the ion thermal energy and $m_i$ the ion mass, which yields for $n_e$ the expression

$$n_e = \frac{4I_{\text{ext}}}{e\pi r^2}\sqrt{\frac{\pi m_i}{8kT_i}}. \tag{2.18}$$

For argon plasma with 1 eV ion energy and 1 mA of extracted beam through extraction aperture with 4 mm radius, the above equation yields plasma density $n_e \sim 10^{11}$ cm$^{-3}$. This result is still in the same order of magnitude as the estimates used for the collision calculations discussed above, suggesting that the ions are collisional even in the plasma

volume in the vicinity of the extraction aperture. However, it is noted that the above approximation does not take into account the effect of the external magnetic field.

Though the ions themselves are not directly magnetized, the ions are bound to the magnetic field lines indirectly through the dynamics of the magnetized electron population, as the experimental results reported in a recent study [48] indicate. In that study the ion and electron current density distributions were spatially resolved near the extraction region of an 11 GHz ECR ion source. It was shown that the strongly magnetized electrons follow the external magnetic field lines, and the ion distribution is localized around the electron distribution maintaining the plasma quasineutrality. This view is also in good agreement with ECRIS plasma simulations taking into account the ion – ion collisions (see e.g. Ref. [49]).

### 2.4.4 Plasma potential

Due to their higher mobility in the plasma, electrons have higher intrinsic loss rate to the plasma chamber walls than ions [50]. In order to retain the quasineutrality, the charge carried by the escaping electrons must be compensated with positive ion charge. As a result, a positive *plasma potential* builds up with respect to the chamber walls to equalize global electron and ion losses by retarding the electrons and accelerating the ions to the walls. The plasma potential of ECR ion sources has been the subject of extensive experimental studies (see e.g. Refs. [50–54]) and has been determined to be in the order of $10^1 - 10^2$ V. It has been observed that low plasma potential values correlate with good ion source performance, yielding enhanced production of highly charged ions.

Furthermore, it has been suggested [55, 56] that the improving electron confinement with electron temperature leads to increased density of hot electrons in the core plasma, creating a local negative potential, which contributes to the confinement of ions.

## 2.5 Introduction of material into ECRIS plasma

In order to produce a beam of desired ion species, the element to be ionized needs to be introduced into the plasma volume to undergo ionization and subsequent extraction. Elements which are in gaseous form in room temperature or solid elements which form gaseous compounds (like $CO_2$, $SF_6$) can simply be injected into the plasma chamber through precision valves. For solid elements a number of different methods have been developed. The solid material can be evaporated with a resistively or inductively heated miniature oven, which is inserted into the plasma chamber either axially or radially [57–59]. If the thermal properties of the material are not suitable for this approach, it can be inserted into the plasma chamber as a solid sample and biased negatively to achieve sputtering by the plasma ions [60]. The sample can also be injected further into the plasma to be directly heated by the energetic plasma electrons

resulting to evaporation of the material, in which case the method is usually referred to as injection technique [61, 62]. Laser ablation can also be used to evaporate solid material directly into the plasma volume [63]. Another option is the MIVOC (Metal Ions from VOlatile Compounds) method [64], where the desired element is part of a volatile organic compound with high room temperature vapour pressure, in the order of $10^{-3}$ mbar or higher. A sample of the compound is connected to the plasma chamber vacuum through a delivery assembly, undergoes evaporation and drifts into the plasma volume.

## 2.6 ECRIS performance

### 2.6.1 ECRIS scaling laws

In 1987 Geller *et al.* proposed a set of semiempirical scaling laws to provide a simplified way to estimate and extrapolate the performance of ECR ion sources in terms of a few controllable parameters [65]. Over the years these scaling laws have proved to be valuable, even if only approximate, guidelines for the design of new ECR ion sources [5, 65, 66]. The scaling laws can be summarized as [65]

$$I^q \propto \omega_{\mathrm{RF}}^2 m_{\mathrm{i}}^{-1} \tag{2.19}$$

$$n_e v_e \tau \propto \begin{cases} B_{\mathrm{avg}}^{3/2} \\ \omega_{\mathrm{RF}}^{7/2} \end{cases} \tag{2.20}$$

$$q_{\mathrm{opt}} \propto \begin{cases} \log B_{\mathrm{avg}}^{3/2} \\ \log \omega_{\mathrm{RF}}^{7/2} \\ P_{\mathrm{RF}}^{1/3} \end{cases} \tag{2.21}$$

where $n_e$ is the electron density, $v_e$ the electron velocity, $\tau$ the ion confinement time, $B_{\mathrm{avg}} = \frac{1}{2}(B_{\mathrm{max}} + B_{\mathrm{min}})$ the average magnetic field, $\omega_{\mathrm{RF}}$ the heating microwave angular frequency, $P_{\mathrm{RF}}$ the microwave power transmitted to the plasma chamber, $q_{\mathrm{opt}}$ the charge state with maximum current, $I^q$ the value of this current and $m_{\mathrm{i}}$ the ion mass.

The scaling laws indicate that the ECR ion source performance strongly depends on the frequency of the heating microwave and the confining magnetic field. Increasing the magnetic field improves the ion and electron confinement, which subsequently increases the plasma density and shifts the charge state distribution to higher values. The performance improvement with increasing microwave frequency has been associated with the increasing critical plasma density (see Eg. (2.4)) [65]. In order to fulfill the resonance condition, the magnetic fields have to be scaled with the frequency. Higher microwave power increases the energy available for electron heating, allowing higher electron energies required for the production of highly charged ions.

It has been observed experimentally that the structure of the ECRIS minimum-$B$ magnetic field has significant and more complex relation to the ion source performance

than suggested by the scaling laws (2.20) and (2.21). The role of the field structure, especially in terms of the axial and radial mirror ratios, on the performance of ECR ion sources has been the subject of extensive studies [67–75]. This has led to the formulation of the semiempirical scaling laws, sometimes referred to as the high-$B$ operation mode, for the ECRIS confining magnetic field. These scaling laws can be combined and expressed as [15, 72]

$$\frac{B_{\text{inj}}}{B_{\text{ECR}}} \geq 4 \qquad \frac{B_{\text{ext}}}{B_{\text{ECR}}} \geq 2 \qquad \frac{B_{\text{rad}}}{B_{\text{ECR}}} \geq 2 \qquad \frac{B_{\text{min}}}{B_{\text{ECR}}} \approx 0.8 \qquad \frac{B_{\text{ext}}}{B_{\text{rad}}} \approx 0.9 \tag{2.22}$$

where $B_{\text{inj}}$ and $B_{\text{ext}}$ are the axial magnetic field maxima at the plasma chamber injection and extraction, $B_{\text{rad}}$ the maximum radial field, $B_{\text{min}}$ the minimum field and $B_{\text{ECR}}$ the resonance field. The magnetic field maxima at the extraction is a compromise between efficient confinement required to produce highly charged ions and allowing particle losses to enable ion extraction. The mirror ratio should be the lowest at extraction to favour particle losses towards the extraction aperture, enhancing the extraction efficiency.

It has been suggested [68, 70] that the improved performance of ECRIS when operated with high magnetic mirror ratios as stated by the above scaling laws follows from the MHD instability limitation. The MHD criteria states that the particle pressure in the plasma must be significantly lower than the magnetic pressure induced by the external field. In ECRIS plasma the electron temperatures are significantly higher than those of ions and neutral particles, so the MHD criteria can be described as [68]

$$n_e k T_e \ll \frac{B^2}{2\mu_0}, \tag{2.23}$$

where $n_e$ is the electron density, $k$ is the Boltzmann constant, $T_e$ is the electron density, $B$ the magnetic field and $\mu_0$ the permeability of vacuum. The equation suggests that the increase in the confining magnetic field allows higher electron densities and temperatures in the plasma before the onset of MHD instabilities, which leads to improved ion source performance.

### 2.6.2 Methods to improve ECRIS performance

Numerous techniques have been developed to improve the performance of ECR ion sources, especially the production of highly charged ions. The most widely adopted ones include (1) the gas mixing technique, (2) a biased disc, (3) multiple frequency heating and (4) optimization of plasma chamber surface material and surface coatings.

In the gas mixing technique an additional, lighter element gas is injected into the plasma chamber, which results into an increase in the beam current of the high charge states of the heavier element [30, 56]. The effect is related to ion cooling, though other contributing processes such as improved plasma stability have also been proposed [76].

Ions of the heavier element experience ion cooling as they transfer momentum to the lighter ions through ion-ion collisions in the plasma. This increases the confinement time of the heavier ions leading to an increase in their mean charge state. Gas mixing also reduces the consumption of the heavier element, because the lighter gas can sustain the bulk plasma, where only small quantities of the heavier element is introduced. This is desirable when using e.g. expensive isotopes.

The production of highly charged ions can be improved by installing an electrode to the injection end of the ECRIS plasma chamber and biasing it negatively up to a few hundred volts [77–79]. The electrode, often called biased disc due to its general shape in most ECR ion sources, acts as an electrostatic mirror, reflecting axially escaping cold electrons back to the plasma, increasing the electron density. Additionally, in order to maintain quasineutrality the ion losses also decrease, increasing the ion confinement time and subsequently the production of highly charged ions. Other processes which have been proposed to contribute to the improved ion source performance are secondary electron emission from the biased disc and alteration of the plasma potential.

The introduction of multiple heating microwave frequencies into the ECR plasma can be used to substantially increase the beam currents of highly charged ions [80–83]. Usually one or two additional frequencies are used in conjunction with the primary heating frequency. According to the current (qualitative) understanding, the improved source performance is the result of the generation of multiple concentric ECR surfaces inside the plasma chamber and the subsequent increase in the volume of efficient electron heating. It has been observed experimentally that multiple frequency heating improves the plasma stability. Also, it has been observed that the spacing of the frequencies should be adequate to achieve optimal performance. For example, the main heating frequency of the JYFL 14 GHz ECRIS is 14.1 GHz and the optimal 2-frequency performance is achieved when the secondary frequency is about 11.5 GHz [54].

The plasma chamber surface material has an impact on the ECRIS performance. This was first observed as an improved ion source performance after production of Si beams, and thus became first to be called the ”silicon effect” [84]. Based on current knowledge, the performance improvement is associated with the formation of an oxide layer on the surface of the plasma chamber with high secondary electron emission coefficient, providing increased flux of cold electrons into the plasma and consequently increasing the plasma electron density. The coating effect has also been observed with $Al_2O_3$ and MgO [85] and subsequently different coating methods, additional coated surfaces and replaceable plasma chamber liners have been studied to boost the ion source performance [86–89]. It has been observed that even without active oxidization aluminium plasma chamber provides improved performance over copper or stainless steel [90]. Consequently aluminium has become a widely adopted material for ECRIS plasma chambers.

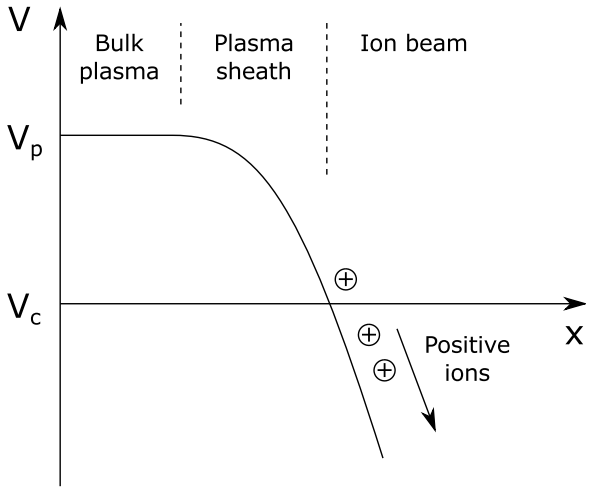


Figure 2.4: Schematic presentation of the positive ion extraction from plasma. The bulk plasma has positive potential $V_p$, from which the ions are extracted through the plasma sheath, where the plasma density and potential drops, and accelerated into ion beam with the potential difference between the plasma chamber (ion source bias, potential indicated as $V_c$) and the following extraction electrodes.

## 2.7 Beam extraction

Ions are extracted from the plasma through the extraction aperture at the end of the plasma chamber and accelerated into an ion beam with a potential difference between the chamber and the first electrode of the following beam extraction system. This potential difference is usually called the extraction (or acceleration) voltage, and the space between the extraction hole and the following electrode is the acceleration gap. In addition to these, the extraction system usually comprises of a set of electrodes immediately downstream from the extraction aperture which are used to manipulate the properties of the ion beam, providing tuning capabilities to match the beam to the following beam transport section. The energy of the extracted beam is defined by the potential difference between the plasma chamber and the beamline, with a small alteration due to the positive potential of the plasma from which the ions are extracted. Usually the most convenient arrangement is to bias the ion source plasma chamber to high positive potential and keep the beamline at ground potential.

The trajectories of the extracted ions determine the initial beam properties and quality, and are influenced by several factors. These include the properties of the plasma, which determines e.g. the ion transverse temperature which contributes to the beam divergence, the electric and magnetic fields present in the extraction region and the space charge of the beam itself. As such, careful beam extraction design is crucial to ensure good beam quality.

A schematic presentation of the positive ion extraction from bulk plasma with plasma potential $V_p$ is presented in Fig. 2.4. The ions are extracted through a *plasma sheath*,

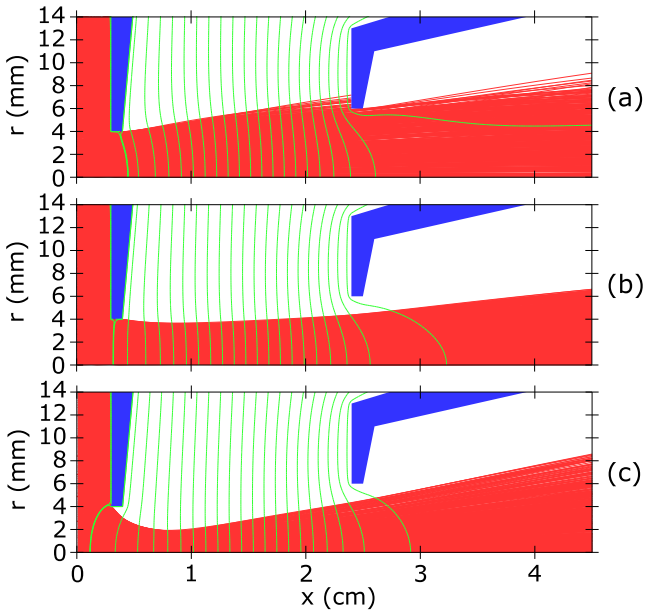


Figure 2.5: The relation between the potential distribution at the extraction aperture and the initial beam behavior demonstrated with a simple two electrode (diode) extraction system. Equipotentials are indicated with green lines. Simulations performed with IBSimu [91] by altering the electric field strength in the acceleration gap.

where the plasma density and potential drop from the values associated with the bulk plasma. This enables the positive ions to be accelerated from the quasineutral bulk plasma to the region where they are influenced by the potential difference (extraction voltage) between the plasma chamber and the following extraction electrode, and accelerated into an ion beam. Several theoretical models have been developed to model the positive ion extraction. These are discussed in detail e.g. in Ref. [92].

As a boundary layer between the bulk plasma and the accelerated beam particles, the plasma sheath has significant impact on the initial properties of the extracted beam. The potential distibution in this region in the immediate vicinity of the extraction aperture has strong influence on the motion of the slow ions before acceleration by the extraction voltage. The distribution can be visualized conveniently with equipotential surfaces, and observation of the shape and location of the surfaces close to the plasma chamber potential provides useful insight into the initial properties of the extracted beam, as is presented in Fig. 2.5. The potential distribution in this region is strongly affected by the balance of the plasma density, the ion and electron temperatures and the electric field in the acceleration gap. Increasing the plasma density and particle temperatures pushes the plasma sheath outwards from the plasma, resulting to convex shape of equipotential surfaces close to the chamber potential. As a result, the extracted beam becomes initially diverging, as presented in Fig. 2.5(a). When the density and temperatures are lowered, or the electric field is increased, the equipotential surfaces

become first flat, producing almost parallel initial beam (Fig. 2.5(b)) and then concave with converging initial beam (Fig. 2.5(c)). Due to the good correlation between the equipotential surface corresponding to the chamber potential and the initial beam behavior, the concept of *plasma meniscus* is often associated with this surface. In this approach the influence of the plasma sheath region on the beam is simplified by reducing it to a boundary surface between the plasma and the beam, from which the ions are emitted. This emitter analogy does over-simplify the ion behavior in the extraction, but it can sometimes be an useful tool to gain insight into the initial beam behavior.

The maximum beam current which can be extracted from the plasma is mainly limited by two factors: the ion production limit and the space charge limit. The production limit is governed by the ion source plasma properties, and can be roughly considered to be the result of the balance between the ionization, recombination and loss rates of ions, which determines the total production rate of ions available in the plasma, the plasma volume, which scales the size of the ion population, and finally the ion losses towards the extraction aperture, determining the fraction of the ion population available for extraction. The space charge limit arises from the charge of the extracted ions in the vicinity of the plasma, shielding it from the extraction electric field. The maximum current density in the space charge limited extraction can be described with the Child–Langmuir law [93, 94]

$$j = \frac{4}{9}\epsilon_0 \sqrt{\frac{2q}{m}} \frac{V_{\text{ext}}^{3/2}}{d^2}, \tag{2.24}$$

where $\epsilon_0$ is the permittivity of vacuum, $q$ and $m$ the charge and mass of the extracted ion species, $V_{\text{ext}}$ the extraction voltage and $d$ the acceleration gap length. The above description assumes that the charged particle emitter and the first electrode are in parallel configuration, their transverse dimensions are large compared to the area under consideration and the emitted ions have no initial velocity. Even though these assumptions rarely hold with real ion source extraction systems, the above equation provides a practical approximation for the space charge limited current.

As Eq. (2.24) shows, the space charge limited current increases with extraction voltage. With low voltages the space charge is the limiting factor defining the maximum beam current, and as the voltage increases the current becomes limited by the ion production in the ECRIS plasma. This is demonstrated in Fig. 2.6. As the ECRIS development aims to increase the ion production capabilities of the ion source plasma, it is necessary to increase the extraction voltage accordingly to take advantage of the increased production limit.

The ECRIS plasma produces a distribution of charge states from all the elements which are present in the plasma and subsequently ionized. This is reflected in the ion population which is extracted from the plasma and formed into an ion beam. As a result, the beams extracted from an ECR ion source can be a combination of tens

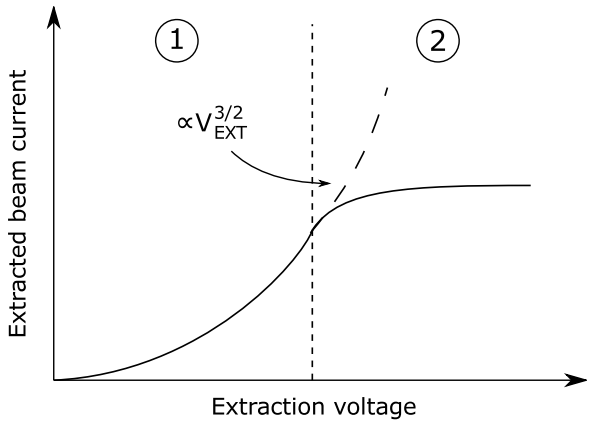


Figure 2.6: Schematic presentation of the extracted beam current as a function of the extraction voltage. With low voltages (section 1) the beam current is space charge limited and follows the $V_{\text{ext}}^{3/2}$ scaling set by the Child-Langmuir law. With higher voltages (section 2) the beam current becomes limited by the ion production in the ion source plasma.

of different ion species with varying element and charge state, depending on the ion source operating conditions. The ion species of interest is usually separated from the total extracted beam with a dipole magnet, usually referred to as the analyzing magnet, located in the beam transport downstream from the extraction region. The separation is based on the difference in the magnetic rigidity of the different ion species. For an ion with mass $m$ and charge $q$, extracted with voltage $V_{\text{ext}}$, the magnetic rigidity is

$$B\rho = \sqrt{\frac{2mV_{\text{ext}}}{q}}, \tag{2.25}$$

where $\rho$ is the radius of curvature of the ion trajectory caused by the magnetic field $B$. As the above equation shows, the trajectories of different ion species are separated based on the ratio of the ion mass and charge, and the ion species of interest is selected for further transport. Consequently, this process is often referred to as $m/q$ separation.

## 2.8 ECRIS beam quality

When discussing ion sources, the most often quoted property regarding the ion beams is the maximum ion current. However, this is only half of the truth, as no matter how high the current is, it is ultimately the beam quality which determines what fraction of the beam can be transported and accelerated for its intended use. With ECR ion sources the beam quality is normally treated in terms of *emittance* and *brightness*, which are introduced in the following sections. This is followed by discussion of the temporal stability of ion beams, which is an important factor in many applications,

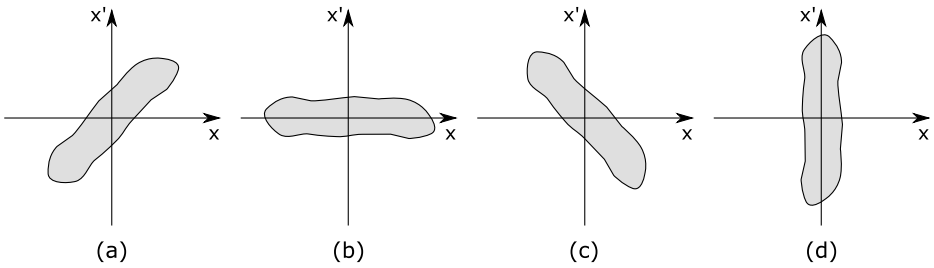


Figure 2.7: Orientation of phase space patterns corresponding to (a) diverging beam, (b) parallel beam, (c) converging beam and (d) beam at focal point.

and beam quality degradation by space charge. Finally, the formation of hollow beam structure and different factors related to it are also discussed.

### 2.8.1 General aspects of beam emittance

Beam emittance is the most widely used measure of the quality of ion beams, and is closely connected to beam transport. Emittance defines the beam quality in terms of the beam focusing properties and the parallelism of the beam particle trajectories. The ion beam propagating towards $z$-direction can be expressed as a distribution of particles in six dimensional phase space composed of three position coordinates $(x, y, z)$ and three momentum coordinates $(p_x, p_y, p_z)$. The volume occupied by the particles in this 6D phase space describes the beam emittance. Small volume, i.e. small emittance, indicates good beam quality, as the variation between the behavior of the individual beam particles is small.

In many cases, especially with cw beams, the transverse beam properties at given location $z$ are of more interest than the longitudinal properties. Thus it is sufficient to limit the emittance analysis to the transverse subspaces $(x, p_x)$ and $(y, p_y)$. Assuming $p_z \gg p_x, p_y$, the transverse momenta can be replaced with angles of propagation

$$x' = \arctan\left(\frac{p_x}{p_z}\right) \approx \frac{p_x}{p_z} \quad \text{and} \quad y' = \arctan\left(\frac{p_y}{p_z}\right) \approx \frac{p_y}{p_z}. \tag{2.26}$$

The beam transverse emittances $\epsilon_x$ and $\epsilon_y$ are determined based on the area occupied by the particles in the $(x, x')$ and $(y, y')$ phase space. This is convenient, as the direct measurement of angles $x'$ and $y'$ are often simpler than the determination of the transverse momenta. The orientation of this transverse phase space pattern can also be used to estimate the collective trends of the particle movement at the given location $z$. Based on this it can be determine if the beam is e.g. converging or diverging. This is demonstrated in Fig. 2.7.

Several different approaches exist for how the exact value of emittance is defined from the area occupied by the beam particles in the phase space [15, 95]. These can be narrowed down to three major cases: (1) determination of the emittance

based on the area of the actual pattern occupied by the particles in the phase space, (2) determination based on the area of an ellipse encompassing this pattern, or (3) statistical determination based on the distribution of particles in the phase space.

The first determination is the most straightforward, and the emittance is determined as the area of the pattern divided by $\pi$. In the $(x, x')$ transverse phase space this can be described as [15]

$$\epsilon_x = \frac{1}{\pi} \int \int dx dx', \tag{2.27}$$

where the integration is performed over the phase space pattern. This definition is sometimes called the *area emittance*. The main shortcoming of this approach is in the evaluation of beams with strong distortions in the phase space and how this relates to beam transport. Beam transport systems are typically described using the concept of *acceptance*, which is the maximum emittance value matching a certain shape in the phase space which the beam can occupy without being collimated during transport. A strongly distorted beam can have small total area, but be impossible to transport as it can not be matched to the acceptance of the beam transport system. In this case the small emittance value, which should indicate good beam quality, is misleading.

The second emittance determination, sometimes called *effective emittance*, strives to amend this problem by enveloping the actual phase space pattern with an ellipse. The ellipse is chosen as it is the shape of the contours of two dimensional Gaussian distribution, and thus often matches quite well with measured emittance patterns. The definition of the emittance is identical to Eq. (2.27), but the integration is performed over the area of the ellipse [95]. With this definition the distortions in the phase space pattern increase the size of the ellipse, giving a better evaluation of the true beam quality, especially in terms of how it is likely reflected in beam transport. An example of this is presented in Fig. 2.8. The main drawback of this definition is the possibility of a gross overestimation of the emittance if the emittance pattern exhibits strong distortions with very low particle density or in the case of low intensity beam halos. This can, however, be amended to some extent by setting density thresholds for the pattern included inside the ellipse.

As the above definitions are based only on the area occupied by the particles in the phase space, they both neglect the variations in the particle density. As a result, the acquired emittance values fail to take into account that certain parts in the phase space with high density are more relevant in the sense of representing the beam (and the beam quality) than other regions with very low density and thus very small contribution to the beam current. These aspects taken into account by the third approach, statistical determination of the emittance, which has gained increased popularity in the accelerator community [96]. The statistical *rms-emittance* is defined as the second moment (i.e. variance) of the distribution of particles $g(x, x')$ which form the ion beam, and can be written as

$$\epsilon_{x,\mathrm{rms}} = \sqrt{\langle x^2 \rangle \langle x'^2 \rangle - \langle x x' \rangle^2} \tag{2.28}$$

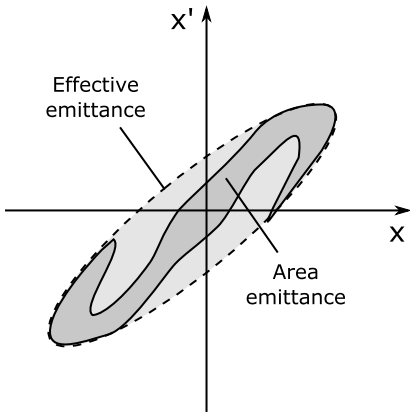


Figure 2.8: Comparison of the area emittance and the effective emittance determined for the same ($x$,$x'$) phase space distribution.

with the expectation values

$$\langle x^2 \rangle = \frac{\sum x^2 g(x,x')}{\sum g(x,x')} \tag{2.29}$$

$$\langle x'^2 \rangle = \frac{\sum x'^2 g(x,x')}{\sum g(x,x')} \tag{2.30}$$

$$\langle xx' \rangle = \frac{\sum xx' g(x,x')}{\sum g(x,x')} \tag{2.31}$$

The rms-emittance value is associated with an elliptical shape in the phase space to visualize the fraction of the beam it represents. Because the elliptical presentation is not limited to be used only with rms-emittance, the transverse emittance is represented with the plain symbol $\epsilon$ without the subscript details in the following equations. The ellipse in $(x, x')$ phase space is defined as

$$\epsilon = \gamma x^2 + 2\alpha x x' + \beta x'^2, \tag{2.32}$$

and the constraint

$$\beta\gamma - \alpha^2 = 1, \tag{2.33}$$

where $\alpha$, $\beta$ and $\gamma$ are known as the *Twiss parameters*. As the definition shows, the Twiss parameters define the orientation and the aspect ratio of the ellipse, and the emittance is the product of the ellipse half-axes (minor and major radii), scaling the ellipse size. The area of the ellipse can thus be expressed as

$$A_{\text{ellipse}} = \pi\epsilon. \tag{2.34}$$

The connection of the Twiss parameters and emittance to the ellipse properties is presented in Fig. 2.9. The Twiss parameters can be defined statistically in similar

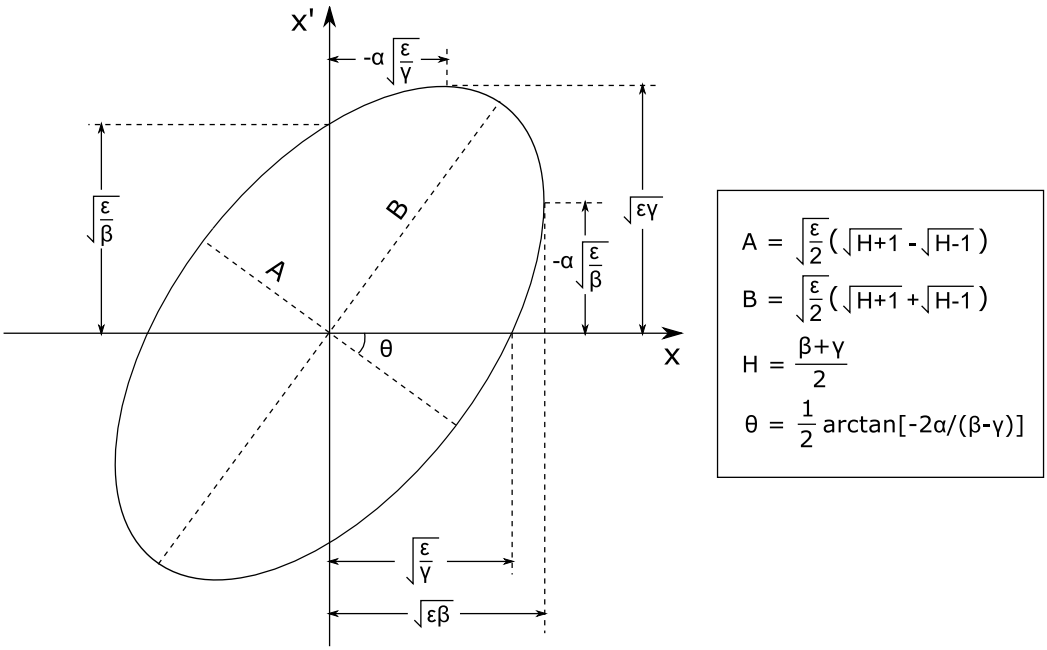


Figure 2.9: The definition of ellipse properties with Twiss parameters.

fashion as the rms-emittance from the distribution $g(x, x')$ with the relations (2.32) and (2.33):

$$\alpha = -\frac{\langle xx' \rangle}{\epsilon} \tag{2.35}$$

$$\beta = \frac{\langle x^2 \rangle}{\epsilon} \tag{2.36}$$

$$\gamma = \frac{\langle x'^2 \rangle}{\epsilon} \tag{2.37}$$

Sometimes emittance values are presented as 4rms-emittance, defined as

$$\epsilon_{x,4\mathrm{rms}} = 4\epsilon_{x,\mathrm{rms}}. \tag{2.38}$$

This convention arises from the observation that for an uniform hard-edge distribution (KV distribution) the phase space ellipse described by the 4rms-emittance exactly covers 100 % of the beam [15]. For beams with more realistic distributions this does not apply, and in order to define the exact percentage of beam inside the rms or 4rms-emittance value, more information is required about the particle distribution. For example, using Bi-Gaussian distribution it can be calculated that the 4rms-emittance covers 86 % of the beam [97]. However, 4rms-emittance is still often used when it is desired to present emittance values that represent a higher fraction of the beam. This can be useful e.g. when statistically calculated emittance results are transfered to beam envelope calculations.

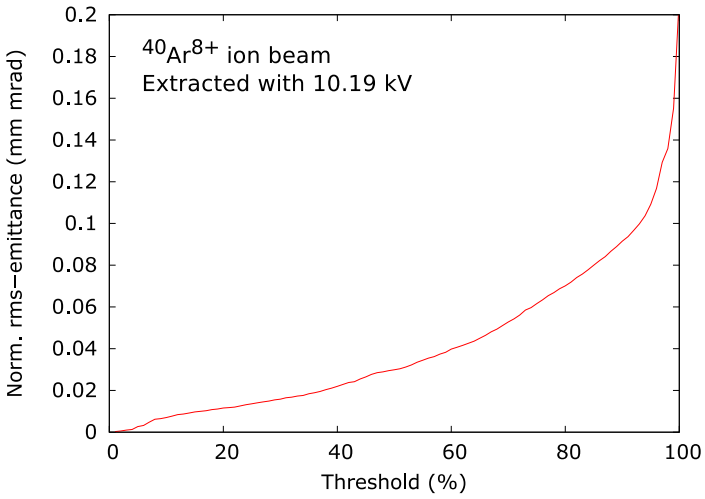


Figure 2.10: An example of the emittance threshold analysis.

Change in the beam energy alters the beam emittance. In acceleration the longitudinal momentum of particles increase, while the transverse momentum remains unaltered. This leads to reduction in $x'$ and $y'$, as is seen from Eq. (2.26), and consequently to decreased emittance. Normalized emittance is used to compare emittances of beams with different energies, and is defined as

$$\epsilon_n = \beta\gamma\epsilon, \tag{2.39}$$

with the relativistic factors $\beta = \frac{v}{c}$ and $\gamma = (1-\beta^2)^{-1/2}$, where $v$ is the speed of the ions and $c$ the speed of light. As ion sources are usually operated with varying extraction voltages, normalized emittance is typically the preferred way to present emittance values.

Sometimes ion beams can exhibit low intensity halos or other distortions at the outer edges of the particle distribution. The structure of the ion beam can be studied by varying the fraction of the distribution in the transverse phase spaces which is included into the emittance calculation, rejecting the low density parts. The beam emittance can then be presented as a function of the beam fraction, as in the example presented in Fig. 2.10. The steady increase in the emittance with low and medium beam fractions represents the core beam, whereas the sharp increase in emittance at the highest beam fractions is contributed by the low intensity beam halo. This technique is called the *emittance threshold analysis*. As the beam halo normally represents a part of the beam which is not usable or will be lost during transport, its contribution to beam emittance is often excluded from the presented emittance values. The fraction of beam used to determine emittance, usually called the threshold value, is usually between 90 and 95 %. If this tradition is used, it is essential to present the threshold value with the emittance values. In the work presented in this thesis, the experimental rms-emittance values have been given with 90 % threshold, unless stated otherwise.

In ideal transport systems the beam emittance is conserved, as is dictated by the Liouville's theorem [95]. However, strictly speaking this only applies to the six dimensional volume definition of beam emittance, not to the transverse subspaces $(x, x')$ and $(y, y')$. If the beam is subjected to nonlinear forces, e.g. due to fringe fields of beamline focusing elements, the particle distributions in the transverse phase spaces can be stretched and distorted, leading to emittance growth.

The connection between the area of the ellipse and the emittance (Eq. (2.34)) has been a source of some confusion, as sometimes $\pi$ is presented with the emittance value and sometimes not, making it unclear whether the numerical values correspond to the emittance (half-axis product) or the area of the ellipse. As a result, it has become the current tradition to include $\pi$ explicitly in to the unit of the emittance as a flag to emphasize that the presented numeric value corresponds to the half-axis product, not the area of the ellipse [95]. However, it has been proposed that this convention should be replaced with clear and unambiguous use of sub- and superscripts in the emittance presentation to describe what the given values represents (e.g. $\epsilon_{x,\mathrm{rms,n}}$ for normalized rms-emittance in $(x, x')$ phase space) [96]. This is used as a guideline when emittance values are presented in this thesis, and all the presented values always correspond to the half-axis product, not the area of the ellipse.

Beam emittance and beam current can be combined to obtain a more comprehensive description of beam quality, linking together the transportability and intensity of beam. This quantity is called the *beam brightness* and is defined as [15]

$$B = \frac{I}{\epsilon_x \epsilon_y}, \tag{2.40}$$

where $I$ is the beam current and $\epsilon_x$, $\epsilon_y$ the beam transverse emittances in $(x, x')$ and $(y, y')$ phase spaces. If the beam and the beam transport follow cylindrical symmetry, it can be assumed that $\epsilon_x \approx \epsilon_y$ and the above equation reduces to

$$B = \frac{I}{\epsilon^2}, \tag{2.41}$$

where $\epsilon$ is either of the transverse emittances.

### 2.8.2 ECRIS specific emittance issues

Two distinct phenomena influence the emittance of ion beams extracted from ECR ion sources that deserve special mentioning. These are the temperature of the extracted ions and the magnetic field where the ions are extracted from.

Assuming Maxwellian temperature distribution for the ions in the ECRIS plasma, the ion temperature contribution to the normalized rms-emittance can be described

as [98][1]

$$\epsilon_{x,\mathrm{rms,n}}^{\mathrm{temp}} = 0.0164\, r \sqrt{\frac{kT_i}{M}}, \tag{2.42}$$

where $r$ is the radius of the extraction aperture (in mm), $kT_i$ is the ion temperature (in eV) and $M$ is the ion mass (in amu).

Due to the minimum-$B$ confinement scheme used with ECR ion sources, the axial magnetic field reaches a local maximum near the extraction aperture. As a result, the ions are extracted from a region of high magnetic field. The decreasing field downstream from the extraction aperture induces beam rotation, which contributes to the beam emittance. Assuming uniform particle density at the extraction aperture and transport of the beam to field free region, the contribution to normalized rms-emittance can be described as

$$\epsilon_{x,\mathrm{rms,n}}^{\mathrm{mag}} = 0.0402\, r^2\, \frac{BQ}{M}, \tag{2.43}$$

where $B$ is the magnetic field at the extraction where the ions originate from and $Q$ is the ion charge state. The derivation of the above equation is presented in detail in the Appendix of Ref. [99] (publication A.VII).

The ion temperatures in ECRIS plasma are in the order of a few eV and the magnetic field at the ion source extraction is in the order of Tesla (e.g. for 14 GHz ECRIS $B_{\mathrm{ext}} \sim 1$ T). Consequently it is seen from equations (2.42) and (2.43) that the magnetic field effect is the dominating contributor to the ECRIS beam emittance.

The magnetic field contribution (2.43) indicates that the beam emittance increases with increasing charge state $Q$. This is, however, contradictory to experimental results, which show decreasing emittance trend with increasing charge state of a particular element [100]. It has been suggested [15, 100] that this is due to high charge states being concentrated closer to the ion source axis than the medium and low charge states. Consequently, the effective extraction aperture is reduced for the high charge states, resulting into lower emittance.

Besides the ion temperature and the magnetic field, the beams extracted from ECR ion sources are also influenced by other phenomena, e.g. space charge effects and field aberrations, which can contribute to the beam emittance. As such, the above emittance contributions should not be regarded as approximations of the actual total emittance, but as theoretical lower limits dictated by two different phenomena.

### 2.8.3 Temporal stability of ion beams

As described above, the ECRIS beam quality is traditionally described mainly in terms of beam emittance and brightness. Recently, however, more interest has been shifting

1. The first edition of the book *The physics and technology of ion sources*, edited by I.G. Brown, is referenced here instead of the newer second edition (Ref. [15]) because the latter includes an error in the equation.

to the temporal stability of ion beams. This has been driven by the requirements of current and forthcoming applications of ECR ion sources. For example, beam current oscillations in high power linear accelerators, which will be utilized by large scale nuclear physics research facilities currently under construction (see e.g. Refs. [101,102]), can cause beam spill at high energies leading to activation of accelerator structures. Also, the increased use and development of medical applications using ion beams, such as carbon radiotherapy, sets strict limitations to the beam current variations (see e.g. Ref. [1]). And, closer to the activities performed at JYFL, many accelerator based industrial applications, such as material modification and testing, require a certain level of temporal stability to maintain high product quality and testing reliability (see e.g. Refs. [2–4]).

The temporal variations exhibited by ion beams can be divided into two categories: long-term fluctuations in the time scales from seconds to days and short-term fluctuations in the millisecond time scales. The long term variations are usually driven by ion source conditioning effects, such as changing gas balance in the plasma chamber and material heating. These phenomena are currently relatively well known and consequently can be taken into account or compensated for in applications.

The exact characteristics of the short-term fluctuations or the processes driving them are not yet well known. A few studies have been published [103, 104], verifying the existence of the beam current oscillations with the 6.4 GHz VEC-ECR, the JYFL 14 GHz ECRIS and the superconducting VENUS with 18 and 28 GHz operation. It has been observed that the oscillations normally occur in the kHz range with amplitudes up to tens of percent of the average beam current. Both the frequency and the amplitude depend on the ECRIS tuning parameters. Increasing the heating microwave power has been shown to increase the oscillation frequency and amplitude, while increasing the biased disc voltage seems to mitigate the oscillations. It has been also demonstrated that double frequency heating shifts the oscillations to higher frequencies. Based on this it is possible that the observations of seemingly improved beam stability often associated to the use of secondary heating frequency are in fact caused by the limitations of the high frequency detection capabilities of the beam current monitoring equipment. The structure of the confining magnetic field also affects the beam fluctuations. Tarvainen *et al.* reported [103] that increasing the minimum magnetic field value in the plasma chamber resulted to pronounced instabilities, while operation at magnetic mirror ratios higher than those suggested by the scaling laws (see Eq. (2.22)) yielded the most stable beams.

Based on the connection between the oscillation characteristics and the ECRIS tuning parameters, it has been suggested by both Tarvainen *et al.* and Taki *et al.* that the short-term beam current fluctuations are caused by plasma processes. Kinetic and MHD instabilities have been proposed as possible candidates.

### 2.8.4 Space charge effects

Ion beam is a collection of charged particles which are in collective motion. Individual particle motion is influenced by the rest of the beam through self-fields, which are generated by the beam charge and current. The electric Coulomb repulsion between the beam particles results into radial force on the individual particles, which is directed outwards from the center of the beam. The beam current exerts force on the particles through the azimuthal magnetic field it produces. This force is radially towards the center of the beam and its impact increases with the beam velocity. The combined radial force is always outwards, and the beam space charge introduces defocusing effect on the beam, which increases the beam divergence and consequently the beam transverse size. This collective effect, which is proportinal to beam current, is sometimes called the *space charge blow up*, discussed e.g. by Mazarakis *et al.* [105].

As an example, lets consider a cylindrical beam with uniform charge density $n$ (i.e. KV distribution), radius $a$ and longitudinal velocity $v$, yielding current density $J = nv$ and total current $I = nv\pi a^2$. The electric and magnetic self-fields can be solved with Gauss's and Ampere's laws, leading to radial electric field and azimuthal magnetic field expressions

$$E_r(r) = \begin{cases} \dfrac{Ir}{2\pi\epsilon_0 v a^2} & \text{if } 0 \le r \le a \\ \dfrac{I}{2\pi\epsilon_0 v r} & \text{if } r > a \end{cases} \tag{2.44}$$

$$B_\theta(r) = \begin{cases} \dfrac{Ir}{2\pi\epsilon_0 c^2 a^2} & \text{if } 0 \le r \le a \\ \dfrac{I}{2\pi\epsilon_0 c^2 r} & \text{if } r > a \end{cases} \tag{2.45}$$

where $c$ is the speed of light and $\epsilon_0$ the permittivity of vacuum. The combined radial force exerted by the self-fields to a beam particle with charge $q$ at radius $r$ is given by the Lorentz law, which simplifies in the used geometry to

$$F_r(r) = q(E_r - vB_\theta) = \underbrace{qE_r}_{F_r^E} - \underbrace{qvB_\theta}_{F_r^B} = \frac{qIr}{2\pi\epsilon_0 v a^2}\left(1 - \beta^2\right) \tag{2.46}$$

where $\beta = v/c$. As the above equation shows, the space charge force of a uniform cylindrical beam is linear and defocusing in the transverse directions. Also, it is seen that when the beam velocity is increased, the force decreases and finally disappears at $v = c$. In the low energy beam transport $v \ll c$, and the contribution of the magnetic force is insignificant. For example, for $^{40}Ar^{8+}$ accelerated with 10 kV the ratio of the magnetic and electric forces is $F_r^B/F_r^E \approx 4 \cdot 10^{-6}$.

The beam potential $\Phi$ can be solved from the radial electric field by integrating and assuming a grounded beam pipe with radius $R$ around the beam. The calculation

yields parabolic potential behavior inside and logarithmic outside the beam:

$$\Phi(r) = \frac{I}{4\pi\epsilon_0 v}\left(1 + 2\ln\frac{R}{a} - \frac{r^2}{a^2}\right) \quad \text{inside the beam} \tag{2.47}$$

$$\Phi(r) = \frac{I}{2\pi\epsilon_0 v}\ln\frac{R}{r} \quad \text{outside the beam} \tag{2.48}$$

The same potential equations have been presented e.g. in Ref. [106].

Even though the assumption of uniform density distribution is rather nonrealistic for real ion beams extracted from ECR ion sources, the above equations can be used to make rough approximations of the space charge effects. As an example, for an argon beam extracted from the JYFL 14 GHz ECRIS with 10 kV extraction voltage, the total beam potential at the center of the beam, including all extracted charge states, varies between 30 and 100 V when the total extracted current is varied between 0.6 and 1.8 mA. The calculation was performed at the location of the $^{40}Ar^{8+}$ waist between the ion source and the analyzing magnet.

A more realistic description of the space charge related forces can be made using a Gaussian charge density distribution

$$n(r) = \frac{I}{2\pi v\sigma^2}e^{-r^2/2\sigma^2}, \tag{2.49}$$

where $\sigma$ is the standard deviation. This distribution yields radial force which can be described as [107]

$$F_r(r) = \frac{qI}{2\pi\epsilon_0 v r}\left(1-\beta^2\right)\left(1 - e^{-r^2/2\sigma^2}\right). \tag{2.50}$$

Unlike in the case of the uniform charge density, the defocusing space charge force of a beam with a more realistic Gaussian distribution is nonlinear. As discussed in section 2.8.1, this nonlinear force is a source of emittance growth. The improved beam emittance due to mitigated beam space charge has also been demonstrated experimentally (see e.g. Refs. [108, 109]).

If charge of opposite sign is introduced into the volume occupied by the ion beam, the effective charge density of the beam decreases, mitigating the space charge effects. This process is called *space charge compensation*, and it occurs naturally when the ion beam passes through the rest gas present in the beam transport system. Interaction of the ion beam with the rest gas leads to inelastic collisions between the ions and the neutral particles, resulting in ionization and charge exchange processes. The ionization processes form slow positive ions and electrons inside or near the volume occupied by the ion beam. In the case of positive ion beam, the ions are expelled from the beam due to the positive beam potential, whereas those electrons which do not have enough energy to escape the potential are trapped by the beam. This process leads to accumulation of negative charge into the ion beam, resulting in formation of beam plasma with effective charge density that can be considerably lower than the initial

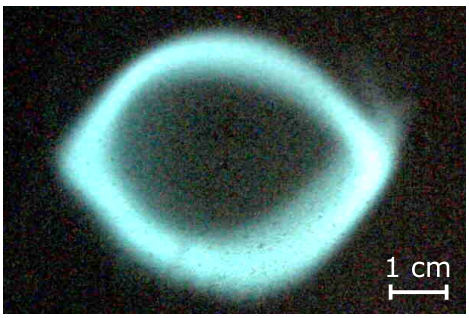


Figure 2.11: Profile of 100 $\mu$A beam of $^{40}Ar^{8+}$, extracted from the JYFL 14 GHz ECRIS with 10 kV extraction voltage and 0.7 mA of total current. The beam has distinctly hollow ring-like structure.

charge density of the beam. It has been shown experimentally that with rest gas pressures in excess of $10^{-4}$ mbar the beam potential can be reduced to less than 1 % of its initial value [98, 110]. However, with high rest gas pressures the collisions between ions and neutral rest gas particles also cause beam losses through charge exchange. Mazarakis *et al.* [105] have shown experimentally that the time required for an ion beam to reach an equilibrium state in terms of space charge compensation decreases with increasing pressure of the rest gas. For 1 mA $Xe^{1+}$ beams accelerated with 80 kV the required time was measured to be in the order of 100 $\mu$s with $10^{-6}$ mbar background pressure and in the order of 10 $\mu$s when the pressure was increased to $10^{-5}$ mbar.

With ECR ion sources the beam current is at its highest in the beam transport section between the ion source extraction and the $q/m$ separation, where all the extracted ion species are still present. Consequently, the space charge effects and related consequences to beam properties are also strongest in this beamline section.

### 2.8.5 Hollow beam structure

Hollow ring-like beam structures are regularly observed with the beams produced by the JYFL 14 GHz ECRIS. The hollowness is exhibited by the low and medium $q/m$ ion species, whereas the particle distribution of ion species with high $q/m$ remain more uniform. For example, with argon beams extracted with 10 kV, the charge states up to $^{40}Ar^{9+}$ are hollow. An example is presented in Fig. 2.11. Similar behavior has been observed also in other laboratories employing ECR ion sources, e.g. at MSU/NSCL [111].

The formation of the hollow beam structure is connected to the space charge effects caused by the magnetic solenoid focusing of multispecies ion beams extracted from the ECR ion source. The influence of the magnetic focusing on the ions can be described with the magnetic rigidity, which is defined in Eq. (2.25). For a given magnetic field the focusing effect experienced by the ions increases with the ratio of the ion charge and

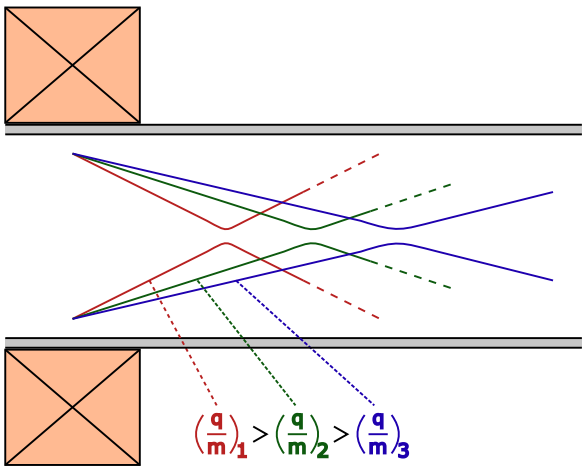


Figure 2.12: Schematic presentation of the $q/m$ dependence in magnetic solenoid focusing with three ion beams of different charge to mass ratios. Due to the selective focusing, the focal points of different ion species are separated in the axial direction.

mass, $q/m$. Consequently, the magnetic solenoid focusing separates ions to different focal points based on this ratio. When the beam component of interest is transported through the analyzing magnet, the other ion species with higher $q/m$ present in the beam are overfocused by the solenoid and can exhibit beam waists, i.e. focal points, during the beam transport before the $q/m$ separation (see Fig. 2.12). At these locations the radius of the beam of interest is larger than the radius of the unwanted beam component. Subsequently, the ions in the beam of interest are influenced by the radial electric field of the unwanted beam, which decreases radially outside the focused beam edge. As a result, the center parts of the beam of interest experiences increased radial divergenge, which can lead to the formation of hollow, ring-like transverse beam structure downstream from the analyzing magnet.

Magnetic solenoid focusing as a source of hollow beam formation has been investigated with simulations and experiments. Particle-in-cell simulations presented by Kazarinov [112] show that solenoid focusing of multispecies beams leads to the formation of hollow beams. In addition, the simulations predict substantial increase in the transverse beam emittance due to this process. The role of the high $q/m$ beam components in the beam hollowness has been also shown experimentally. The hollowness is significantly mitigated and pushed to lower $q/m$ when the current of the high $q/m$ ion species are decreased in the total beam extracted from an ECR ion source [111, 113]. At MSU/NSCL the magnetic solenoid focusing between the ECR ion source and the analyzing magnet has been replaced with electrostatic focusing, which focuses all $q/m$ to the same focal point. It has been reported that as a result the hollow ring-like structure is no more evident in the measured beam profiles [114].

However, other sources have also been suggested as contributors to the beam hollowness. The inhomogeneity of the ion distribution inside the ECR plasma can be reflected

in the structure of the extracted beams. This is most clearly seen in the triangular beam shapes often associated with the ECR ion sources, which are caused by the magnetic hexapole field inside the ion source plasma chamber, defining the plasma flux shape towards the extraction. This effect has been successfully reproduced with several computational models of the ion dynamics inside the ECRIS plasma (see e.g. Refs. [49, 115–117]). In a similar manner the ion distribution could also exhibit features which contribute to the formation of hollow beam structures later on during the beam transport. This is supported by the observation of some degree of hollowness exhibited by proton beams extracted from an ECR ion source [115]. For protons the $q/m = 1$, and as such the observed hollowness can not be due to the magnetic solenoid focusing effect discussed above. Also, a few computational models of ion dynamics inside ECRIS suggest that plasma conditions can contribute to the formation of hollow beam structures [115, 116, 118].

# Chapter 3

# Experimental setup and methods

The experimental work presented in this thesis has been performed at the accelerator laboratory of the Department of Physics, University of Jyväskylä. The equipment used for the studies include the JYFL 14 GHz ECR ion source, the low energy beam transport (LEBT) from the ion source to the JYFL K-130 cyclotron and the first section of the high energy beam transport after the cyclotron. A detailed description of the JYFL 14 GHz ECRIS is presented in the following section.

The low and high energy beam transport sections are presented in Figs. 3.1 and 3.2. The ion optics in the low energy beam transport is realized with magnetic solenoids and

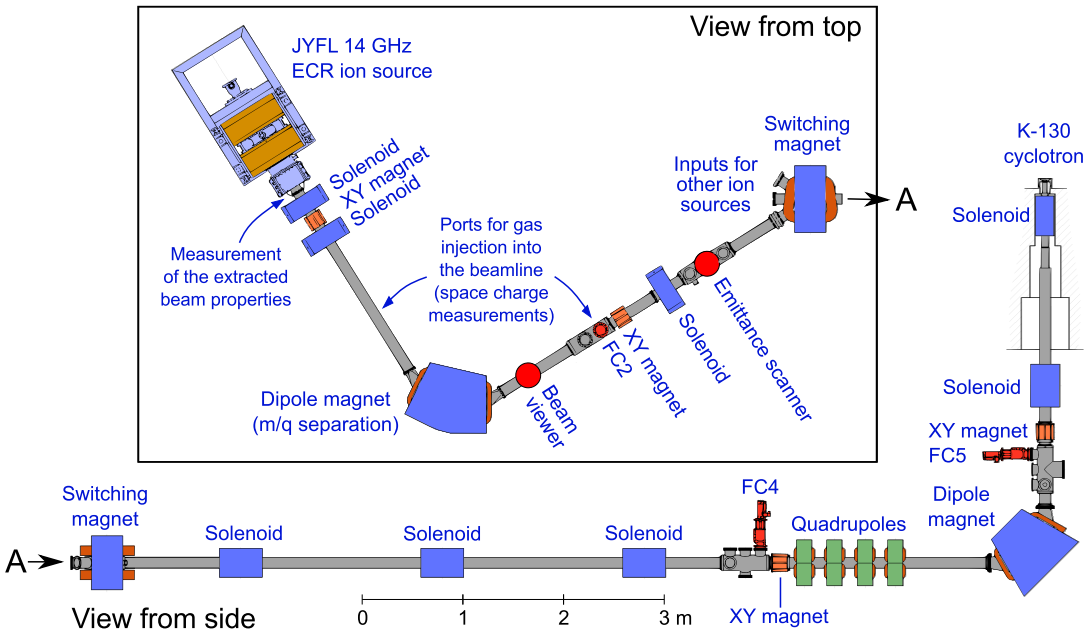


Figure 3.1: Schematic presentation of the low energy beam transport from the JYFL 14 GHz ECR ion source to the JYFL K-130 cyclotron.

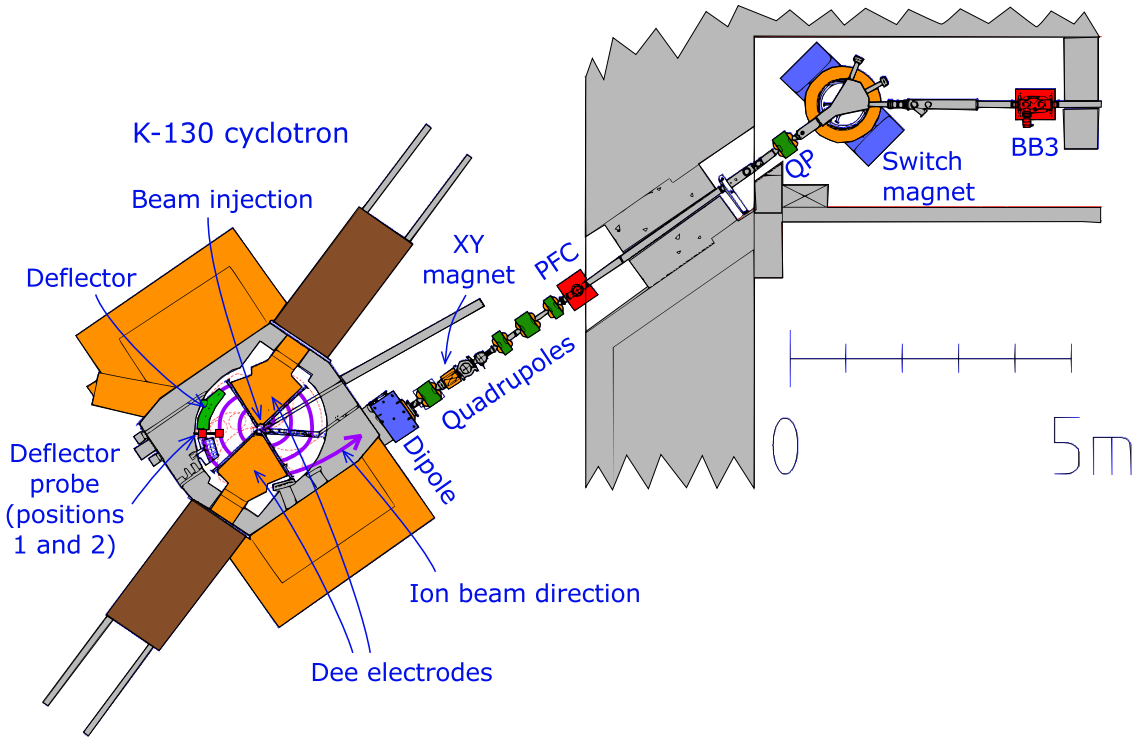


Figure 3.2: Schematic presentation of the JYFL K-130 cyclotron and the first section of the high energy beamline.

dipoles with additional steering magnets to fine tune the beam path in the transverse ($x$ and $y$) directions. A set of four magnetic quadrupoles is located upstream from the last dipole preceding the cyclotron to provide improved beam matching to the cyclotron injection. Downstream from the cyclotron the high energy beamline ion optics is also mainly managed with magnetic solenoids and quadrupoles and is divided into separate sections leading to different target stations.

## 3.1 JYFL 14 GHz ECRIS

The JYFL 14 GHz ECRIS [8] is a second generation room temperature ECR ion source. It is based on the design of the highly successful AECR-U at the Lawrence Berkeley National Laboratory (LBNL), which is the upgraded version of the original AECR with increased magnetic fields to improve the plasma confinement [119, 120]. Other ECR ion sources belonging to this ion source family include the two ARTEMIS ion sources at MSU/NSCL (the National Superconducting Cyclotron Laboratory, Michigan State University, USA) [121], the 14 GHz ECRIS at the ATLAS facility at ANL (the Argonne National Laboratory, USA) [122] and the 14 GHz ECRIS at KVI (Kernfysisch Versnellerinstituut, The Netherlands) [123].

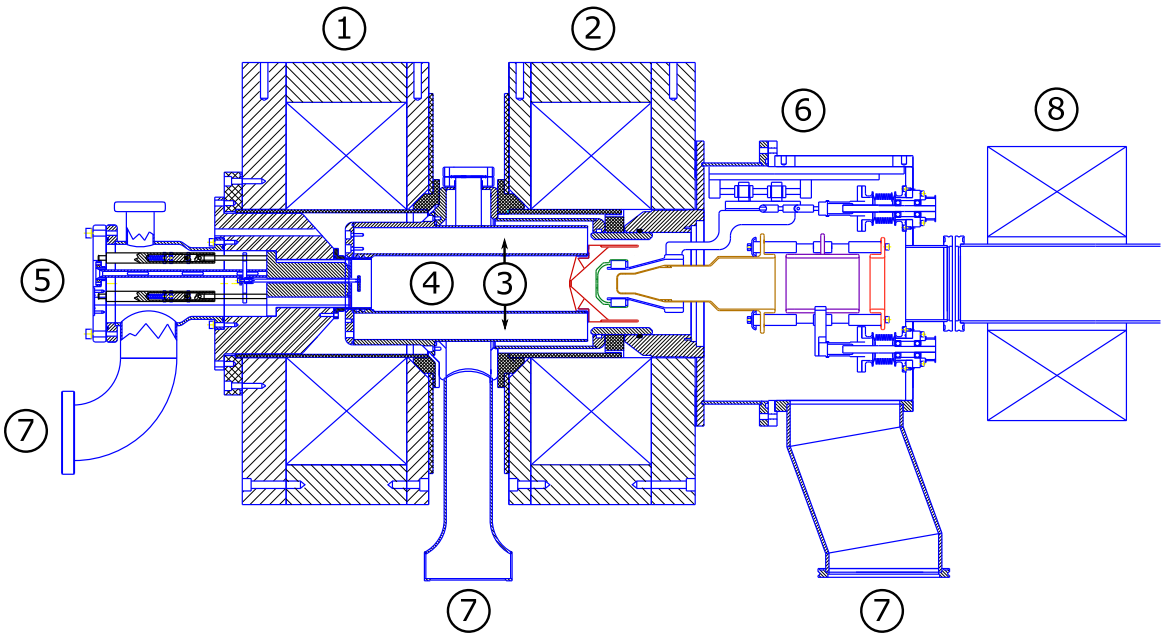


Figure 3.3: The JYFL 14 GHz ECRIS. The magnetic system consists of injection (1) and extraction (2) coils and permanent magnet hexapole (3) around the plasma chamber (4). The injection chamber (5) includes gas injection, two waveguides for primary and secondary microwaves and port for oven or MIVOC. The extraction chamber (6) houses the extraction electrodes. Old extraction system is presented in the figure and the different electrodes have been indicated with varying colors for clarity. The ion source is pumped with three turbomolecular pumps (7). The first focusing solenoid of the beamline (8) is also shown.

The structure of the JYFL 14 GHz ECRIS is presented in Fig. 3.3. The main microwave frequency is 14.1 GHz, which is produced with a klystron and injected into the plasma chamber through the injection end iron plug with WR62 rectangular waveguide. A secondary microwave input with variable frequency between 10.75 and 12.40 GHz is produced with a Traveling Wave Tube Amplifier (TWTA) and injected axially into the plasma chamber through a WR75 rectangular waveguide. The maximum output power of the klystron is 2.5 kW, limited to 1 kW in normal operation. The maximum TWTA output is about 400 W.

The minimum-$B$ magnetic field is produced with the combination of two water cooled solenoid coils (axial magnetic field) and NdFeB permanent magnet open hexapole (radial magnetic field). The axial magnetic field at the injection and extraction ends of the plasma chamber are about $B_{\mathrm{inj}} = 2.0$ T and $B_{\mathrm{ext}} = 1.0$ T, the exact values depending on the ion source tuning (coil current settings). The field minimum $B_{\mathrm{min}}$ at the center of the chamber varies normally between $0.3 - 0.4$ T and the radial field at the plasma chamber wall is about $B_{\mathrm{rad}} = 1.1$ T. The main microwave frequency of 14.1 GHz corresponds to resonance field $B_{\mathrm{ECR}} \approx 0.5$ T (see Eq. (2.1)), which yields

the following mirror ratios

$$R_{\text{inj}} = \frac{B_{\text{inj}}}{B_{\text{ECR}}} = 4.0 \tag{3.1}$$

$$R_{\text{ext}} = \frac{B_{\text{ext}}}{B_{\text{ECR}}} = 2.0 \tag{3.2}$$

$$R_{\text{rad}} = \frac{B_{\text{rad}}}{B_{\text{ECR}}} = 2.2 \tag{3.3}$$

which fulfill the magnetic field scaling laws, presented in Eq. (2.22).

The ion source plasma chamber is manufactured from aluminium with 76 mm inner diameter and about 300 mm length. The open hexapole structure allows radial pumping of the chamber through openings between the magnetic poles. In addition, the slits can be used for diagnostics (e.g. bremsstrahlung, light emission and pressure measurements) and introduction of materials into the plasma chamber to be ionized. For example, a radial sputtering equipment has been developed for this purpose to serve in the production of metal ion beams. The gaseous elements are introduced into the plasma axially from the injection end of the chamber. The injection end also includes biased disc and a channel for the axial insertion of ovens or MIVOC equipment. The ion source is normally operated with extraction voltages around 10 kV, which is dictated by the properties of the JYFL K-130 cyclotron injection. To provide an example of the typical performance of the JYFL 14 GHz ECRIS, the beam currents of selected charge states of $^{131}$Xe were measured, yielding the following result: 52 $\mu$A (23+), 47 $\mu$A (24+), 33 $\mu$A (25+), 20 $\mu$A (27+), 7 $\mu$A (28+), 4 $\mu$A (29+) and 2 $\mu$A (30+).

## 3.2 Diagnostics and instrumentation

### 3.2.1 Beam current and transmission efficiency

The current of the ion beams produced with the JYFL 14 GHz ECRIS can be measured along the LEBT and after the cyclotron with Faraday cups. The primary measurements used to quantify the ion source performance are conducted after the analyzing magnet at Faraday cup FC2. Two other cups, FC4 and FC5, are used to measure the beam current along the LEBT. The beam current injected into the cyclotron can be measured at the spiral inflector, which turns the incoming beam into the acceleration plane of the cyclotron. During acceleration the beam current can be measured with a radial main probe and at the cyclotron extraction with a deflector probe. The current of the accelerated and extracted beam is measured at Faraday cup PFC, located in the high energy beamline after the cyclotron (see Fig. 3.2).

*Transmission efficiency* is often used to quantify the performance of beam transport. The transmission efficiency through the LEBT and the cyclotron is defined as

$$T = \frac{I_{\text{PFC}}}{I_{\text{FC2}}} \cdot 100\ \%, \tag{3.4}$$

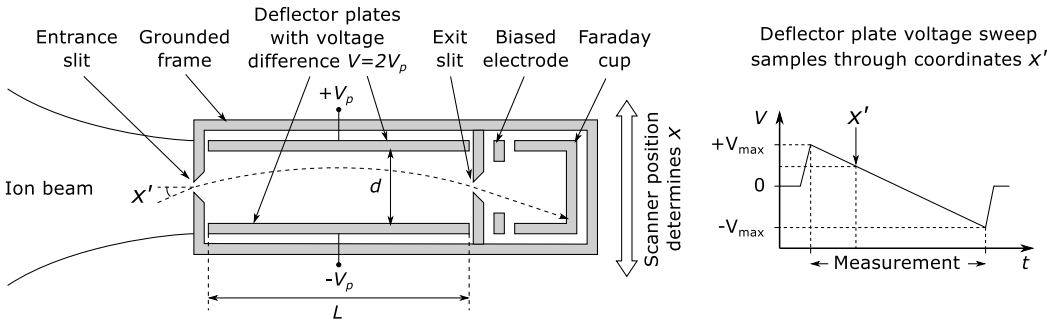


Figure 3.4: A schematic presentation of an Allison type emittance scanner and the voltage sweep between the deflector plates. The scanner position determines the coordinate $x$ and the deflector voltage all the coordinates $x'$ at this position. A beamlet trajectory with an angle $x'$ is shown as an example.

where $I_{\mathrm{PFC}}$ and $I_{\mathrm{FC2}}$ are the beam currents at Faraday cups PFC and FC2, respectively.

### 3.2.2 Beam transverse emittance

The transverse emittance of the ion beams is measured with an Allison type emittance scanner [124], located downstream from the Faraday cup FC2 (see Fig. 3.1). The scanner is oriented in the beamline to perform measurements in the vertical direction perpendicular to the bending plane of the analyzing magnet. A schematic presentation of the scanner is presented in Fig. 3.4.

The scanner position fixes the location of the entrance slit and determines the coordinate $x$ in the phase space. While the scanner is at this location, the voltage $V$ between the deflector plates is swept from $+V_{\mathrm{max}}$ to $-V_{\mathrm{max}}$, while simultaneously measuring the current arriving at the Faraday cup behind the plates and the second slit. The voltages of the individual deflector plates are $\pm V_p$, and as such $V = 2V_p$, as is presented in Fig. 3.4. The voltage $V$ determines the angle of incoming particles which can pass through the second slit, i.e. the phase space coordinate $x'$. The relation can be described as

$$V = \frac{4dV_{\mathrm{ext}}}{L}x', \tag{3.5}$$

where $V_{\mathrm{ext}}$ is the ion source extraction voltage determining the incoming beam energy, $L$ the length of the deflector plates and $d$ the gap between them (see Fig. 3.4). This procedure is repeated for all positions $x$ through the beam profile to determine the transverse phase space occupied by the beam. The transverse rms-emittance is then calculated based on the measured current distribution over the phase space pattern.

### 3.2.3 Beam profile

The beam profile is recorded with potassium bromide (KBr) scintillation screens. Potassium bromide is chosen as the scintillation material as it yields good performance

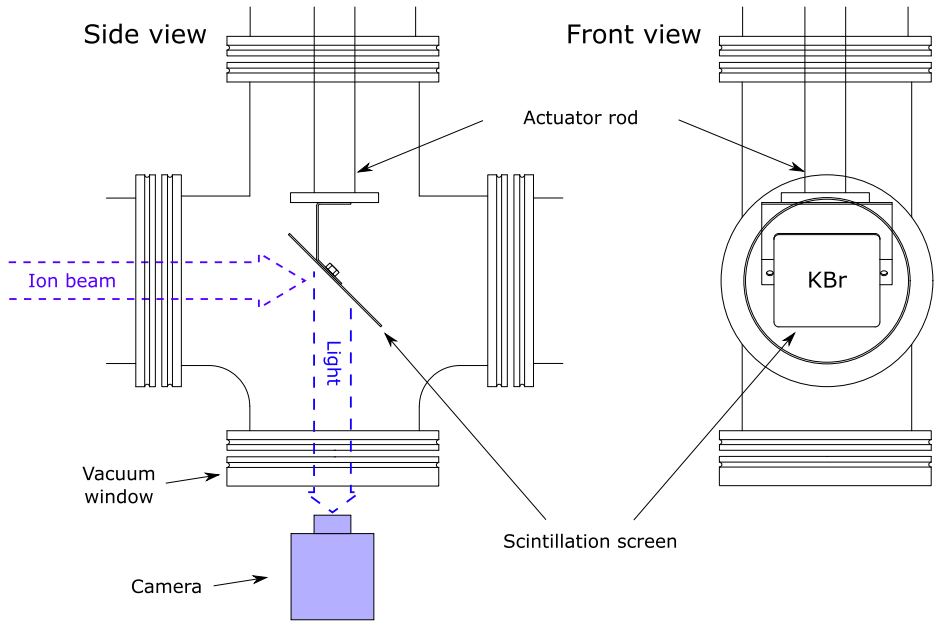


Figure 3.5: Scintillation screen assembly inside a cross chamber. The actuator is used to move the screen in or out of the ion beam path.

with the range of beam energies and $q/m$ separated beam currents normally extracted from the JYFL 14 GHz ECRIS. Other possible candidates include e.g. barium fluoride ($BaF_2$). The scintillation material is applied as a thin coating on a grounded aluminium plate, to prevent charge build up. During experiments a scintillation screen is located after the analyzing magnet inside a cross chamber. The screen is placed into a 45 degree angle with respect to the optical axis of the beamline to allow observation from one of the chamber branches. Another branch is used to move the screen in and out of the beam path. The assembly is presented in Fig. 3.5. Interaction with the beam particles results to photon emission in the visible light range. The light emission pattern on the scintillation screen, observed with a camera through a vacuum window, correlates with the beam current distribution of the beam. This method provides direct, real time monitoring of the beam profile.

### 3.2.4 Measurement of plasma loaded cavity resonance properties

A dual port measurement technique has been developed for the studies of the microwave frequency dependent properties of the JYFL 14 GHz ECRIS plasma chamber, discussed in section 4.1. The purpose of the technique is to isolate and remove the influence of the microwave transmission line leading to the plasma chamber from the results and thus gain direct measurement of only the properties of the plasma chamber. In addition, the technique decouples the diagnostics signal probing the chamber properties from the main plasma heating microwave signal.

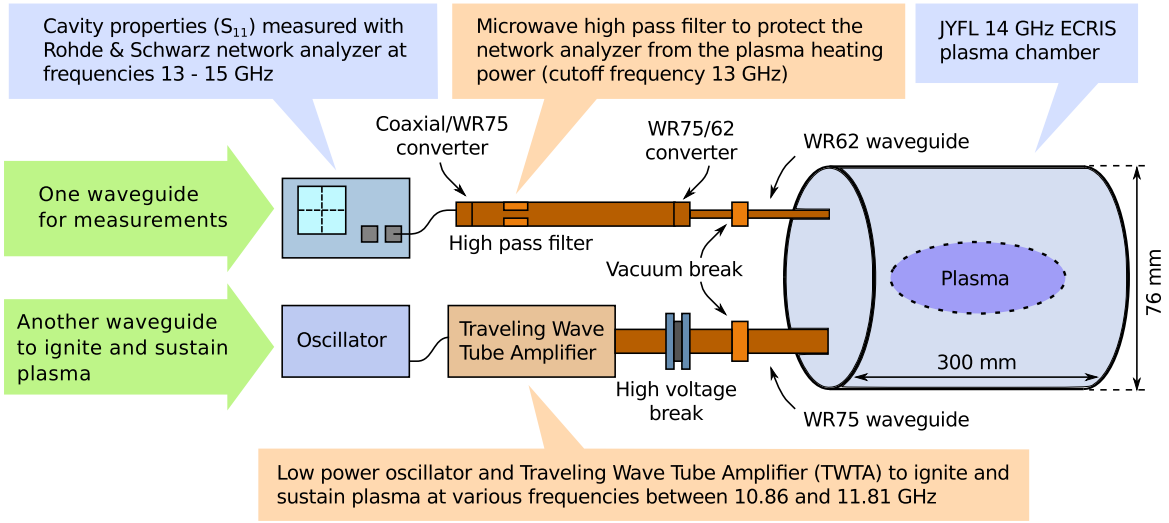


Figure 3.6: Schematic presentation of the dual port measurement technique used to determine the microwave frequency dependent properties of the JYFL 14 GHz ECRIS plasma chamber.

The experimental setup for the technique is presented in figure 3.6. The plasma is ignited and sustained with microwave emission from a TWTA operating around 11 GHz, which is transmitted into the plasma chamber through a rectangular waveguide. The frequency dependent properties of the chamber are measured with a network analyzer through another waveguide with probing signal around 14 GHz, i.e. around the normal operation frequency of the JYFL 14 GHz ECRIS. The power of the probing signal is 10 mW, which does not contribute significantly to the plasma properties compared to the microwave power of up to 300 W from the TWTA. In addition, it has been verified that the probing signal power is not sufficient to ignite plasma without microwave input from the TWTA, and consequently this technique can be used to measure the properties of the plasma chamber without plasma loading. The network analyzer is protected from the main plasma heating power with a microwave high pass filter with 13 GHz cutoff frequency, placed between the analyzer and the chamber. Consequently, the technique can not be used to measure the chamber properties at the frequencies used to sustain the plasma. With the presented setup the plasma chamber is kept at ground potential and no beam is extracted during the measurements.

The plasma chamber diagnostics is performed by determining the *reflection coefficient* $S_{11}$ of the measured system, defined as

$$S_{11} = 10 \log_{10} \left( \frac{P_r}{P_f} \right), \tag{3.6}$$

where $P_r$ and $P_f$ are reflected and forward power of the probing signal, as a function of frequency. $S_{11}$ describes the systems ability to absorb and transmit microwave power.

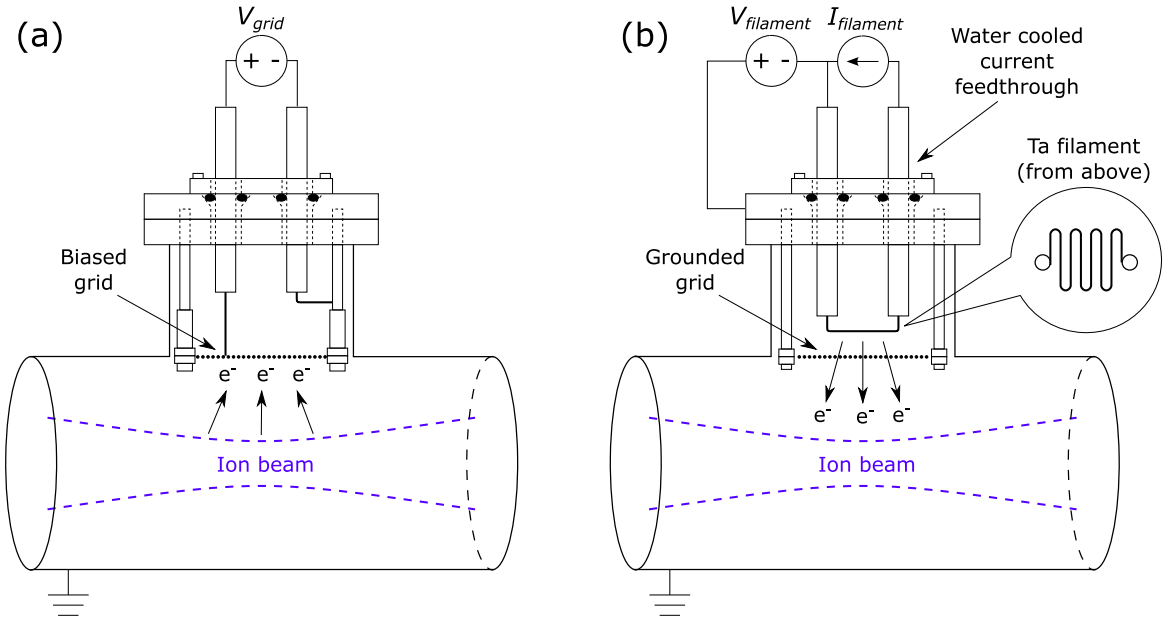


Figure 3.7: Schematic presentation of (a) the biased grid assemby and (b) the heated filament assembly.

In the case of the ECRIS plasma chamber, this includes the possible microwave power leaks through the chamber apertures. When the plasma is ignited, $S_{11}$ describes the combined behavior of the chamber and the plasma it contains. The resolution of the measurement is defined by the data acquisition properties of the network analyzer, and depends on the studied frequency range. As an example, the measurement of 250 MHz frequence band yields point separation of 62.5 kHz.

### 3.2.5 Space charge measurements

Three different experimental methods have been used in order to study the impact of the ion beam space charge compensation degree to beam quality and transport. The results of these experiments are presented in section 4.2.1.

The first method is the injection of additional neutral gas into the beamline to increase the production of compensating electrons from the rest gas which is ionized by the ion beam. The gas can be injected into the JYFL 14 GHz ECRIS branch of the JYFL low energy beamline through two venting ports, one upstream and one downstream from the the analyzing magnet. The port locations are indicated in Fig. 3.1. The gas feed into the beamline from a high pressure gas source is adjusted with a pressure regulator and a high precision valve. Gas injection into beamline as a way to enhance space charge compensation has been studied earlier with singly charged He [110] and proton beams [108, 109] with good results.

The second method uses a grid introduced inside the beamline, near the vacuum

vessel wall. A variable positive bias is applied to the grid to collect electrons from the beamline in order to gain information regarding the consequences of degraded space charge compensation. The grid assemby is presented in Fig. 3.7.

The third method aims to introduce additional compensating electrons into the beamline from an external source. The electrons are produced with a heated tantalum filament, which is placed inside the beamline and shielded from the ion beam with a grounded grid. The electrons are accelerated towards the beam with the voltage difference applied between the filament and the grid. The filament assembly is presented in Fig. 3.7.

The biased disc and the heated filament have been used at the same locations in the beamline as the gas injection.

### 3.2.6 Determination of beam properties after ECRIS extraction

In order to study the properties of beams extracted from an ECR ion source, especially when determining the performance of the beam extraction system itself, it is advantageous to be able to do measurements immediately downstream from the extraction region, before the beam is subjected to beamline ion optics. However, in the case of the JYFL 14 GHz ECRIS the space available for this is very limited due to the arrangement of the first beamline solenoids (see Fig. 3.1), restricting the possible diagnostics. A simple and compact pepperpot-like (see e.g. Ref. [125]) system, presented in Fig. 3.8, has been constructed to determine the diameter and divergence of beams leaving the extraction region. The system is installed to the end of the JYFL 14 GHz ECRIS extraction chamber (see Fig. 3.3), and utilizes a pepperot plate to collimate the incoming beam into separate beamlets. As the location and size of the apertures on the plate are known, as well as the distance from the plate to the following flange acting as the screen plane, the beam divergence can be estimated from the beam indiced markings on the flange. The pepperpot plate also includes a slot which allows a section of the full beam to pass to the flange, which is used to determine the beam radius at the flange. The system does not significantly alter the ion source vacuum thanks to the efficient pumping of the extraction vacuum chamber. With beam some initial outgassing was observed, duration of which was however short compared to the time used to obtain clear markings on the screen plane. This system was mainly used in the extraction studies of the JYFL 14 GHz ECRIS, described in section 4.3.2.

### 3.2.7 Determination of ion beam temporal characteristics

As discussed in section 2.8.3, temporal stability is one of the factors defining the quality of ions beams. The current oscillations exhibited by ECRIS beams are often periodic in nature, especially those observed in the millisecond time scales [103, 104]. In order to identify and analyze the periodic temporal characteristics of ion beam current, it is convenient to perform signal analysis in the frequency domain in addition to time

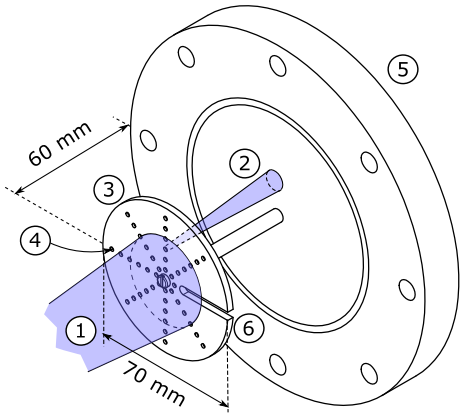


Figure 3.8: Schematic presentation of the pepperpot-like setup used to measure the beam diameter and divergence after the extraction chamber of the JYFL 14 GHz ECRIS. (1) is the incoming beam, (2) a collimated beamlet, (3) a pepperpot plate, (4) pepperpot aperture (2 mm diameter), (5) flange (screen plane) and (6) slot for the determination of beam radius. Figure from Ref. [99].

domain. A new measurement software was developed for the temporal beam stability studies, which are presented in section 4.2.2 of this thesis and in Ref. [126] (publication A.V). In the following the main properties of the measured signal transformation from time domain to frequency domain are presented, followed by a description of the measurement software.

In frequency domain the original signal is represented as a sum of periodic (sine and cosine) components. The amplitude determines the contribution of given component in the original time domain signal, and consequently the frequency domain signal is usually presented in frequency, amplitude coordinates as a frequency spectrum. In power spectrum the amplitudes are squared, which enhances the detection of dominant frequencies.

In a real measurement scenario like the measurement of beam current from a Faraday cup, a finite number of samples represent the complete time domain signal. This windowed segment can be transformed to frequency domain with the Discrete Fourier Transform (DFT), which is described as [127]

$$X[k] = \frac{1}{N} \sum_{n=0}^{N-1} x[n] e^{-i2\pi \frac{k}{N} n}, \tag{3.7}$$

where $k$ is an index number representing the frequency domain variable and $N$ the number of samples. The output of DFT is a complex number, i.e. $X[k] = Re(X[k]) + i \cdot Im(X[k]) \equiv A_k + i \cdot B_k$, where $A_k$ and $B_k$ are the amplitudes of the cosine and sine terms of the $k$ frequency component of the original signal. The frequency spectrum combines these terms as $\sqrt{A_k^2 + B_k^2}$ and the power spectrum as its square, $A_k^2 + B_k^2$, with

$k$ ranging from 0 to $N-1$. In practice in numerical calculations the DFT is determined using Fast Fourier Transform (FFT), which is a collective name for algorithms to perform DFT (and other transforms) efficiently. With large data sets the use of FFT can reduce the computational time several orders of magnitude [127].

In order to obtain the frequency domain information in the units of Hz instead of frequency index $k$, the frequency axis must be scaled accordingly. If the original time domain signal is sampled with sampling interval $\Delta t$, i.e. sampling rate of $f_s = 1/\Delta t$, the frequency resolution in the frequency domain is $\Delta f = f_s/N = 1/N\Delta t$ [127]. Increasing the number of time domain samples improves the frequency resolution and reduces spectral leakage (smearing of the frequency spectrum peaks to surrounding frequencies) arising from the mismatch between the sampling frequency and the frequency components of interest in the measured signal. Thus longer data acquisition times enhance the representation of periodic signals and suppress random noise.

In the case of beam current measurement the original time domain signal is real (no imaginary component), and the frequency domain signal between $k = 0$ and $k = N/2$ contains all of the acquired information. This means the DFT only gives frequency information up to half the sampling frequency (Nyquist sampling theorem) [127]. In order to mitigate aliasing, it is advantageous to suppress the frequencies above the $f_s/2$ limit in the measured signal.

Many development platforms are currently available offering high performance basic routines for signal processing and manipulation which are required for the above discussed transforms and the following signal analysis. Constructing the measurement software using one of them was considered to be a more flexible alternative compared to commercially available systems. This approach gives full control over the signal acquisition and manipulation procedures, and thus the implementation of special features and automated measurement routines becomes more transparent and straightforward. This is an important property as the measurement system is planned to act as a platform for additional features required by future studies.

The measurement software, nick-named *Beam-N-SPECTR* (Novel SPECtral Tool for Research) [128], was realized with the National Instruments LabVIEW development environment. The program utilizes the inbuilt high performance FFT algorithms of the LabVIEW to perform the basic signal transformation from time domain to frequency domain. Rest of the data manipulation, including data acquisition, calculations and analysis, both in the time and frequency domains, are built around this feature.

Figure 3.9 shows a schematic presentation of the core structure of the program and the data flow between different segments. Multiple run modes exist for online and offline monitoring, data recording and data analysis. The choice of run mode selects which features and routines of the program are used but they all essentially include three main steps: acquisition of time domain data, primary data analysis and postprocessing where results are combined into more presentable form. During these steps the produced data is stored and displayed to the user. When all steps have been completed, the

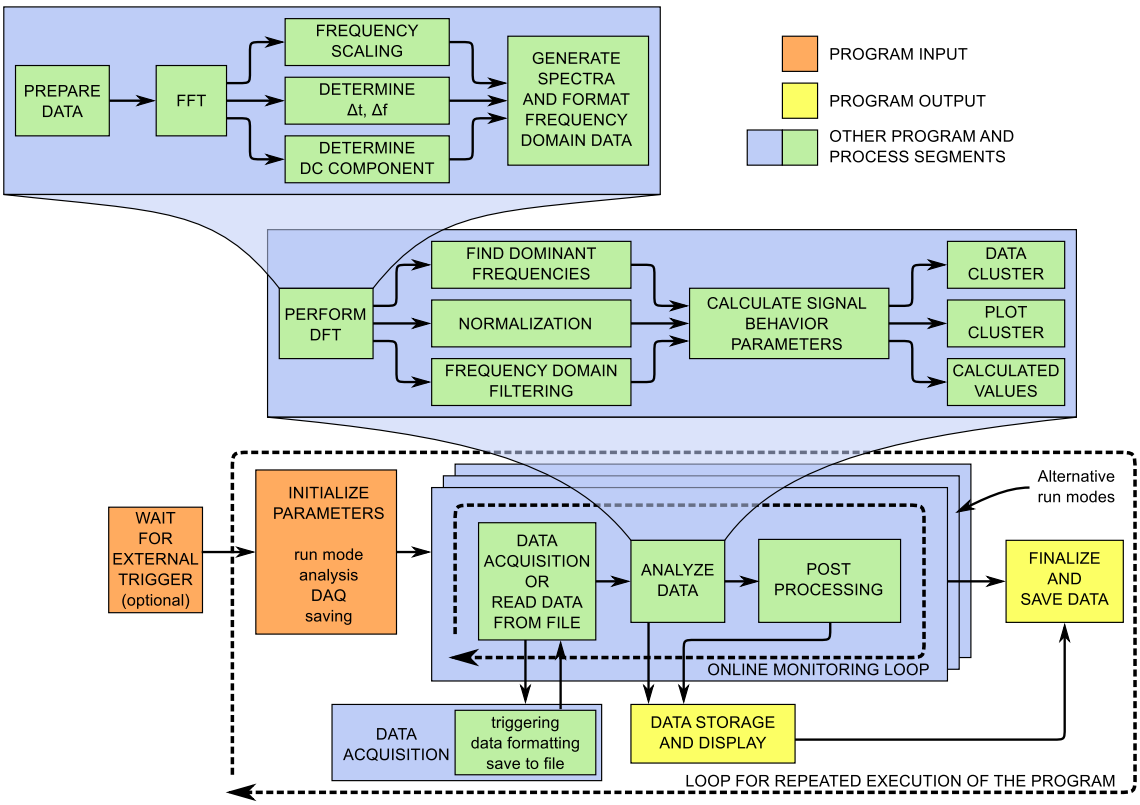


Figure 3.9: The structure of the measurement program *Beam-N-SPECTR* and the data flow. Figure from Ref. [126].

acquired data and analysis results are written into files (depending on the settings) and the main program terminates.

The functionality of the analysis block can be divided roughly into four steps. First, (1) the transform from time to frequency domain is performed with the DFT block which utilizes the LabVIEW FFT capabilities. Then (2) the frequency domain information is modified to desired form, including finding of the dominant frequencies, optional normalization of the frequency amplitudes, optional frequency domain filtering of the data and inverse transforming to generate a frequency filtered time domain signal. After this (3) the program calculates signal variation parameters, such as the standard deviation and fluctuation amplitudes to better describe the temporal oscillations of the signal. Finally (4) the produced information is collected and returned to the main program.

The program output includes graphical representations of the measured signal, its frequency spectrum and, if requested, frequency filtered reconstruction of the time domain signal. If the frequency spectrum of the background noise and electrical pickup is known, filtering of these frequencies can be very useful in order to acquire purified

signal of interest. The time domain signal fluctuation characteristics (with optional frequency filtering) are calculated and presented. The user can also choose to determine these beam properties averaged over multiple measurements and construct frequency histograms from the measured spectra to better describe the stability of the measured signal. All measured data, produced graphs and calculated values can be saved into files for later use, either with the same program or with other applications.

# Chapter 4

# Experimental work

This chapter summarizes the experimental work and presents the main results. The detailed documentation of the experiments is presented in Refs. [99, 126, 129–133], which are attached as appendices A.I – A.VII.

The aim of the presented work was to study new ways to improve the performance of the JYFL 14 GHz ECRIS and the properties of the extracted ion beams. The experimental work includes studies connected to the three major factors which determine ECR ion source performance: ECRIS plasma, beam formation and beam transport. The experimental work is correspondingly divided into three sections.

The first section focuses on the ECRIS plasma and presents the studies related to microwave – plasma coupling by fine tuning of the microwave frequency. The second section describes the beam transport studies, including experiments aiming to determine the role of space charge on the beam quality and studies of the temporal stability of the beam. The third section brings together the first two, describing the work performed to improve the beam formation from the ECRIS plasma. This consists of experiments with a collar structure attached to the ECRIS plasma electrode and culminates to the design and construction of a new and improved extraction system for the JYFL 14 GHz ECR ion source.

Chronologically the new extraction system represents the last experimental work of this thesis. Consequently, all the other experiments have been performed with the old extraction system, apart from part of the work related to the temporal beam stability.

## 4.1 Plasma heating microwave frequency fine tuning

In 2008 Celona *et al.* presented that the performance of the 14.5 GHz Caprice ion source at GSI (Gesellschaft für Schwerionenforschung, Germany) could be significantly affected by the altering the plasma heating microwave frequency in a span of a few tens of MHz around the primary frequency [29]. This phenomena, dubbed *frequency tuning effect*, was shown to have pronounced effect on the extracted beam currents and the spatial current distribution over the recorded beam profiles. In order to further

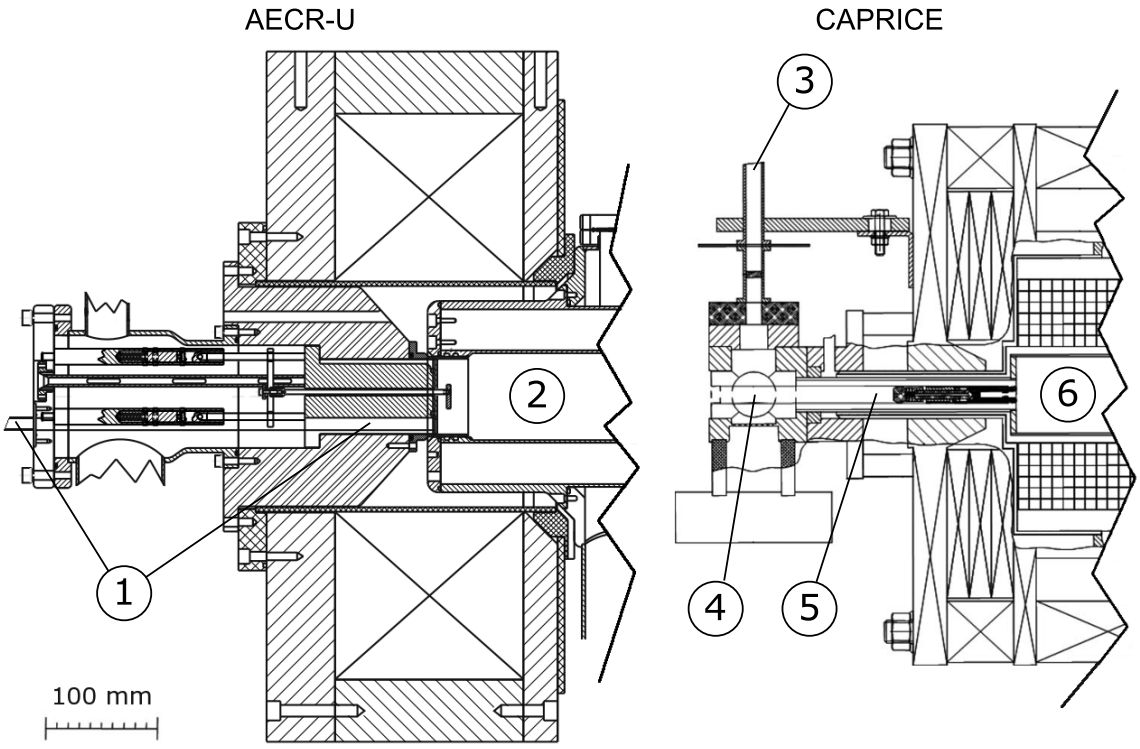


Figure 4.1: Comparison of the microwave coupling schemes of AECR-U and Caprice type ECR ion sources. AECR-U: (1) rectangular waveguide, (2) plasma chamber. Caprice: (3) rectangular waveguide, (4) tunable matching cavity, (5) coaxial transmission line, (6) plasma chamber. The presented ion sources are the JYFL 14 GHz ECRIS (AECR-U) and the 14.5 GHz Caprice at GSI.

study these effects, a collaboration was formed with the JYFL ion source group and the Catania ion source team, members of which were among the main contributors in the previously published studies, to continue the experiments with the JYFL 14 GHz ECRIS. Among other structural differences, the microwave delivery system from the emitter to the plasma chamber is profoundly different in the AECR-U type JYFL 14 GHz ECRIS compared to the Caprice type ion sources, as is presented in Fig. 4.1. With AECR-U the rectangular waveguide from the emitter is connected directly to the ion source plasma chamber through the injection plug. With Caprice the waveguide is connected to a tunable matching cavity, from which the microwaves are transported to the plasma chamber through a coaxial transmission line. Consequently the aim of the collaboration was to study if the effects observed with the Caprice are also present with the AECR-U, and whether the frequency tuning can be used to improve the ion source performance. The detailed documentation of the experiments is presented in Refs. [129–131] (publications A.I, A.II and A.III).

The frequency fine tuning experiments were conducted by varying the primary plasma heating microwave frequency of the JYFL 14 GHz ECR ion source. The frequency

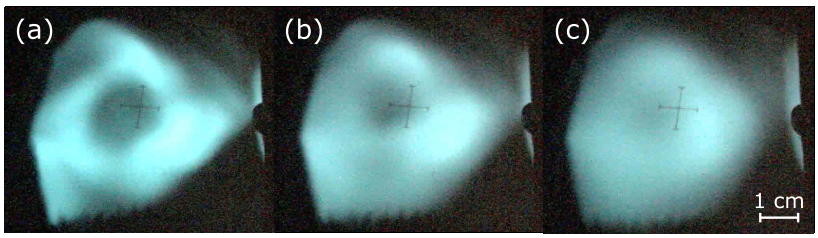


Figure 4.2: An example of $^{40}Ar^{9+}$ beam profile with varying microwave frequency. Forward power of 428 W and frequency of (a) 14.050 GHz, (b) 14.090 GHz and (c) 14.108 GHz. Figure reproduced from Ref. [129].

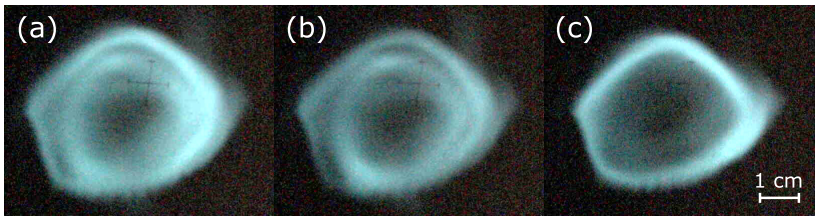


Figure 4.3: $^{40}Ar^{8+}$ beam profiles with varying primary microwave frequency at 203 W and 11.56 GHz from TWTA at 30 W. With these ion source settings the beam exhibits profile structure of two concentric rings at 14.070 GHz (a) and 14.100 GHz (b), while at 14.135 GHz (c) the normal (one ring) hollow beam structure is observed. Figure reproduced from Ref. [129].

was varied between 14.050 and 14.135 GHz around the normal operation frequency of 14.085 GHz. The frequency range was dictated by the bandwidth of the klystron providing constant output power. The effects of the frequency alteration on the properties of extracted beams were studied by measuring the beam current, emittance and profile after the $q/m$ separation. The coupling of the microwave power to the ECRIS plasma chamber was studied by monitoring the klystron forward and reflected power.

It was observed that varying the microwave frequency can affect the distribution of particles in the beam profile. An example of $^{40}Ar^{9+}$ profile is presented in Fig. 4.2. When the frequency is adjusted, the hollow ring-like beam structure exhibited by the low and medium charge state ion beams becomes more or less pronounced. The transitions normally occured smoothly over a span of tens of MHz. At which frequencies the changes in the profile occur was found to be very sensitive to the ECRIS tuning, to the extent that with certain ion source settings the beam profile remained unaltered during the whole frequency sweep. It was observed that the profile could be further affected when the primary microwave frequency was varied during double frequency heating. The secondary microwave with a power of a few tens of watts was introduced into the plasma chamber through a separate waveguide from the TWTA at fixed 11.56 GHz frequency. In these conditions the beam profile exhibited a structure of

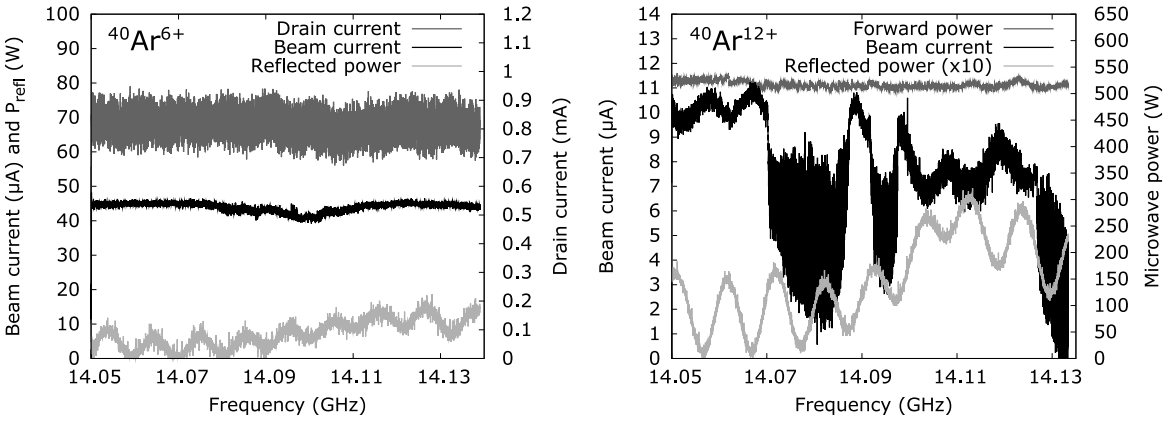


Figure 4.4: $^{40}Ar^{6+}$ and $^{40}Ar^{12+}$ beam current and reflected microwave power with varying microwave frequency. The drain current, i.e. total extracted beam current, and forward microwave power signals are also presented. Figure reproduced from Ref. [129].

two concentric rings at certain frequencies of the primary microwave. An example is presented in Fig. 4.3. The beamline optics between the ion source and the beam viewer can not produce a concentric beam structure like this from homogeneous distribution, which strongly indicates that the observed structure is linked to the plasma conditions inside the ECRIS plasma chamber. Consequently, these observations indicate that plasma conditions contribute to the formation of hollow beams.

The beam emittance is also affected by the varying microwave frequency, and variations in the order of a few tens of percent were normally observed. The emittance variations are associated with the changes in the beam profile, reflecting the shape of the transverse particle distribution. The altered beam quality due to the frequency tuning is also reflected in the transmission efficiency from the ion source through the cyclotron [134].

An example of recorded beam current and reflected power behavior is presented in Fig. 4.4. The reflected power exhibits periodic oscillatory variations as a function of the microwave frequency, while the forward power from the klystron remains constant. The reflected power oscillations are also seen in the beam current, with the current maxima corresponding to reflected power minima. In addition the beam current exhibits regions of pronounced instability at certain frequencies. The appearance and location of these instabilities is strongly influenced by the ion source tuning. The variations exhibited by the beam current increase with charge state. The current of low charge states was observed to be virtually unaffected by the microwave frequency, whereas the medium and high charge states exhibit significant variation.

The oscillations of the reflected power were initially associated to be the result of changing electromagnetic mode structure inside the ECRIS plasma chamber, as was discussed in Ref. [129]. However, the oscillations were virtually unaffected by the ion source tuning parameters, like microwave power, magnetic confinement and neutral gas pressure, which should have significant impact on the plasma conditions inside

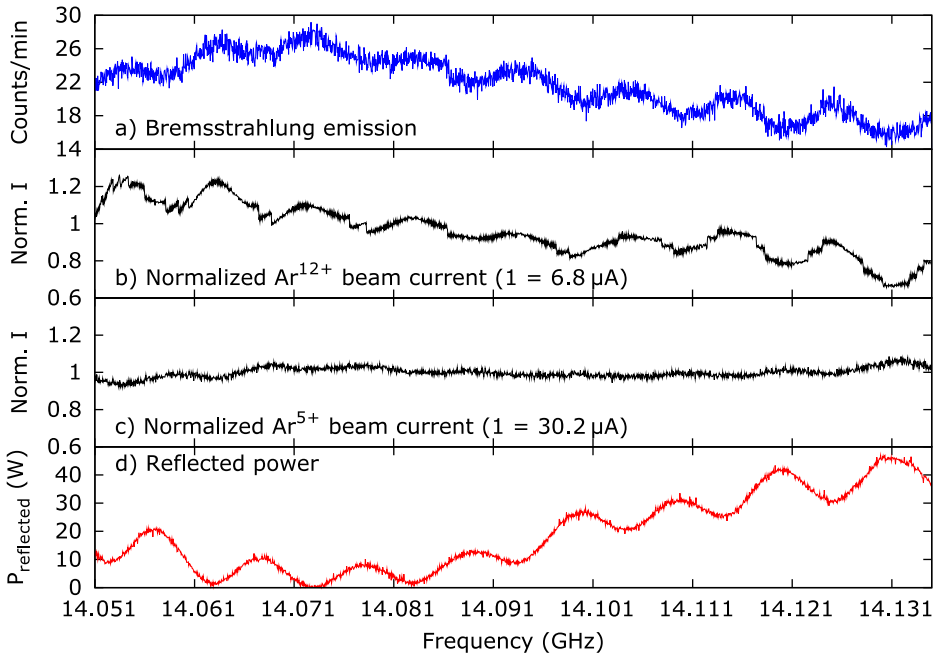


Figure 4.5: Correlation of reflected microwave power, normalized beam currents of $^{40}Ar^{5+}$ and $^{40}Ar^{12+}$ and bremsstrahlung emission from the ion source plasma. The forward microwave power remains constant and the input power fluctuations due to varying reflected power are clearly seen in the $^{40}Ar^{12+}$ beam current and bremsstrahlung signals. Figure reproduced from Ref. [134].

the plasma chamber. Further investigation revealed that the reflected power signal is strongly influenced by the microwave delivery system between the klystron and the ion source plasma chamber. It was discovered that altering the waveguide length between the klystron and the ion source resulted into varied number of oscillation minima and maxima in the measured frequency range. Furthermore, when the waveguide was disconnected from the ion source and then connected to a load element, the oscillating behavior remained. These results indicate that the oscillations observed in the reflected power are not connected to plasma effects or mode structure variations in the ion source plasma chamber, but are instead caused by the microwave delivery system. This frequency dependent behavior can be explained by considering the waveguide as a long rectangular resonator. Around 14 GHz the separation of the resonance frequencies, corresponding to the minima of reflected power in the system, matches the distance between the measured reflected power minima, as is discussed in Ref. [131].

The verification of the waveguide influenced oscillations in the reflected power signal has important consequences. Firstly, the oscillatory behavior observed in the beam currents is the result of the variation of total microwave power transmitted into the ECRIS plasma chamber, and is not connected to possible changes in the electromagnetic mode structure. This is especially clearly seen in the comparison of reflected power

and current signals presented in Fig. 4.5. The figure shows that the influence of the oscillating input power is also clearly observed in the bremsstrahlung emission from the ion source plasma.

Secondly, if the mode structure variations inside the plasma chamber influence the reflected power signal, this behavior is obscured by the waveguide induced oscillations. Furthermore, any possible narrow frequency range (in the order of a few MHz) effects coming from the mode structure must be weak in comparison to the influence of the waveguide, as such effects are not evident in the measured reflected power signal. However, in addition to the periodic oscillations, the reflected power signal does exhibit level variation in a broader frequency range (see the reflected power signal e.g. in Fig. 4.5). This variation was absent when the waveguide was connected to the load element (see Fig. 1 in Ref. [130]), and as such it could originate from the plasma chamber.

In order to accurately study the properties of the ECRIS plasma chamber and how the microwave power absorption is affected by the frequency fine tuning, the influence of the microwave transmission line on the results had to be isolated and carefully removed. This was achieved with the so-called dual port measurement technique, which enables direct measurement of the resonance properties of the ECRIS plasma chamber with plasma loading. The measurement is performed with a network analyzer through one of the two waveguides leading to the ECRIS plasma chamber, probing the system consisting of the chamber and the plasma with microwave signal around 14 GHz. The influence of the transmission line between the analyzer and the plasma chamber is removed with the network analyzer calibration feature. The second waveguide is used to ignite and sustain the plasma with microwaves around 11 GHz from the TWTA, decoupling the measurement from the plasma heating. The dual port measurement technique is described in detail in section 3.2.4.

Figure 4.6 presents the microwave power absorption properties of the JYFL 14 GHz ECRIS plasma chamber without plasma (case (a)) and with plasma using different microwave power levels from the TWTA (cases (b) – (e)). The power absorption is presented with the reflection coefficient $S_{11}$, described by Eq. (3.6) in section 3.2.4. It is immediately seen that the periodic oscillation observed previously is absent from the signals, further verifying that it originates from the properties of the microwave transmission line. Without plasma loading the measured signal exhibits a number of narrow minima, corresponding to electromagnetic modes (i.e. cavity resonance) with efficient power absorption and indicating good coupling between the probing microwave signal and the plasma chamber. With plasma the signal properties change significantly. The number of observed minima decreases with the increasing microwave power and the remaining minima become less pronounced. With the highest measured microwave powers the frequency dependent behavior is strongly damped and only smooth level variations over tens or hundreds of MHz remain in the measured signal. This order of frequency dependence in the microwave power absorption agrees well with the broad frequency range variations observed previously in the reflected power signal (see e.g. Fig. 4.5).

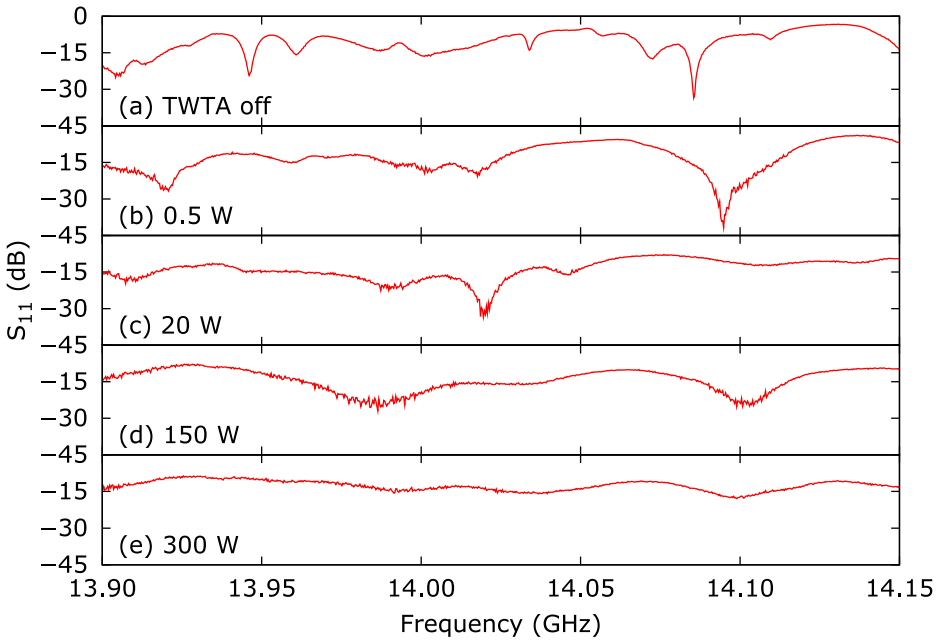


Figure 4.6: Plasma chamber reflection coefficient $S_{11}$ with varying microwave frequency, measured with different microwave power levels from the TWTA. The case (a) corresponds to empty cavity without plasma and cases (b) – (e) to plasma loaded cavity. Figure reproduced from Ref. [131].

It was observed that apart form the microwave power, the ECRIS tuning parameters do not have strong influence on the frequency dependent behavior of the plasma loaded cavity when varied around the normal operation values. Increase in the neutral gas injected into the plasma chamber leads to less pronounced frequency behavior, but the effect is considerably weaker than increasing the microwave power. Varying the magnetic confinement leads to subtle changes in the measured signal when the ion source is operated with high field values known to be prone to plasma instabilities. Varying the biased disc, plasma species or TWTA plasma heating frequency does not yield significant alteration of the $S_{11}$ signal.

The $Q$ value of the plasma chamber can be evaluated from the measured $S_{11}$ signal for the observed modes, which are represented by the local signal minima. As it is not possible to separate different sources of power dissipation in the measurement, the $Q$ values discussed here include all the power absorption inside the plasma chamber, whether it is caused by the resistive heating of the cavity walls or the plasma. The $Q$ values associated with the plasma chamber without power input from the TWTA (no plasma) are in the order of $10^3$, calculated with Eq. (2.2). With plasma and the highest measured microwave power of 300 W the $Q$ values decrease to the order of $10^2$, corresponding to the broadening of the $S_{11}$ signal minima. These values are in good agreement with the results obtained with the LBL 6.4 GHz ECRIS, which indicate that the loaded cavity $Q$ value drops to about 10 % of the empty cavity value [135].

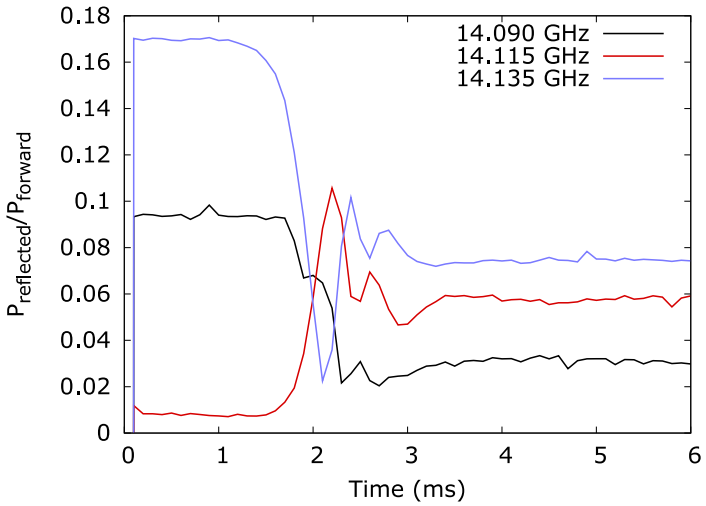


Figure 4.7: Ratio of reflected to forward power at plasma ignition with various microwave frequencies. Klystron output set to 430 W. Microwaves turned on at $t = 0$ ms. Figure reproduced from Ref. [131].

The results obtained with the network analyzer indicate that the mode structure observed with the empty chamber is strongly damped with the plasma. To acquire more information regarding the transition from the empty chamber to the plasma loaded situation, a series of time sampled measurements has been performed by pulsing the microwave power from the klystron. Figure 4.7 presents the ratio of reflected to forward power with various microwave frequencies during the first milliseconds after turning the microwaves on. It is observed that the microwave frequency affects significantly the initial power absorption conditions inside the plasma chamber, as is evident from the different initial levels of the reflected to forward power ratios. When the plasma density builds up the differences between the different frequency cases are mitigated and the signal behavior saturates after about 3.5 ms. The differences in the saturation values are caused by the superimposed effects of the waveguide and the cavity behavior (see the reflected power behavior e.g. in Fig. 4.5). The klystron output power rise time is $\sim$10 $\mu$s, and consequently does not contribute significantly to the observed behavior.

## 4.2 Studies of beam transport

### 4.2.1 Effect of space charge compensation on beam properties

The observation that some beams produced with the JYFL 14 GHz ECRIS are hollow also suggests the possibility that the beam quality degradation is contributed by space charge related effects. In addition, the relatively low ion source extraction voltages used at JYFL compared to the operation of many other ECR ion sources amplifies the

space charge effects, as they increase with decreasing beam velocity (see section 2.8.4). However, the extent of how the space charge influences the quality of beams produced with the JYFL 14 GHz ECRIS was not known. As a result, a series of measurements has been performed to study the connection between space charge and beam quality at JYFL and to dictate whether the quality could be improved by enhancing the space charge compensation.

The experimental apparatus and the methods used in the space charge studies are presented in section 3.2.5. Detailed documentation of the gas injection experiments is presented in Ref. [132] (publication A.IV). The results obtained with the biased grid and the heated filament which are presented here have not been published previously.

The beam properties were characterised in the experiments with the beam current, transverse emittance and profile of $q/m$ separated argon beams with varied charge states and acceleration voltages. In the gas injection experiments the beamline pressure was varied between $1 \cdot 10^{-7}$ and $3 \cdot 10^{-5}$ mbar by injecting He, $N_2$ or Ar gases into the beamline close to the focal points (beam waists) of the beam of interest in order to enhance the space charge compensation. A series of measurements were performed to ensure that the observed effects on beam properties do not depend on the ion source tuning and are not influenced by gas diffusion into the plasma chamber [132]. The experiments were performed upstream and downstream from the analyzing magnet. Upstream all ion species extracted from the ECR ion source are still present and the total beam current in the beamline is normally around 1-2 mA. Downstream from the analyzing magnet only one $q/m$ is present and the beam currents are one or two orders of magnitude lower, depending on the studied ion species. In order to gain a more complete picture of the relation between the beam properties and the space charge, a positively biased grid was installed to the same locations in the beamline to study the effects of degraded space charge compensation by removal of electrons. The potential of the grid was varied between 0 and 140 V.

It was observed that gas injection into the beamline section upstream from the analyzing magnet results into significant improvement in beam quality. This is characterized by a pronounced reduction in the beam emittance and increase in the beam brightness. The emittance reduction is associated with a decreasing level of distortions observed in the phase space distribution as well as decreased beam size and angular spread. As the beamline pressure is further increased, the emittance reaches a minimum and starts to slowly increase. The emittance growth is most likely related to the increased interactions between ions and neutral atoms. This is indicated by the increasing angular spread at the highest pressures. The beam current decreases steadily with increasing pressure due to interactions between ions and the neutral atoms or molecules leading to charge exchange. As a result, the beam brightness exhibits a maximum in the $10^{-6}$ mbar ($10^{-5}$ mbar for He injection) pressure region, as is presented in Fig. 4.8. The beam diameter decreases with increasing beamline pressure, as is presented in Fig. 4.9.

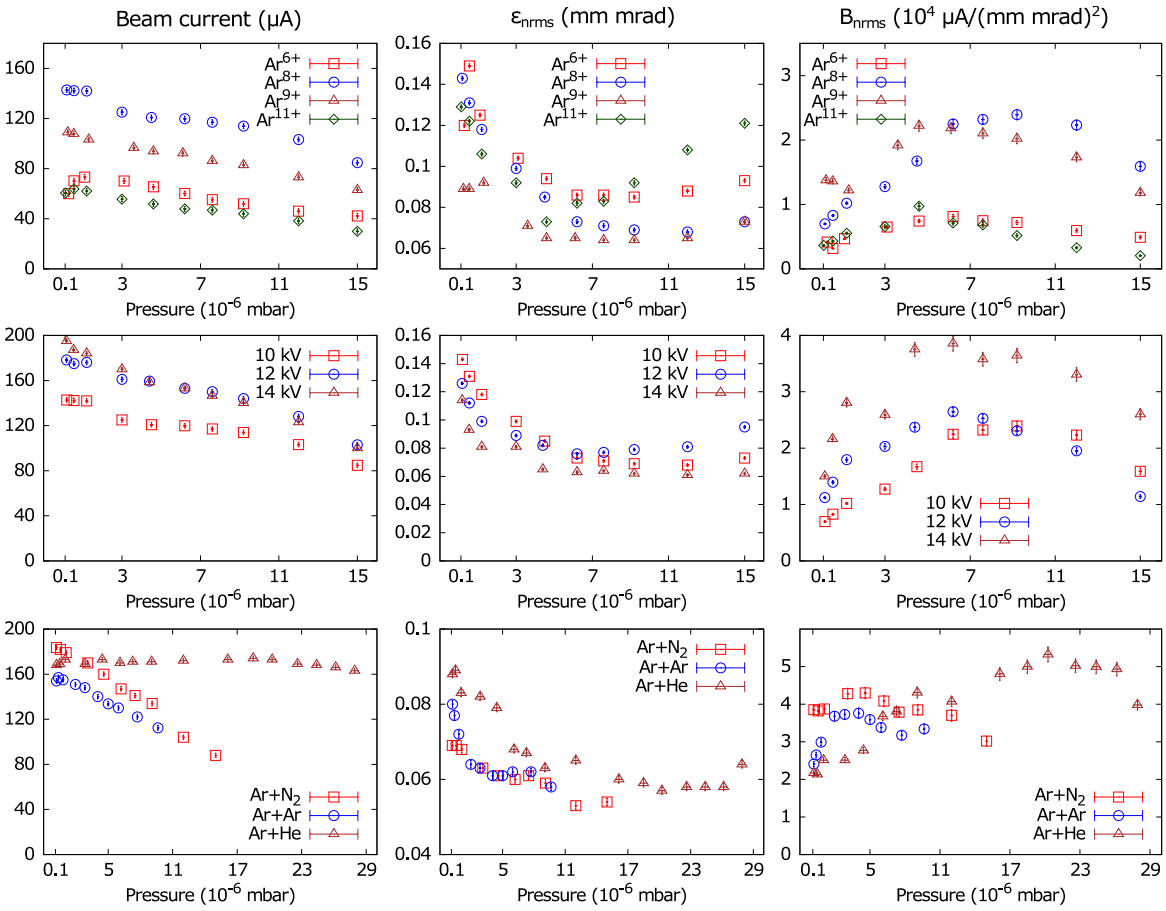


Figure 4.8: Beam current, normalized transverse rms emittance and normalized rms brightness of Ar ion beams with varying beamline pressure. First row: different Ar charge states with N gas injected into the beamline. Second row: different extraction voltages, $^{40}Ar^{8+}$, and N injection. Third row: different injected gas species, $^{40}Ar^{8+}$ and 10 kV extraction voltage. Figure reproduced from figures in Ref. [132].


Figure 4.9: Beam profile of $^{40}Ar^{8+}$, extracted with 10 kV, with various beamline pressures. Nitrogen as buffer gas and injected into the beamline. Part of the $^{14}N^{3+}$ beam can be seen at the left edge of the viewer plate. Figure from Ref. [132].

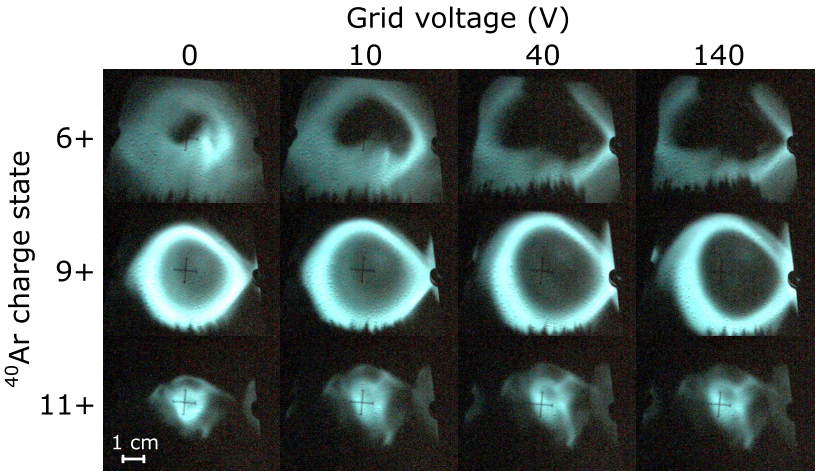


Figure 4.10: Profiles of selected Ar charge states with different grid voltages.

Increasing the grid potential has the opposite effect on beam quality. The beam emittance and the diameter of the beam spot increase with the potential. In addition, the low charge states become increasingly hollow, as is presented in Fig. 4.10. The beam transverse emittance as a function of the grid voltage with different extraction voltages and argon charge states is presented in Figs. 4.11 and 4.12. The results are presented in comparison with the gas injection data to emphasize the complementary nature of these two experiments. The beam current exhibited decrease with saturating behavior, as presented in Fig. 4.13.

The trends described above were exhibited by all measured argon charge states and extraction voltages. The clear variations seen in the size and structure of the recorded beam profiles are in good agreement with enhanced space charge compensation with gas feeding and degraded compensation with biased grid. With gas injection the high charge states exhibited higher beam losses than the low ones, which is consistent with increasing charge exchance cross section with ion charge [136]. With biased grid the beam losses increase with decreasing charge state. This is probably caused by increased losses during beam transport due to degrading profile structure and increasing beam diameter, which are more pronounced for the low charge states (see Fig. 4.10). The beam losses also increased with decreasing extraction voltage.

The emittance improvement with gas injection and degradation with biased grid is more pronounced with low charge states and low extraction voltages. The voltage behavior is in good agreement with the $v^{-1}$ dependency of the beam potential (see Eq. (2.47)), i.e. increased beam velocity $v$ due to increased extraction voltage mitigates the space charge effects. The stronger emittance variation of the low charge states is linked to the stronger variations seen in the beam structure, especially in terms of hollowness. When the low charge states are measured, they are transported over the focal points of the higher $q/m$ ion species, as discussed in 2.8.5. Thus the impact of the space charge variation is stronger for the low charge states.

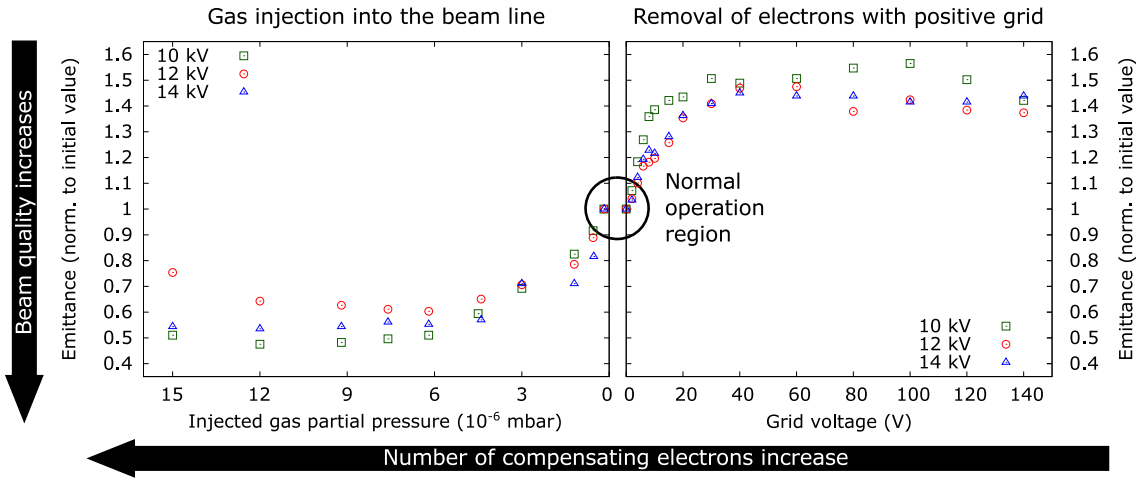


Figure 4.11: Combined presentation of the transverse emittance behavior with different extraction voltages obtained with gas injection and biased grid. Gas injection measurement performed with $^{40}Ar^{8+}$, biased grid with $^{40}Ar^{9+}$.

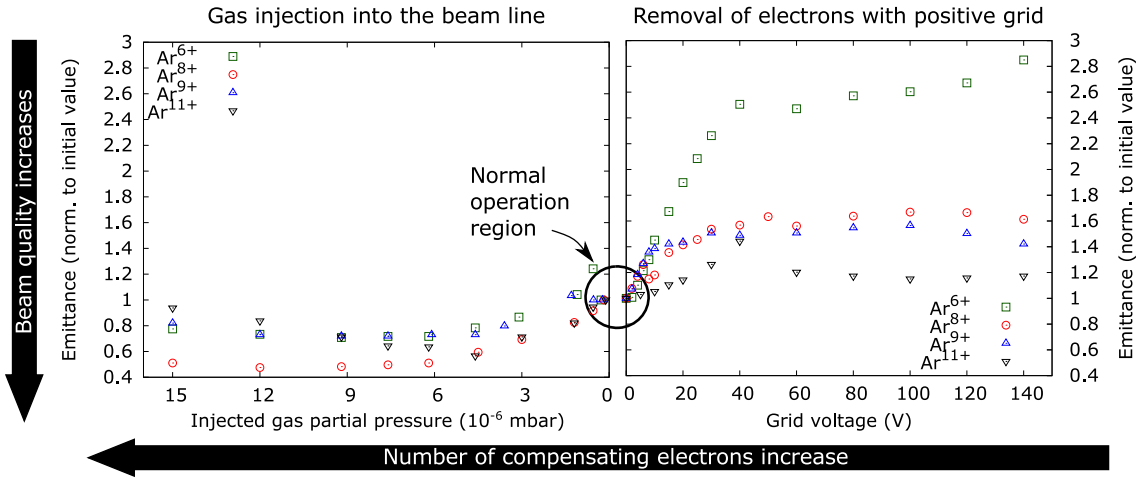


Figure 4.12: Combined presentation of the transverse emittance behavior with different Ar charge states obtained with gas injection and biased grid. 10 kV extraction voltage.

Two phenomena were observed with different injected gas species. Firstly, the magnitude of the beam losses caused by the increased beamline pressure is gas species dependent. For a given beamline pressure, He caused the the least amount of losses, followed by Ar and N. Secondly, it was observed that the slope of the emittance decrease as a function of the beamline pressure is steeper with the heavier gases. Both of these effects are explained with the charge exchange and ionization cross section inverse dependency on the ionization potentials of the injected gases [136, 137].

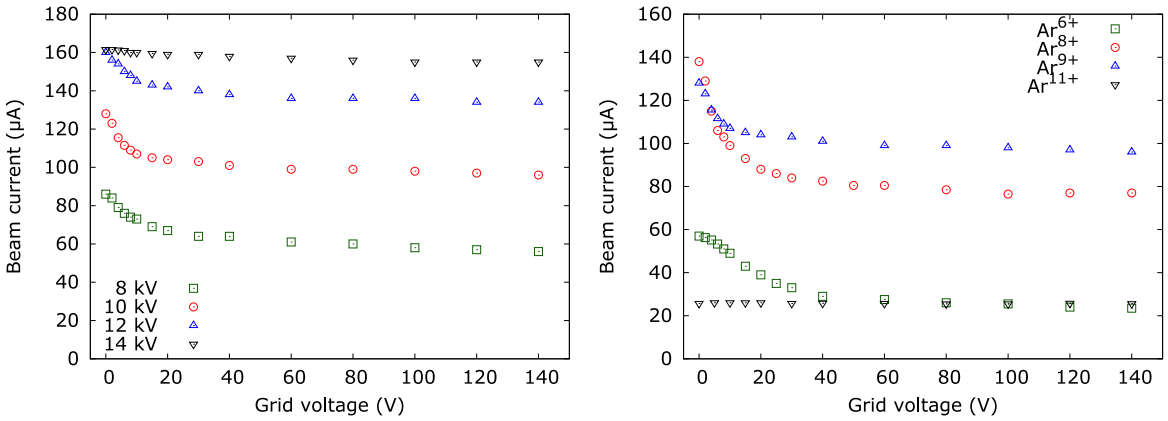


Figure 4.13: Argon beam currents with varied grid voltage. Left: $^{40}Ar^{9+}$ beam current with different extraction voltages. Right: beam current of different argon charge states extracted with 10 kV.

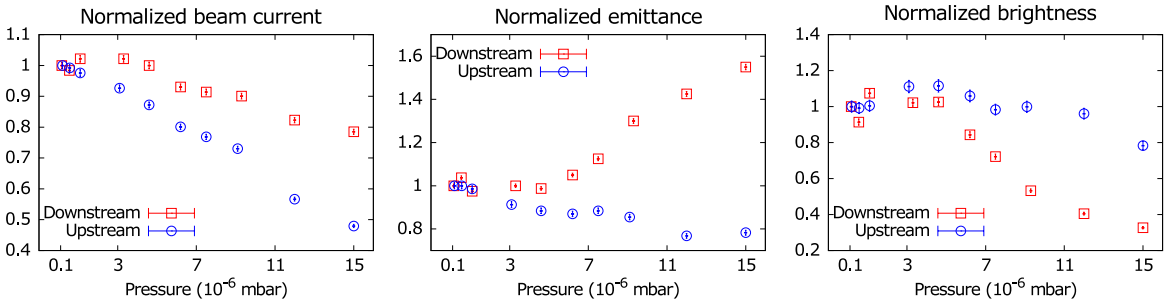


Figure 4.14: The normalized beam current, emittance and brightness of $^{40}Ar^{8+}$ beam with gas injection upstream and downstream from the analyzing magnet. Figure reproduced from Ref. [132].

The effects of the gas injection and biased grid were also measured downstream from the analyzing magnet. In this beamline section the gas injection did not yield improved beam quality, as is presented in Fig. 4.14. The beam current decreases with increasing beamline pressure, but the decrease is less pronounced than with gas injection upstream from the analyzing magnet. The beam emittance increases with pressure, which leads to degraded beam brightness. No shrinking of the beam profile was observed. The effects of the biased grid are also weaker. A comparison of the beam current and emittance behavior upstream and downstream from the analyzing magnet with varying grid potential is presented in Fig. 4.15.

The combined results of gas injection and biased grid indicate that the ion beams produced with the JYFL 14 GHz ECRIS are not fully space charge compensated and the beam quality is susceptible to variations in the compensation degree. The experiments also show that the strong space charge effects are localized to the beamline section upstream from the analyzing magnet where all extracted ion species are present.

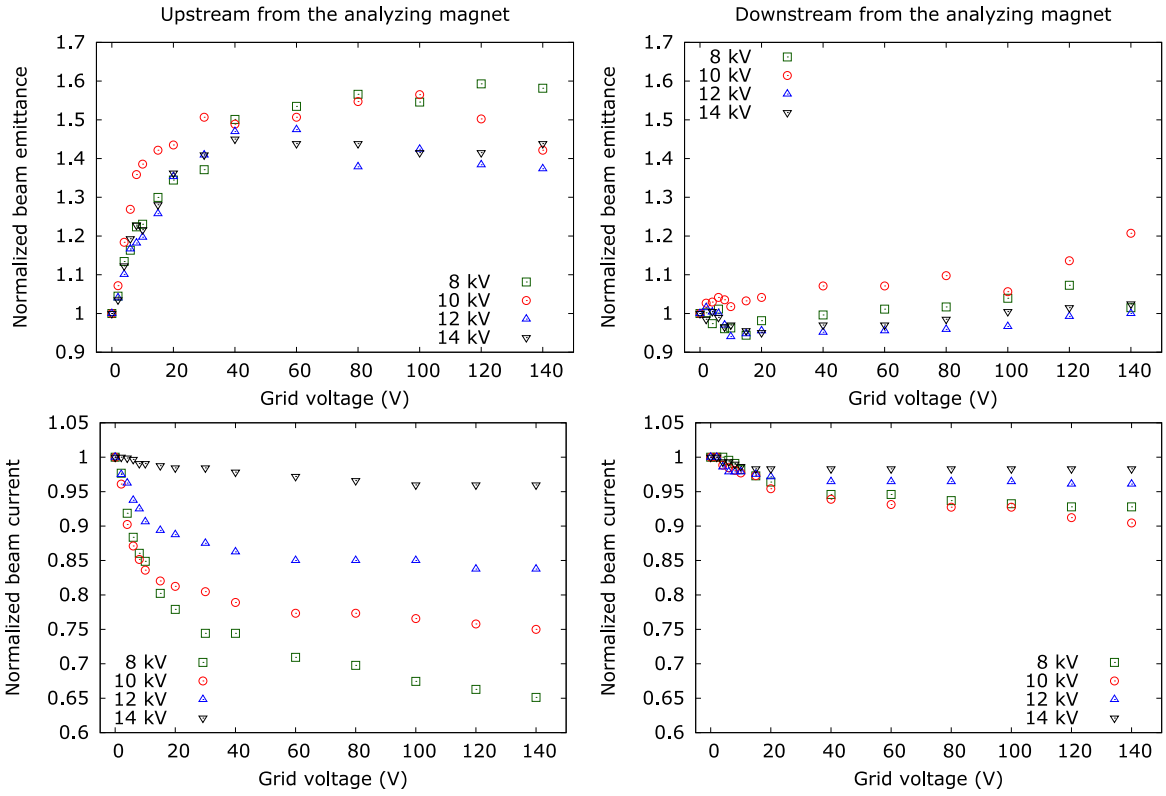


Figure 4.15: Normalized $^{40}Ar^{9+}$ beam current and transverse emittance measured with varied extraction voltages with the biased grid installed upstream and downstream from the analyzing magnet. The effect of the grid voltage on the beam properties is significantly mitigated in the downstream location.

Downstream from the analyzing magnet the decreased beam current due to $q/m$ separation mitigates the space charge effects substantially, and it ceases to be a significant contributor to the beam quality.

The effect of the improved beam quality to the beam transport was studied by measuring the transmission efficiency from the ion source through the cyclotron for $^{40}Ar^{8+}$ and $^{40}Ar^{9+}$ beams with normal beamline vacuum conditions and with gas injection upstream from the analyzing magnet to obtain the maximum beam brightness. The measurements were performed with varied ion source extraction voltages and He, N and Ar gases were injected into the beamline. Operation with gas injection yielded improved transmission in all measured cases. The improvements varied between 3.8 and 32.0 %. However, the decrease in the initial beam current measured after the $q/m$ separation caused by the gas injection matches closely the improved transmission. As a result, the accelerated beam current measured after the cyclotron is not significantly different.

The transmission results indicate that beam quality improvement by enhanced space

charge compensation can yield improved transmission performance. However, in order to gain significant increase to the accelerated beam current, the enhanced compensation must be realized without introducing significant beam losses. Thus the gas injection method is not a practical approach to this, especially as the increasing charge exchange cross section with the neutral atoms is an additional limitation for highly charged ions.

A heated tantalum filament has been tested as an external source of compensating electrons in the beamline section upstream from the analyzing magnet. The filament was located at the same point as the gas injection and the biased grid. The filament bias voltage, which accelerates the electrons from the filament towards the ion beam through a grounded grid, was varied between 0 and $-90$ V. The current of thermally emitted electrons was varied between 0 and 50 mA. However, no significant variation in the beam properties, i.e. beam current, emittance and profile, was observed. This is most likely due to the electrons not being trapped into the positive beam potential. In order to emit electrons towards the beam, the filament is biased to negative potential with respect to the beam pipe and the grid. The beam potential, on the other hand, is positive with respect to the beam pipe. As such, the electron traverses the beam without being trapped into the beam potential, unlike in the case of rest gas ionization, where the electrons are produced inside the beam potential. Without being trapped into the beam potential and being accumulated and distributed along the beam, the compensating effect of the emitted electrons remains localized on the immediate vicinity of the filament. The experiments show that this is not enough to provide significant impact on the beam properties.

### 4.2.2 Beam current temporal stability

As discussed in section 2.8.3, the long-term beam fluctuations observed with ECRIS beams in time scales from seconds to days are rather well known and understood. In contrast, the knowledge on the short-term beam fluctuations in the millisecond scale is still sparse, and only a few tentative studies have been published [103, 104], providing insight into how the fluctuations are affected by the ECRIS tuning parameters. This is discussed in section 2.8.3. In order to acquire further information about the characteristics of the short-term beam current fluctuations and their relation to beam transport, a series of measurements has been performed with the JYFL 14 GHz ECRIS and the JYFL K-130 cyclotron. A specialized measurement and analysis software was developed for these studies and is presented in section 3.2.7. Detailed documentation of the experiments is presented in Ref. [126] (publication A.V).

The measurements were performed with $^{16}O^{6+}$ and $^{40}Ar^{8+}$ beams with varying ion source settings. The beam current oscillations were studied in the frequency range of $10^2 - 10^3$ Hz. It was observed that the beams produced with the JYFL 14 GHz ECRIS exhibit clear beam current oscillations at broad range of frequencies and amplitudes when the ion source settings are varied. The oscillation frequencies vary from 100 Hz up to 1.5 kHz, while the relative oscillation amplitude, defined as the $2\sigma$ variation

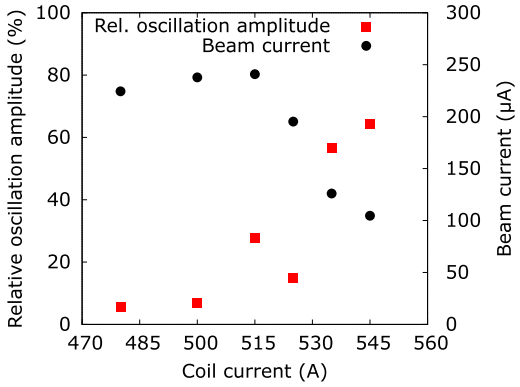


| Ion source settings | | | |
|---|---|---|---|
| RF power: 600 W | | | |
| RF on pressure: 1.3E-7 mbar | | | |
| Extraction voltage: 12.04 kV | | | |
| Coil current (A) | Axial solenoid magnetic field $B_{inj}$ (T) | $B_{min}$ (T) | $B_{ext}$ (T) |
| 480 / 480 | 1.91 | 0.33 | 0.92 |
| 500 / 500 | 1.95 | 0.35 | 0.95 |
| 515 / 515 | 1.97 | 0.36 | 0.97 |
| 525 / 525 | 1.99 | 0.37 | 0.98 |
| 535 / 535 | 2.01 | 0.38 | 1.01 |
| Max radial field, $B_{rad}$ (T) = 1.09 T | | | |

Figure 4.16: Relative oscillation amplitude and average beam current of $^{16}O^{6+}$ with varying coil currents and the corresponding axial solenoid magnetic field values. Figure from Ref. [126].

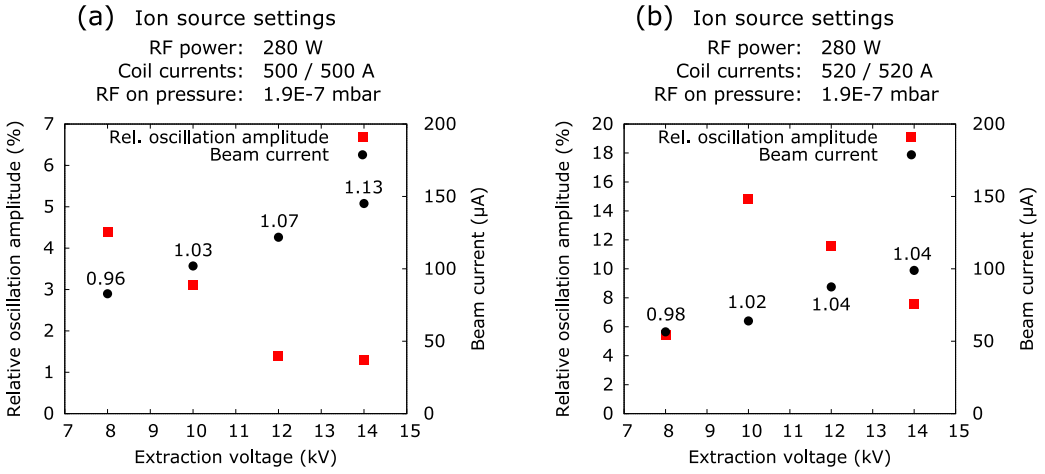


Figure 4.17: Relative oscillation amplitude and beam current of $^{40}Ar^{8+}$ as a function of ion source extraction voltage. Data is shown for two different ion source settings. Total extracted current (in mA) is indicated on top of the beam current data points. Figure from Ref. [126].

of the beam current compared to the average value, varies from ∼1 up to ∼65 %. When the ion source settings were varied, it was observed that the beam current oscillations often seemed to favor two distinct "oscillations modes". The first mode is characterised by frequencies around a few hundred Hz, while the second is localized to higher frequencies around 1 kHz. The low frequency mode was observed to usually exhibit higher oscillation amplitudes than the high frequency mode.

Besides the microwave power and the biased disc voltage dependencies which have been reported in Ref. [103] for the JYFL 14 GHz ECRIS, it was observed that the

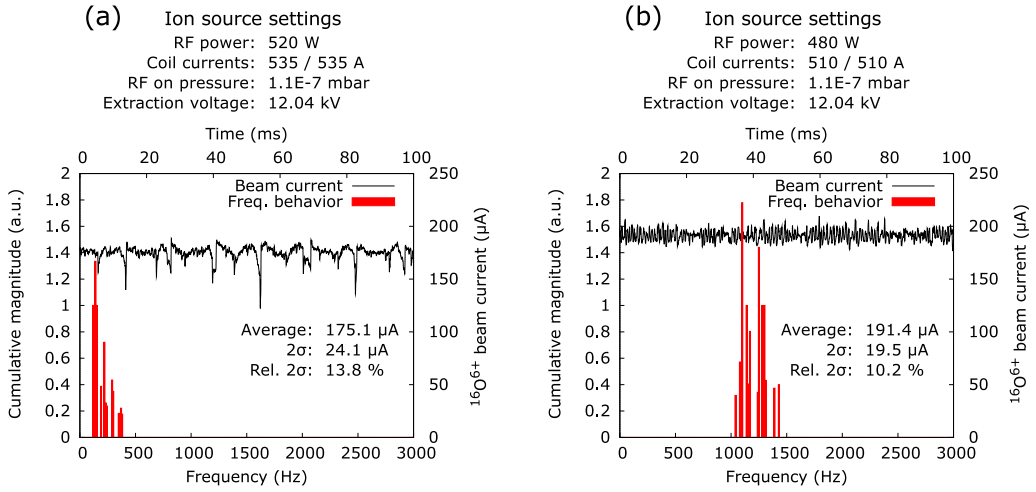


Figure 4.18: $^{16}O^{6+}$ beams used for the transmission studies with (a) low and (b) high frequency beam current oscillations. Figure from Ref. [126].

beam current oscillations depend strongly on the ion source solenoidal magnetic field and extraction voltage. Increasing the solenoidal magnetic field in the plasma chamber by increasing the coil currents yields strong increase in both the absolute and relative oscillation amplitudes, as is presented in Fig. 4.16. In addition to affecting the axial magnetic field minimum and maxima, the varied coil currents also affect the field gradient at the electron cyclotron resonance. Increasing the extraction voltage has the opposite effect to the magnetic field, as it was observed to mitigate the oscillation amplitude. This is presented in Fig. 4.17. No clear trends concerning the oscillation frequency were observed in either case.

The beam current oscillations were measured with three Faraday cups along the low energy beam transport between the JYFL 14 GHz ECRIS and the JYFL K-130 cyclotron (FC2, FC4 and FC5), and with two Faraday cups after the cyclotron (PFC, BB3). The locations of the Faraday cups are presented in Figs. 3.1 and 3.2. The measurements showed that the distinct oscillations originating from the ECRIS are preserved along the LEBT all the way to the cyclotron, but are not observed in the high energy beamline after the cyclotron. This result was verified by repeating the measurement with two different ion beams ($^{16}O^{6+}$ and $^{40}Ar^{8+}$) and two different cyclotron tunings, both yielding the same result.

The consequences of different ion beam temporal characteristics to beam transport were studied by measuring the transmission efficiency from the ion source through the cyclotron with two $^{16}O^{6+}$ beams with comparable beam currents but different oscillation characteristics corresponding to the two ”oscillation modes” often observed with the JYFL 14 GHz ECRIS. The properties of the beams are presented in Fig. 4.18. With the high frequency mode the measured total transmission was 2.1 %, which is about 30 % higher than the transmission obtained with the low frequency mode, 1.6 %.

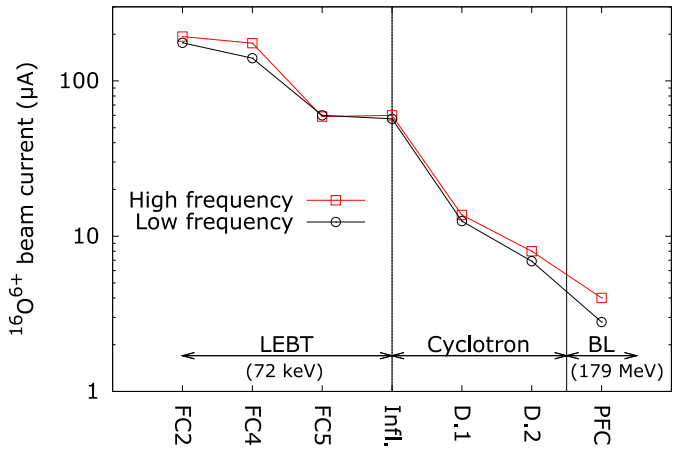


Figure 4.19: The measured beam currents through the low energy beam transport (LEBT) and the cyclotron into the first Faraday cup in the high energy beamline (BL) with two different oscillation modes. FC2 - FC5 are the LEBT Faraday cups, Infl. is the cyclotron inflector (injection), D.1 and D.2 are the cyclotron deflector probe positions 1 (last rotation before the deflector) and 2 (beam through the deflector). PFC is the first Faraday cup after the cyclotron. Figure from Ref. [126].

This is a significant difference, because at the time of the measurements (before the ion source extraction upgrade) ∼2 % represents the normal transmission performance. The difference in the transmission occurs inside the cyclotron, as is shown in Fig. 4.19. The transmission through the LEBT remained virtually unaltered (32.4 % with the low frequency oscillations and 31.1 % with the high frequency oscillations).

## 4.3 Improvement of ECRIS beam formation

### 4.3.1 Plasma electrode collar structure

Over the years numerous techniques have been developed to improve the performance of ECR ion sources, as is discussed in section 2.6.2. In 2009 Mironov *et al.* proposed [138] the use of a so-called collar, a cylindrical structure around the extraction aperture extruding towards plasma, as a new method to improve ECRIS performance by shifting the charge state distribution of extracted ions to higher values. However, no systematic studies were published. As a result a series of collar experiments were performed at JYFL with the JYFL 14 GHz ECRIS to study the influence of the collar structure to the ion source performance. Detailed documentation is presented in Ref. [133] (publication A.VI).

The collar structure used in the experiments is presented in Fig. 4.20. Experiments were performed with varying collar lengths between 5 and 60 mm and different

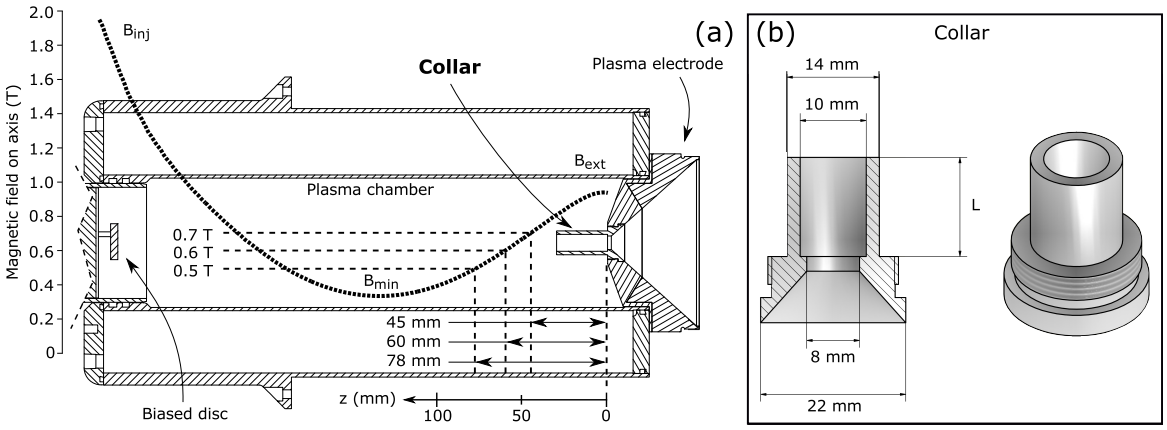


Figure 4.20: A schematic presentation of the collar installed to the plasma electrode of the JYFL 14 GHz ECRIS (a) and the structure of a separate collar (b). The collar length $L$, defined in part (b) of the figure, was varied between 0 and 60 mm. In the figure $L = 30$ mm in the schematic plasma chamber assembly (a) and $L = 15$ mm for the presented separate collar (b). Figure from Ref. [133].

collar materials, namely nonmagnetic stainless steel, aluminium and aluminium oxide. Different plasmas ranging from $^{14}$N to $^{82}$Kr and gas mixing with $^{40}$Ar + $O_2$ were used.

Three main conclusions can be derived from the collar experiments. Firstly, the collar structure itself does not provide remarkable improvement to the performance of the JYFL 14 GHz ECRIS. With collar lengths up to 30 mm the ion species for which the ion source was optimized exhibited moderate beam current and transverse emittance improvement, as is presented in Fig. 4.21 for $^{40}Ar^{12+}$. The performance of other charge states exhibited more variation, and no clear charge state dependent behavior was observed, as is demonstrated in Fig. 4.22. Between different plasmas, the results with the optimized ion species seem to suggest weak $m/q$ dependence. However, this behavior becomes obscured when all extracted ion species are considered. With collar lengths over 30 mm the ion source performance was substantially degraded, which was most pronounced for high charge states. This is due to the collar disturbing the ECRIS plasma, which is evident from the damage observed around the collar tip. The damaged length of the collar corresponds to the location of the electron cyclotron resonance for hot 100 - 200 keV electrons in the plasma chamber, and the existence of electron population at these energies in the JYFL 14 GHz ECRIS plasma has been confirmed with bremsstrahlung measurements [36, 37]. Up to 30 mm the collar exhibited very little evidence of interaction with plasma particles.

Secondly, the collar experiments provide information concerning the dynamics of the extracted ions. The results suggest that the extracted ions originate from a plasma volume further away from the extraction aperture in the axial direction. This is supported by the observation that even though the collar structure severely limits the radial direction around the extraction aperture, up to 30 mm the collar exhibited very

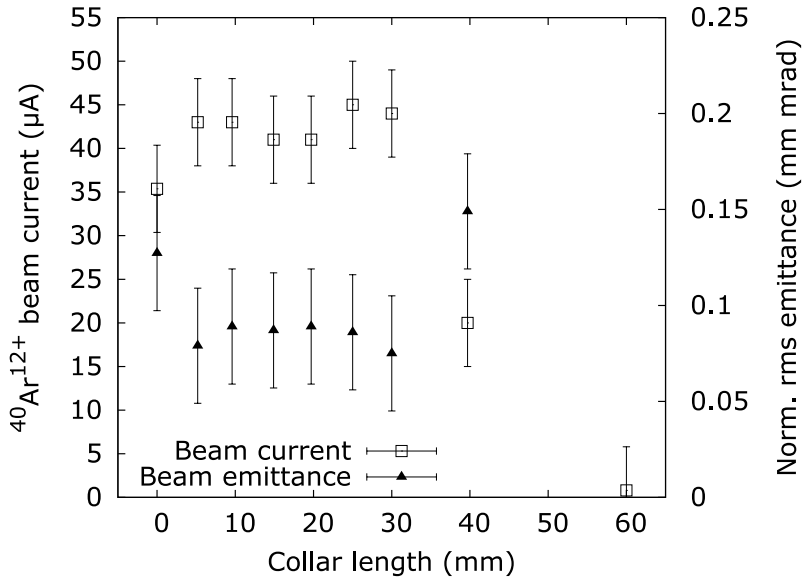


Figure 4.21: Beam current and normalized rms emittance of $^{40}Ar^{12+}$ with varying collar length. Figure from Ref. [133].

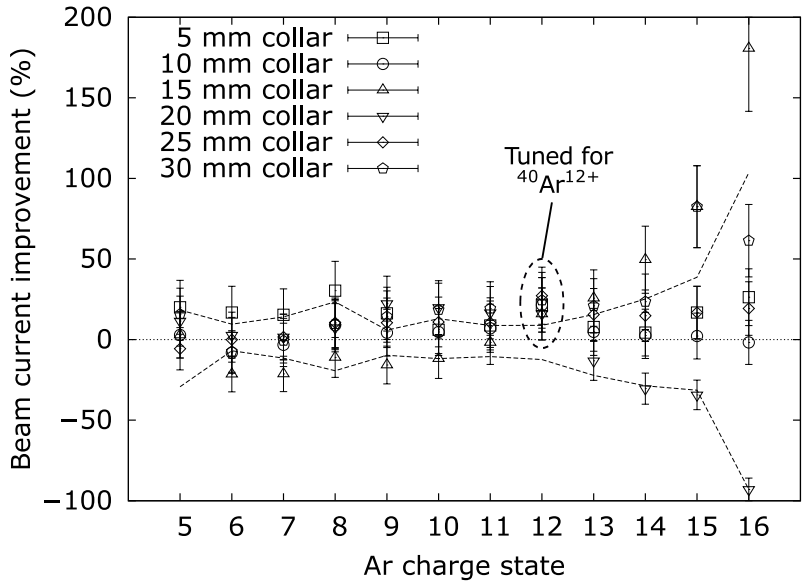


Figure 4.22: Beam current improvement of different argon charge states compared to baseline average (normal operation without collar) with varying collar length. The dashed lines correspond to the maximum baseline variation around the average. Ion source optimized for $^{40}Ar^{12+}$. The data in the figure corresponds to Table 1 of Ref. [133].

little evidence of interaction with the plasma. Furthermore, no significant performance differencies were observed between the different collar materials and the recorded beam profiles with collars did not exhibit significant variation compared to the baseline measurements without collar. This indicates that particle interaction with the collar material does not contribute significantly to the properties of the extracted beams. The result is also in good agreement with the predictions obtained from several computational models of the ion dynamics inside ECRIS plasma [49, 115–118], albeit they employ rather different assumptions, and the results of the recent experimental work by Panitzsch *et al.* [48] concerning the current densities and sputter marks near the ECRIS extraction.

Thirdly, and perhaps most interestingly, the experiments indicate that the volume around the collar could be utilized without compromising the ion source performance. This opens up a discussion on novel techniques to improve the ECRIS performance that could be implemented in this region near the extraction aperture. As an example, these possibilities could include hexapole correction of extracted ion beams with compact magnetic design around the extraction aperture, or enhancement of ion extraction by local manipulation of the ECRIS solenoidal magnetic field with a small solenoid assembly around the extraction aperture.

### 4.3.2 New extraction system for the JYFL 14 GHz ECRIS

The initial conditions of beams extracted form an ion source are crucial for the following beam transport, having strong impact on the transport performance. Based on the operation experience of the JYFL 14 GHz ECRIS it was known that the performance of the old extraction system of the ion source was not perfect and had several undesired features. As a result, in order to provide improved beam quality and increase the flexibility of operation to accommodate possible future beam transport improvements, it was necessary to determine the problems of the old system and improve the situation with a new extraction system. Detailed documentation of the work is presented in Ref. [99] (publication A.VII).

The structure of the old extraction system as part of the JYFL 14 GHz ECRIS is presented in Fig. 3.3. The performance of the system was studied with a combination of simulations and measurements. The simulations were performed with the ion optical code IBSimu, which has been developed at JYFL by T. Kalvas and used successfully e.g. in the development of light ion source extraction systems [91, 139–141].

An example of the simulation results for the old extraction system is presented in Fig. 4.23. The main challenge of the beam extraction is the relatively low extraction voltages around 10 kV. As a result, the extracted beams are the subject of strong space charge forces, which are further strenghtened by the inclusion of beam deceleration during beam formation, which unfortunately is necessary for the extraction system ion optics. Combined with the weak einzel lens, this leads to increased beam diameter inside the extraction and subsequent degradation of beam quality. In addition, the

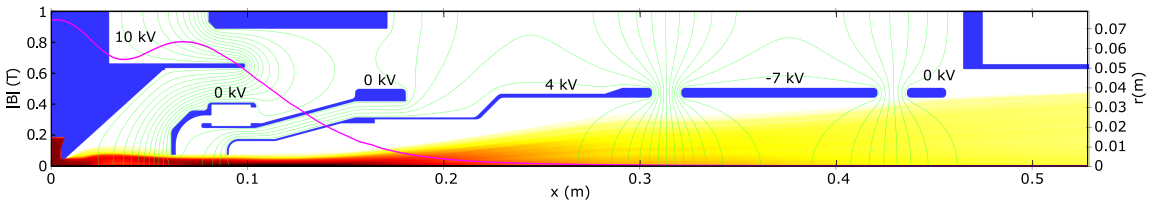


Figure 4.23: Simulation result (trajectory density) of the old extraction system for 1 mA argon beam. Extraction voltage 10 kV, puller electrode at 0 kV, decelerating electrode at 4 kV and einzel electrode at -7 kV. Magnetic field on axis is indicated with the solid purple line. Figure from Ref. [99].

conical shape of the plasma electrode weakens the electric field in the vicinity of the extraction aperture, resulting to poor electric field structure in the acceleration gap between the plasma and puller electrodes, and extraction of diverging beams from the ECRIS plasma. Consequently, the beam extraction is unable to handle beam currents in excess of 1 mA without decreased transmission through the extraction region and degraded beam quality. These effects have been also indicated experimentally [11].

The simulations were compared to experimental results by performing a set of measurements right after the extraction chamber, which corresponds to the end of the simulated region. The beam diameter and divergence was determined using the pepperpot-like system described in section 3.2.6. The experimental data was in good agreement with the simulated beam properties [99].

The results obtained for the old extraction system prompted the designing of new beam extraction system to improve the properties of extracted beams and the overall ECRIS performance. IBSimu was chosen as the main simulation tool for the design based on the good correlation achieved between the simulated and experimental results with the old extraction system.

The mechanical structure of the new extraction system, including modified planar plasma electrode, puller electrode and two accelerating einzel lenses, is presented in Fig. 4.24 and a photo of the system installed inside the JYFL 14 GHz ECRIS extraction chamber is presented in Fig. 4.25. The two accelerating einzel lenses, designed to be used with up to $-30$ kV voltages, provide improved focusing properties compared to the old system. Both of the lenses are independently movable along the optical axis, providing a high degree of tuning flexibility. The improved shape of the plasma electrode, providing more uniform electric field distribution between the plasma and puller electrodes, and the adjustable acceleration gap length offer improved beam extraction from the ECRIS plasma. An example of simulation of the new extraction system is presented in Fig. 4.26, showing clearly improved performance compared to the old system (see Fig. 4.23).

Measurements of transverse beam emittance as a function of einzel lens voltages and acceleration gap length provided good correlation with simulated values. In addition,

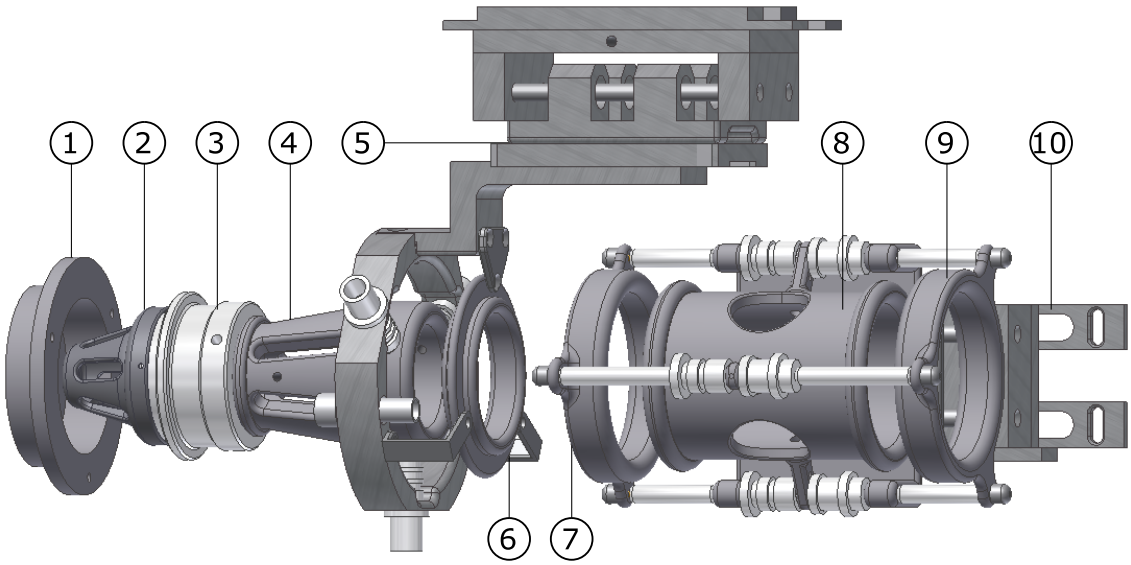


Figure 4.24: Mechanical design of the new extraction system including the plasma (1), puller (2) and einzel electrodes (4 and 8). The puller electrode is separated from the first einzel electrode with MACOR insulator (3). The einzel lenses are completed with grounded electrodes (6, 7 and 9) and are independently movable on rails (5, 10). The electrodes have open structure for improved pumping. Figure from Ref. [99].

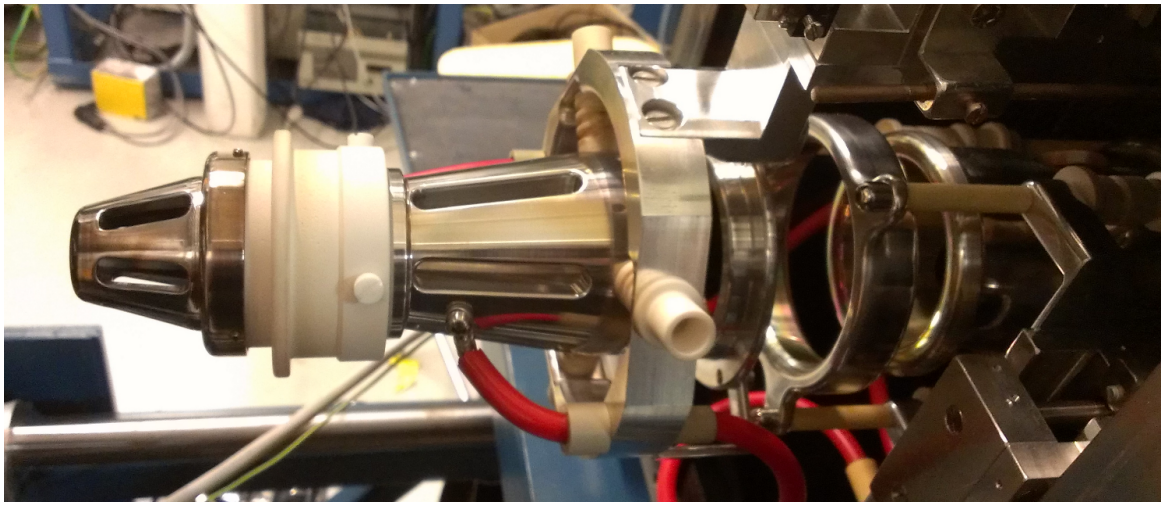

Figure 4.25: Photo of the new extraction system installed into the extraction chamber of the JYFL 14 GHz ECRIS.

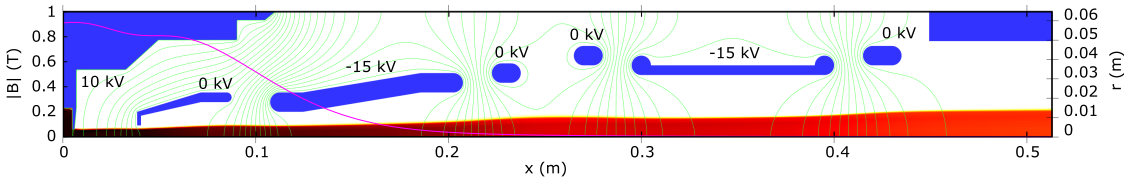


Figure 4.26: Simulation result (trajectory density) of the new extraction system for 1 mA argon beam. Extraction voltage 10 kV, puller at 0 kV and both einzel lenses at -15 kV. Magnetic field on axis is indicated with the solid purple line. Figure from Ref. [99].

the diameter and divergence of selected beams with different extraction settings were determined immediately downstream from the extraction chamber. The experimental results agree well with the simulated values [99].

The new extraction system provides improved performance compared to the old system. Firstly, the new extraction yields improved beam quality, indicated by the decrease in the measured transverse beam emittances. For example, with the old extraction system the transverse normalized rms-emittance of $0.10 \pm 0.01$ mm mrad was measured for $^{40}Ar^{8+}$ beam with 170 $\mu$A beam current, as the new extraction system yields $0.07 \pm 0.01$ mm mrad for comparable beam current of 187 $\mu$A (values from Table 2 of Ref. [99]). The improved beam quality is also seen in the beam profile measurements, which show improved current distribution with the new extraction system. Two examples with $^{40}Ar^{8+}$ are presented in Fig. 4.27.

Secondly, and closely related to the improved beam quality, the transmission efficiency from the ion source through the cyclotron is almost doubled with the new extraction system. This is shown by the experiments performed with $^{40}Ar^{8+}$ and $^{84}Kr^{16+}$ beams with varying beam currents yielding an average improvement of 90 and 80 %, respectively, in transmission efficiency.

Thirdly, the new extraction is capable of handling higher beam currents. The improvement is seen clearly with beams which were earlier extraction limited instead of production limited. As an example, $^{4}He^{+}$ and $^{4}He^{2+}$ beams have been produced with record beam currents of 1120 and 720 $\mu$A, respectively, which are a factor of two higher than the records obtained with the old extraction.

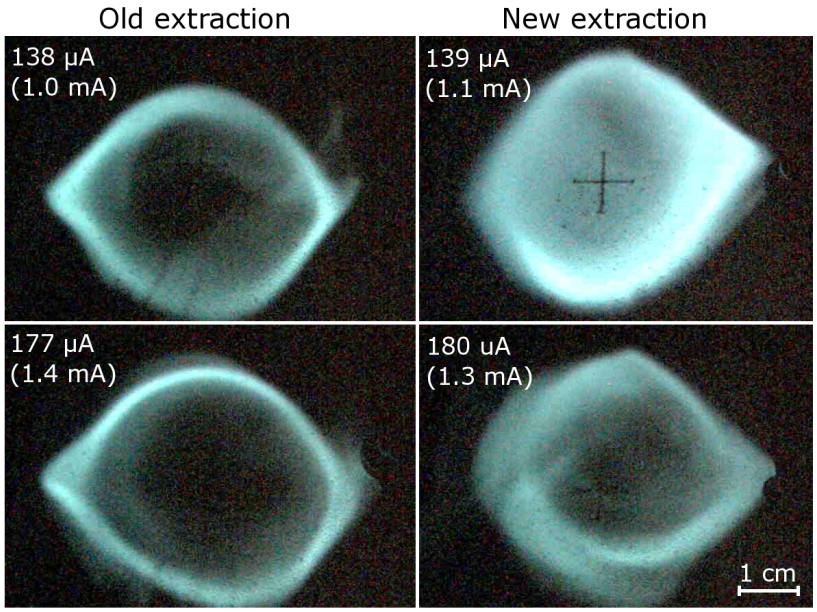


Figure 4.27: Comparison of profiles of $^{40}Ar^{8+}$ beams produced with the old and the new extraction systems with beam currents of about 140 and 180 $\mu$A. Figure from Ref. [99].

# Chapter 5

# Discussion and conclusions

The experimental work presented in this thesis comprises of five major studies which focus on different phenomena in ECRIS plasma, beam formation and beam transport. As such, the presented results provide a relatively extensive view of the different processes influencing the properties of the beams extracted from the JYFL 14 GHz ECR ion source.

The frequency tuning experiments show that the current distribution over the beam profile is influenced by plasma processes, which are affected by the variation of the heating microwave frequency. This agrees with the results obtained with the GSI Caprice [29]. The observation of the beam structure with two concentric rings, achieved with double frequency heating, further indicates that these effects originate from the ECRIS plasma, as formation of such a beam structure later on during the beam formation and transport is highly unlikely. In addition to beam structure, the current and emittance of beams extracted from the JYFL 14 GHz ECRIS are also influenced by the varying microwave frequency. The variations occur smoothly over the span of tens of MHz, which matches well the observed variations in the power absorption of the plasma loaded chamber. This indicates that with plasma the frequency dependent behavior of the ion source is strongly damped, and only wider frequency range variations remain, produced by the overlapping of a large number of cavity modes. Consequently, tuning the plasma heating microwave frequency in the frequency range of hundreds of MHz can yield improvement to the ion source performance, but the exact frequency ceases to play a crucial role. This is also supported by the results of the collar experiments, which indicate that alteration of the chamber inner structure near the extraction aperture by the introduction of the collar structure does not disturb the ion source performance (until the collar is long enough to interact with the plasma itself).

The frequency dependent behavior observed with the JYFL 14 GHz ECRIS is somewhat different than that reported with the Caprice type ion source [29]. Both ion sources exhibit beam structure and beam current variations with varied microwave frequency, but with the Caprice these variations are stronger and occur at narrower frequency ranges than with the JYFL 14 GHz ECRIS. Two possible reasons can be presented for the different behavior. Firstly, the Caprice has somewhat smaller plasma chamber,

which makes it less overmoded. This increases the mode spacing inside the chamber, and can contribute to stronger frequency dependent behavior with plasma loading. Secondly, as already mentioned at the beginning of section 4.1 and presented in Fig. 4.1, the microwave delivery systems of the Caprice and the AECR-U type JYFL 14 GHz ECRIS are significantly different. It is possible that the more complex microwave coupling scheme in the Caprice yields stronger variation of the plasma conditions when the injected microwave frequency is varied. With Caprice the strong effect of the altered microwave frequency makes the frequency fine tuning an effective tool in the optimization of the ion source performance. With AECR-U type ion sources the structural differencies compared to the Caprice seem to damp these effects substantially. As such the effect of frequency tuning is weakened. On the other hand, this can also be seen as an advantage of the AECR-U, as operation at a certain exact frequency is not a critical parameter for the ion source performance.

The space charge experiments indicate that the ion beams produced with the JYFL 14 GHz ECRIS are only partially compensated and the beam properties are strongly influenced by space charge effects. Furthermore, the experiments suggest that significant beam quality improvements can be achieved if the space charge effects are mitigated, leading to improved transmission efficiency. However, the studies performed with gas injection into the beamline and the heated filament demonstrate that increasing the compensation degree during beam transport is not a trivial matter. In the case of gas injection the improved beam quality and transmission efficiency was successfully demonstrated, but the beam losses render this method impractical.

A clear link between space charge and beam structure was observed. Improved compensation yielded decreased beam diameter and improved structure, whereas with degraded compensation the beam size and the degree of hollowness observed with the low and medium charge states increased substantially. This result is in good agreement with the work performed at MSU/NSCL, which connects the hollow beam formation to the space charge effects generated by the solenoid focusing [111, 113, 114].

The space charge plays an important role in the determination of the beam quality only in the beam transport section between the ECR ion source and the $q/m$ separation. Consequently the space charge related beam quality degradation could be mitigated by minimizing the length of the beamline section where the ion beam is subjected to strong space charge. In practice this can be achieved by moving the ion source as close to the analyzing magnet as possible. With this configuration it would also be possible to arrange the ion optics in such a way that solenoid focusing is not required after the ion source, or only weak focusing is used to optimize the beam transport without focal points between the ion source and the analyzing magnet. Optimally the beam manipulation would be performed only using the electrostatic lenses which are part of the beam extraction system. This beam transport scheme would not only mitigate the space charge effects in general, but would also remove the contribution to hollow beam formation caused by the solenoid focusing. This approach has been chosen to be one of the future low energy beam transport upgrades at JYFL.

It was observed that the ECR ion source tuning has significant effect on the temporal stability of the extracted beam current. With varying tune the short term oscillations exhibited by the beam current can alternate substantially in frequency and amplitude. Knowledge of this can be crucial for some applications, because the beam current monitoring systems normally utilized in accelerator laboratories often operate at low sampling rates or use averaging features, and consequently might be unable to detect the presence of fast current fluctuations. Taking into account that the measured oscillation amplitudes varied from 1 % to over 60 % of the average beam current, the properties of the short term fluctuations can have significant impact on sensitive experiments. Also, it was observed that the oscillation characteristics influence the beam transport through the JYFL K-130 cyclotron, indicating that the short term fluctuations can alter accelerator performance.

The dependence of the beam current temporal characteristics on the ECRIS tuning parameters suggests that the current fluctuations originate from the ion source plasma. It is unlikely that the oscillations originate from beamline optics, as the oscillations have been observed with both the old and the new extraction systems of the JYFL 14 GHz ECRIS, which have different ion optical properties. The influence of background and beamline effects are further ruled out by the fact that other ECR ion sources have also been reported to exhibit short term current fluctuations in similar time scales. These include VENUS at LBNL [103], SuSI at MSU/NSCL [142], NIRS-HEC at HIMAC [143] and VEC-ECR at VECC [104].

It was observed that increasing the axial solenoidal magnetic field leads to increased oscillation amplitude, whereas scaling the radial magnetic field with the axial field yields improved beam stability. This has been demonstrated with the JYFL 14 GHz ECRIS and the VENUS at LBNL [103]. The strong dependence on the microwave power, reported in Refs. [103, 104], and the confining magnetic field structure suggest connection to electron heating and plasma confinement processes. However, more experimental work and new diagnostics is required to determine the exact processes in the ECR heated plasma which lead to the observed temporal variations in the extracted beam currents. These could include direct measurement of plasma behavior through light or bremsstrahlung diagnostics in coincidence with the beam current, or determination of the spatial distribution of the beam current oscillation characteristics over the beam profile. These will be the subject of future studies.

The collar structure did not turn out to be a source of remarkable performance improvement in the case of the JYFL 14 GHz ECRIS. However, it did provide important insight into the ion dynamics near the extraction aperture. The results indicate that the region around the collar structure does not contribute significantly to the extracted ions or the overall performance of the ion source. This information provides a basis for future work to find new ways to utilize this space in order to improve the ion source performance, especially in terms of improved beam extraction. These studies will act as a natural continuation of the presented work.

The new extraction system of the JYFL 14 GHz ECRIS has proven to be a success. It offers improved performance in terms of beam current, beam quality and transmission efficiency, and the system has proven to be reliable and flexible to operate. This indicates that the double accelerating einzel lens approach is a viable option to realize a flexible, high performance ECRIS extraction, especially when the ion source extraction voltages are relatively low, which increases the requirements for beam focusing. However, with high extraction voltages the HV insulation of the lenses can become a technical challenge. The new system is the first ECRIS extraction which has been designed with the IBSimu code and subsequently constructed and installed. This provides important benchmarking result for the code, indicating its suitability for ECR ion source development.

Comparison of beams produced with the old and the new extraction systems shows that the new system yields improved beam structure. This indicates that the beam formation also contributes to the formation of the hollow beams. The observed improvement can be linked to the improved matching between the plasma and the electric field in the acceleration gap, providing improved initial beam conditions. Another possible contributor is the improved space charge conditions in the beam extraction due to the removal of the beam deceleration, a feature which was present in the old extraction system. If the beam structure improvement is caused by improved matching between the plasma and the extraction electric field, this effect could have also been a contributor to the beam structure variations seen in the frequency tuning experiments due to varying plasma conditions.

The initial beam conditions play an important role in the beam transport. This was clearly demonstrated as improved transmission with the new extraction system, and it shows that the ion source beam formation can have substantial impact on the performance of the whole accelerator laboratory. The increased beam tuning flexibility achieved with the new extraction system provides good initial beam conditions for all the subsequent beam transport upgrades to improve the performance even further.

# Bibliography


[1] S. Braccini, U. Amaldi, R. Bonomi, M. Crescenti, A. Degiovanni, M. Garlasché, A. Garonna, G. Magrin, C. Mellace, P. Pearce, G. Pittà, P. Puggioni, E. Rosso, S. V. Andrés, R. Wegner, *Accelerators for hadrontherapy: from Lawrence cyclotrons to linacs*, Nucl. Instrum. Meth. A **620** (2010) 563–577.

[2] A. Denker, H. Homeyer, H. Kludge, J. Opitz-Coutureau, *Industrial and medical applications of high-energy ions*, Nucl. Instrum. Meth. B **240** (2005) 61–68.

[3] A. Virtanen, *The use of particle accelerators for space projects*, J. Phys.: Conf. Ser. **41** (2006) 101–114.

[4] A. Virtanen, J. Hyvönen, K. Ranttila, I. Rekikoski, J. Tuppurainen, *Heavy ion and proton test site at JYFL-accelerator laboratory*, Nucl. Instrum. Meth. A **426** (1999) 68–71.

[5] R. Geller, *Electron Cyclotron Resonance Ion Sources and ECR Plasmas*, Taylor & Francis, 1996.

[6] H. Koivisto, *Electron cyclotron resonance ion sources for highly-charged ion beams*, in: Proceedings of the 20$^{\text{th}}$ Internation Conference on Application of Accelerators in Research and Industry, Fort Worth, USA, 2008, pp. 25–30.

[7] H. Koivisto, E. Liukkonen, M. Moisio, V. Nieminen, P. Suominen, *The modifications of the JYFL 6.4 GHz ECR ion source*, Nukleonika **48** (Supp. 2) (2003) S81–S84.

[8] H. Koivisto, P. Heikkinen, V. Hänninen, A. Lassila, H. Leinonen, V. Nieminen, J. Pakarinen, K. Ranttila, J. Ärje, E. Liukkonen, *The first results with the new JYFL 14 GHz ECR ion source*, Nucl. Instrum. Meth. B **174** (2001) 379–384.

[9] E. Liukkonen, *New K130 cyclotron at Jyväskylä*, in: Proceedings of the 13$^{\text{th}}$ International Conference on Cyclotrons and their Applications, Vancouver, Canada, 1992.

[10] V. Toivanen, *Ionisuihkun laadun ja siirtolinjan toiminnan kartoittaminen Jyväskylän yliopiston fysiikan laitoksen kiihdytinlaboratoriossa*, Master's thesis, University of Jyväskylä (2008).

[11] H. Koivisto, P. Suominen, T. Ropponen, J. Ropponen, T. Koponen, M. Savonen, V. Toivanen, X. Wu, G. Machicoane, J. Stetson, P. Zavodszky, M. Doleans, P. Spädtke, R. Vondrasek, O. Tarvainen, *Ion beam development for the needs of the JYFL nuclear physics programme*, Rev. Sci. Instrum. **79** (2008) 02A303.

[12] H. Postma, *Multiply charged heavy ions produced by energetic plasmas*, Phys. Lett. A **31** (1970) 196–197.

[13] S. Bliman, R. Geller, W. Hess, B. Jacquot, C. Jacquot, *A high intensity E.C.R stripped ion source*, IEEE Trans. Nucl. Sci. **NS-19** (1972) 200–203.

[14] P. Apard, S. Bliman, R. Geller, B. Jacquot, C. Jacquot, *Production of multiply charged xenon ions*, Phys. Lett. A **44** (1973) 432–434.

[15] I. G. Brown (Ed.), *The physics and technology of ion sources*, John Wiley & Sons, Inc., 2004.

[16] R. Geller, *Electron cyclotron resonance multiply charged ion sources*, IEEE Trans. Nucl. Sci. **23** (1976) 904–912.

[17] C. M. Lyneis, in: Proceedings of the 6$^{\text{th}}$ International Workshop on ECR Ion Sources, Berkeley, USA, 1985, p. 51.

[18] T. A. Antaya, Z. Q. Xie, *Initial results woth a vertical, full iron yoke, 2 × 6.4 GHz ECR source for the NSCL heavy ion cyclotrons*, in: Proceedings of the 7$^{\text{th}}$ International Workshop on ECR Ion Sources, Jülich, Germany, 1986, p. 72.

[19] B. Jacquot, M. Pontonnier, *La source CAPRICE 10 GHz en mode harmonique* $2(\omega_{HF} - \omega_{ce}) = 0$, Nucl. Instrum. Meth. A **287** (1990) 341–347.

[20] C. M. Lyneis, Z. Xie, D. J. Clark, R. S. Lam, S. A. Lundgren, *Preliminary performance of the LBL AECR*, in: Proceedings of the 10$^{\text{th}}$ International Workshop on ECR Ion Sources, Knoxville, USA, 1990, pp. 47–62.

[21] D. Leitner, C. M. Lyneis, S. R. Abbott, D. Collins, R. D. Dwinell, M. L. Galloway, M. Leitner, D. S. Todd, *Next generation ECR ion sources: first results of the superconducting 28 GHz ECRIS – VENUS*, Nucl. Instrum. Meth. B **235** (2005) 486–493.

[22] H. W. Zhao, L. T. Sun, X. Z. Zhang, X. H. Guo, Y. Cao, W. Lu, Z. M. Zhang, P. Yuan, M. T. Song, H. Y. Zhao, T. Jin, Y. Shang, W. L. Zhan, B. W. Wei, D. Z. Xie, *Intense beam production of highly charged heavy ions by the superconducting electron cyclotron resonance ion source SECRAL*, Rev. Sci. Instrum. **79** (2008) 02A315.

[23] T. Nakagawa, Y. Higurashi, J. Ohnishi, T. Aihara, M. Tamura, A. Uchiyama, H. Okuno, K. Kusaka, M. Kidero, E. Ikezawa, M. Fujimaki, Y. Sato, Y. Watanabe, M. Komiyama, M. Kase, A. Goto, O. Kamigaito, Y. Yano, *First results from the new RIKEN superconducting electron cyclotron resonance ion source*, Rev. Sci. Instrum. **81** (2010) 02A320.

[24] C. M. Lyneis, D. Leitner, D. S. Todd, G. Sabbi, S. Prestemon, S. Caspi, P. Ferracin, *Fourt generation electron cyclotron resonance ion sources*, Rev. Sci. Instrum. **79** (2008) 02A321.

[25] C. Lyneis, P. Ferracin, S. Caspi, A. Hodgkinson, G. L. Sabbi, *Concept for a fourt generation electron cyclotron resonance ion source*, Rev. Sci. Instrum. **83** (2012) 02A301.

[26] T. Nakagawa, *ECR ion sources: a brief history and look into the next generation*, in: Proceedings of the 23$^{\text{rd}}$ Particle Accelerator Conference, Vancouver, Canada, 2009.

[27] F. Consoli, L. Celona, G. Ciavola, S. Gammino, F. Maimone, S. Barbarino,

R. S. Catalano, D. Mascali, *Microwave field distribution and electron cyclotron resonance heating process*, Rev. Sci. Instrum. **79** (2008) 02A308.

[28] *CST Microwave Studio*, http://www.cst.com/Content/Products/MWS/Overview.aspx (2013).

[29] L. Celona, G. Ciavola, F. Consoli, S. Gammino, F. Maimone, D. Mascali, P. Spädtke, K. Tinschert, R. Lang, J. Mäder, J. Roßbach, S. Barbarino, R. S. Catalano, *Observations of the frequency tuning effect in the 14 GHz CAPRICE ion source*, Rev. Sci. Instrum. **79** (2008) 023305.

[30] G. Melin, A. G. Drentje, A. Girard, D. Hitz, *Ion behavior and gas mixing in electron cyclotron resonance plasmas as sources of highly charged ions*, J. Appl. Phys. **86** (1999) 4772–4779.

[31] D. H. Crandall, *Electron impact ionization of multicharged ions*, Phys. Scripta **23** (1981) 153–162.

[32] W. Lotz, *An empirical formula for the electron-impact ionization cross-section*, Z. Physik **206** (1967) 205–211.

[33] W. Lotz, *Electron-impact ionization cross-sections and ionization rate coefficients for atoms and ions from hydrogen to calcium*, Z. Physik **216** (1968) 241–247.

[34] W. Lotz, *Electron-impact ionization cross-sections and ionization rate coefficients for atoms and ions from scandium to zinc*, Z. Physik **220** (1969) 466–472.

[35] W. Lotz, *Electron-impact ionization cross-sections for atoms up to* $Z = 108$, Z. Physik **232** (1970) 101–107.

[36] T. Ropponen, O. Tarvainen, P. Jones, P. Peura, T. Kalvas, P. Suominen, H. Koivisto, J. Ärje, *The effect of magnetic field strength on the time evolution of high energy bremsstrahlung radiation created by an electron cyclotron resonance ion source*, Nucl. Instrum. Meth. A **600** (2009) 525–533.

[37] T. Ropponen, O. Tarvainen, I. Izotov, J. Noland, V. Toivanen, G. Machicoane, D. Leitner, H. Koivisto, T. Kalvas, P. Peura, P. Jones, V. Skalyga, V. Zorin, *Studies of plasma breakdown and electron heating on a 14 GHz ECR ion source through measurement of plasma bremsstrahlung*, Plasma Sources Sci. Technol. **20** (2011) 055007 (14 pp).

[38] H. Tawara, T. Kato, Atomic Data and Nuclear Data Tables, Vol. 36, No. 2 (1987).

[39] A. Müller, E. Salzborn, *Scaling of cross sections for multiple electron transfer to highly charged ions colliding with atoms and molecules*, Phys. Lett. A **62** (1977) 391–394.

[40] E. Salzborn, A. Müller, *Electron capture by multi-charged ions colliding with multi-electron targets*, in: Proceedings of the $11^{\text{th}}$ International Conference on the Physics of Electronic and Atomic Collisions, Kyoto, Japan, 1979, pp. 407–426.

[41] H. Tamagawa, I. Alexeff, C. M. Jones, P. D. Miller, *Use of the hot-electron mirror machine INTEREM as a high-Z ion source*, IEEE Trans. Nucl. Sci. **NS-23** (1976) 994–998.

[42] Y. Jongen, C. M. Lyneis, *Experimental results from an ECR source using an octupole*, Nucl. Instrum. Meth B **9** (1985) 529–531.

[43] K. Halbach, *Design of permanent multipole magnets with oriented rare earth cobalt material*, Nucl. Instrum. Methods **169** (1980) 1–10.

[44] P. Suominen, O. Tarvainen, H. Koivisto, *First results with a modified multipole structure electron cyclotron resonance ion source*, Rev. Sci. Instrum. **77** (2006) 03A332.

[45] P. Suominen, T. Ropponen, H. Koivisto, *Modified multipole structure for electron cyclotron resonance ion sources*, High Energ. Phys. Nucl. **31** (Supp. 1) (2007) 142–146.

[46] R. J. Goldston, P. H. Rutherford (Eds.), *Introduction to plasma physics*, Institute of Physics Publishing, 1995.

[47] A. Girard, D. Hitz, G. Melin, K. Serebrennikov, *Electron cyclotron resonance plasmas and electron cyclotron resonance ion sources: physics and technology*, Rev. Sci. Instrum. **75** (2004) 1381–1388.

[48] L. Panitzsch, T. Peleikis, S. Böttcher, M. Stalder, R. F. Wimmer-Schweingruber, *Current density distributions and sputter marks in electron cyclotron resonance ion sources*, Rev. Sci. Instrum. **84** (2013) 013303.

[49] V. Mironov, J. P. M. Beijers, *Three-dimensional simulations of ion dynamics in the plasma of an electron cyclotron resonance ion source*, Phys. Rev. ST Accel. Beams **12** (2009) 073501.

[50] A. G. Drentje, *Techniques and mechanisms applied in electron cyclotron resonance sources for highly charged ions*, Rev. Sci. Instrum. **74** (2003) 2631–2645.

[51] Z. Q. Xie, C. M. Lyneis, *Plasma potentials and performance of the advanced electron cyclotron resonance ion source*, Rev. Sci. Instrum. **65** (1994) 2947–2952.

[52] O. Tarvainen, P. Suominen, H. Koivisto, *A new plasma potential measurement instrument for plasma ion sources*, Rev. Sci. Instrum. **75** (2004) 3138–3145.

[53] O. Tarvainen, P. Suominen, T. Ropponen, T. Kalvas, P. Heikkinen, H. Koivisto, *Effect of the gas mixing technique on the plasma potential and emittance of the JYFL 14 GHz electron cyclotron resonance ion source*, Rev. Sci. Instrum. **76** (2005) 093304.

[54] O. Tarvainen, P. Suominen, T. Ropponen, H. Koivisto, *Emittance and plasma potential measurements in double-frequency heating mode with the 14 GHz electron cyclotron resonance ion source at the university of Jyväskylä*, Rev. Sci. Instrum. **77** (2006) 03A309.

[55] G. Melin, F. Bourg, P. Briand, J. Debernadi, M. Delaunay, R. Geller, B. Jacquot, P. Ludwig, T. K. N'Guyen, L. Pin, M. Pontonnier, J. C. Rocco, F. Zadworny, *Some particular aspects of the physics of the ECR sources for multicharged ions*, Rev. Sci. Instrum. **61** (1990) 236–238.

[56] G. D. Shirkov, *A classical model of ion confinement and losses in ECR ion sources*, Plasma Sources Sci. Technol. **2** (1993) 250–257.

[57] D. J. Clark, C. M. Lyneis, *The production of beams from solid materials at LBL ECR source*, J. Phys. (Paris) Colloq. **50** (1989) C1–759.

[58] R. Harkewicz, *Efficient production of a $^{48}Ca$ beam from oxide material in an*

*electron cyclotron resonance ion source using a low power miniature oven*, Rev. Sci. Instrum. **67** (1996) 2176–2178.

[59] H. Koivisto, P. Frondelius, T. Koponen, P. Lappalainen, T. Ropponen, M. Savonen, P. Suominen, O. Tarvainen, K. Tinschert, G. Ciavola, *Development work at JYFL: plasma potential measurements, electron heating simulations, JYFL-MMPS, high temperature ovens*, High Energ. Phys. Nucl. **31** (Supp. 1) (2007) 41–45.

[60] R. Harkewicz, P. J. Billquist, J. P. Greene, J. J. A. Nolen, R. C. Pardo, *Ion plasma sputtering as a method of introducing solid material into an electron cyclotron resonance ion source*, Rev. Sci. Instrum. **66** (1995) 2883–2887.

[61] R. Geller, P. Ludwig, G. Melin, *Metal ion production in ECRIS*, Rev. Sci. Instrum. **63** (1992) 2795–2800.

[62] T. Nakagawa, T. Kageyama, E. Ikezawa, M. Hemmi, Y. Miyazawa, *Recent developments of RIKEN ECR ion source*, in: Proceedings of the 10$^{\text{th}}$ International Workshop on ECR ion sources, Oak Ridge, USA, 1990, pp. 163–172.

[63] R. Harkewicz, J. Stacy, J. Greene, R. C. Pardo, *Solid material evaporation into an electron cyclotron resonance source by laser ablation*, Rev. Sci. Instrum. **65** (1994) 1104–1106.

[64] H. Koivisto, J. Ärje, M. Nurmia, *Metal ion beams from an ECR ion source using volatile compounds*, Nucl. Instrum. Meth. B **94** (1994) 291–296.

[65] R. Geller, *ECRIS: The Electron Cyclotron Resonance Ion Sources*, Annu. Rev. Nucl. Part. Sci. **40** (1990) 15–43.

[66] R. Geller, *Concluding remarks*, in: Proceedings of the 10$^{\text{th}}$ International Workshop on ECR ion sources, Oak Ridge, USA, 1990, pp. 381–390.

[67] G. Ciavola, S. Gammino, *A superconducting electron cyclotron resonance source for the L.N.S.*, Rev. Sci. Instrum. **63** (1992) 2881–2882.

[68] T. A. Antaya, S. Gammino, *The superconducting electron cyclotron resonance 6.4 GHz high-B mode and frequency scaling in electron cyclotron resonance ion sources*, Rev. Sci. Instrum. **65** (1994) 1723–1727.

[69] S. Gammino, G. Ciavola, T. Antaya, K. Harrison, *Volume scaling and magnetic field scaling on SC-ECRIS at MSU-NSCL*, Rev. Sci. Instrum. **67** (1996) 155–160.

[70] S. Gammino, G. Ciavola, R. Harkewicz, K. Harrison, A. Srivastava, P. Briand, *Effects of frequency and magnetic field scaling on the superconducting electron cyclotron resonance ion source at MSU-NSCL*, Rev. Sci. Instrum. **67** (1996) 4109–4113.

[71] S. Gammino, G. Ciavola, L. Celona, D. Hitz, A. Girard, G. Melin, *Operation of SERSE superconducting electron cyclotron resonance ion source at 28 GHz*, Rev. Sci. Instrum. **72** (2001) 4090–4097.

[72] D. Hitz, A. Girard, G. Melin, S. Gammino, G. Ciavola, L. Celona, *Results and interpretation of high frequency experiments at 28 GHz in ECR ion sources, future prospects*, Rev. Sci. Instrum. **73** (2002) 509–512.

[73] H. Arai, M. Imanaka, S. Lee, Y. Higurashi, T. Nakagawa, M. Kidera, T. Kageyama, M. Kase, Y. Yano, T. Aihara, *Effect of minimum strength of*

*mirror magnetic field ($B_{min}$) on production of highly charged heavy ions from RIKEN lquid-He-free super conducting electron-cyclotron resonance ion source (RAMSES)*, Nucl. Instrum. Meth. A **491** (2002) 9–14.

[74] D. Hitz, A. Girard, K. Serebrennikov, G. Melin, D. Cormier, J. M. Mathonnet, J. Chartier, L. Sun, J. P. Briand, M. Benhachoum, *Production of highly charged ion beams with the Grenoble test electron cyclotron resonance ion source*, Rev. Sci. Instrum. **75** (2004) 1403–1406.

[75] D. Leitner, C. M. Lyneis, T. Loew, D. S. Todd, S. Virostek, O. Tarvainen, *Status report of the 28 GHz superconducting electron cyclotron resonance ion source VENUS*, Rev. Sci. Instrum. **77** (2006) 03A302.

[76] A. G. Drentje, A. Girard, D. Hitz, G. Melin, *Role of low charge state ions in electron cyclotron resonance ion source plasma*, Rev. Sci. Instrum. **71** (2000) 623–626.

[77] G. Melin, C. Barué, F. Bourg, P. Briand, J. Debernardi, M. Delaunay, R. Geller, A. Girard, K. S. Golovanivsky, D. Hitz, B. Jacquot, J. M. Mathonnet, T. K. Nguyen, L. Pin, M. Pontonnier, J. C. Rocco, F. Zadworny, *Recent developments and future projects on ECR ion sources at Grenoble*, in: Proceedings of the 10$^{\text{th}}$ International Workshop on ECR Ion Sources, Knoxville, USA, 1990, pp. 1–15.

[78] S. Gammino, J. Sijbring, A. G. Drentje, *Experiment with a biased disk at the K.V.I. ECRIS*, Rev. Sci. Instrum. **63** (1992) 2872–2874.

[79] S. Runkel, O. Hohn, K. E. Stiebing, A. Schempp, H. Schmidt-Böcking, V. Mironov, G. Shirkov, *Time resolved experiments at the Frankfurt 14 GHz electron cyclotron resonance ion source*, Rev. Sci. Instrum. **71** (2000) 912–914.

[80] Z. Q. Xie, C. M. Lyneis, *Improvements on the LBL AECR source*, in: Proceedings of the 12$^{\text{th}}$ International Workshop on ECR Ion Sources, Riken, Japan, 1995, pp. 24–28.

[81] G. D. Alton, F. W. Meyer, Y. Liu, J. R. Beene, D. Tucker, *Enhancing the performances of traditional electron cyclotron resonance ion sources with multiple-discrete-frequency microwave radiation*, Rev. Sci. Instrum. **69** (1998) 2305–2312.

[82] R. C. Vondrasek, R. H. Scott, R. C. Pardo, *Two frequency operation of the Argonne ECR ion source*, in: Proceedings of the 15$^{\text{th}}$ International Workshop on ECR Ion Sources, Jyväskylä, Finland, 2002, pp. 63–66.

[83] R. C. Vondrasek, R. Scott, R. C. Pardo, *ECRIS operation with multiple frequencies*, Rev. Sci. Instrum. **77** (2006) 03A337.

[84] Z. Xie, C. M. Lyneis, R. S. Lam, S. A. Lundgren, *Enhanced ECR ion source performance with an electron gun*, Rev. Sci. Instrum. **62** (1991) 775–778.

[85] T. Nakagawa, *Effect of coating on the plasma chamber wall in RIKEN electron cyclotron resonance ion source*, Jpn. J. Appl. Phys. **30** (1991) L930–L932.

[86] T. Nakagawa, Y. Yano, *Recent performance of Japanese electron cyclotron resonance ion sources*, Rev. Sci. Instrum. **71** (2000) 637–642.

[87] L. Schächter, K. E. Stiebing, S. Dobrescu, A. I. Badescu-Singureanu, L. Schmidt, O. Hohn, S. Runkel, *Effect of a metal–dielectric structure introduced in the*

*plasma chamber of the Frankfurt 14 GHz electron cyclotron resonance ion source*, Rev. Sci. Instrum. **70** (1999) 1367–1369.

[88] L. Schächter, S. Dobrescu, K. E. Stiebing, *Role of a metal–dielectric structure for the high-charge-state-ion production in electron cyclotron resonance ion sources*, Rev. Sci. Instrum. **73** (2002) 4172–4175.

[89] L. Schächter, S. Dobrescu, G. Rodrigues, A. G. Drentje, *Enhanced highly charged ion production using a metal-dielectric liner in the KVI 14 GHz ECR ion source*, Rev. Sci. Instrum. **73** (2002) 570–572.

[90] D. Hitz, F. Bourg, P. Ludwig, G. Melin, M. Pontonnier, T. K. Nguyen, *The new 1.2 T CAPRICE source: presentation and results*, in: Proceedings of the 12$^{\text{th}}$ International Workshop on ECR ion sources, Riken, Japan, 1995, pp. 126–130.

[91] T. Kalvas, O. Tarvainen, T. Ropponen, O. Steczkiewicz, J. Ärje, H. Clark, *IBSIMU: a three-dimensional simulation software for charged particle optics*, Rev. Sci. Instrum. **81** (1994) 02B703.

[92] J. H. Whealton, E. F. Jaeger, J. C. Whitson, *Optics of ion beams of arbitrary perveance extracted from a plasma*, J. Comput. Phys. **27** (1978) 32–41.

[93] C. D. Child, *Discharge from hot CaO*, Phys. Rev. **32** (1911) 492–511.

[94] I. Langmuir, *The effect of space charge and residual gases on thermionic currents in high vacuum*, Phys. Rev. **2** (1913) 450–486.

[95] J. S. Humphries, *Charged Particle Beams*, John Wiley & Sons, Inc., 1990.

[96] R. Becker, W. B. Herrmannsfeldt, *Why $\pi$ and mrad?*, Rev. Sci. Instrum. **77** (2006) 03B907.

[97] T. Kalvas, presentation at the CERN Accelerator School on Ion Sources, June 7, 2012, Senec, Slovakia and private communication (2012).

[98] I. G. Brown (Ed.), *The physics and technology of ion sources*, John Wiley & Sons, Inc., 1989.

[99] V. Toivanen, T. Kalvas, H. Koivisto, J. Komppula, O. Tarvainen, *Double einzel lens extraction for the JYFL 14 GHz ECR ion source designed with IBSimu*, J. Instrum. **8** (2013) P05003.

[100] D. Wutte, M. A. Leitner, C. M. Lyneis, *Emittance measurements for high charge state ion beams extracted from the AECR-U ion source*, Phys. Scripta **T92** (2001) 247–249.

[101] X. Wu, M. Doleans, W. Hartung, M. Johnson, E. Pozdeyev, E. Tanke, F. Marti, R. C. York, Q. Zhao, *The overview of the accelerator system for the facility for rare isotope beams at Michigan State University*, in: Proceedings of the 25$^{\text{th}}$ Linear Accelerator Conference, Tsukuba, Japan, 2010.

[102] S. Gales, *SPIRAL2 at GANIL: Next generation of ISOL facility for intense secondary radioactive ion beams*, Nucl. Phys. A **834** (1992) 717–723.

[103] O. Tarvainen, V. Toivanen, H. Koivisto, J. Komppula, T. Kalvas, C. M. Lyneis, M. Strohmeier, *An experimental study of ECRIS plasma stability and oscillation of beam current*, in: Proceedings of the 20$^{\text{th}}$ International Workshop on Electron Cyclotron Resonance Ion Sources, Sydney, Australia, 2012.

[104] G. S. Taki, P. R. Sarma, D. K. Chakraborty, A. G. Drentje, T. Nakagawa, P. K. Ray, R. K. Bhandari, *Study of the dependence of ECR ion current on periodic plasma disturbance*, in: Proceedings of the 18th International Workshop on Electron Cyclotron Resonance Ion Sources, Chicago, USA, 2008.

[105] M. G. Mazarakis, R. J. Burke, E. P. Colton, S. Fenster, J. S. Moenich, D. K. Nikfarjam, D. W. Price, N. Q. Sesol, J. M. Watson, *Transport experiments with neutralized and space charge dominated deneutralized 2 mA 80 keV $Xe^{+1}$ beams*, IEEE Trans. Nucl. Sci. **NS-26** (1979) 3042–3044.

[106] P. Spädtke, *Beam formation*, in: Proceedings of the CERN Accelerator School, Small Accelerators, CERN-2006-012, Zeegse, The Netherlands, 2005, pp. 71–93.

[107] K. Schindl, *Space charge*, in: Proceedings of the CERN Accelerator School, Intermediate Accelerator Physics, CERN-2006-002, Zeuthen, Germany, 2003, pp. 305–320.

[108] R. Gobin, P.-Y. Beauvais, R. Ferdinand, P.-A. Leroy, L. Celona, G. Ciavola, S. Gammino, *Improvement of beam emittance of the CEA high intensity proton source SILHI*, Rev. Sci. Instrum. **70** (1999) 2652–2654.

[109] P.-Y. Beauvais, R. Ferdinand, R. Gobin, J. M. Lagniel, P.-A. Leroy, L. Celona, G. Ciavola, S. Gammino, B. Pottin, J. Sherman, *Emittance improvement of the electron cyclotron resonance high intensity light ion source proton beam by gas injection in the low energy beam transport*, Rev. Sci. Instrum. **71** (2000) 1413–1416.

[110] A. J. T. Holmes, *Theoretical and experimental study of space charge in intense ion beams*, Phys. Rev. A **19** (1979) 389–407.

[111] M. Doleans, S. Chouhan, D. Cole, G. Machicoane, F. Marti, P. Miller, J. Moskalik, M. Steiner, J. Stetson, X. Wu, P. Zavodszky, A. Zeller, Q. Zhao, *Optics improvements of the K500 axial injection line*, in: Proceedings of the 18th International Conference on Cyclotrons and their Applications, Giardini Naxos, Italy, 2007, pp. 319–324.

[112] N. Y. Kazarinov, *Nonlinear distortion of multicomponent heavy ion beam emittance caused by space charge fields*, Rev. Sci. Instrum. **75** (2004) 1665–1666.

[113] G. Machicoane, M. Doleans, J. Stetson, X. Wu, P. A. Zavodszky, *Experimental evidences for emittance degradation by space charge effect when using a focusing solenoid below an electron cyclotron resonance ion source*, Rev. Sci. Instrum. **79** (2008) 02B714.

[114] J. W. Stetson, G. Machicoane, F. Marti, P. Miller, M. Steiner, P. Zavodszky, N. Y. Kazarinov, *A comparison of electrostatic and magnetic focusing of mixed species heavy ion beams at NSCL/MSU*, in: Proceedings of the 21st Particle Accelerator Conference, Knoxville, USA, 2005, pp. 2281–2283.

[115] P. Spädtke, K. Tinschert, R. Lang, J. Mäder, J. Roßbach, J. W. Stetson, L. Celona, *Prospects of ion beam extraction and transport simulations*, Rev. Sci. Instrum. **79** (2008) 02B716.

[116] P. Spädtke, *Model for the description of ion beam extraction from electron cyclotron resonance ion sources*, Rev. Sci. Instrum. **81** (2010) 02B725.

[117] D. S. Todd, D. Leitner, C. M. Lyneis, D. P. Grote, *Simulation and beamline experiments for the superconducting electron cyclotron resonance ion source VENUS*, Rev. Sci. Instrum. **79** (2008) 02A316.

[118] D. Mascali, S. Gammino, L. Celona, G. Ciavola, *Towards a better comprehension of plasma formation and heating in high performance electron cyclotron resonance ion sources*, Rev. Sci. Instrum. **83** (2012) 02A336.

[119] Z. Q. Xie, C. M. Lyneis, *Performance of the upgraded LBNL AECR ion source*, in: Proceedings of the 13$^{\text{th}}$ International Workshop on ECR Ion Sources, Texas, USA, 1997, pp. 16–21.

[120] Z. Q. Xie, *Production of highly charged ion beams from electron cyclotron resonance ion sources*, Rev. Sci. Instrum. **69** (1998) 625–630.

[121] H. Koivisto, D. Cole, A. Fredell, C. Lyneis, P. Miller, J. Moskalik, B. Nurnberger, J. Ottarson, A. Zeller, J. DeKamp, R. Vondrasek, P. A. Zavodszky, Z. Q. Xie, *ARTEMIS – The new ECR ion source for the coupled cyclotron facility at NSCL/MSU*, in: Proceedings of the Workshop on the Production of Intense Beams of Highly Charged Ions, Catania, Italy, 2000, pp. 135–139.

[122] M. Schlapp, R. C. Pardo, R. C. Vondrasek, J. Szczech, P. J. Billquist, J. Vieregg, Z. Q. Xie, C. M. Lyneis, R. Harkewicz, *A new 14 GHz electron-cyclotron-resonance ion source for the heavy ion accelerator facility ATLAS*, Rev. Sci. Instrum. **69** (1998) 631–633.

[123] H. R. Kremers, J. P. M. Beijers, S. Brandenburg, *Characteristics of the KVI electron cyclotron resonance ion source*, Rev. Sci. Instrum. **77** (2006) 03A3111.

[124] P. W. Allison, J. D. Sherman, D. B. Holtkamp, *An emittance scanner for intense low-energy ion beams*, IEEE T. Nucl. Sci. **NS-30** (1983) 2204–2206.

[125] J. G. Wang, D. X. Wang, M. Reiser, *Beam emittance measurement by the pepper-pot method*, Nucl. Instrum. Meth. A **307** (1991) 190–194.

[126] V. Toivanen, O. Tarvainen, J. Komppula, H. Koivisto, *Oscillations of ECR ion source beam current along the beam transport of the JYFL K-130 cyclotron*, J. Instrum. **8** (2013) T02005.

[127] D. C. Swanson, *Signal processing for intelligent sensor systems*, Marcel Dekker, 2000.

[128] *Beam-N-SPECTR, a program designed for studies of signal spectral properties*, https://www.jyu.fi/fysiikka/en/research/accelerator/ionsources/projects/beam-n-spectr (2013).

[129] V. Toivanen, H. Koivisto, O. Steczkiewicz, L. Celona, O. Tarvainen, T. Ropponen, S. Gammino, D. Mascali, G. Ciavola, *Effect of electron cyclotron resonance ion source frequency tuning on ion beam intensity and quality at Department of Physics, University of Jyväskylä*, Rev. Sci. Instrum. **81** (2010) 02A319.

[130] V. Toivanen, H. Koivisto, O. Steczkiewicz, L. Celona, O. Tarvainen, T. Ropponen, S. Gammino, D. Mascali, G. Ciavola, *Erratum: Effect of electron cyclotron resonance ion source frequency tuning on ion beam intensity and quality at Department of Physics, University of Jyväskylä*, Rev. Sci. Instrum. **82** (2011) 029901.

[131] V. Toivanen, O. Tarvainen, C. Lyneis, J. Kauppinen, J. Komppula, H. Koivisto, *Electron cyclotron resonance ion source plasma chamber studies using a network analyzer as a loaded cavity probe*, Rev. Sci. Instrum. **83** (2012) 02A306.

[132] V. Toivanen, O. Steczkiewicz, O. Tarvainen, T. Ropponen, J. Ärje, H. Koivisto, *The effects of beam line pressure on the beam quality of an electron cyclotron resonance ion source*, Nucl. Instrum. Meth. B **268** (2010) 1508–1516.

[133] V. Toivanen, O. Tarvainen, J. Komppula, H. Koivisto, *The effect of plasma electrode collar structure on the performance of the JYFL 14 GHz electron cyclotron resonance ion source*, accepted for publication in Nucl. Instrum. Meth. A.

[134] V. Toivanen, V. Aho, P. Jones, J. Kauppinen, H. Koivisto, P. Peura, T. Ropponen, O. Tarvainen, J. Ärje, L. Celona, G. Ciavola, S. Gammino, D. Mascali, A. Galatà, *Effects of microwave frequency fine tuning on the performance of JYFL 14 GHz ECRIS*, in: Proceedings of the 19$^{\text{th}}$ International Workshop on Electron Cyclotron Resonance Ion Sources, Grenoble, France, 2010.

[135] C. Lyneis, J. Benitez, D. Leitner, J. Noland, M. Strohmeier, H. Koivisto, O. Tarvainen, *Characterization of the microwave coupling to the plasma chamber of the LBL ECR ion source*, in: Proceedings of the 19$^{\text{th}}$ International Workshop on Electron Cyclotron Resonance Ion Sources, Grenoble, France, 2010.

[136] H. Knudsen, H. K. Haugen, P. Hvelplund, *Single-electron-capture cross section for medium- and high-velocity, highly charged ions colliding with atoms*, Phys. Rev. A **23** (1981) 597–610.

[137] I. D. Kaganovich, E. Startsev, R. C. Davidson, *Scaling and formulary of cross-sections for ion-atom impact ionization*, New J. Phys. **8** (2006) 278.

[138] V. Mironov, presentation at the 37th European Cyclotron Progress Meeting, October 28 – 31, 2009, Groningen, The Netherlands and private communication (2009).

[139] T. Kalvas, O. Tarvainen, H. Clark, J. Brinkley, J. Ärje, *Application of 3D code IBSimu for designing an $H^-$ / $D^-$ extraction system for the Texas A&M facility upgrade*, in: Proceedings of the 2$^{\text{nd}}$ International Symposium on Negative Ions, Beams and Sources, Takayama, Japan, 2010.

[140] T. Kalvas, R. F. Welton, O. Tarvainen, B. X. Han, M. P. Stockli, *Simulation of $H^-$ ion source extraction systems for the Spallation Neutron Source with Ion Beam Simulator*, Rev. Sci. Instrum. **83** (2012) 02A705.

[141] T. Kalvas, S. K. Hahto, F. Gicquel, M. King, J. H. Vainionpää, J. Reijonen, K. N. Leung, T. G. Miller, *Fast slit-beam extraction and chopping for neutron generator*, Rev. Sci. Instrum. **77** (2006) 03B904.

[142] G. Machicoane, private communication (2012).

[143] A. Kitagawa, *Two-frequency heating technique for stable ECR plasma*, in: Proceedings of the 20$^{\text{th}}$ International Workshop on Electron Cyclotron Resonance Ion Sources, Sydney, Australia, 2012.

# Appendix A

# Publications

# APPENDIX A.I

# Effect of electron cyclotron resonance ion source frequency tuning on ion beam intensity and quality at Department of Physics, University of Jyväskylä[a)]

V. Toivanen,[1] H. Koivisto,[1,b)] O. Steczkiewicz,[1] L. Celona,[2] O. Tarvainen,[1] T. Ropponen,[1] S. Gammino,[2] D. Mascali,[2] and G. Ciavola[2]
[1]*Department of Physics, University of Jyväskylä (JYFL), Finland*
[2]*Instituto Nazionale di Fisica Nucleare, Laboratori Nazionali del Sud, 95123 Catania, Italy*

(Presented 21 September 2009; received 14 September 2009; accepted 25 October 2009; published online 12 February 2010)

Ion beam intensity and quality have a crucial effect on the operation efficiency of the accelerator facilities. This paper presents the investigations on the ion beam intensity and quality after the mass separation performed with the Department of Physics, University of Jyväskylä 14 GHz electron cyclotron resonance ion source by sweeping the microwave in the 14.05–14.13 GHz range. In many cases a clear variation in the ion beam intensity and quality as a function of the frequency was observed. The effect of frequency tuning increased with the charge state. In addition, clear changes in the beam structure seen with the beam viewer were observed. The results confirmed that frequency tuning can have a remarkable effect on ion beam intensity and quality especially in the case of highly charged ion beams. The examples presented here represent the typical charge state behavior observed during the measurements. © *2010 American Institute of Physics.*
[doi:10.1063/1.3267287]

## I. INTRODUCTION

The work to improve the ion beam quality has an increasing role in the field of electron cyclotron resonance (ECR) ion sources. The parameters affecting the ion beam quality have been studied with the aid of simulations and experiments. For example, at National Superconducting Cyclotron Laboratory/Michigan State University (NSCL/MSU) a comprehensive set of measurements to find the effect of different beam optical components on the beam transport efficiency has been carried out.[1] According to the experiments the solenoidal focusing before the q/M separation can result in strong degradation of the beam quality and can create a hollow beam structure due to different focal points of different charge states. The hollow beam structure, observed by several ion source groups, could possibly be avoided, at least partially, by increasing the space charge compensation and by using electrostatic focusing. Intensive research work to understand the parameters affecting the beam quality has also been done at Department of Physics, University of Jyväskylä (JYFL).[2] This work has now been extended to cover also the so-called frequency tuning effect.

Frequency tuning has been studied by the Instituto Nazionale di Fisica Nucleare-Laboratori Nazionali del Sud (INFN-LNS) ion source team in order to see the effect of different electromagnetic wave modes excited in the plasma chamber on the beam intensity and the beam profile (see Refs. 3–5). According to the experiments, strong variations in the beam intensity and profile were observed. For example, the ion beam distribution changed from uniform to hollow when the frequency for the plasma heating was changed. These measurements were performed in the extraction area of the electron cyclotron resonance ion source (ECRIS) before any solenoid focusing. The main motivation for the experiments at JYFL was to measure the effect of frequency tuning on the beam emittance of mass separated beams and to get more information about the formation of the hollow beam structure.

## II. FREQUENCY TUNING

In the frequency tuning the microwave frequency is varied in order to select the efficient heating mode inside the plasma chamber of ECRIS. In the experiments the input frequency for the klystron was swept from 14.05 to 14.13 GHz in 100 s with Rohde & Schwartz signal generator. This bandwidth was found adequate to maintain the constant output power over the whole frequency sweep using the automatic level control feature of the klystron.

### A. Effect on ion beam intensity

The measurements were started using $Ar^{8+}$ and $Ar^{9+}$ ion beams, because they have been used as a benchmark beams for the transmission experiments at JYFL. Figure 1 shows a typical intensity behavior of $Ar^{9+}$ ion beam and the drain current as a function of microwave frequency while other tuning parameters of the ECRIS were kept constant. Clear intensity variation in $Ar^{9+}$ ion beam was observed. In the end of the frequency scan very unstable intensity behavior was observed and can be associated to unfavorable mode struc-

[a)]Contributed paper, published as part of the Proceedings of the 13th International Conference on Ion Sources, Gatlinburg, Tennessee, September 2009.
[b)]Electronic mail: hannu.koivisto@phys.jyu.fi.

 

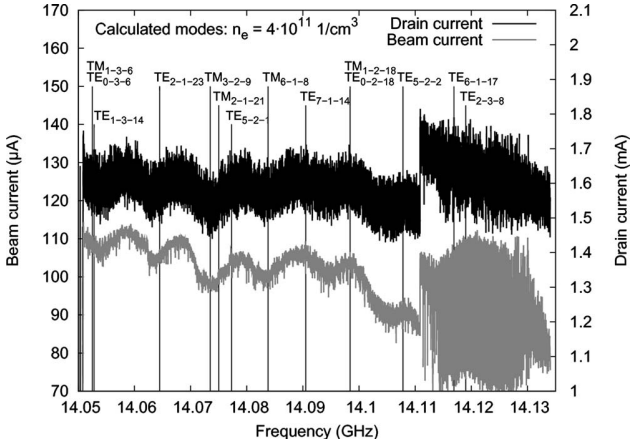


FIG. 1. The intensity of $Ar^{9+}$ and drain current as a function of the microwave frequency. Figure also shows the calculated TE and TM modes in the plasma chamber (OD=76 mm, length 280 mm). Uniformly distributed electron density of $4 \times 10^{11}$ cm$^{-3}$ was used in calculations. The ripple seen in the drain current is attributed to inadequate noise shielding and filtering. RF-power=430 W, pressure=$3.8 \times 10^{-7}$ mbar, and BD=−180 V.

ture. Similar behavior was seen frequently and was more pronounced for higher charge states. The measurement with lower charge states show that the intensity variations in ion beam is very small or does not exist at all. This behavior seems to be independent of the RF-power level (see Fig. 2 for $Ar^{6+}$). This indicates that the production of low charge states is not very sensitive to the changes in the plasma conditions. According to the measurements the effect of frequency tuning seems to get highlighted with increasing charge state. This is demonstrated in Fig. 3, which shows the intensity variation in $Ar^{12+}$. Figures 2 and 3 also show the behavior of forward and reflected microwave power read from the klystron. Similar behavior in reflected power and intensity was seen also in the measurement corresponding to Fig. 1. However, for the clarity the reflected power was not included (variations 3–25 W). It was noted that in the case of high charge states the reflected power had a local minima at the frequencies corresponding to local maxima in the ion beam current. In all three measurements (Figs. 1–3) same

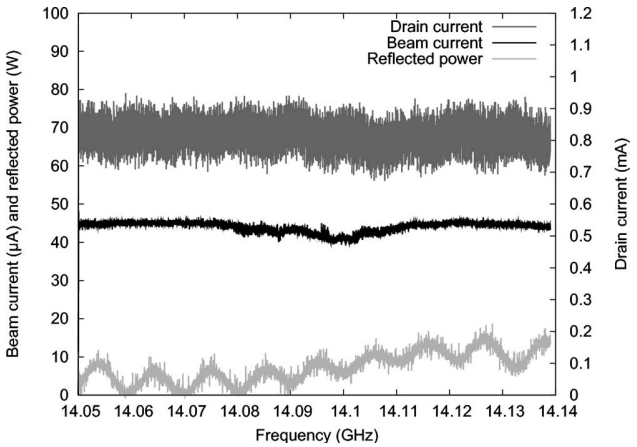


FIG. 2. The intensity of $Ar^{6+}$ ion beam, corresponding drain current and reflected microwave power as a function of microwave frequency. The used RF-power of 110 W gave the highest intensity. Pressure=$2.8 \times 10^{-7}$ mbar, BD=−80 V.

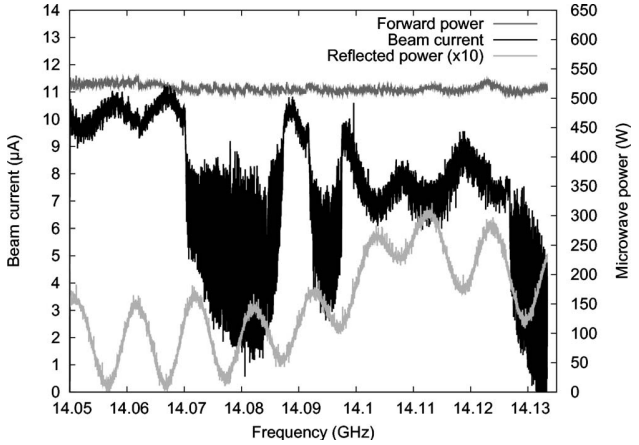


FIG. 3. The intensity of $Ar^{12+}$ ion beam, forward and reflected microwave power as a function of microwave frequency. RF-power=520 W, pressure=$1.8 \times 10^{-7}$ mbar, and BD=−180 V.

number of maxima (8) in reflected power was observed during the frequency scan. Consequently, surprisingly small changes in the behavior of reflected power between different ion source settings were seen. Only the frequency for maximum power absorption changes slightly. However, the measured changes in the ion beam intensity cannot be caused by corresponding changes in the total microwave power inside the plasma chamber ($P_{forward} - P_{reflected}$). Thus it is plausible to claim that the variations are related to the changes in the plasma-electromagnetic wave coupling.

In order to explain the observed behaviors TE and TM modes inside the used frequency range were calculated. To study the effect of plasma to the mode structure uniform electron distribution in the volume of the plasma chamber was assumed in the calculations. However, for the complexity of the system, no energy absorption was included—i.e., the electrons only affect the permittivity of the space inside the vacuum chamber. Calculations show that even a small change in electron density affects the frequency of each mode excitation and consequently changes the mode structure. Because of that, it is impossible to calculate the correct mode excitations as the spatial electron density variations in ECRIS plasma remain unknown. Taking into account the plasma absorption makes the system even much more complex. However, the calculations demonstrated that several modes can be excited within the range of the narrow frequency scan. The calculations also show that the density of calculated modes is at the same order as the density of measured intensity variations. This is demonstrated in Fig. 1 where the electron density of $4 \times 10^{11}$ cm$^{-3}$ was used as an example.

### B. Effect on beam structure and emittance

The beam emittance and the beam structure were studied as a function of the frequency with the aid of an Allison type emittance scanner[6] and KBr beam viewer. Figure 4 shows three beam viewer pictures corresponding to the data shown in Fig. 1. The beam structure varies strongly with the microwave frequency as an indication of the plasma-wave coupling changing during the scan. However, no unequivocal

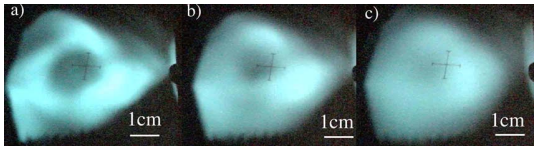


FIG. 4. (Color online) The structure of the $Ar^{9+}$ ion beam with different plasma heating frequencies: (a) 14.050 GHz, (b) 14.090 GHz, and (c) 14.108 GHz.

explanation concerning the origin of beam structure variations can be given: they could originate from the changes in the plasma in electron ion dynamics due to electromagnetic field variations and/or in the beam line due to changes in ion beam intensity (and space charge). On the other hand, the intensity at the frequencies of 14.050 and 14.090 GHz is practically same (see Fig. 1), which indicates that changes in the beam structure shown in Fig. 4 are at least partially due to varying plasma conditions. Figure 5 shows the beam structure in the case of double frequency heating. With some frequency combinations two concentric hollow beam structures can be seen, which indicates that this time the hollow beam structure is formed inside the plasma as the structure cannot be generated by the beam optical components.

Table I shows the emittance (normalized 1 rms, 90% threshold) and the intensity of the $Ar^{8+}$ and $Ar^{9+}$ ion beams for the frequencies of 14.07, 14.10, and 14.13 GHz. The intensity and percentage of the beam within the acceptance of the K130 cyclotron are also shown (100 $\pi$ mm mrad as area emittance). Strong intensity variations within the acceptance of the cyclotron can be obtained as a result of the frequency tuning. The measurement proves that the frequency tuning has a strong effect also on the beam quality—not only on the intensity. However, no explanation for the behavior shown in the Table I can be given: the high charge states (9+ and higher) had a lowest emittance in the beginning of the frequency scan while the lower charge states in the middle of the frequency scan.

## III. DISCUSSION

The experiments demonstrated that frequency tuning can be an efficient tool for improving the ion beam intensity and the ion beam quality produced by ECR ion sources. The effect increases with the charge state of ions. One possible explanation for the phenomenon seen in the experiments is the variation in plasma—electromagnetic wave coupling. Typically the maximum reflected power was about 5% compared to the forward microwave power. Consequently the intensity variations in highly charged ion beams cannot be

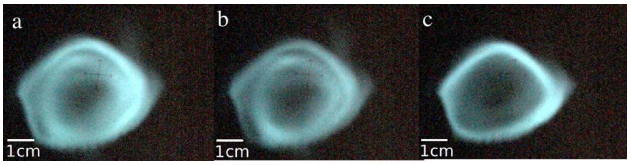


FIG. 5. (Color online) Two concentric hollow beams can be obtained with two frequency heating: (a) 14.070 GHz+11.56 GHz, (b) 14.100 GHz +11.56 GHz, and (c) 14.135 GHz+11.56 GHz. RF-power=203 W +30 W, pressure=$3.9\times10^{-7}$ mbar, and BD=−68 V.

TABLE I. The normalized 1 rms emittance and ion beam intensities of $Ar^{8+}$ and $Ar^{9+}$ (measured intensity and calculated intensity within the acceptance of the K130 cyclotron) and emittances in the case of three different frequencies. The ion source was tuned for $Ar^{8+}$. RF-power=200 W, pressure=$3.3\times10^{-7}$ mbar, and bias disk (BD) voltage=−110 V.

| Ion | Frequency (GHz) | $\varepsilon_{\text{nrms }90\%}$ ($\pi$ mm mrad) | $I_{\text{meas}}$ ($\mu$A) | I within 100 $\pi$ mm mrad |
|---|---|---|---|---|
| $Ar^{8+}$ | 14.07 | 0.100 | 117.0 | 59.6 $\mu$A (50.9%) |
| $Ar^{8+}$ | 14.10 | 0.084 | 84.7 | 55.9 $\mu$A (66.0%) |
| $Ar^{8+}$ | 14.13 | 0.104 | 101.5 | 57.9 $\mu$A (57.0%) |
| $Ar^{9+}$ | 14.07 | 0.068 | 67.5 | 56.0 $\mu$A (82.9%) |
| $Ar^{9+}$ | 14.10 | 0.110 | 37.8 | 30.2 $\mu$A (79.9%) |
| $Ar^{9+}$ | 14.13 | 0.101 | 51.0 | 36.2 $\mu$A (70.9%) |

explained by relatively small power variations inside the plasma chamber. Calculations show that changes in coupling can appear because different modes are excited even during the narrow frequency scan. It was observed also that the frequency tuning has a strong effect on the ion beam structure. This is also an indication about the changes in plasma-wave coupling. Clear evidence was seen that in some cases the hollow beam structure is at least partially formed already inside the ion source (two concentric rings were seen with some 2-frequency combinations). However, we have seen some evidences with space charge compensation measurements that the hollow beam structure can be produced also in the beam line.[7] Consequently, the formation of the hollow beam structure can be a superposition of these two phenomena.

Interesting speculations concerning the quality factor Q can be done if it is assumed that the intensity variations shown in Fig. 1. are related to the changes in the mode excitation (Q=*stored peak energy/dissipated energy per cycle*). In order to see the mode structure the quality factor Q of the system has to be high. This is due to the fact that the Q-value characterizes the bandwidth $\Delta f$ [full width at half maximum (FWHM)] of a resonating system relative to its center frequency $f_0$ ($\Delta f=f_0/Q$). The Q-values differ from mode to mode and were calculated to be between about 20 000 and 100 000 for the system described in the figure caption of Fig. 1. The Q-values correspond to the bandwidth of 700 and 140 kHz, respectively. This is a very narrow peak in the scale presented in Fig. 1. The difference can be explained by the fact that no absorption of plasma has been taken into account in the calculations. However, in order to see any intensity variation as a function of the frequency the Q-value has to be relatively high. For example, the Q-value of 100 would give the FWHM-value (i.e., $\Delta f$) of 140 MHz, which is more than the frequency scan performed during the experiments.

A more accurate Q-value approximation can be done using the reflection coefficient, presented, for example, in Ref. 3. From our measurement the Q-value of about 2200 was obtained by the reflection coefficient analysis. Furthermore, it was noticed that the Q-values corresponding to Figs. 1–3 are all on the same order of magnitude. The value is much lower than was obtained by the calculations. This is because the measurement also includes the energy absorption by the plasma. The values indicate (20 000–100 000 versus ≈2200)

that the most of the power is dissipated by the plasma and only a small fraction by the walls via Joule heating (naturally walls are also heated by the plasma particles). The approximated value is much higher than Q-value of 3 used in Ref. 8 but is in good agreement with the experiments described in Ref. 3.

## ACKNOWLEDGMENTS

This work has been supported by the Academy of Finland under the Finnish Centre of Excellence Programme 2006–2011 (Nuclear and Accelerator Based Physics Programme at JYFL). H.K. and O.T. acknowledge Väisälä foundation, T.R. and V.T. acknowledge Ehrnrooth foundation and V.T. acknowledges Nyyssönen foundation for financial support. The support of Fifth INFN National Commission (HELIOS experiment) is acknowledged.

[1] G. Machicoane, M. Doleans, J. Stetson, X. Wu, and P.A. Zavodszky, Rev. Sci. Instrum. **79**, 02B714 (2008).
[2] H. Koivisto, P. Suominen, T. Ropponen, J. Ropponen, T. Koponen, M. Savonen, V. Toivanen, X. Wu, G. Machicoane, J. Stetson, P. Zavodszky, M. Doleans, P. Spädtke, R. Vondrasek, and O. Tarvainen, Rev. Sci. Instrum. **79**, 02A303 (2008).
[3] L. Celona, G. Ciavola, F. Consoli, S. Gammino, F. Maimone, D. Mascali, P. Spädtke, K. Tinschert, R. Lang, J. Mäder, J. Roßbach, S. Barbarino, and R. S. Catalano, Rev. Sci. Instrum. **79**, 023305 (2008).
[4] S. Gammino, High Energy Phys. Nucl. Phys., Chinese Physical Society, **31**, 137 (2007).
[5] S. Gammino, G. Ciavola, L. Celona, D. Mascali, and F. Maimone, IEEE Trans. Plasma Sci. **36**, 1552 (2008).
[6] D. Wutte, M. A. Leitner, and C. M. Lyneis, Phys. Scr. **T92**, 247 (2001).
[7] V. Toivanen, O. Steczkiewicz, O. Tarvainen, T. Ropponen, J. Ärje, and H. Koivisto, "The effects of beam line pressure on the beam quality of an electron cyclotron resonance ion source," Nucl. Instrum. Methods Phys. Res. B (to be published).
[8] Y. Jongen, Proceedings of the Sixth Workshop on ECRIS, 1985 (unpublished), p. 238.

# APPENDIX A.II

# Erratum: "Effect of electron cyclotron resonance ion source frequency tuning on ion beam intensity and quality at Department of Physics, University of Jyväskylä" [Rev. Sci. Instrum. 81, 02A319 (2010)]

V. Toivanen,[1] H. Koivisto,[1] O. Steczkiewicz,[1] L. Celona,[2] O. Tarvainen,[1] T. Ropponen,[1] S. Gammino,[2] D. Mascali,[2] and G. Ciavola[2]
[1]*Department of Physics, University of Jyväskylä (JYFL), 40500 Jyväskylä, Finland*
[2]*Instituto Nazionale di Fisica Nucleare, Laboratori Nazionali del Sud, 95123 Catania, Italy*

(Received 1 October 2010; accepted 22 December 2010; published online 10 February 2011)
[doi:10.1063/1.3541812]

In Sec. III of the article, speculations concerning the quality factor Q of the plasma chamber of JYFL 14 GHz electron cyclotron resonance ion source were presented. The discussion was based on the behavior of the reflected power as a function of the microwave frequency. It was assumed that all the observed minima in the fine structure of the reflection coefficient, calculated from the reflected power, represent electromagnetic wave modes excited in the plasma chamber and can, thus, be used to estimate corresponding Q values. However, recent measurements have shown that the observed behavior of the reflected power is strongly affected by the wave guide system, as described in the following chapters, and cannot be directly used for Q value evaluations. The other conclusions of the original article remain unaffected.

In the new experiments, the behavior of the reflected power was studied using different lengths of wave guide between the microwave emitter and the ion source. As a result, it was observed that the number of maxima and minima of the reflected power in a fixed frequency range changed with the length of the wave guide [see Figs. 1(a) and 1(b)] while keeping the ion source settings (magnetic field, neutral gas pressure, etc.) constant. Furthermore, at high microwave powers it was observed that the minima and maxima of the reflected power drifted slightly toward lower frequency with time as length of the wave guide increased due to heat expansion. The measured ion beam currents exhibited similar behavior as in the measurements discussed in the original article. In all measurements of high charge state ion beams, the beam currents follow the behavior of the reflected power fluctuations with local current maxima occurring at the same frequencies as the local reflected power minima.

To further study the connection between the behavior of reflected power and phenomena originating from the plasma chamber, the plasma chamber was disconnected from the wave guide and replaced with a low voltage standing wave ratio load element. The oscillatory fine structure of the reflected power remained, as shown in Fig. 1(c). The exact locations of the minima and maxima [see Figs. 1(a) and 1(c)] are affected by the difference in the wave guide length due to the connectors.

These two studies show that in the case of JYFL 14 GHz ECRIS, the periodic oscillations seen in the reflected power cannot be associated to the mode structure inside the plasma chamber and, thus, cannot be used to estimate the Q values of the plasma chamber.

Some considerations concerning the oscillatory behavior of the reflected power can be presented. The wave guide between the microwave emitter and the ion source is of the WR75 type, which allows for microwaves around 14 GHz the propagation of $TE_{01}$ mode only. The energy propagates in the wave guide with group velocity, which also determines the wave length. When the phase of the propagating electromagnetic wave is calculated at the end of the wave guide for two consecutive reflected power maxima, it is observed that the frequency shift between the maxima corresponds very closely to a phase shift of $\pi/2$ ($\lambda/4$). This holds very well for all the studied cases, suggesting the existence of a phase dependent process behind the reflected power behavior.

Furthermore, if a clear mode structure persists with plasma, as the observed changes in the extracted beam current and beam shape presented in the article imply, the reflected power behavior must be a superposition of the effects caused by the wave guide and the mode structure. This obstructs the mode evaluation from the reflected power signal

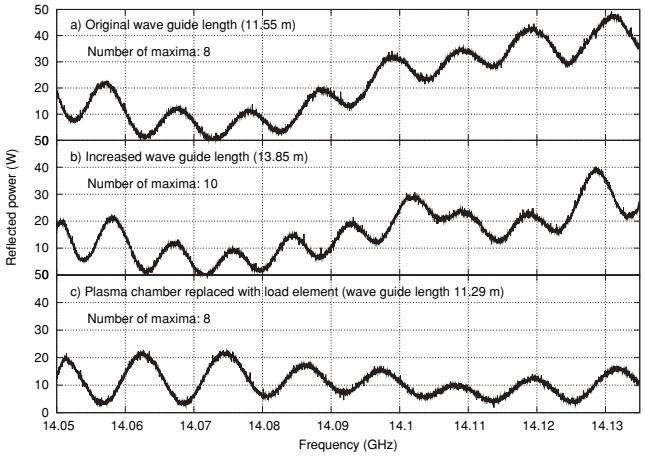


FIG. 1. Reflected power measured at klystron with (a) original 11.55 m wave guide, (b) 13.85 m wave guide, and (c) when plasma chamber was disconnected from the wave guide and replaced with a load element at the end of the wave guide (notice the slight difference in the wave guide length due to the length of the connectors). Automatic level control function of the klystron and a set output power level of about 500 W were used in the measurements.

 

even further. If the mode structure causes narrow frequency range effects (a few MHz), it is evident from the measured results that these effects must be very weak compared to the effects caused by the wave guide. However, the global trend of the reflected power across the whole studied frequency range (ignoring the periodic ripple) is somewhat different for the plasma and the load element. It is possible that this trend corresponds to the actual mode structure. Unfortunately, it is impossible to identify the origin or role of this behavior from the narrow frequency range used in the measurements.

# APPENDIX A.III

# Electron cyclotron resonance ion source plasma chamber studies using a network analyzer as a loaded cavity probe[a)]

V. Toivanen,[1,b)] O. Tarvainen,[1] C. Lyneis,[2] J. Kauppinen,[1] J. Komppula,[1] and H. Koivisto[1]
[1]*Department of Physics, University of Jyväskylä, Jyväskylä 40500, Finland*
[2]*Lawrence Berkeley National Laboratory, Berkeley, California 94720, USA*

(Presented 14 September 2011; received 7 September 2011; accepted 15 September 2011; published online 2 February 2012)

A method and first results utilizing a network analyzer as a loaded cavity probe to study the resonance properties of a plasma filled electron cyclotron resonance ion source (ECRIS) plasma chamber are presented. The loaded cavity measurements have been performed using a dual port technique, in which two separate waveguides were used simultaneously. One port was used to ignite and sustain the plasma with a microwave source operating around 11 GHz and the other was used to probe the cavity properties with the network analyzer using a frequency range around 14 GHz. The first results obtained with the JYFL 14 GHz ECRIS demonstrate that the presence of plasma has significant effects on the resonance properties of the cavity. With plasma the frequency dependent behavior is strongly damped and this trend strengthens with increasing microwave power. © *2012 American Institute of Physics*. [doi:10.1063/1.3660818]

## I. INTRODUCTION

The electron cyclotron resonance ion source (ECRIS) plasma chamber can be considered as an overmoded cavity for the microwaves that are used for plasma heating. The resulting microwave electric fields in the cavity play an important role during the plasma ignition by transferring energy to the electron population and sustaining the following stepwise ionization to high ion charge states. Thus the electric field configurations, or modes, inside the cavity with plasma are of interest considering the performance of the ion source.

The first measurements of the microwave frequency dependent behavior of the AECR-U-type 14 GHz ion source at Department of Physics, University of Jyväskylä (JYFL 14 GHz ECRIS (Ref. 1)) were performed utilizing microwave power probes integrated with the microwave emitter.[2] Further studies[3,4] revealed that the waveguide transmission line connecting the emitter to the ion source exhibits strong frequency dependent behavior, which was considerably more pronounced in the studied narrow frequency range than the actual chamber behavior, obscuring the results. The frequency dependent behavior of the waveguide can be explained by considering it as a long rectangular resonator. This can happen if a mismatch exists near both ends of the waveguide. As only $TE_{01}$ mode propagates in the waveguide, the resonance frequency $f_r$ of such a cavity can be expressed as[5]

$$(f_r)^{TE}_{01p} = (c/2\pi)\sqrt{(\pi/b)^2 + (p\pi/d)^2}, \quad (1)$$

where $c$ is the speed of light in vacuum, $b$ is the longer waveguide transverse inner dimension, $d$ is the length of the waveguide, and $p$ is the longitudinal resonance index. Each of the resonance frequencies, i.e., values of index $p$, corresponds to a minimum of reflected power in this system. Around 14 GHz, the separation of these resonance frequencies matches the measured distance between the minima of reflected power seen in earlier measurements.[3,4]

In order to measure the loaded plasma chamber properties, the influence of the transmission line on the results must be isolated and carefully removed. In this paper, a technique is presented which enables this.

## II. DUAL PORT MEASUREMENT TECHNIQUE

The plasma loaded cavity properties were studied using a dual port measurement technique. In this approach, the plasma was ignited and sustained by using one waveguide for launching the microwave power. The cavity properties were measured with a Rohde & Schwarz vector network analyzer (frequency range up to 15 GHz) through another port. A microwave frequency high pass filter with cutoff at 13 GHz was installed into the waveguide between the plasma chamber and the network analyzer to prevent the transmitted microwave power from reaching and potentially damaging the device. The actual measurements were performed using a frequency range which does not include the heating frequency. In the case of the measurements presented in this paper, the plasma was sustained with frequencies between 10.86 and 11.81 GHz using a traveling wave tube amplifier (TWTA) and frequencies between 13 and 15 GHz were used to probe the chamber properties. The effect of 0.1 mW probe signal can be considered insignificant for the plasma behavior compared to the TWTA output with forward powers of 0.5–300 W. A schematic presentation of the measurement setup is shown in Fig. 1.

In order to measure only the chamber properties, the network analyzer was calibrated with the transmission line up to the interface of the waveguide and the plasma chamber using its inbuilt calibration feature. A three-reference calibration

[a)]Contributed paper, published as part of the Proceedings of the 14th International Conference on Ion Sources, Giardini Naxos, Italy, September 2011.
[b)]Electronic mail: ville.toivanen@jyu.fi.

 

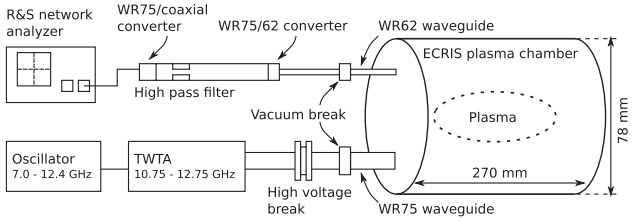


FIG. 1. Schematic presentation of the measurement setup.

was performed with two WR62 waveguide offset shorts and a load element, each connected in turn to the end of the waveguide. This procedure enables the network analyzer to take into account the frequency dependent behavior of the transmission line.

The plasma chamber properties were studied by measuring the $S_{11}$ reflection coefficient, defined $S_{11} = 10\log_{10}(P_{\text{refl}}/P_{\text{inc}})$, where $P_{\text{refl}}$ and $P_{\text{inc}}$ are the reflected and incident power of the probing signal, as a function of frequency. $S_{11}$ describes the system's ability to absorb and transmit microwave power, including the possible power leaks through the cavity apertures. When the plasma is ignited, the measured $S_{11}$ describes the combined behavior of the cavity and the plasma it contains. The maximum resolution of the network analyzer depends on the studied frequency range. The narrowest frequency range used in the measurements, 250 MHz, yields point separation of 62.5 kHz.

## III. EXPERIMENTAL RESULTS

To ensure that no plasma ignition took place due to the probing signal in the empty cavity measurements, the cavity was also measured at atmospheric pressure (vented with $N_2$). The results with vented chamber were identical compared to the case with vacuum. Empty cavity behavior is presented as part of Fig. 2.

The loaded cavity properties were studied by varying the ECRIS parameters around those representing normal operational values, except the microwave power, which was limited to the TWTA maximum output value (300 W with the oscillator input used in the measurements) and the microwave frequency (11.56 GHz, normal operation utilizes a klystron at 14.085 GHz frequency). No high voltages were used during the measurements and consequently no beam was extracted from the ion source.

The TWTA microwave power was varied between 0 and 300 W. The $S_{11}$ behavior of the chamber with increasing microwave power is presented in Fig. 2. The number of $S_{11}$ minima decreases with increasing microwave power and the minima become less pronounced. The location of the minima moves to higher frequencies as microwave power is increased, as is presented in Fig. 3.

The negative biased disc voltage (varied between 0–300 V), gas species (argon and oxygen, matched calibrated pressures), and TWTA frequency (10.86–11.81 GHz) had no significant effect on the $S_{11}$ behavior. Increasing gas pressure (1.4–32 $\times$ $10^{-7}$ mbar, calibrated argon neutral gas pressure) makes the $S_{11}$ minima somewhat less pronounced but the effect is very frequency specific (localized between 13.6 and 14.1 GHz) and weaker than with increasing power. The changes saturated after 7 $\times$ $10^{-7}$ mbar. The magnetic field was varied between 1.95/0.90/0.32 T and 2.11/1.02/0.39 T (inj./ext./min.). Only the highest magnetic field values changed the $S_{11}$ behavior, yielding subtle shifts in the $S_{11}$ minima location and level. The ion source is known to be prone to plasma instabilities with high magnetic field values, which can contribute to this result.

## IV. DISCUSSION

The presented results demonstrate that the presence of plasma changes the cavity resonance properties significantly, damping the mode behavior. This was observed to take place in the whole measured frequency band of 13–15 GHz, giving reason to assume that the same trends also apply beyond this frequency range.

The plasma chamber $Q$ value for a certain mode can be defined as $Q = f_0/\Delta f$, where $f_0$ is the center frequency and $\Delta f$ is the FWHM value of the mode, represented by the frequency and bandwidth of a measured $S_{11}$ minimum. The $Q$

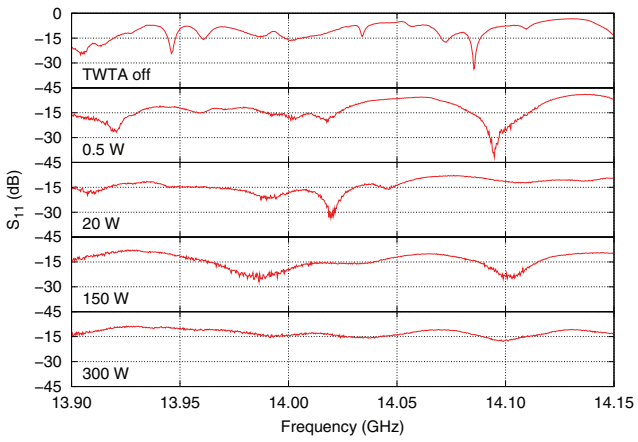


FIG. 2. (Color online) Plasma chamber $S_{11}$ behavior with various microwave power levels from TWTA.

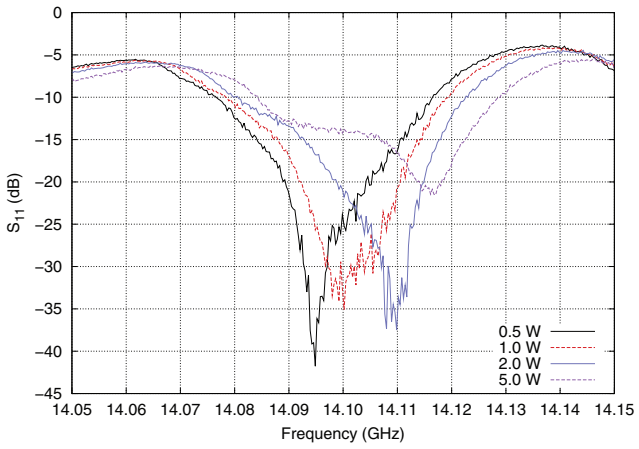


FIG. 3. (Color online) Example of the movement of $S_{11}$ minima with increasing microwave power.

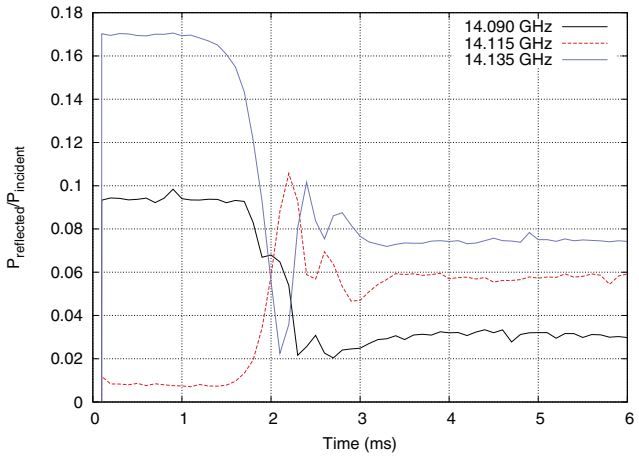


FIG. 4. (Color online) The ratio of reflected and incident power with various microwave frequencies at the plasma ignition. Microwaves turned on at $t = 0$ ms (klystron, 430 W).

values discussed here include all the power absorption inside the cavity, whether it is caused by the cavity walls (resistive heating) or the plasma. With no power input from the TWTA (no plasma), the calculated $Q$ values are in the order of $10^3$. With plasma at 300 W of microwave power, the $Q$ values drop to the order of $10^2$. These values match well with the results obtained with the LBL 6.4 GHz ECRIS, which indicate that the loaded cavity $Q$ value drops to ∼10% of the empty cavity value.[6] The chamber diameter to wavelength ratio of the JYFL 14 GHz ECRIS is 3.7 (for the normal operation frequency of 14.085 GHz), making it overmoded compared to the value of 2.0 of the LBL 6.4 GHz ECRIS.

After careful calibration of the measurement system, the ∼11 MHz ripple observed in earlier measurements[2–4] is absent, confirming it originates from waveguide imperfections. Comparison with the earlier results also shows that when the ripple is ignored, only one broad $S_{11}$ minimum remains with high microwave powers in the klystron frequency range of 14.050–14.135 GHz used in the earlier experiments (see Fig. 1(a) in Ref. 3), which matches very well with the new results (see the 300 W case in Fig. 2).

The frequency of the microwaves sustaining the plasma had no significant effect on the resonant properties of the cavity at the measured frequency range. However, pulsed operation of the JYFL 14 GHz ECRIS has shown that the microwave frequency plays an important role during the plasma ignition as the temporal behavior of the ratio of reflected to incident power in Fig. 4 indicates. Initially, at low plasma density the frequency has a substantial effect on the structure and amplitude of the electric fields in the cavity. Plasma breakdown leads to rapid increase in plasma density and the collapse of the electric field amplitudes and the rate of energy transfer to individual plasma electrons.[7] Consequently, as the results presented in this paper indicate, the resonant properties of the chamber are damped, the effective mode structure of the combined system of cavity and plasma weakens considerably (as shown in Fig. 2) and the exact frequency ceases to play as critical a role in the plasma behavior as it does during the ignition. The differences in the saturation values of the $P_r/P_i$ ratio in Fig. 4 are caused by the superimposed effects of the waveguide and the cavity behavior.

The results presented in this paper differ somewhat from the data obtained with a Caprice-type ECR ion source.[8] With Caprice the mode structure remained considerably more pronounced even with higher microwave powers. Also, with Caprice the $S_{11}$ exhibited strong behavior with varied magnetic field and gas pressure, a phenomenon which was not observed in the measurements presented here. These differences can be due to the different microwave coupling schemes used with the ion sources. Caprice has a more complex microwave coupling including a waveguide to coaxial transition compared to the AECR-U-type ion sources which use a simpler design in which the rectangular waveguides are inserted directly into the plasma chamber. Also, AECR-U has larger plasma chamber diameter than Caprice, increasing the mode density.

## ACKNOWLEDGMENTS

This work has been supported by the Academy of Finland under the Finnish Centre of Excellence Programme 2006–2011 (Nuclear and Accelerator Based Physics Programme at JYFL) and the European Union Seventh Framework Programme FP7/2007–2013 under Grant Agreement No. 262010 - ENSAR. The European Commission is not liable for any use that can be made on the information contained herein.

[1] H. Koivisto, P. Heikkinen, V. Hänninen, A. Lassila, H. Leinonen, V. Nieminen, J. Pakarinen, K. Ranttila, J. Ärje, and E. Liukkonen, Nucl. Instrum. Methods Phys. Res. B **174**, 379 (2001).
[2] V. Toivanen, H. Koivisto, O. Steczkiewicz, L. Celona, O. Tarvainen, T. Ropponen, S. Gammino, D. Mascali, and G. Ciavola, Rev. Sci. Instrum. **81**, 02A319 (2010).
[3] V. Toivanen, H. Koivisto, O. Steczkiewicz, L. Celona, O. Tarvainen, T. Ropponen, S. Gammino, D. Mascali, and G. Ciavola, Rev. Sci. Instrum. **82**, 029901 (2011).
[4] V. Toivanen, V. Aho, L. Celona, G. Ciavola, A. Galata, S. Gammino, P. Jones, J. Kauppinen, H. Koivisto, D. Mascali, P. Peura, T. Ropponen, O. Tarvainen, and J. Ärje, in Proceedings. of the 19th InternationalWorkshop on ECRIS, Grenoble, (2010); see jacow.org.
[5] C. A. Balanis, *Advanced Engineering Electromagnetics* (Wiley, New York, 1989).
[6] C. Lyneis, J. Benitez, D. Leitner, J. Noland, M. Strohmeier, H. Koivisto, O. Tarvainen, in Proceedings of the 19th International Workshop on ECRIS, Grenoble, (2010); see jacow.org.
[7] T. Ropponen, O. Tarvainen, I. Izotov, J. Noland, V. Toivanen, G. Machicoane, D. Leitner, H. Koivisto, T. Kalvas, P. Peura, P. Jones, V. Skalyga, and V. Zorin, Plasma Sources Sci. Technol. **20**, 055007 (2011).
[8] L. Celona, G. Ciavola, F. Consoli, S. Gammino, F. Maimone, D. Mascali, P. Spädtke, K. Tinschert, R. Lang, J. Mäder, J. Roßbach, S. Barbarino, and R. S. Catalano, Rev. Sci. Instrum. **79**, 023305 (2008).

# APPENDIX A.IV

Nuclear Instruments and Methods in Physics Research B 268 (2010) 1508–1516

Contents lists available at ScienceDirect

Nuclear Instruments and Methods in Physics Research B

journal homepage: www.elsevier.com/locate/nimb

# The effects of beam line pressure on the beam quality of an electron cyclotron resonance ion source

V. Toivanen *, O. Steczkiewicz, O. Tarvainen, T. Ropponen, J. Ärje, H. Koivisto

*University of Jyväskylä, Department of Physics, Accelerator Laboratory, P.O. Box 35 (YFL), 40500 Jyväskylä, Finland*

ARTICLE INFO

*Article history:*
Received 22 September 2009
Received in revised form 3 December 2009
Available online 22 January 2010

*Keywords:*
Beam quality
Beam transport
Space charge compensation
Beam potential
Electron cyclotron resonance ion source
Emittance

ABSTRACT

The results of a series of measurements studying the possibility to use neutral gas feeding into the beam line as a way to improve the quality of the heavy ion beams produced with an electron cyclotron resonance ion source (ECRIS) are presented. Significant reduction of the beam spot size and emittance can be achieved with this method. The observed effects are presumably due to increased space charge compensation degree of the ion beam in the beam line section between the ion source and the analyzing magnet. This is the region where the neutral gas was injected. It is shown that the effects are independent of the ion source tuning. Transmission measurements through the beam line and K-130 cyclotron have been carried out to study the effects of improved ion beam quality to the transmission efficiency.



## 1. Introduction

At the JYFL (University of Jyväskylä, Department of Physics) accelerator laboratory 6.4 GHz and 14 GHz electron cyclotron resonance ion sources [1] are used for production of intensive highly charged heavy ion beams. Earlier studies [2] have shown that the transmission efficiency from the 14 GHz ECRIS through the cyclotron decreases when the beam current extracted from the ion source increases. This is caused by degradation of the beam quality. At high beam currents the ion beam is hollow [3] and the beam emittance is considerably higher than the K-130 cyclotron acceptance ($100\,\pi$ mm mrad). This is believed to be caused at least partly by space charge effects in the beam line between the ion source and the analyzing magnet. In this beam line section all the ion species produced by the ECR ion source are still present.

Feeding neutral gas into the beam line offers a possibility to enhance the space charge compensation of the ion beam. As the ion beam passes through neutral gas, ionizing and charge exchange collisions are constantly occurring. As a result of these interactions slow ions and electrons are formed. The slow ions are repelled away from the beam and the electrons are trapped into the beam potential. The overall charge density of the resulting plasma is lower than the charge density of the uncompensated ion beam and thus space charge compensation is achieved [4,5]. This method has been used earlier to study emittance reduction of high intensity proton beams with good results [6,7]. In this article the results of measurements studying the effects of gas feeding on the quality and transmission of medium charge state heavy ion beams produced with the JYFL 14 GHz ECR ion source are presented.

## 2. Theoretical background

In this paper normalized 1-rms emittance is used when presenting emittance values. Beam brightness $B$ is used to combine the emittance and current information and quantify the beam quality. The brightness is defined as

$$B = \frac{I}{\epsilon_{yy'}\epsilon_{xx'}}, \tag{1}$$

where $I$ is the beam current and $\epsilon_{yy'}$ and $\epsilon_{xx'}$ are the beam emittances in $(y,y')$ and $(x,x')$ phase spaces. The emittance scanner used at JYFL can only measure emittance in one plane and thus we have to approximate $\epsilon_{yy'} = \epsilon_{xx'}$. This approximation is supported by ion optics simulations done for the JYFL low energy beam line. Also, it can be assumed that the effects caused by the gas feeding into the beam line are symmetric in both transverse planes.

The space charge of the ion beam creates a potential (beam potential) which is parabolic inside the beam and logarithmic outside the beam. For a cylindrical beam in grounded beam line the potential $\Phi$ at radius $r$ is given by [8]:

* Corresponding author. Tel.: +358 14 260 2466; fax: +358 14 260 2351.
*E-mail address:* ville.toivanen@jyu.fi (V. Toivanen).

0168-583X/$ - see front matter © 2010 Elsevier B.V. All rights reserved.
doi:10.1016/j.nimb.2010.01.016

$$\Phi(r) = \frac{(1-\eta)I}{4\pi\epsilon_0 v}\left(1 + 2\ln\frac{r_w}{r_b} - \frac{r^2}{r_b^2}\right) \quad \text{inside the beam} \tag{2}$$

$$\Phi(r) = \frac{(1-\eta)I}{2\pi\epsilon_0 v}\ln\frac{r_w}{r} \quad \text{outside the beam} \tag{3}$$

where $\eta$ is the space charge compensation degree, $I$ is the beam current, $\epsilon_0$ is the permittivity of vacuum, $v$ is the longitudinal velocity of the ions, $r_w$ is the beam pipe radius and $r_b$ is the beam radius. The above equations are valid with the assumption of a beam with a homogeneous density distribution. As will be seen later, this is not the case in the measurements that are presented here. However, the equations can still be used to obtain rough approximations of the beam potential.

The beam potential depends strongly on beam current, velocity and beam size. In non-relativistic cases for a beam with only one ion species the beam velocity can be written as $v = \sqrt{2qV/m}$, where $q$ is the ion charge, $m$ is the ion mass and $V$ is the ion source acceleration (i.e. extraction) voltage. Thus increasing the extraction voltage decreases the beam potential and consequently the space charge effects. The dependency on the beam size shows that during the beam transport the beam potential varies and the space charge effects are strongest at beam waists (focal points), where the beam size is smallest.

A rough approximation of the beam potential can be calculated using a measured charge state distribution. For this purpose the distribution of argon charge states was measured from JYFL 14 GHz ECR ion source with 10 kV extraction voltage. The portion of the beam for each charge state was estimated from the distribution and the beam potential was calculated at the center of the beam with Eq. (2) for each charge state. The beam pipe radius is 5 cm and the beam radius was estimated separately for each charge state. The estimations are based on simulations in which $Ar^{8+}$ was optimized through the beam line. The values of the radii were taken close to the focal point of $Ar^{8+}$ between the ion source and the analyzing magnet and they varied between 0.4 and 5 cm.[1] The sum of the potentials of each charge state gives an approximation for the potential of the whole beam. When the total extracted beam current is varied between 0.6 and 1.8 mA and no space charge compensation is assumed ($\eta = 0$) the beam potential varies between 30 and 100 V.

The degree of space charge compensation depicts what portion of the full non-compensated potential (as calculated above) affects the beam particles. With high beam line pressures the ions of the beam exhibit more collisions with residual gas, which leads to enhanced production of compensating electrons. At pressures over $1 \times 10^{-4}$ mbar over 99% of the beam potential can be compensated (compensation degree $\eta > 0.99$) but some beam losses are also introduced [4]. At low pressures the collision rate decreases, which leads to reduction of compensation. Comparison of measurements and simulations conducted at Lawrence Berkeley National Laboratory (LBNL) for helium beams have given an estimate of 70–80% compensation degree for beam line pressures in the $10^{-8}$ mbar region [9]. As the compensation degree is reduced, the radial electric field, and consequent transverse forces, generated by the space charge get stronger and increase the beam size [10]. This has been shown experimentally, for example, by Mazarakis et al. for 1 mA $Xe^{1+}$ ion beam [5].

## 3. Experimental setup

The ion beams used in the measurements were produced with the JYFL 14 GHz ECR ion source. The beam line of the ion source is presented in Fig. 1. The ion beams are focused with two solenoids (SOLJ1 and SOLJ2) through an analyzing magnet. Downstream from the magnet the ion beam is focused with a third solenoid (SOLJ3) through a bending magnet (labeled as switch magnet in Fig. 1) that merges the beam lines coming from different ion sources into the main injection line of the K-130 cyclotron. The beam diagnostics include a beam viewer, a Faraday cup, a plasma potential measurement device [11] and an Allison type emittance scanner (see e.g. [12]) as shown in Fig. 1.

The beam viewer consists of a small vacuum chamber with a window and an actuator, a digital video camera and a KBr coated scintillation screen. The emittance scanner can be used to measure the beam emittance $\epsilon_{yy'}$ in the plane perpendicular to the analyzing magnet bending plane.

The beam line between the ion source and the switch magnet offers two locations for feeding neutral gas into the beam line (referred to as gas feeding from now on) through the beam line venting ports. The ports are located upstream (port 1) and downstream (port 2) from the analyzing magnet (see Fig. 1). The neutral gas pressure was measured with Penning ionization gauges, located next to the gas feeding ports and also in the ion source extraction and plasma chamber. The gauge readings were corrected for different feeding gases according to a calibration table provided by the manufacturer.

The measurements were performed with argon ion beams. The effect of gas feeding was studied with different argon charge states and ion source extraction voltages. The beam currents were optimized to the Faraday cup downstream from the analyzing magnet and the neutral gas flow was controlled with a pressure regulator and a precision valve. Nitrogen ($N_2$), helium and argon were used as feeding gases.

Some of the injected gas diffuses into the ion source, increasing the ion source pressure. To mitigate the effects caused by the diffusion, the same gas species was also used as a buffer gas in addition to argon. Consequently the ion source could be tuned to maintain optimal plasma conditions for maximum beam currents of argon as the pressure in the beam line varied within the range of $1 \times 10^{-7}$ mbar to $3 \times 10^{-5}$ mbar. The beam current was optimized by adjusting the ion source buffer gas feeding and the beam line solenoids upstream from the analyzing magnet separately for each beam line pressure. A beam viewer image, beam emittance and beam current were recorded for each value of neutral gas pressure in the beam line. The current of the solenoid between the Faraday cup and the emittance scanner was kept constant in all measurements.

## 4. Experimental procedure and results

In the following measurements, if not mentioned otherwise, the buffer gas feeding into the ion source was tuned to achieve maximum beam currents with each beam line pressure and port 1 (between the ion source and the analyzing magnet) was used for gas feeding. Tuning the ion source this way does not affect the tendencies that are seen in the results. This is shown in Section 4.4.

### 4.1. Effects of gas feeding on different charge states

The ion source was tuned for $Ar^{8+}$ and the emittance, beam current and beam viewer images were measured for argon charge states 6+, 8+, 9+ and 11+. Different charge states were selected by changing the beam optics. Nitrogen ($N_2$) was fed into the beam line between the ion source and the analyzing magnet and also used as a buffer gas. The ion source extraction voltage was 10 kV (typical value for cyclotron injection at JYFL) for all charge states. The beam line pressure was increased from $1.8 \times 10^{-7}$ mbar to

[1] Due to insufficient focusing $r_b > r_w$ in the simulations for the lowest charge states. In these cases $r_b = r_w$ is assumed in the beam potential calculations.

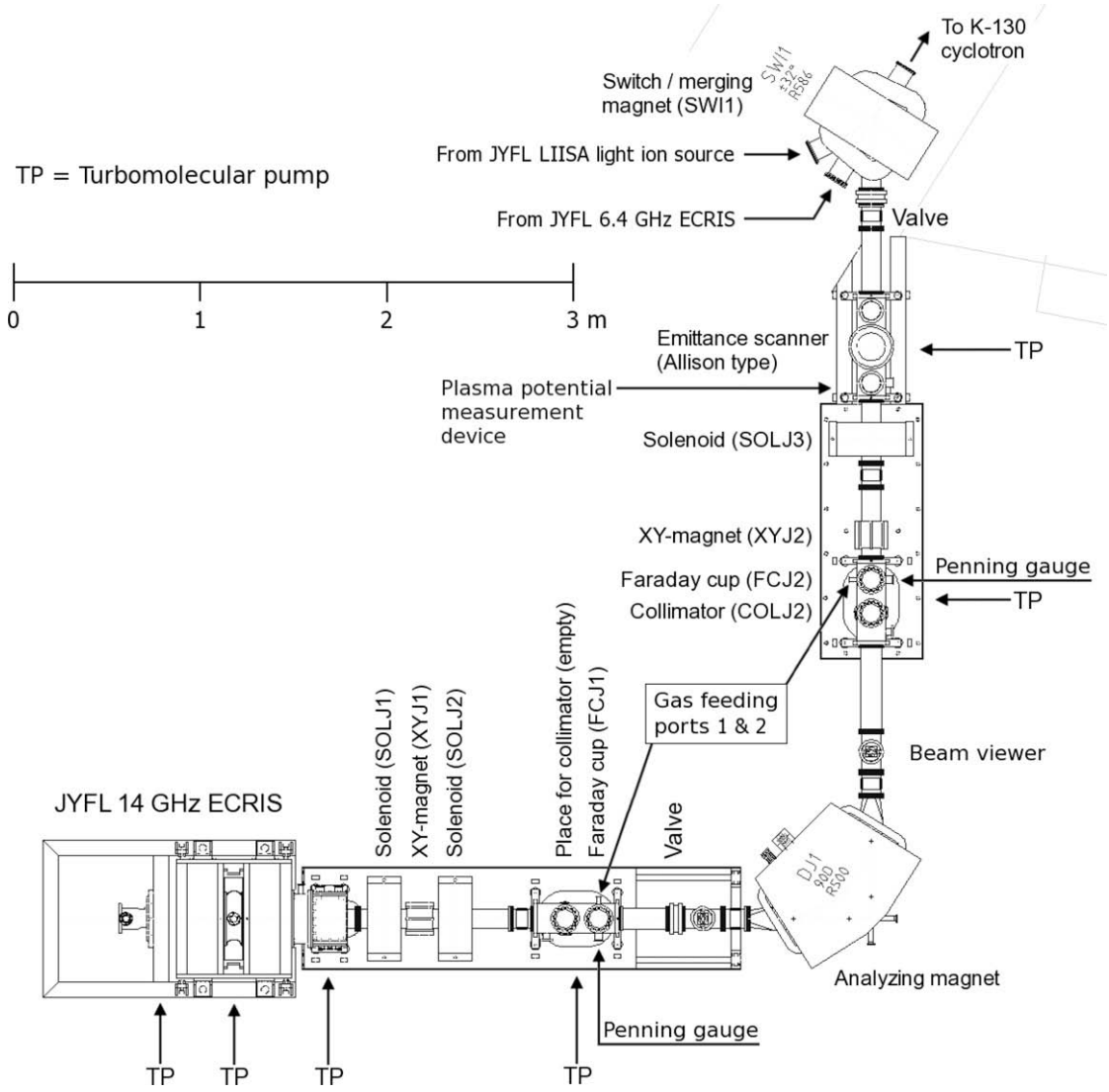


**Fig. 1.** Layout of the JYFL 14 GHz ECR ion source beam line.

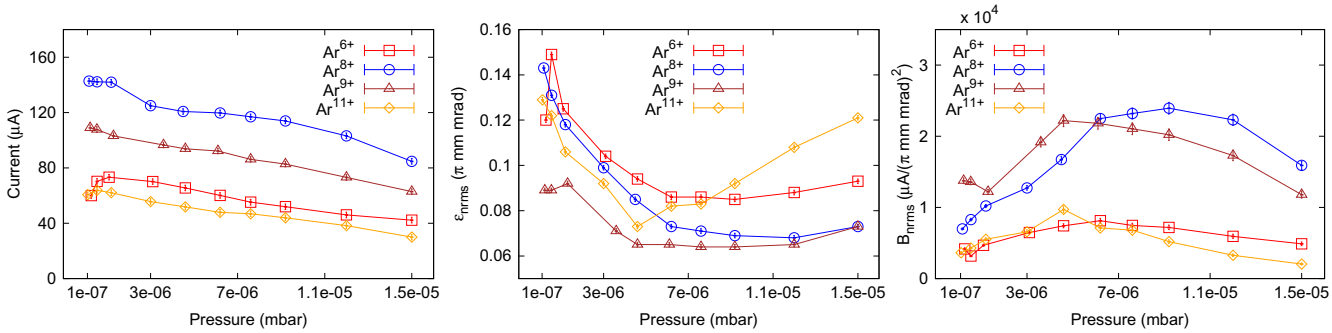


**Fig. 2.** The current, emittance and brightness values of different charge states of argon with various beam line pressures. $N_2$ as feeding gas.

$1.5 \times 10^{-5}$ mbar in ten steps and the viewer image, beam emittance and beam current were recorded for each pressure value. The results are presented in Figs. 2 and 3.

The behavior of the beam current, emittance and brightness as a function of the beam line pressure is similar for all charge states. The beam current decreases with increasing beam line pressure. The beam emittance also decreases but unlike the beam current, the emittance values exhibit a minimum between pressures of $4.6 \times 10^{-6}$ mbar and $1.2 \times 10^{-5}$ mbar depending on the charge state. As a result the brightness values reach maximum in the same pressure region. The emittance data is analyzed in more detail in Section 4.6.

Gas feeding into the beam line causes beam losses. These are due to interactions between ions and neutral atoms (or molecules)

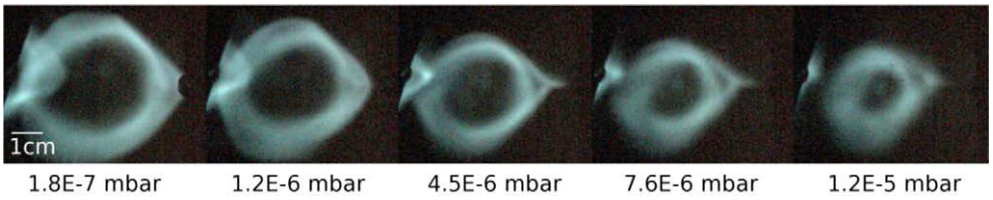


**Fig. 3.** The beam viewer image of $Ar^{8+}$ with various beam line pressures. Nitrogen as feeding and buffer gas. Note the hollow beam structure. Part of the $N^{3+}$ beam can be seen at the left edge of the viewer plate.

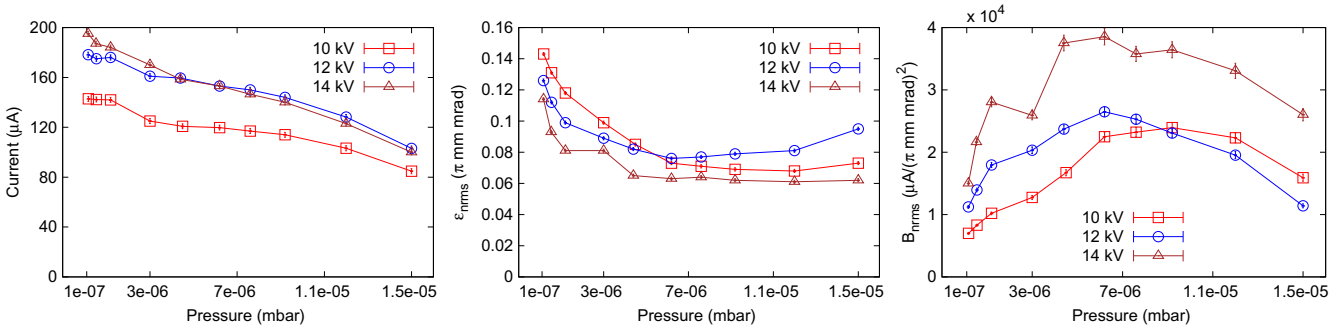


**Fig. 4.** The current, emittance and brightness values of $Ar^{8+}$ with 10 kV, 12 kV and 14 kV extraction voltages and various beam line pressures.

that lead to charge exchange [5]. The relative beam losses are greater for higher charge states. This behavior is explained by the charge exchange cross section which increases with charge state [13]. For high charge states the emittance minimum is reached at lower beam line pressures. The corresponding beam line pressures of brightness maxima of charge states 6+, 8+, 9+ and 11+ are $6.2\times 10^{-6}$ mbar, $9.2\times 10^{-6}$ mbar, $4.6\times 10^{-6}$ mbar and $4.6\times 10^{-6}$ mbar, respectively.

A clear shrinkage of the beam spot can be observed as the pressure increases. This behavior was very similar with all charge states. Therefore only the beam viewer images of $Ar^{8+}$ with different pressures are presented as an example in Fig. 3.

### 4.2. Effects of gas feeding with different ion source extraction voltages

Three different ion source extraction voltages, 10 kV, 12 kV and 14 kV, were used to study the gas feeding effects. The measurements were performed with $Ar^{8+}$ ion beam. Nitrogen was fed into the beam line and used as a buffer gas. The ion source was optimized with 10 kV extraction voltage. For other voltages only the beam line optics were adjusted. The measured beam currents and emittances, as well as calculated brightness values, are presented in Fig. 4.

The behavior observed with different voltages is very similar. The beam current of $Ar^{8+}$ increases significantly when extraction voltage is increased from 10 kV to 12 kV. Compared to this, the increase with 14 kV is very modest, indicating that the beam extraction is no more space charge limited. The relative beam losses are slightly higher with 14 kV compared to the other measured extraction voltages. However, this is not caused by changes in the charge exchange cross section, which is virtually independent of ion velocity at low (pre-accelerator) energies [13]. As such, the reason for this behavior remains unknown.

The maximum brightness for 10 kV, 12 kV and 14 kV voltages are achieved with $9.2\times 10^{-6}$ mbar, $6.2\times 10^{-6}$ mbar and $6.2\times 10^{-6}$ mbar beam line pressures, respectively. The shrinkage of the beam spot with increasing pressure can be seen with all voltages. With higher voltages the beam size is smaller to begin with, resulting to even smaller beam size with highest pressures. Fig. 5 shows an example measured with 14 kV.

### 4.3. Experiments with different feeding gas species

As a next step, helium, nitrogen and argon were injected into the beam line separately. Hydrogen and krypton were also tried but due to the gas mixing effects they do not work well as a buffer gas for argon. Because of this the resulting beam currents are not comparable with other gases. Also, these gases are never used as buffer gases in practice. For these reasons the results for hydrogen and krypton are not presented. However, it can be mentioned that the observed tendencies were similar to the ones obtained with nitrogen, argon and helium. In the case of argon no additional buffer gas was needed as argon was already injected into the ion source to produce the desired ion beam. All measurements were performed with 10 kV extraction voltage and $Ar^{8+}$ ion beam.

The beam current, emittance and brightness for different gases and pressures are presented in Fig. 6. Argon yields less beam losses (27% decrease in the beam current with the highest beam line pressure) than the lighter nitrogen (52% decrease), which is in good agreement with the results obtained with high intensity proton beams [6]. With helium the losses are even smaller. With the highest beam line pressure the beam current is only 3% lower than the intensity without any gas feeding. The charge exchange cross section decreases with increasing ionization potential [14,15]. The ionization potentials of nitrogen, argon and helium are about 15.58 eV, 15.76 eV and 24.59 eV, respectively [16]. As can be seen, the measured beam losses correlate well with the ionization potentials of the injected gases. With the heavier gases ($N_2$, Ar) the drop of the emittance is steeper as the beam line pressure increases. This is understandable because the ionization cross section in ion–atom collisions increases with the target atom element number [17] and thus less gas is needed to produce the same amount of compensating electrons than with lighter gas species like helium. This result is also in good agreement with the proton beam experiments [6].

The beam line pressures for maximum brightness are $2.0\times 10^{-5}$ mbar for helium, $4.6\times 10^{-6}$ mbar for nitrogen and

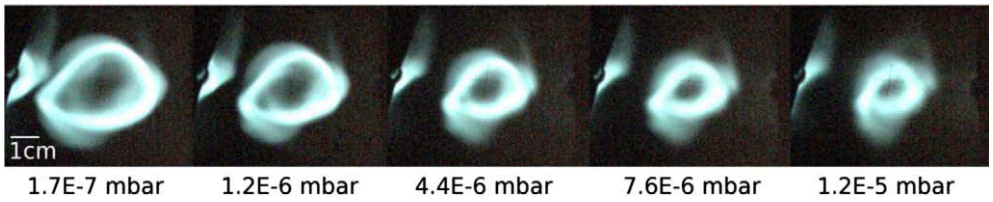


**Fig. 5.** The beam viewer image of $Ar^{8+}$ with 14 kV extraction voltage. Nitrogen was used as feeding and buffer gas. Part of the $N^{3+}$ beam can be seen at the left edge of the viewer plate.

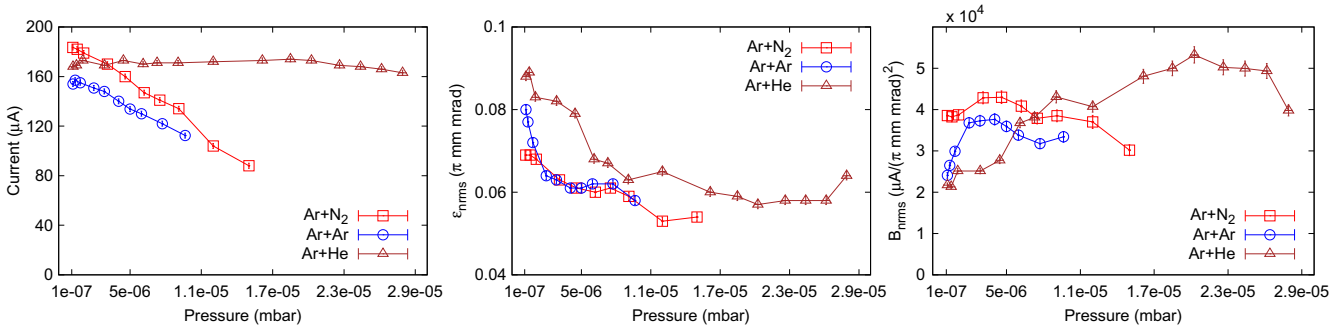


**Fig. 6.** The current, emittance and brightness values of $Ar^{8+}$ as a function of beam line pressure with different gas species injected into the beam line.


**Fig. 7.** The beam viewer image of $Ar^{8+}$ with helium as feeding gas with various beam line pressures.

$4.0 \times 10^{-6}$ mbar for argon. The shrinkage of the beam size could be seen with all gases. As an example the beam viewer images with helium as the feeding gas are presented in Fig. 7.

With nitrogen the increase in brightness is smaller than in the previous measurements. This is caused by different tuning of the beam line solenoids upstream from the analyzing magnet, leading to lower emittance values. However, the behavior of the emittance and current with increasing beam line pressure is still the same. This highlights the fact that the gas feeding effects are independent of the beam optics i.e. solenoid settings.

### 4.4. Complementary experiments

Injecting neutral gas into the beam line resulted to small variation of the ion source operating pressure even when the buffer gas feed rate was tuned for optimum beam current. To rule out the possibility that the presented results are due to changing plasma conditions in the ion source, the experiment was repeated keeping the ion source pressure constant instead of optimizing the beam current with buffer gas feed rate separately for each beam line pressure. In Fig. 8 the beam current, emittance and brightness values are presented in the cases of optimized current and constant ion source pressure. Nitrogen was used as a feeding and buffer gas and the ion source extraction voltage was 10 kV. The behavior of current, emittance and brightness is very similar in both cases. The shrinkage of the beam size was also identical in both cases.

To rule out the effects of ion source pressure even further, the behavior of the ion beam was studied with the beam viewer while only the pressure inside the ion source was varied. No gas was fed into the beam line during this measurement. Small changes could be seen in the shape of the beam but not the same kind of shrinkage that was achieved with gas feeding.

To show that the effects of gas feeding are truly independent of the ion source settings, the beam current and emittance were measured for various beam line pressures without optimizing the ion source performance. This resulted to a much lower $Ar^{8+}$ beam current of 73 μA compared to the beam currents around 190 μA in earlier measurements. The results for beam current, emittance and brightness are presented in Fig. 9. The values have been normalized to make the comparison easier. In the beam current plot the value 1 corresponds to 183.5 μA for optimized case and 73 μA for unoptimized case. For emittance and brightness the values are 0.069 π mm mrad and 38542 $\mu A/(\pi \text{ mm mrad})^2$ for optimized case and 0.114 π mm mrad and 5617 $\mu A/(\pi \text{ mm mrad})^2$ for unoptimized case. Without optimization the beam emittance is much higher, resulting to lower brightness. This shows that lowering the beam current does not necessarily lead to lower emittance by itself. However, when gas is fed into the beam line, the behavior of the emittance and brightness is very similar compared to the good ion source tuning. These results confirm that the effects observed with the gas feeding do not originate in the ion source but are due to phenomena in the beam line.

In order to verify that the observed effects are due to the compensation of space charge, the location of the gas feeding was changed to the port downstream from the analyzing magnet (port 2). Nitrogen was injected into the beam line and used as a buffer

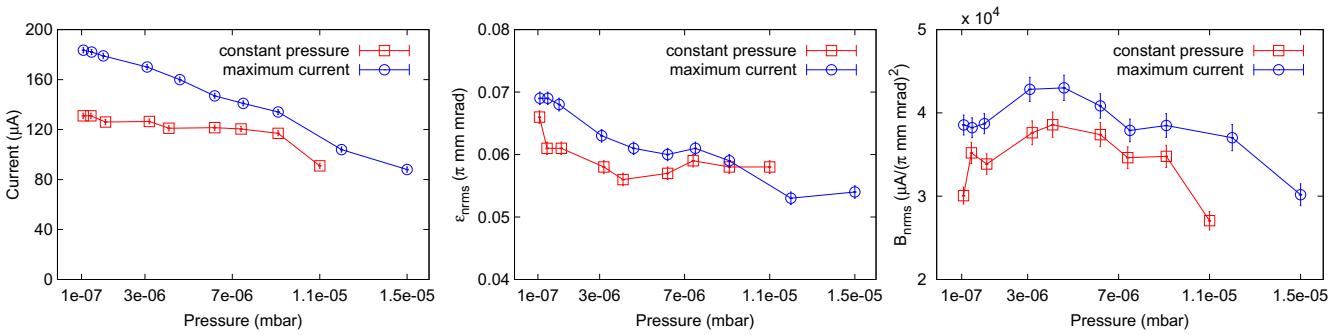


**Fig. 8.** The current, emittance and brightness values of $Ar^{8+}$ with various beam line pressures with two different ion source gas tunings: maximum beam current and constant ion source pressure.

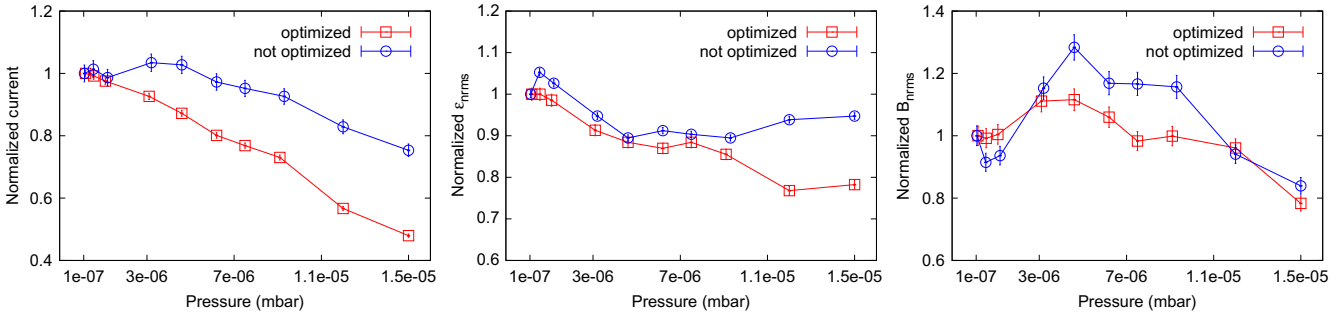


**Fig. 9.** The normalized current, emittance and brightness values of $Ar^{8+}$ with various beam line pressures for optimized and unoptimized ion source performance.

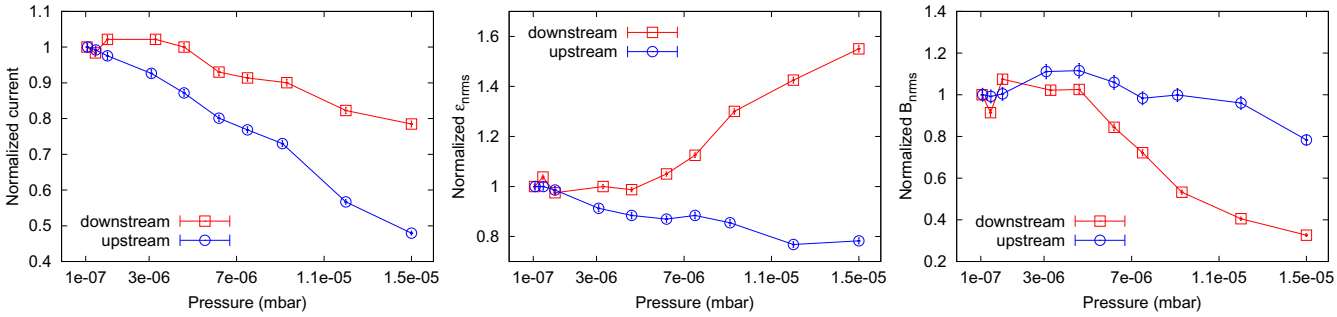


**Fig. 10.** The normalized beam current, emittance and brightness values of $Ar^{8+}$ with various pressures when nitrogen gas is fed either upstream or downstream from the analyzing magnet.

gas in the ion source. The ion source extraction voltage was 10 kV. Normalized beam current, emittance and brightness results for both feeding locations are presented in Fig. 10. In the beam current plot the value 1 corresponds to 183.5 μA upstream from the dipole and 186 μA downstream from the dipole. For emittance and brightness the values are 0.069 π mm mrad and 38542 μA/(π mm mrad)$^2$ upstream from the dipole and 0.080 π mm mrad and 29063 μA/(π mm mrad)$^2$ downstream from the dipole.

When the gas is fed downstream from the analyzing magnet the emittance starts to increase. As a result the brightness starts to decrease almost immediately with increasing beam line pressure. The beam spot remained virtually unaffected with all measured pressures.

Downstream from the analyzing magnet the beam current is much lower as only one $m/q$ value is separated from the total beam produced by the ion source. Consequently, the beam potential is also lower and the effects of gas feeding should be weaker. The results are in very good agreement with this. Therefore, it can be claimed that the observed effects are caused by space charge compensation.

A plasma potential measurement device was used to study the effects of gas feeding on the longitudinal energy spread of the ion beam. The device was installed in the beam line downstream from the analyzing magnet as shown in Fig. 1. A retarding voltage was applied to a mesh inside the device and the ion beam current was measured behind it. The plasma potential and longitudinal energy spread were determined from the voltage needed to stop the ion beam and the behavior of the beam current as a function of the retarding voltage. The structure and the working principle of the device and measurement procedure are explained in detail in Ref. [11]. The measurements were performed without gas feeding into the beam line ($2.2 \times 10^{-7}$ mbar beam line pressure) and with $6.2 \times 10^{-6}$ mbar beam line pressure (maximum brightness). Nitrogen was used as a feeding and buffer gas for $Ar^{8+}$ ion beam with

**Table 1**
Results of the transmission measurements. $V_{ext}$ is the ion source extraction voltage, $E_{fin}$ is the energy of the accelerated beam, $I_i$ is the beam current in the Faraday cup downstream from the ion source analyzing magnet (in μA) and $I_f$ is the beam current in the first Faraday cup downstream from the cyclotron (in μA). $T = (I_f/I_i) \times 100\%$ is the transmission efficiency through the injection line and the cyclotron. $\uparrow T$ is the increase in transmission, $\downarrow I_i$ is the decrease in beam current $I_i$ and $\Delta I_f$ is the difference in accelerated beam current caused by the gas feeding.

| Setup | No gas feeding | | | Maximum $B_{nrms}$ | | | $\uparrow T$ | $\downarrow I_i$ | $\Delta I_f$ |
|---|---|---|---|---|---|---|---|---|---|
| (Ion/feeding gas/$V_{ext}$/$E_{fin}$) | $I_i$ | $I_f$ | $T$ (%) | $I_i$ | $I_f$ | $T$ (%) | (%) | (%) | (μA) |
| $Ar^{8+}/N_2$/9.66 kV/190 MeV | 192 | 10.8 | 5.6 | 136 | 10.1 | 7.4 | 32.0 | 29.2 | −0.7 |
| $Ar^{8+}/N_2$/11.15 kV/220 MeV | 177 | 5.0 | 2.8 | 167 | 5.0 | 3.0 | 6.0 | 5.7 | ±0 |
| $Ar^{8+}$/He/9.66 kV/190 MeV | 157 | 9.7 | 6.2 | 141 | 10.0 | 7.1 | 14.7 | 10.2 | +0.3 |
| $Ar^{8+}$/Ar/9.66 kV/190 MeV | 136 | 7.4 | 5.4 | 134 | 8.4 | 6.3 | 15.3 | 1.5 | +1.0 |
| $Ar^{9+}$/Ar/9.75 kV/216 MeV | 121 | 7.3 | 6.0 | 107 | 6.7 | 6.3 | 3.8 | 11.6 | −0.6 |
| $Ar^{9+}$/Ar/12.14 kV/269 MeV | 124 | 8.1 | 6.5 | 102 | 7.9 | 7.8 | 18.7 | 17.7 | −0.2 |

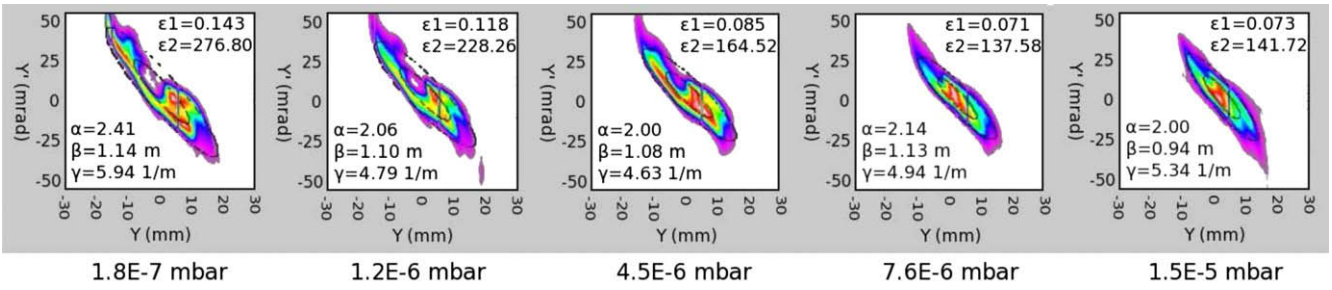


**Fig. 11.** Emittance phase space plots with various beam line pressures for $Ar^{8+}$ ion beam accelerated with 10 kV. Nitrogen as a feeding gas. $\epsilon 1$ and $\epsilon 2$ are the normalized 1-rms emittance and (not normalized) 4-rms emittance, respectively. $\alpha$, $\beta$ and $\gamma$ are the Twiss parameters defining the elliptic fit of the emittance.

10 kV extraction voltage. The measurements showed no change in the ion source plasma potential nor in the longitudinal energy spread of the beam.

### 4.5. Transmission experiments

In the transmission measurements the ion beams were transported through the injection line and the JYFL K-130 cyclotron [18]. The injection line elements and the cyclotron were optimized to achieve maximum beam currents in the first Faraday cup downstream from the accelerator. The optimization was done first without gas feeding into the beam line and subsequently with the beam line pressure yielding the maximum beam brightness in the injection line. The extraction voltages were chosen to match accelerated beam energies that have been used for actual nuclear physics experiments. Table 1 summarizes the results.

Gas feeding increases the transmission in all of the measured cases. Unfortunately the decrease in beam current $I_i$ (measured in the Faraday cup downstream from the analyzing magnet) due to the beam losses caused by the gas feeding match closely to the overall increase. As a result, the amount of beam current after the cyclotron is not significantly altered, as can be seen in the last column of Table 1.

### 4.6. The effects of gas feeding on the beam emittance – detailed analysis

In all measurements the beam emittance is reduced when gas is fed into the beam line between the ion source and the analyzing magnet. This reduction of emittance is not only due to decreasing beam current. With highest beam line pressures the emittance saturates and even starts to increase again even though the beam current continues to decrease. Also, separate measurements have shown that when only beam current is reduced (by varying the microwave power), the dependency of the emittance on beam current is not as strong as was measured with gas feeding.

Fig. 11 shows the measured emittance phase space plots, emittance values and Twiss parameters (also called Courant–Snyder parameters) for $Ar^{8+}$ ion beam accelerated with 10 kV with various beam line pressures and nitrogen as feeding gas. When the pressure in the beam line increases, the aberrations become smaller and the shape of the plot becomes more elliptical. The Twiss parameters define the elliptic fit for the beam emittance in phase space. Using them it is possible to estimate the beam size and angular spread at the emittance scanner. The beam radius is defined with Twiss parameters as $r = \sqrt{\beta\epsilon}$ and the maximum angular spread as $y'_{max} = \sqrt{\gamma\epsilon}$ [4]. Using the values given in Fig. 11 it can be seen that the beam size, i.e. maximum $r$, decreases with increasing beam line pressure. This is also seen with beam viewer downstream from the analyzing magnet. Also the angular spread decreases but starts to increase again with the highest beam line pressure. The reduction of aberrations and the decrease of transverse beam size and angular spread are indications of improved beam quality.

The reduction of aberrations is most likely caused by the shrinkage of the beam, which in turn is the result of enhanced space charge compensation. When the distance from optical axis increases, second and higher order effects are introduced into the magnetic fields of solenoids and dipoles. When an ion beam with large radius passes through the elements these effects cause aberrations and consequently emittance growth. At higher beam line pressures the beam continues to get smaller but the beam emittance saturates to a certain value or reaches a minimum and starts to increase again. The saturation is most likely achieved when the beam is small enough to avoid all aberrations caused by the beam line elements. Another possibility is that the ion beam becomes fully compensated. When the beam line pressure is further increased, the interactions between ions and neutral atoms increase, causing emittance growth. The increase of angular spread at the highest pressures fits well with this interpretation.

The JYFL K-130 cyclotron has an acceptance of roughly 100 $\pi$ mm mrad, expressed as an area emittance value for

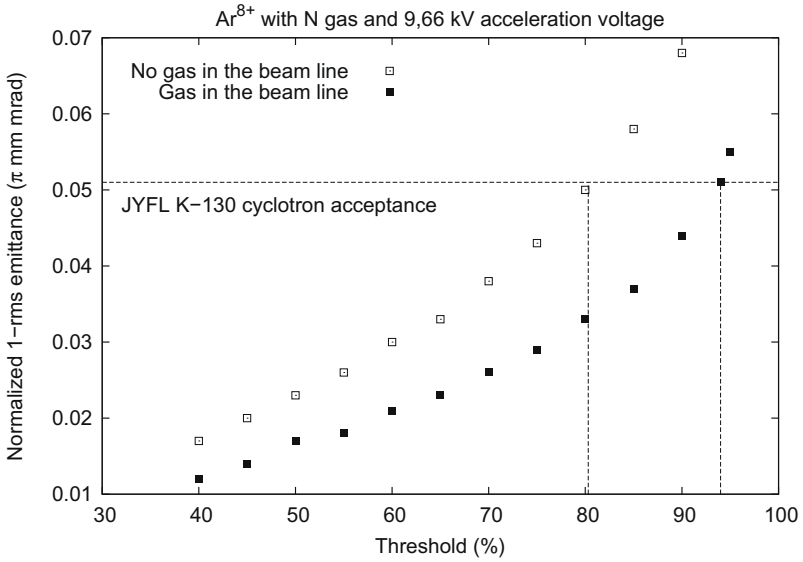


**Fig. 12.** Emittance threshold analysis for the transmission measurement with $Ar^{8+}$ ion beam accelerated with 9.66 kV and nitrogen as feeding gas.

convenience. For $Ar^{8+}$ ion beam accelerated with 9.66 kV this equals to 0.051 $\pi$ mm mrad in normalized 1-rms emittance. The portion of the beam outside this emittance value cannot be injected into the cyclotron. In order to study how much of the beam is inside given acceptance value, the threshold percentage of the emittance analysis was varied. When the threshold percentage is lowered, part of the beam is left out from the emittance calculation, starting from the pairs of $(y, y\prime)$ with the lowest intensity. As a result, threshold value of 90% takes only 90% of the beam into account when the emittance value is calculated. Determining the amount of beam inside given acceptance value is then possible by lowering the threshold until the calculated beam emittance fits inside the acceptance limit. As an example the analysis for the first transmission measurement with $Ar^{8+}$ ion beam, nitrogen feeding gas and 9.66 kV extraction voltage is presented in Fig. 12. The threshold analysis was first carried out for emittance measurement without gas feeding into the beam line and then with the pressure yielding the optimum brightness. Without gas feeding the amount of beam inside the cyclotron acceptance is about 80%. When gas is fed into the beam line this value is increased to 94%.

## 5. Discussion

It has been shown that feeding neutral gas into the high beam current section of the beam line upstream from mass separation has significant effects on the ion beam size and emittance. The reduction of the beam size with increasing beam line pressure is an indication of enhanced space charge compensation. This shows that the ion beams produced with the JYFL 14 GHz ECR ion source are not fully compensated at the nominal beam line operation pressures. This result is in good agreement with the work done at LBNL [9].

The enhancement of space charge compensation is achieved by increased production of electrons by the ionization of the injected gas. In addition to ionization, some amount of electrons are also produced from the beam pipe walls when they are hit by ions. Especially when high charge states are focused through the beam line before mass separation the insufficient focusing for low $q/m$ ions leads to a situation where part of these ions hit the beam pipe walls. The resulting outgassing is seen regularly in the operation of JYFL 14 GHz ECRIS, as the neutral gas pressure in the beam line before the analyzing magnet increases slightly when the ion beam is switched on. The simulations of the behavior of different charge states in the beam line agree with these results. However, the role of these electrons in the space charge compensation is not yet specified.

The enhancement of the space charge compensation leads to improved ion beam quality, characterized by the increase in beam brightness. It was revealed that the maximum of beam brightness is not achieved at the nominal beam line operation pressures of low $10^{-7}$ mbar (or even $10^{-8}$ mbar) region but rather in the region of $10^{-6}$ mbar. This was seen with all measured ion beam charge states, ion source extraction voltages and feeding gas species.

The improvement on beam brightness leads to higher transmission efficiency through the JYFL K-130 cyclotron and its injection line. However, because of the increased beam losses this method does not offer significant increase in the current of accelerated beam in the case of JYFL K-130 cyclotron. The increasing charge exchange cross section with neutral atoms and consequent increase of beam losses is also a limitation for highly charged ion beams.

If the beam losses could be reduced, the enhancement of the space charge compensation can be a powerful tool to improve the beam quality of highly charged ions on a practical level in accelerator facilities. Further studies are planned to achieve this by introducing compensating electrons into the beam line using other methods than gas feeding. These include, for example, the use of heated filament.

## Acknowledgments

This work has been supported by the Academy of Finland under the Finnish Centre of Excellence Programme 2006–2011 (Nuclear and Accelerator Based Physics Programme at JYFL). VT acknowledges Nyyssönen and Ehrnrooth foundations and OT and HK Väisälä foundation for financial support.

## References

[1] H. Koivisto, P. Heikkinen, V. Hänninen, A. Lassila, H. Leinonen, V. Nieminen, J. Pakarinen, K. Ranttila, J. Ärje, E. Liukkonen, Nucl. Instrum. Meth. Phys. Res. B 174 (2001) 379–384.
[2] H. Koivisto, P. Suominen, T. Ropponen, J. Ropponen, T. Koponen, M. Savonen, V. Toivanen, X. Wu, G. Machicoane, J. Stetson, P. Zavodsky, M. Doleans, P. Spädtke, R. Vondrasek, O. Tarvainen, Rev. Sci. Instrum. 79 (2008) 02A303.
[3] H. Koivisto, T. Ropponen, V. Toivanen, M. Savonen, Ion beam research and development work at JYFL, in: Proceedings of the 18th International Workshop on ECR Ion Sources (ECRIS08), Chicago, USA, 2008.

[4] A.J.T. Holmes, Beam transport, in: I.G. Brown (Ed.), The Physics and Technology of Ion Sources, John Wiley and Sons, New York, 1989, pp. 53–106.
[5] M.G. Mazarakis, R.J. Burke, E.P. Colton, S. Fenster, J.S. Moenich, D.K. Nikfarjam, D.W. Price, N.Q. Sesol, J.M. Watson, IEEE Trans. Nucl. Sci. NS-26 (1979) 3042–3044.
[6] R. Gobin, P.-Y. Beauvais, R. Ferdinand, P.-A. Leroy, L. Celona, G. Ciavola, S. Gammino, Rev. Sci. Instrum. 70 (1999) 2652–2654.
[7] P.-Y. Beauvais, R. Ferdinand, R. Gobi, J.M. Lagniel, P.-A. Leroy, L. Celona, G. Ciavola, S. Gammino, B. Pottin, J. Sherman, Rev. Sci. Instrum. 71 (2000) 1413–1416.
[8] P. Spädtke, Beam formation, in: D. Brandt (Ed.), Proceedings of the CERN Accelerator School, Small Accelerators, CERN-2006-012.
[9] D.S. Todd, private communication, 2009.
[10] A.J.T. Holmes, Phys. Rev. A 19 (1979) 389–407.
[11] O. Tarvainen, P. Suominen, H. Koivisto, Rev. Sci. Instrum. 75 (2004) 3138.
[12] D. Wutte, M.A. Leitner, C.M. Lyneis, Phys. Scr. T92 (2001) 247–249.
[13] H. Knudsen, H.K. Haugen, P. Hvelplund, Phys. Rev. A 23 (1981) 597–610.
[14] A. Müller, E. Salzborn, Phys. Lett. A 62 (1977) 391–394.
[15] T. Kusakabe, T. Horiuchi, N. Nagai, H. Hanaki, I. Konomi, M. Sakisaka, J. Phys. B 19 (1986) 2165–2174.
[16] D.R. Lide (Ed.), CRC Handbook of Chemistry and Physics, 85th ed., CRC Press, New York, 2004, p. 10-185. pp. 10-189, 10-190.
[17] I.D. Kaganovich, E. Startsev, R.C. Davidson, Evaluation of multielectron ionization cross-section in energetic ion–atom collisions, in: Proceedings of the Particle Accelerator Conference, Chicago, USA, 2001.
[18] E. Liukkonen, New K130 Cyclotron at Jyväskylä, Proceedings of the 13th International Conference on Cyclotrons and their Applications, Vancouver, Canada, 1992.

# APPENDIX A.V

PUBLISHED BY IOP PUBLISHING FOR SISSA MEDIALAB

RECEIVED: *November 13, 2012*
REVISED: *December 19, 2012*
ACCEPTED: *January 21, 2013*
PUBLISHED: *February 27, 2013*

**TECHNICAL REPORT**

# Oscillations of ECR ion source beam current along the beam transport of the JYFL K-130 cyclotron

**V. Toivanen,[1] O. Tarvainen, J. Komppula and H. Koivisto**

*Department of Physics (JYFL), University of Jyväskylä, 40500 Jyväskylä, Finland*

*E-mail:* ville.toivanen@jyu.fi

ABSTRACT: A versatile measurement system has been developed to study the temporal characteristics of ion beams in millisecond time scale. The system is composed of data acquisition hardware and LabVIEW based measurement and analysis program. The measurement system and ion beam current oscillation results measured with a 14 GHz AECR-U type ion source at University of Jyväskylä, Department of Physics (JYFL), are presented. It is shown that the ion beams exhibit periodic current fluctuations at frequencies from 100 Hz to 1.5 kHz with amplitudes ranging from 1 to 65 percent of the average beam current. It is argued that these oscillations originate from the ion source plasma since their characteristics depend on the ion source tuning. It is shown that increasing the ion source solenoid magnetic field increases the relative oscillation amplitude. Increasing the ion source extraction voltage has the opposite effect. The beam current oscillations were measured along the low energy beam transport (LEBT) connecting the ion source to the JYFL K-130 cyclotron as well as in the following high energy beamline. It is shown that the beam current oscillations originating from the ion source are preserved during the LEBT but are not observed after the cyclotron. The transmission efficiency from the ion source through the cyclotron was measured with two beams of comparable beam currents but different oscillation frequency and amplitude, corresponding with the two cases typically seen when the ion source is tuned for high charge state production. The transmission of the LEBT remained unaltered but the cyclotron performance was affected by the varying oscillation characteristics.

KEYWORDS: Ion sources (positive ions, negative ions, electron cyclotron resonance (ECR), electron beam (EBIS)); Coherent instabilities; Beam-line instrumentation (beam position and profile monitors; beam-intensity monitors; bunch length monitors)

[1]Corresponding author.



doi:10.1088/1748-0221/8/02/T02005

## Contents



## 1 Introduction

The quality of the ion beams extracted from electron cyclotron resonance ion sources (ECRIS) [1] is traditionally described with the beam current $I$ and transverse emittances $\varepsilon_{xx'}$ and $\varepsilon_{yy'}$, often combined as beam brightness $B = I/\varepsilon_{xx'}\varepsilon_{yy'}$ [2]. More attention has recently been shifting to the temporal stability of the ion beams. The increased interest in the stability of the ion beams arises from the requirements set by current and forthcoming applications for ECR ion sources. Several large scale nuclear physics research facilities currently under construction will be utilizing high power linear accelerators (see e.g. [3, 4]) in which beam current oscillations can cause beam spill at high energy, leading to activation of the accelerator structures. Many accelerator based industrial applications, e.g. material modification and testing, require a certain level of temporal stability to sustain high product quality and testing reliability (see e.g. [5, 6]). Also the increased use and active development of medical applications, such as carbon radiotherapy (see e.g. [7]), set strict limitations to the beam current variations.

The temporal oscillations of ion beams produced with ECR ion sources can be divided into two distinct categories: (1) the long-term trends in the scale from seconds to days, and (2) the short-term fluctuations in the millisecond scale. The long term trends are usually driven by factors such as changing gas balance in the ion source plasma chamber and material heating, i.e. ion source conditioning. These effects are relatively well known and understood, and can usually be taken into account or compensated for in the applications.

The work presented here concentrates on the periodic beam current oscillations in the millisecond scale. Published work on current oscillations of continuous highly charged heavy ion beams in this temporal region is scarce. Previous work includes studies by Tarvainen et al. [8] with



2013 JINST 8 T02005

the JYFL 14 GHz ECRIS [9] and VENUS [10] (18 and 28 GHz) and Taki et al. with the 6.4 GHz VEC-ECR [11], where the beam current oscillation dependencies on microwave power, biased disc and magnetic confinement were studied. These experiments suggest that the oscillations are due to the plasma behavior and/or are related to the electron heating efficiency and plasma confinement. However, these studies only consider the beam behavior right after the ion source mass over charge separation and the consequences of observed oscillations to performance are not studied. The work presented here concentrates on the persistence of the oscillations along the low energy beam transport and through the K-130 cyclotron [12] at JYFL. One of the main motivations has been to determine the consequences of the beam current oscillations to the performance of the beam transport and acceleration. Also understanding of the dependencies of beam current oscillation on ion source parameters is further advanced with systematic studies of varying axial magnetic confinement of plasma and ion source extraction voltage.

The standard beam current monitoring systems used in most accelerator laboratories have relatively low sampling rates and/or rely on averaging features. For example, at JYFL the beam current monitoring samples the LEBT current signals at 60 kHz and averages it over 500 samples. After the cyclotron the sampling rate drops to 1.5–10 kHz and averages over 100 samples. Moreover, the added capacitance of the long coaxial cables used to carry the current signals from the Faraday cups to the measurement panels further degrades the temporal resolution. Consequently, the system can not detect beam current fluctuations at frequencies over $\sim$100 Hz. For this purpose a versatile measurement system with capabilities to measure and analyze the ion beam behavior with sufficient temporal resolution has been developed. The system will act as a platform for new features required by future studies.

The measurement setup used for recording the ion beam temporal behavior and subsequent transformation to frequency domain (to enable quantitative analysis) are described in the following chapter. This is followed by the presentation of the functionality and features of the developed measurement program, which is used for the data acquisition and the transformations between time and frequency domains. The experimental results describing the observed beam current oscillations and their consequences to beam transport through the LEBT and the JYFL K-130 cyclotron are presented and discussed in the last chapters.

## 2 Experimental methods

### 2.1 Measurement setup for the time domain signal acquisition

The ion beams used for the experiments were produced with the AECR-U type JYFL 14 GHz electron cyclotron resonance ion source. The temporal behavior of the ion beams was recorded from five Faraday cups, three located in the beamline between the JYFL 14 GHz ECRIS and the K-130 cyclotron and two after the cyclotron. The measurements were conducted using the setup presented in figure 1 for the first Faraday cup after the ion source. The same setup was used for all the Faraday cups. The switch $S$ is used to select whether the current signal from the Faraday cup is measured with a Keithley picoammeter or connected to the oscillation measurement. The picoammeter is normally used for the ion source tuning. In the oscillation measurement the current flows through a shunt resistor $R = 10\,\mathrm{k}\Omega$ and the voltage difference across the resistor is measured with National



2013 JINST 8 T02005

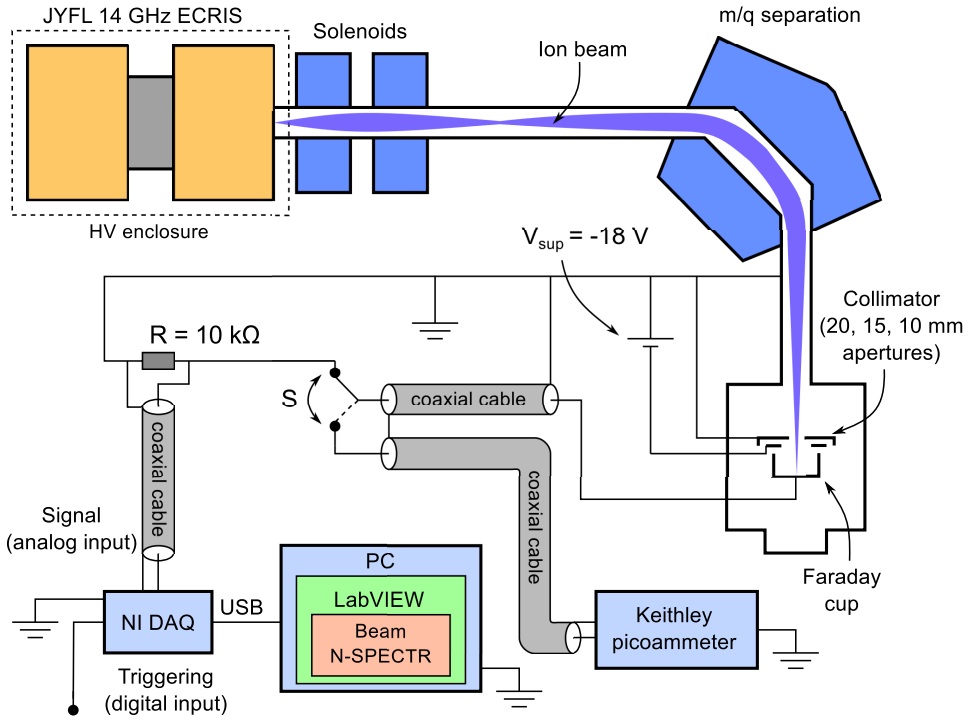


**Figure 1**. Schematic presentation of the measurement setup for the first Faraday cup after the JYFL 14 GHz ECR ion source.

Instruments USB-6255 16-Bit, 1.25 MS/s, M Series Multifunction DAQ. The NI USB-6255 is connected via USB to a PC running a LabVIEW based measurement program, presented in detail in section 2.3.

The Faraday cups and the cables used for the measurements have capacitance $C$ (in parallel). This combined with the shunt resistor $R$ used for the measurement of the current signal creates a current driven parallel RC circuit acting as a low pass filter. The cutoff frequency (3 dB attenuation) of the circuit is

$$f_{\text{cutoff}} = \frac{1}{2\pi RC}. \tag{2.1}$$

The measurements were performed using as short cables as practically possible. The combined capacitance of each Faraday cup and the cables was measured to be up to 2.3 nF. With 10 kΩ shunt resistor this corresponds to a cutoff frequency of about 7 kHz. In the following chapters only beam current oscillations up to this cutoff limit are considered.

The measurements from the Faraday cups after the cyclotron were performed with external triggering due to radiation safety reasons. The measurement setup was assembled next to the Faraday cup, which minimizes the cable length and subsequently the stray capacitance and pickup of electrical noise. The measurement software was prepared and primed before removing the personnel from the area. The measurement was then performed by triggering the software via one of the digital inputs of the NI USB-6255 after allowing the accelerated beam into the high energy beam line.



2013 JINST 8 T02005

### 2.2 Signal transformation from the time domain to the frequency domain

Frequency domain processing is an essential technique when it comes to extracting information from the measured time domain signal and especially for enhancing the detection of its periodic components. When the measured signal is transformed to the frequency domain, it is represented as a sum of periodic (sine and cosine) components, amplitudes of which are presented in a frequency spectrum. In order to enhance the detection of the dominant components, the values in the frequency spectra are often squared, resulting into the frequency power spectrum. In a real measurement scenario a finite number of measured samples represent the complete time domain signal. This windowed segment can be transformed to frequency domain with the Discrete Fourier Transform (DFT) [13].

The frequency resolution in the frequency domain is described as $\Delta f = f_s/N = 1/N\Delta t$, where $f_s = 1/\Delta t$ is the sampling rate, $\Delta t$ the sampling interval and $N$ the number of samples. The DFT only gives frequency information up to half the sampling frequency (Nyquist sampling theorem). As the sampling frequencies $f_s$ used in the presented measurements varied between 40 and 100 kHz, the limit $f_s/2$ was always over the RC cutoff of the measurement system (7 kHz). This enhances the results, as it mitigates aliasing by strongly attenuating the frequencies above $f_s/2$ [13]. In practice the DFT is calculated with Fast Fourier Transform (FFT), which is a collective name for algorithms designed for solving the DFT computationally efficiently.

### 2.3 Measurement software

A new measurement software to monitor, record and analyze the beam current oscillations was developed and used for the studies presented in this paper. Many development platforms currently available include high performance basic routines for signal processing and manipulation, and this approach was considered to be a more flexible alternative to the commercially available systems. As this gives full control over the signal acquisition and manipulation procedures, the implementation of special features and automated measurement routines becomes more transparent and straightforward. This is an important property as the measurement system is planned to act as a platform for additional features required by future studies.

The measurement software was realized with the National Instruments LabVIEW development environment and nick-named *Beam-N-SPECTR* (Novel SPECtral Tool for Research) [14]. The program utilizes the inbuilt high performance FFT algorithms of the LabVIEW to perform the basic signal transformation from time domain to frequency domain. Rest of the data manipulation, including data acquisition, calculations and analysis, both in the time and frequency domains, are built around this feature. The structure of the program is modular to allow future additions and modification.

Figure 2 shows a schematic presentation of the core structure of the program and the data flow between different segments. Multiple run modes exist for online and offline monitoring, data recording and data analysis. The choice of run mode selects which features and routines of the program are used but they all essentially include three main steps: acquisition of time domain data, primary data analysis and postprocessing where some results are combined into more presentable form. During these steps the produced data is stored and displayed to the user. When all steps have



2013 JINST 8 T02005

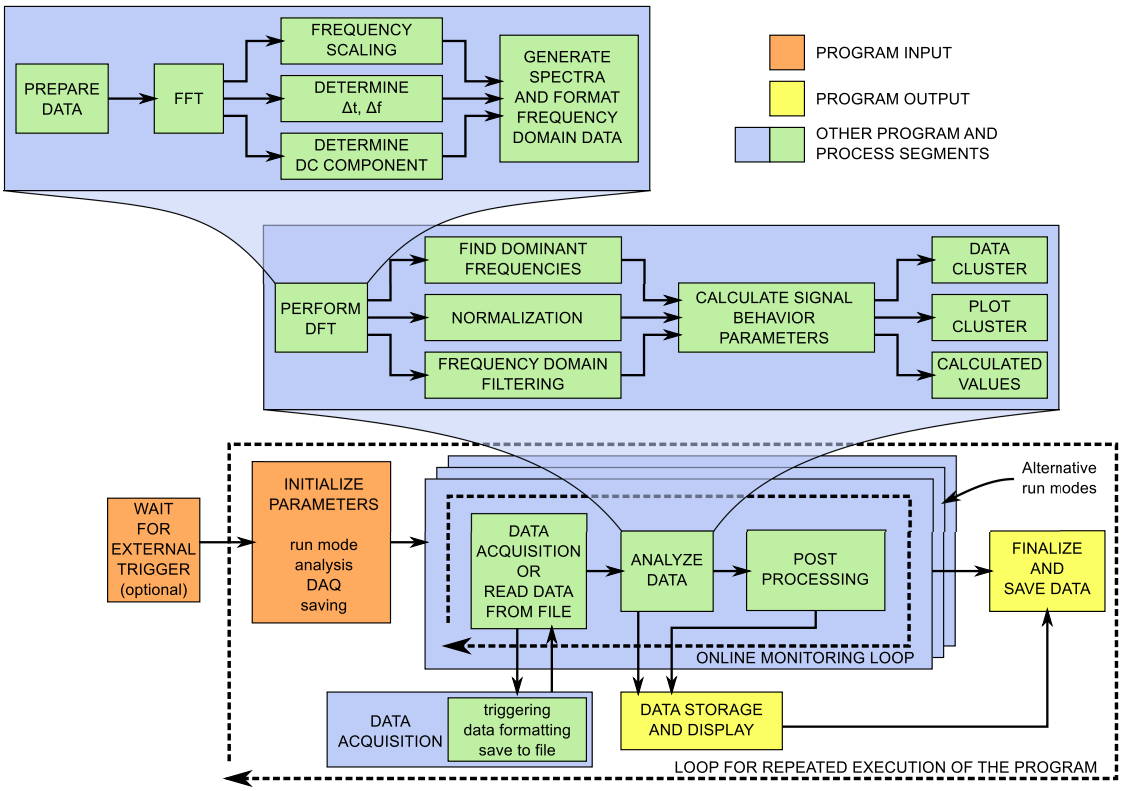


**Figure 2**. The structure of the measurement program *Beam-N-SPECTR* and the data flow.

been completed, the acquired data and analysis results are written into files (depending on the run mode) and the main program terminates.

The functionality of the analysis block can be divided roughly into four steps. First, (1) the transform from time to frequency domain is performed with the DFT block which utilizes the LabVIEW FFT capabilities. Then (2) the frequency domain information is modified to desired form, including finding the dominant frequencies, optional normalization of the frequency amplitudes, optional frequency domain filtering of the data and inverse transform to generate a frequency filtered time domain signal. After this (3) the program calculates signal variation parameters, such as the standard deviation and fluctuation amplitudes to better describe the temporal oscillations of the signal. Finally (4) the produced information is collected and returned to the main program.

The program output includes graphical representations of the measured signal, its frequency spectrum and, if requested, frequency filtered reconstruction of the time domain signal. If the frequency spectrum of the background noise and electrical pickup is known, filtering of these frequencies can be very useful in order to acquire purified signal of interest. The time domain signal fluctuation characteristics (with optional frequency filtering) are calculated and presented. The user can also choose to determine these beam properties averaged over multiple measurements and construct frequency histograms from the measured spectra to better describe the stability of the measured signal (see the next chapter). All measured data, produced graphs and calculated values can be saved into files for later use, either with the same program or with other applications.



2013 JINST 8 T02005

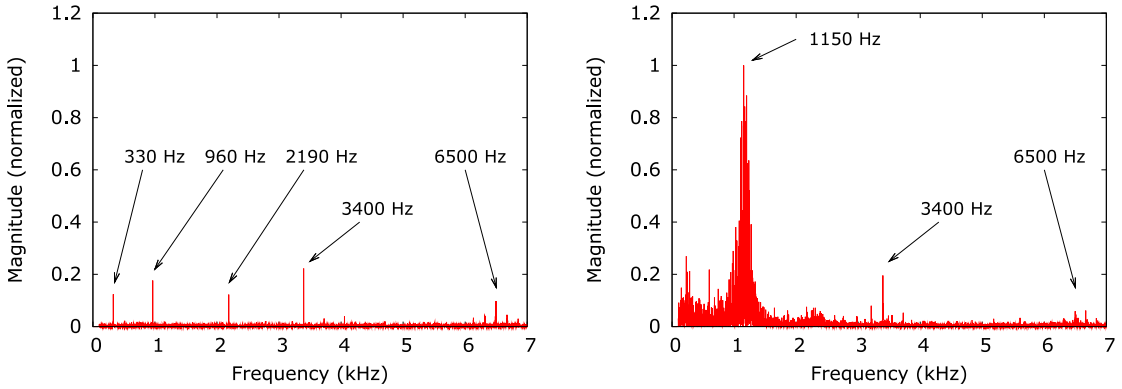


**Figure 3**. Left: typical background frequency spectrum measured from the first Faraday cup after m/q separation (FC2). Right: the frequency spectrum with 110 $\mu$A $^{40}Ar^{8+}$ beam. The spectra are shown up to the RC circuit cutoff of the measurement system (7 kHz).

### 2.4 Signal and spectrum considerations

Figure 3 shows a comparison of typical frequency power spectra measured from the Faraday cup FC2 shown in figure 1 without the ion beam (background) and with 110 $\mu$A $^{40}Ar^{8+}$ beam. The influence of the beam on the spectrum is concentrated to frequencies of $\sim$1 kHz and dominates over the background.

It was verified that the measurement program functions reliably with the signal levels corresponding to the beam currents along the beamline, i.e. in the order of 1–100 $\mu$A. This was done with a $^{40}Ar^{8+}$ beam exhibiting distinct oscillations of a few $\mu$A located around 1.1 kHz (see figure 4). The frequency power spectrum of the beam was measured with varying average beam currents between 1.55 and 111.1 $\mu$A at the Faraday cup after the m/q separation (FC2). To preserve the oscillation characteristics, the beam current was varied by adjusting the beamline optics (dipole current) while the ion source settings were kept constant. As shown in figure 4, the beam current oscillation is clearly visible at all beam current levels (see corresponding background in figure 3). It is thus concluded that the data acquisition setup and the program are suitable for performing measurements at the required signal levels.

It was observed that the beam current oscillation characteristics vary slightly with time, resulting to small jitter in the frequency and amplitude of the spectral peaks. To better characterize the oscillations, each of the studied cases (ion source tunes, etc.) was measured up to 20 times in sequence. The highest peaks from each individual sample were detected from the power spectrum and normalized with respect to the maximum (non-DC) value. This normalization was used as a weighting factor to construct a frequency histogram summing the highest peaks from all the individual measurements. The histogram presentation mitigates the effect of background fluctuations and suppresses momentary interferences causing additional peaks to appear in individual samples. It also characterizes the jitter of the frequency peaks, i.e. the width of the histogram distribution describes the stability of the periodic oscillations. The process to create a histogram from multiple measurement samples is presented in figure 5 showing three measurements. The beam current characteristics, such as the average beam current and the oscillation amplitude, are averaged over the individual measurements.



2013 JINST 8 T02005

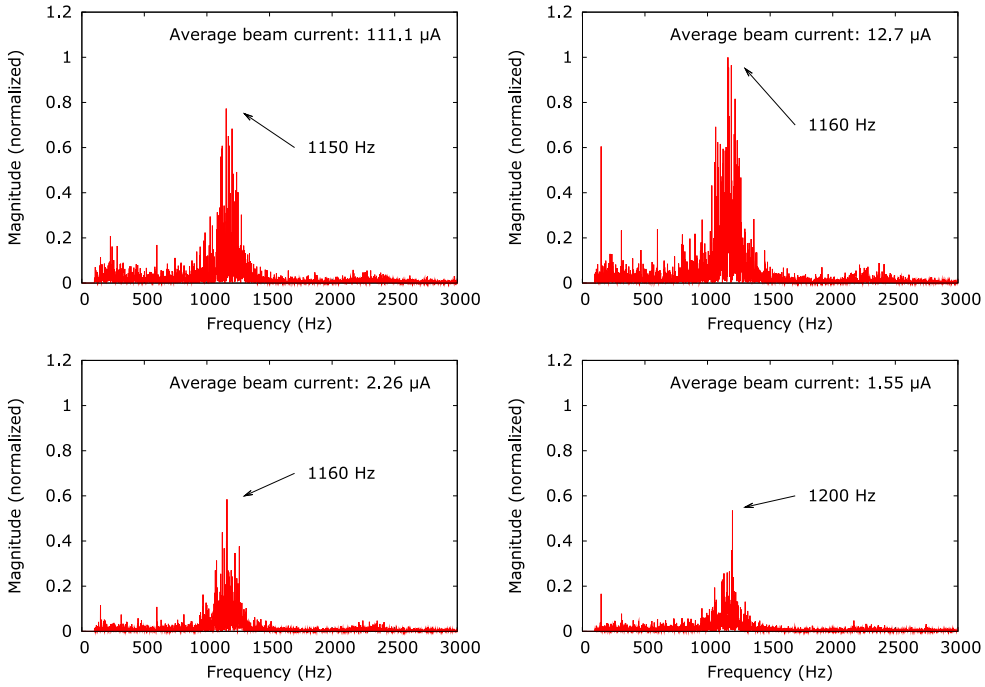


**Figure 4**. Measured frequency spectra with varying beam currents between 1.55 and 111.1 $\mu$A of 80 keV $^{40}Ar^{8+}$. The spectra are normalized to the highest peak (present in the 12.7 $\mu$A case). Measured with 40 kHz sampling rate and 2 s data acquisition time.

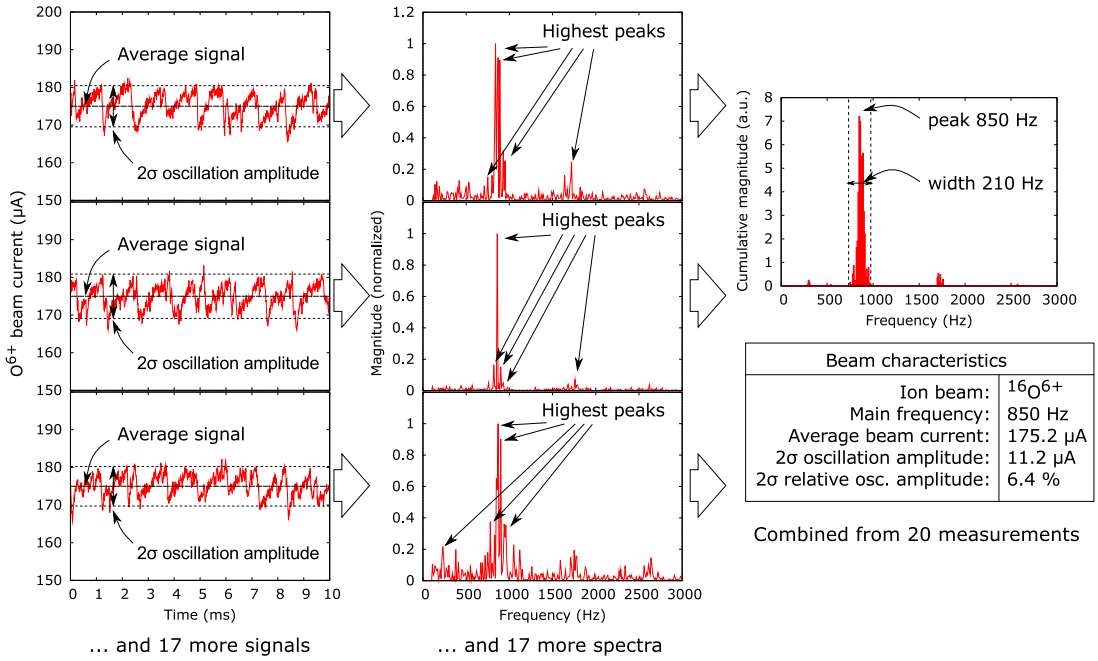


**Figure 5**. The process to create the oscillation frequency histograms. First the time domain signal (beam current) is measured multiple times. The signals are transformed to the frequency domain, normalized and finally combined into a single histogram.

2013 JINST 8 T02005

In order to remove rogue points from the beam variation measurements, the *oscillation amplitude* is defined as $2\sigma$ standard deviation of the time domain signal, rejecting $\sim$5 % of the data points (see figure 5). This is a compromise when effectively mitigating the possibility of a severe overestimation of the oscillation amplitude caused by a few erroneous data points, it can also reduce the real amplitude value if the signal exhibited sharp peaks, which is often the case (see figure 5). The *relative oscillation amplitude* is defined as the percentage of the oscillation amplitude with respect to the average signal.

Frequencies over 7 kHz (RC cutoff) and below 100 Hz were excluded from the analysis. This was done in order to suppress the background signals, e.g. the influence of AC line frequency (50 Hz) and other electrical pickup. As can be seen in figure 3, only few background peaks exist in this frequency range. The influence of the remaining background was studied by filtering away all frequencies around the peaks caused by the beam and reconstructing the current signal. It was found by comparing the reconstructed signals with the original ones that the remaining background accounts for a constant 0.4 $\mu$A increase in the oscillation amplitudes. The effect was found to be negligible for the observed trends.

## 3 Experimental results

The measurements presented in this section were performed using $^{16}O^{6+}$ and $^{40}Ar^{8+}$ ion beams with varying ion source settings. As the aim of these measurements was to study the current oscillations exhibited by the ion beams, the presented ion currents do not represent the maximum performance of the JYFL 14 GHz ECR ion source but they can be considered typical for the K-130 cyclotron operation.

The measurements were carried out using sampling rates between 40 and 100 kHz and the number of collected samples varied to yield total data acquisition times between 0.1 and 2 seconds. As a result the frequency resolution varied between 1 and 10 Hz.

### 3.1 Effects of ion source tuning

The ion source tuning affects the characteristics of the ion beam current oscillations. The effects of microwave power and biased disc voltage on the beam current oscillations of the JYFL 14 GHz ECRIS have already been reported in reference [8].

The sensitivity to the ion source tune is depicted in figure 6. Variation of the ion source settings (in this case the microwave power) alters the beam current oscillation behavior of $^{16}O^{6+}$ beam dramatically. In figure 6(a) the oscillations are concentrated around 800 Hz. The average beam current is 188 $\mu$A with an oscillation amplitude of 8.3 $\mu$A (4.4 % relative oscillation amplitude). In figure 6(b) the oscillations are shifted to lower frequencies around 100–200 Hz. The average beam current of 180 $\mu$A is almost identical to the previous case, but the oscillation amplitude is increased to 84.9 $\mu$A (47.2 %). With conventional beam current monitoring equipment and techniques both beams seem equally stable. These two presented cases are the typical ones often observed during the tuning procedure of the JYFL 14 GHz ECRIS.

The observed beam current oscillations vary strongly when the ion source magnetic field (plasma confinement) is adjusted by altering the coil currents. No clear trends connecting the oscillation frequencies to magnetic field values are observed, but the oscillation amplitude (relative and



2013 JINST 8 T02005

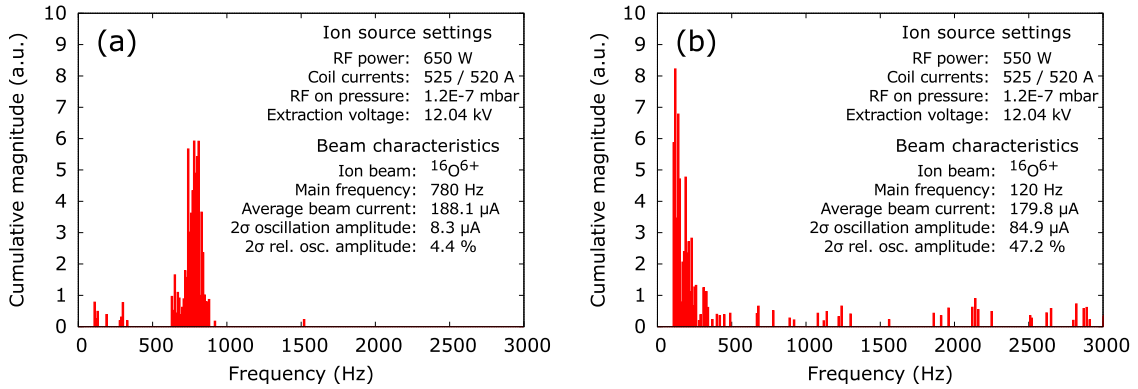


**Figure 6**. Oscillation frequency histograms of $^{16}O^{6+}$ beam with two different ion source tunes. Corresponding ion source settings and beam characteristics are presented in the plot legends. Both histograms are combined from 20 measurements.

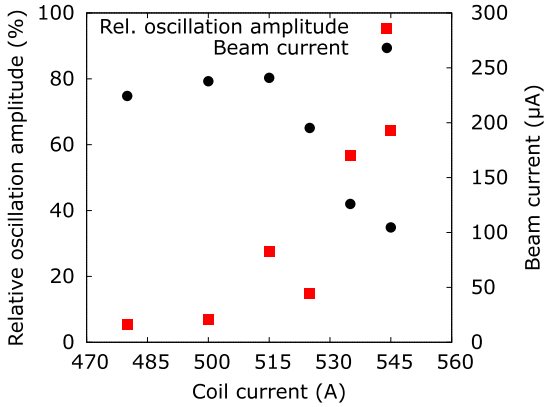


| Ion source settings | |
|---|---|
| RF power: | 600 W |
| RF on pressure: | 1.3E-7 mbar |
| Extraction voltage: | 12.04 kV |

| Coil current (A) | Axial solenoid magnetic field $B_{inj}$ (T) | $B_{min}$ (T) | $B_{ext}$ (T) |
|---|---|---|---|
| 480 / 480 | 1.91 | 0.33 | 0.92 |
| 500 / 500 | 1.95 | 0.35 | 0.95 |
| 515 / 515 | 1.97 | 0.36 | 0.97 |
| 525 / 525 | 1.99 | 0.37 | 0.98 |
| 535 / 535 | 2.01 | 0.38 | 1.01 |

Max radial field, $B_{rad}$ (T) = 1.09 T

**Figure 7**. Relative oscillation amplitude and average beam current of $^{16}O^{6+}$ with varying coil currents (both extraction and injection) and the corresponding axial solenoid magnetic field values.

absolute) increases with increasing coil currents, as shown in figure 7. The average beam current increases first with increasing coil currents, but turns to strong decrease with the highest values.

The effect of the ion source extraction voltage on the beam current oscillations was studied by varying the source potential around the normal operation value of 10 kV, dictated by the injection of the K-130 cyclotron. The measurements were performed with two different ion source tunes for $^{40}Ar^{8+}$ beam and the results are presented in figure 8. It was observed that the relative oscillation amplitude decreases with increasing extraction voltage. This is not exclusively due to the increasing beam current, as the absolute value of the oscillation amplitude also decreases. No clear trends concerning the dominant oscillation frequencies with varying extraction voltage were observed.

The results show that the properties of the measured oscillations exhibit clear dependencies on the ion source settings. This behavior confirms that the observed peaks in the frequency spectrum originate from the ion beam, not from external sources.

2013 JINST 8 T02005

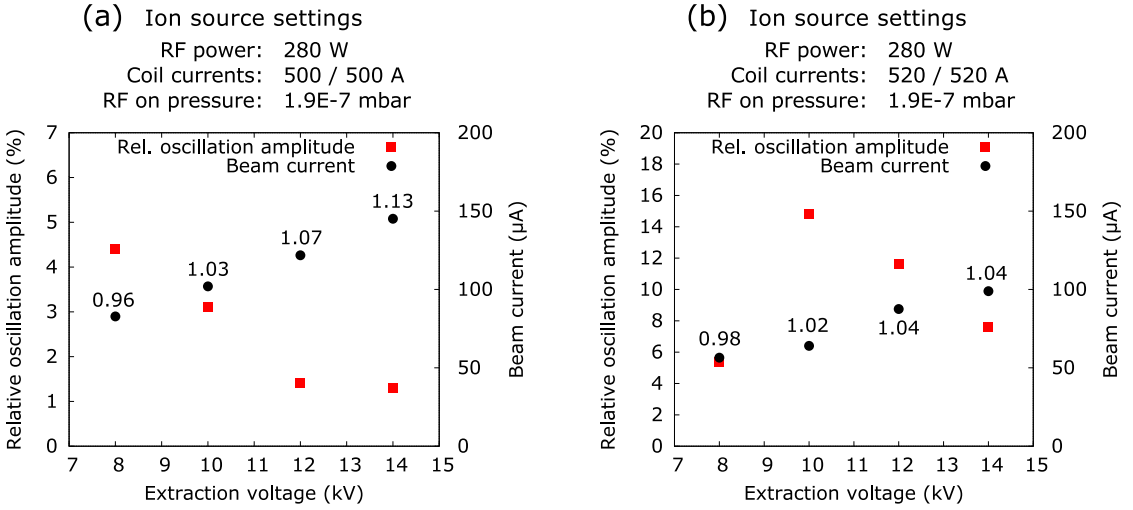


**Figure 8**. Relative oscillation amplitude and beam current of $^{40}Ar^{8+}$ as a function of ion source extraction voltage. Data is shown for two different ion source settings. Total extracted current (in mA) is indicated on top of the beam current data points.

### 3.2 Beam current oscillations along the LEBT and through the cyclotron

The oscillation behavior of $^{16}O^{6+}$ beam was studied along the beam transport. The temporal characteristics of the beam were measured from three Faraday cups between the ion source and the cyclotron and from two Faraday cups after the cyclotron. The beam transport and the location of the Faraday cups are presented in figures 9 and 10. To ensure that the properties of the initial beam remained unchanged, the beam current oscillation characteristics were measured from FC2 between all the other measurements from different Faraday cups.

Figure 11 presents the beam current oscillations measured from Faraday cups FC2, FC4 and FC5 between the ion source m/q separation and the cyclotron (LEBT). The beam is focused into Faraday cups FC2 and FC5 through 20 mm aperture collimators placed right in front of the cups. There is no collimator in front of FC4. Table 1 summarizes the beam properties measured from each Faraday cup. The beam current is lower at FC4 than at FC5 due to the ion optics, making the beam matching to FC4 more difficult.

The results show that the oscillations are preserved along the low energy beam transport all the way to the cyclotron. The variation of the relative oscillation amplitude measured from different Faraday cups is a few percentage points, which is considerably less than what is seen with varying ion source tuning parameters (see figures 7 and 8). With lower beam currents at FC4 and FC5 the magnitude of the peaks in the frequency spectra are naturally decreased in comparison to FC2. It was observed that the magnitude of the ∼800 Hz peak in the frequency spectra is reduced considerably more than the magnitude of the lower frequency peak of ∼150 Hz (also visible in the FC2 measurement, see figure 11). This leads to a situation where the peak magnitudes in these two frequency regions become comparable. When the outer parts of the beam are cut using smaller collimator apertures at the FC2 the oscillation amplitudes decrease with the decreasing average beam currents but the relative oscillation amplitudes tend to remain about constant or increase slightly. Similar behavior is seen at all Faraday cups (see table 1). However, the ratio of peak magnitudes



2013 JINST 8 T02005

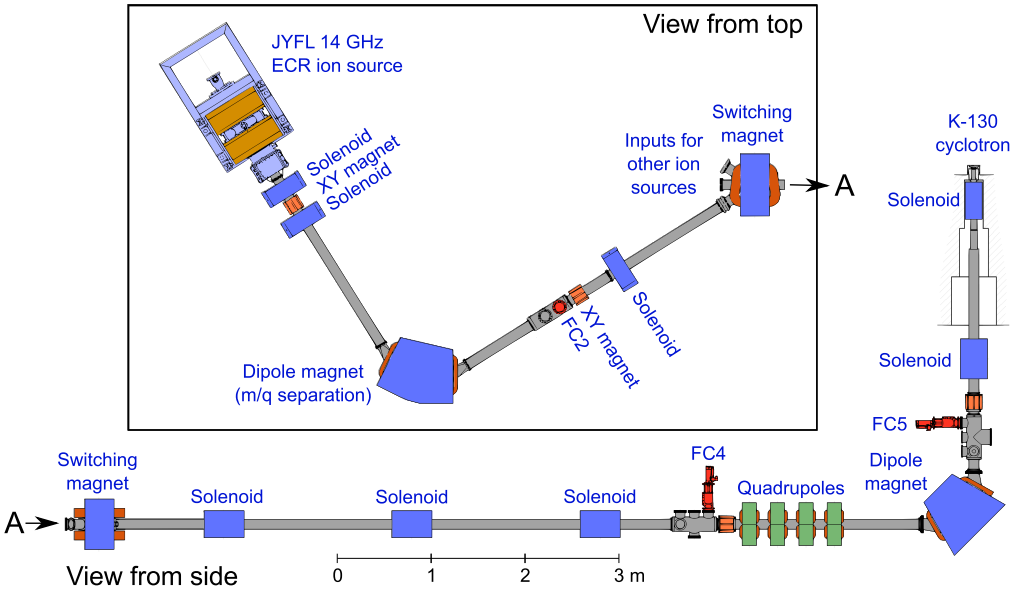


**Figure 9**. Schematic presentation of the beam transport from the 14 GHz ECR ion source through the K-130 cyclotron.

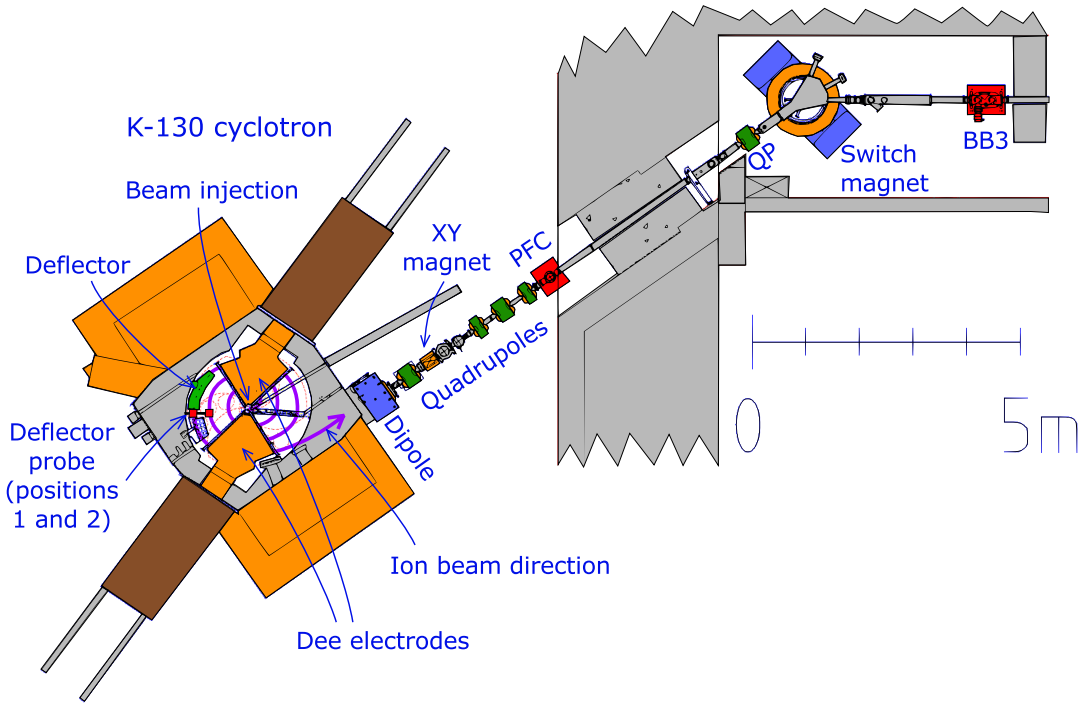


**Figure 10**. Schematic presentation of the beam transport through the K-130 cyclotron to the high energy beamline Faraday cups PFC and BB3. Deflector probe measures the beam current inside the cyclotron before deflector (position 1) and through it (position 2).



2013 JINST 8 T02005

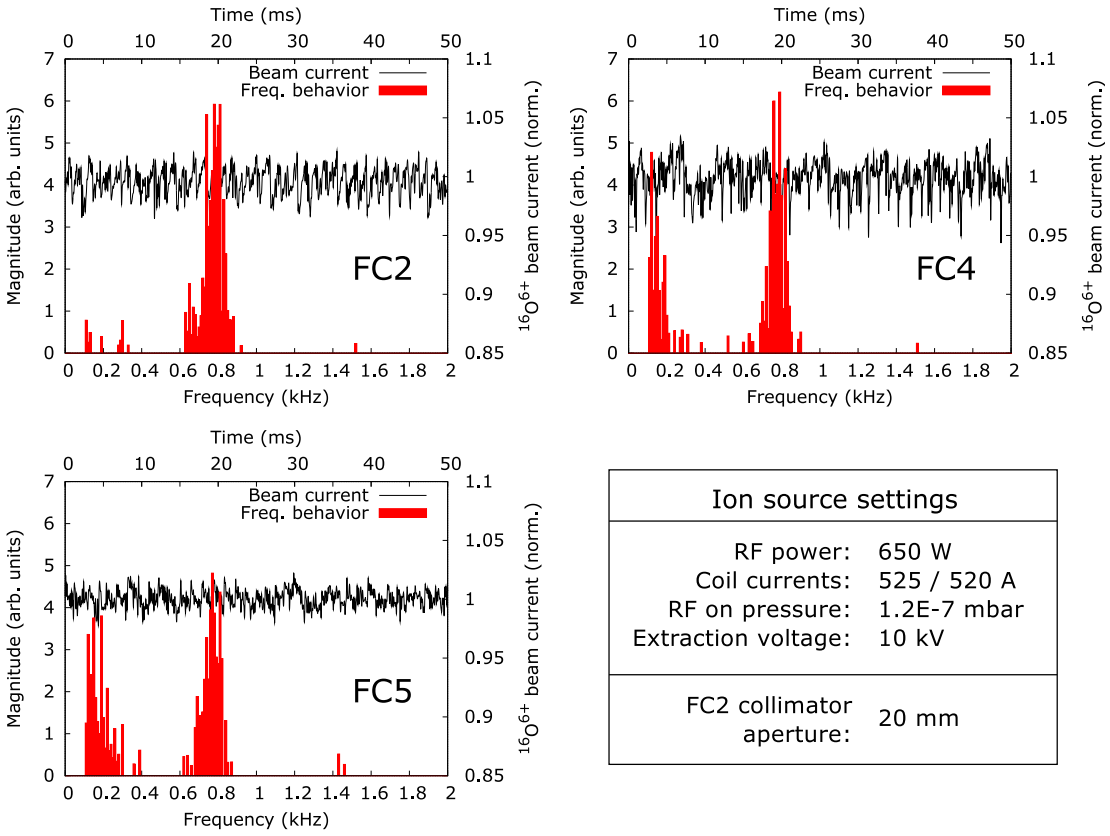


**Figure 11**. Beam currents and current oscillation frequency histograms measured from Faraday cups FC2, FC4 and FC5 between the ion source and the cyclotron. FC2, FC4 and FC5 beam currents normalized to 188.9 $\mu$A, 81.1 $\mu$A and 94.7 $\mu$A, respectively. Each histogram is combined from 20 measurements.

**Table 1**. Average beam currents, oscillation amplitudes and relative oscillation amplitudes of 60 keV $^{16}O^{6+}$ beam measured from the LEBT Faraday cups.

| Faraday cup | FC2 collimator diameter (mm) | Average current ($\mu$A) | Oscillation amplitude ($\mu$A) | Relative oscillation amplitude (% of average) |
|---|---|---|---|---|
| FC2 | 20 | 188.9 | 8.3 | 4.4 |
| | 15 | 146.9 | 6.1 | 4.1 |
| | 10 | 107.8 | 5.2 | 4.8 |
| FC4 | 20 | 81.1 | 4.4 | 5.4 |
| | 15 | 63.4 | 4.3 | 6.8 |
| | 10 | 53.9 | 3.5 | 6.5 |
| FC5 | 20 | 94.7 | 2.7 | 2.9 |
| | 15 | 88.2 | 2.3 | 2.6 |
| | 10 | 78.9 | 3.3 | 4.1 |

2013 JINST 8 T02005

between different frequency regions (∼800 Hz and ∼150 Hz) exhibited no clear tendencies with varying FC2 collimator sizes and remained mainly unaltered.

The beam current behavior was measured after the cyclotron from two Faraday cups, PFC and BB3. The $^{16}O^{6+}$ beam was extracted from the ion source with 12.04 kV extraction voltage and accelerated to 179 MeV energy with the cyclotron. The ion source gas feed was adjusted to achieve identical oscillations at FC2 around ∼800 Hz as presented in figure 11 with 204.1 $\mu$A average beam current and 14.1 $\mu$A (6.9 %) oscillation amplitude. Other ion source settings remained unaltered. The average beam currents at PFC and BB3 were 1.08 and 0.74 $\mu$A, repectively. The background level at PFC, located inside the cyclotron vault, was considerably higher than at the Faraday cups along the LEBT, preventing the observation of possible oscillation peaks originating from the beam. BB3 is located outside the cyclotron vault and the background was again at the same level as with the LEBT Faraday cups. Figure 12 shows the beam current oscillation histogram and examples of original frequency power spectra measured from BB3 with and without the beam. No influence of the beam is observed in the studied frequency range in the frequency histogram or in the frequency spectrum. This is further demonstrated in figure 13, which shows comparison of the 1.55 $\mu$A beam measured from FC2 exhibiting a clear peak at 1.2 kHz (from figure 4) and the 0.74 $\mu$A beam measured from BB3 which is indistinguishable from the background. The correct average beam current is still measured by the program, which verifies that the signal is correctly delivered to the measurement system. The oscillation amplitude of the beam at BB3 is 0.20 $\mu$A (28 %), produced by the background noise distributed in the whole measured frequency range. This was confirmed with the background measurement without the beam, which yielded the same oscillation amplitude value around zero average beam current. To further verify this result, the measurement was repeated with different ion beam and cyclotron settings. Beam of $^{40}Ar^{8+}$ was extracted from the ion source with 9.25 kV extraction voltage and accelerated with the cyclotron using the third harmonic ($\omega_{RF} = 3\omega_c$, where $\omega_{RF}$ and $\omega_c$ are the cyclotron RF frequency and the ion cyclotron frequency), compared to the second harmonic used with the oxygen beam. The average beam current at FC2 was 83 $\mu$A with 3.8 $\mu$A (4.6 %) oscillation amplitude. In the frequency spectrum the beam exhibited clear dominant peak at about 470 Hz with negligible background. The beam was accelerated to the energy of 182 MeV with the cyclotron and the beam current behavior of 0.34 $\mu$A of $^{40}Ar^{8+}$ was measured at BB3. As presented in figure 14, the measurement yielded the same result as with the oxygen beam. No influence of the beam was observed in the frequency spectra.

### 3.3 Consequences of beam current oscillations to transmission efficiency

The influence of the beam current oscillations to the transmission through the LEBT and the K-130 cyclotron was studied with two different ion sources tunes, yielding comparable $^{16}O^{6+}$ beam currents after the ion source m/q separation but with different temporal characteristics presented in figure 15. These cases represent the two typical beam current oscillation characteristics often seen when the ion source is optimized for highly charged ion production. The conventional current measurement system presented both beams as equally stable. The beams were accelerated with the cyclotron to 179 MeV energy.

The first beam (figure 15(a)) exhibits oscillations localized at low frequencies below 300 Hz with highest peak at 140 Hz. The average beam current at FC2 is 175.1 $\mu$A with 24.1 $\mu$A oscillation amplitude (13.8 %). However, the beam current exhibits sharp drops, which are mitigated in the



2013 JINST 8 T02005

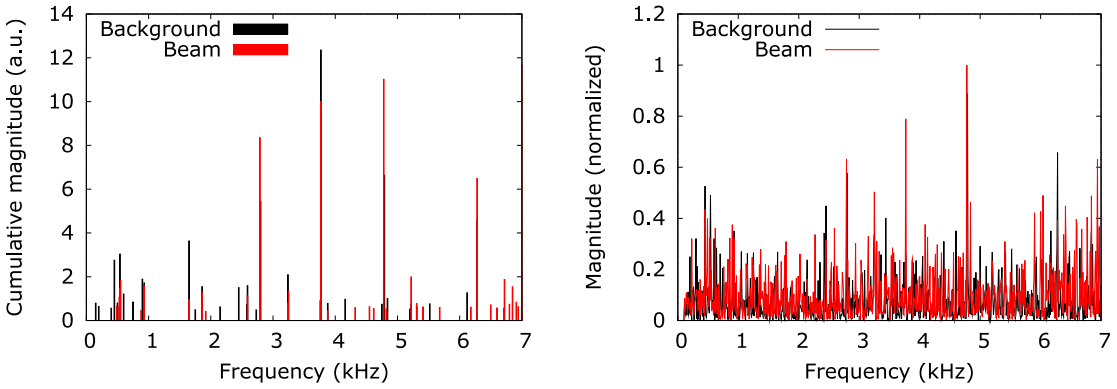


**Figure 12**. Beam current oscillation histograms and example frequency spectra measured from the Faraday cup BB3 after the cyclotron with and without the ion beam (0.74 $\mu$A of 179 MeV $^{16}O^{6+}$). Histograms are combined from 20 measurements. As in PFC, the influence of the beam is not observed in the original spectra nor in the histograms.

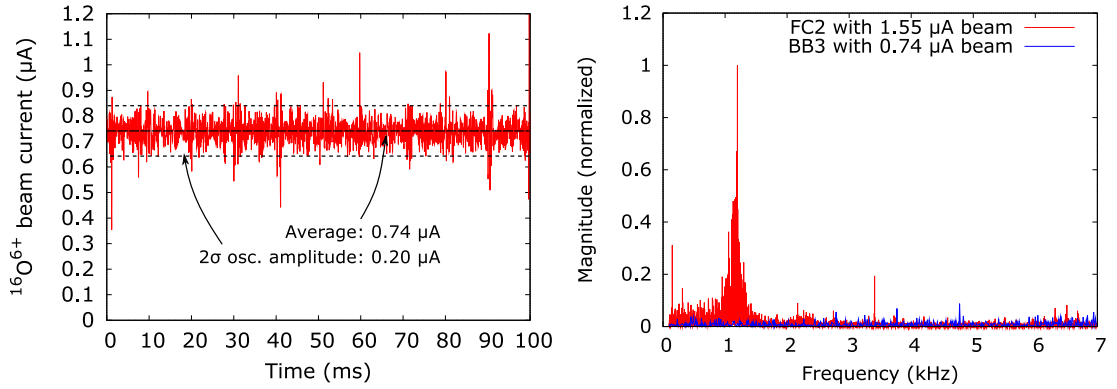


**Figure 13**. 0.74 $\mu$A beam current signal measured from BB3 (left) and the corresponding frequency power spectrum compared to the 1.55 $\mu$A beam measured from FC2 (right). The influence of the beam at BB3 is not observed in the studied frequency range.

statistical $2\sigma$ calculation. The beam current at PFC was measured to be 2.8 $\mu$A, corresponding to a total transmission efficiency of 1.6 % through the LEBT and the cyclotron.

The second beam (figure 15(b)) exhibits oscillations localized at higher frequencies, between 1 and 1.5 kHz with highest peaks at 1.1 and 1.25 kHz. The average beam current is 191.4 $\mu$A with 19.5 $\mu$A oscillation amplitude (10.2 %). The beam current at PFC was measured to be 4.0 $\mu$A, yielding a transmission efficiency of 2.1 %. This gives over 30 % increase in transmission compared to the first case with low frequency oscillations. Total transmission efficiency of $\sim$2 % represents the normal performance of the JYFL K-130 cyclotron with high intensity highly charged heavy ion beams. Thus the difference seen in the absolute transmission efficiency is significant. All ion optical components of LEBT (see figure 9) and the cyclotron parameters were tuned for both cases. The low frequency oscillations case was measured first, and switching the oscillations to higher frequencies yielded practically immediate performance improvement. Further tuning only slightly improved the result.



2013 JINST 8 T02005

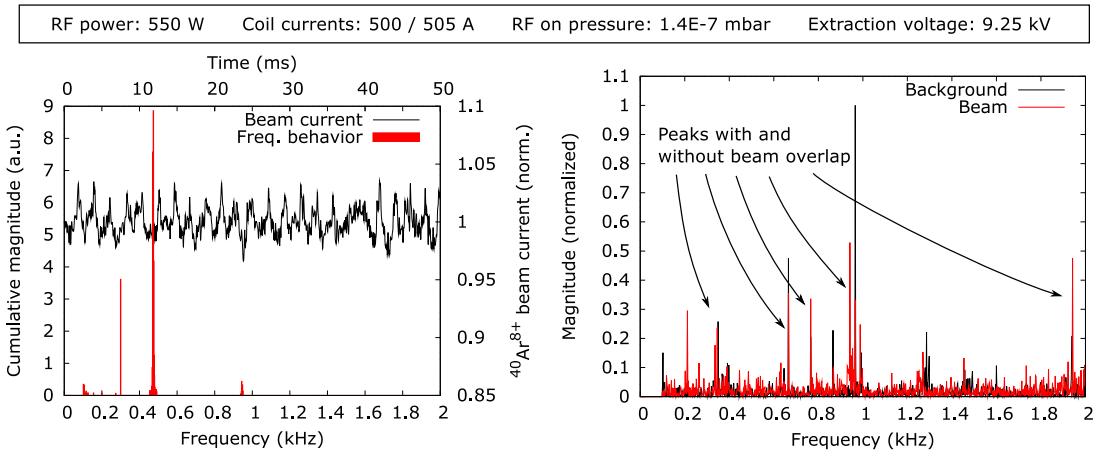


**Figure 14**. Left: 83 $\mu$A average beam of $^{40}Ar^{8+}$ measured from FC2 and the corresponding frequency histogram. Right: frequency power spectrum measured from BB3 with and without 0.34 $\mu$A of $^{40}Ar^{8+}$ beam. As with the oxygen beam, the influence of the beam is not observed at BB3. Ion source settings presented at the top of the figure.

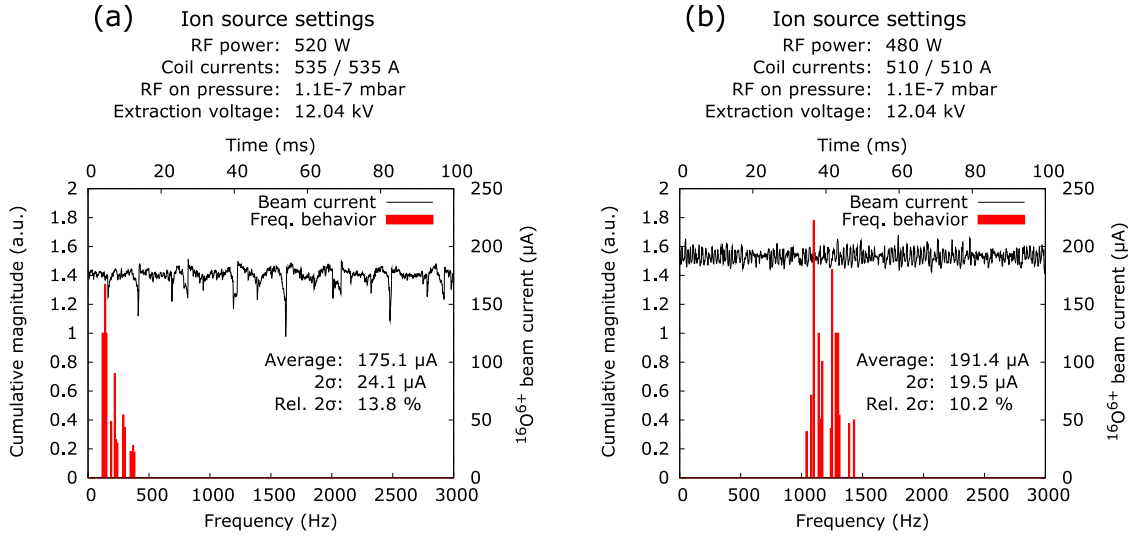


**Figure 15**. $^{16}O^{6+}$ beams used for the transmission studies with low (a) and high (b) frequency beam current oscillations. Both histograms are combined from 3 measurements.

The beam currents through the LEBT and the cyclotron are presented in figure 16. In both measured cases the transmission through the LEBT (from FC2 to the cyclotron inflector) remained virtually the same; for the low frequency case it was 32.4 % and for the high frequency case 31.1 %. Thus the differences in total transmission are due to different transport through the cyclotron. In the case of low frequency oscillations the increase in beam losses becomes evident at the outer radius and extraction of the cyclotron (delflector probe positions 1 and 2) and the high energy beamline (PFC).



2013 JINST 8 T02005

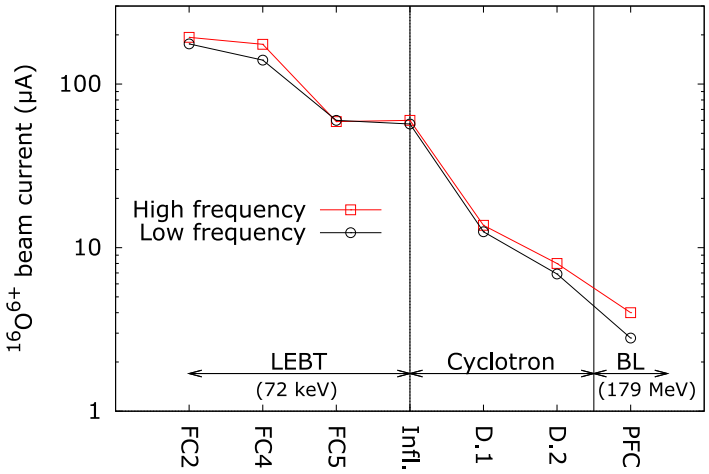


**Figure 16**. The measured beam currents through the low energy beam transport (LEBT) and the cyclotron into the first Faraday cup in the high energy beamline (BL) with two different oscillation modes. FC2–FC5 are the LEBT Faraday cups, Infl. is the cyclotron inflector (injection), D.1 and D.2 are the cyclotron deflector probe positions 1 (last rotation before the deflector) and 2 (beam through the deflector). PFC is the first Faraday cup after the cyclotron.

## 4 Discussion and conclusions

The new measurement system *Beam-N-SPECTR* has proven to be a versatile and reliable tool for studying the temporal characteristics of ion beams, i.e. recording, identifying and analysing periodic oscillations exhibited by the signal. In the presented measurements the ion beam current behavior was studied in the frequency range of $10^2 - 10^3$ Hz. Studies of beam current behavior at higher frequencies can be achieved by replacing the shunt resistor in the measurement setup with a transimpedance amplifier, preferably connected directly to the Faraday cup (as an example, see [15]). Considering most of the applications utilizing highly charged ion beams, the current oscillation amplitude and frequencies are usually the most important factors characterizing the beam temporal behavior. However, improving the time constant of the measurement could be beneficial in determining the shape of the signal variations more accurately, possibly yielding more information on the exact origin of these oscillations.

The presented results indicate that the observed periodic oscillations of the beam current originate from the ion source plasma. This is supported by the fact that the properties of these oscillations, namely the frequencies and the fluctuation amplitudes, are clearly dependent on the ion source settings. It is unlikely that the observed phenomena originate from the beamline ion optics, as the same beam current oscillation behavior has been observed with two different extraction systems of the JYFL 14 GHz ECRIS. The systems have very different ion optical properties (see reference [16]) but exhibit similar beam current oscillation trends. To further rule out the background and beamline effects, it is noted that different ECR ion sources including VENUS at LBNL [8], SuSI at MSU/NSCL [17], NIRS-HEC at HIMAC [18] and VEC-ECR at VECC [11] have been reported to exhibit similar beam current oscillations at $10^2 - 10^3$ Hz range. However, it is also noted that varying space charge compensation, driven by beam current variations, can possibly amplify or mitigate the observed current oscillations, as suggested by the results presented in [19].



2013 JINST 8 T02005

The ion beam current oscillations have strong dependencies on the ion source parameters, which suggests a connection between plasma processes and measured ion beam temporal characteristics. The dependency on microwave power reported by Taki et al. [11] and Tarvainen et al. [8] suggests connection to electron heating. The reported dependency on the magnetic confinement (axial solenoid field) indicates the same, as it also affects the energy transfer from microwaves to electrons by altering the magnetic field gradient at the electron cyclotron resonance (for experimental evidence, see [20], for JYFL 14 GHz ECRIS, see [21]). Stronger axial solenoid field yielded increase in oscillation amplitude, but stronger radial confinement, produced with sextupole magnets, seems to mitigate the beam current oscillations, as reported by Tarvainen et al. [8]. This behavior has important consequences for the beam quality of highly charged ions, production of which require high magnetic confinement. Defining the exact plasma instability processes leading to the observed beam current oscillations is beyond the scope of this paper. However, it is noted that the strong dependencies on magnetic confinement and electron heating suggest kinetic and/or magnetohydrodynamic (MHD) instability processes as possible candidates. Kinetic instabilities arise from the anisotropy and shape of the electron energy distribution function (EEDF) with respect to the external magnetic field (see e.g. [22, 23]). MHD instabilities are connected to the magnetic field topology (see e.g. [24–26]). Depletion of neutral density by efficient ionization and consequent plasma density oscillation through neutral-plasma coupling has also been suggested as a source of periodic plasma instabilities in ECR heated plasmas (see e.g. [27, 28]). Further identification of the plasma processes behind the observed beam current behavior is a subject of future studies with additional diagnostics methods.

The observed dependence on the ion beam extraction voltage, namely the mitigation of the oscillation amplitude with increasing extraction field, can also be connected to plasma effects. For example, periodic variation of plasma properties such as the plasma potential in the region where ions are extracted from the plasma could affect the properties of the formed ion beam. Increase of extraction voltage decreases the energy spread $\Delta E/E$ and could thus suppress the resulting beam oscillations. However, as the two presented cases demonstrate (see figure 8), even with high extraction voltages different ion source tuning can still result in considerable beam current fluctuation. This is also seen with VENUS, which exhibits beam current oscillations of up to 25 % with extraction voltages over 20 kV [8].

The observed ion beam current oscillations occur in a broad range of frequencies and amplitudes. The frequencies vary from 100 Hz up to about 1.5 kHz. At the same time the relative oscillation amplitude, describing the fluctuation of the ion beam compared to the average value, varies from $\sim$1 up to $\sim$65 %. With conventional beam current monitoring systems the difference between such ”oscillation modes” is often undetected. However, as the transmission results indicate, the oscillations can affect the beam acceleration. The performance of the low energy beam transport remained practically unchanged with varying oscillation characteristics but the transmission through the cyclotron was degraded when the ion beam exhibited low frequency, high amplitude oscillations. The connection between the temporal characteristics of the beam and the functionality of the cyclotron is further underlined by the observation that the oscillations clearly present in the LEBT are not detected after the cyclotron. To verify this surprising phenomenon, the study of the beam current behavior after the cyclotron was performed with two different ion beams ($^{16}O^{6+}$ and $^{40}Ar^{8+}$) with different cyclotron settings, both yielding the same results. The cause of this



2013 JINST 8 T02005

phenomenon remains unknown but some possible reasons can be suggested based on the observed trends of the beam current oscillations. As stated above, the oscillations are damped with increasing extraction voltage of the ion source. If this trend is indeed connected to the fluctuating energy spread, $\Delta E/E$, this leads to a periodic variation of the beam properties as it passes through dipole magnets, which can contribute to the observed current oscillations at the LEBT Faraday cups. As the beam passes through the cyclotron, the energy spread is decreased substantially, which can subsequently lead to the absence of those oscillations observed in the LEBT, at the Faraday cups after the cyclotron. Another possibility for this behavior is the collimation of the ion beam in the cyclotron injection, and subsequent acceleration of only a part of the injected ion beam, which could exhibit different behavior in the frequency domain, as discussed below. Bunching of the ion beam before the cyclotron injection is an unlikely source for this phenomenon, as it occurs at much higher frequencies around $10^7$ Hz.

The results obtained with varying the collimator aperture sizes of the Faraday cups along the LEBT suggest that the oscillations are not only localized in the beam halo, but are either uniformly distributed in the beam profile or have some more complex distribution. Thus, future plans concerning the studies of beam current oscillations include further development of the beam instrumentation and diagnostics. The measurement program will be extended to include a feature to perform simultaneous measurements from multiple input channels. Using this in combination with a Faraday cup divided into multiple sectors should offer valuable information on the distribution of oscillation characteristics in the beam profile and could consequently shed more light on the beam oscillation behavior after the cyclotron.

## Acknowledgments

This work has been supported by the EU $7^{\text{th}}$ framework programme "Integrating Activities - Transnational Access", project number: 262010 (ENSAR) and by the Academy of Finland under the Finnish Centre of Excellence Programme 2006 - 2011 (Nuclear and Accelerator Based Physics Research at JYFL).

## References

[1] R. Geller, *Electron Cyclotron Resonance Ion Sources and ECR Plasmas*, Taylor & Francis, New York U.S.A. (1996).

[2] I. Brown, *The Physics and Technology of Ion Sources*, John Wiley & Sons, New York U.S.A. (1989).

[3] X. Wu et al., *The overview of the accelerator system for the facility for rare isotope beams at Michigan State University*, in the proceedings of the *25th Linear Accelerator Conference (LINAC2010)*, Tsukuba Japan, 12–17 September 2010.

[4] S. Gales, *SPIRAL2 at GANIL: Next generation of ISOL facility for intense secondary radioactive ion beams*, *Nucl. Phys.* **A 834** (2010) 717.

[5] A. Denker et al., *Industrial and medical applications of high-energy ions*, *Nucl. Instrum. Meth.* **B 240** (2005) 61.

[6] A. Virtanen et al., *Heavy ion and proton test site at JYFL-accelerator laboratory*, *Nucl. Instrum. Meth.* **A 426** (1999) 68.



2013 JINST 8 T02005

[7] S. Braccini et al., *Accelerators for hadrontherapy: from Lawrence cyclotrons to linacs*, *Nucl. Instrum. Meth.* **A 620** (2010) 563.

[8] O. Tarvainen et al., *An experimental study of ECRIS plasma stability and oscillation of beam current*, in the proceedings of the *20th International Workshop on Electron Cyclotron Resonance Ion Sources (ECRIS2012)*, Sydney Australia, 25–28 September 2012.

[9] H. Koivisto et al., *The first results with the new JYFL 14 GHz ECR ion source*, *Nucl. Instrum. Meth.* **B 174** (2001) 379.

[10] D. Leitner et al., *Status report of the 28 GHz superconducting electron cyclotron resonance ion source VENUS*, *Rev. Sci. Instrum.* **77** (2006) 03A302.

[11] G.S. Taki et al., *Study of the dependence of ECR ion current on periodic plasma disturbance*, in the proceedings of the *18th International Workshop on Electron Cyclotron Resonance Ion Sources (ECRIS2008)*, Chicago U.S.A., 15–18 September 2008.

[12] E. Liukkonen, *New K130 cyclotron at Jyväskylä*, in the proceedings of the *13th International Conference on Cyclotrons and their Applications*, Vancouver Canada, 6–10 July 1992.

[13] D.C. Swanson, *Signal Processing for Intelligent Sensor Systems*, Marcel Dekker, New York U.S.A. (2000).

[14] V. Toivanen, *Beam-N-SPECTR measurement software*, LabVIEW VIs available online at: http://users.jyu.fi/∼vialtoiv/shared/beam-n-spectr/.

[15] W.R. Rawnsley et al., *Bunch shape measurements using fast Faraday cups and an oscilloscope operated by LabVIEW over ethernet*, in the proceedings of the *9th Workshop on Beam Instrumentation (BIW2000)*, Cambridge U.S.A., 8–11 May 2000.

[16] V. Toivanen et al., *New extraction design for the JYFL 14 GHz ECRIS*, in the proceedings of the *20th International Workshop on Electron Cyclotron Resonance Ion Sources (ECRIS2012)*, Sydney Australia, 25–28 September 2012.

[17] G. Machicoane, private communication, October 2012.

[18] A. Kitagawa et al., *Two-frequency Heating Technique for Stable ECR Plasma*, in the proceedings of the *20th International Workshop on Electron Cyclotron Resonance Ion Sources (ECRIS2012)*, Sydney Australia, 25–28 September 2012.

[19] A. Dudnikov, *Simplified beam line with space charge compensation of low energy ion beam*, in the proceedings of the *23th Russian Particle Accelerator Conference (RUPAC2012)*, Saint-Petersburg Russia, 24–28 September 2012.

[20] D. Leitner et al., *Measurement of the high energy component of the x-ray spectra in the VENUS electron cyclotron resonance ion source*, *Rev. Sci. Instrum.* **79** (2008) 033302.

[21] T. Ropponen et al., *The effect of magnetic field strength on the time evolution of high energy bremsstrahlung radiation created by an electron cyclotron resonance ion source*, *Nucl. Instrum. Meth.* **A 600** (2009) 525.

[22] A.G. Shalashov et al., *Maser based on cyclotron resonance in decaying plasma*, *JETP Lett.* **84** (2006) 314.

[23] S.V. Golubev et al., *Cyclotron-resonance maser driven by magnetic compression of rarefield plasma*, *Phys. Rev. Lett.* **99** (2007) 205002.

[24] R.F. Post, *The magnetic mirror approach to fusion*, *Nucl. Fusion* **27** (1987) 1579.

2013 JINST 8 T02005

[25] M.S. Ioffe, R.I. Sobolev, *Confinement of a plasma in a trap formed by a combined magnetic field*, *J. Nucl. Energy* **C 7** (1965) 501.

[26] J. Berkowitz et al., *Cusped geometries*, in the proceedings of the *2nd United Nations International Conference on the Peaceful Uses of Atomic Energy. Vol. 31*, Geneva Switzerland, September 1–13 1958, pg. 171.

[27] E.S. Aydil et al., *Multiple steady states in electron cyclotron resonance plasma reactors*, *J. Vac. Sci. Technol.* **A 11** (1993) 2883.

[28] P.W. Lee et al., *Undriven periodic plasma oscillation in electron cyclotron resonance Ar plasma*, *Appl. Phys. Lett.* **69** (1996) 2024.

2013 JINST 8 T02005

# APPENDIX A.VI

Nuclear Instruments and Methods in Physics Research A 726 (2013) 41–46

Contents lists available at SciVerse ScienceDirect

Nuclear Instruments and Methods in Physics Research A

journal homepage: www.elsevier.com/locate/nima

# The effect of plasma electrode collar structure on the performance of the JYFL 14 GHz electron cyclotron resonance ion source

V. Toivanen *, O. Tarvainen, J. Komppula, H. Koivisto

*University of Jyväskylä, Department of Physics (JYFL), P.O. Box 35, FI-40014, Finland*

ARTICLE INFO

*Article history:*
Received 25 March 2013
Received in revised form
25 April 2013
Accepted 25 May 2013
Available online 1 June 2013

*Keywords:*
Electron cyclotron resonance ion source
ECRIS plasma
Beam extraction
Collar structure

ABSTRACT

The influence of a so-called collar structure on the performance of the JYFL 14 GHz electron cyclotron resonance ion source (ECRIS) has been studied experimentally at the Department of Physics, University of Jyväskylä (JYFL). The collar is a cylindrical structure extruding inwards from the plasma electrode. The collar length was varied between 5 and 60 mm. For some ion species a moderate performance improvement was achieved in terms of extracted beam current and transverse emittance up to 30 mm collar length. Longer collars resulted in a substantial performance decrease. Different collar materials, i.e. nonmagnetic stainless steel, aluminum and $Al_2O_3$, and a wide range of ion species for elements ranging from $^{14}N$ to $^{82}Kr$ were studied. No clear material or ion species dependent behavior was observed. The experiments suggest that the extracted ions originate from a plasma volume which is at a considerable axial distance from the extraction aperture. Furthermore it is concluded that a substantial space exists surrounding the collar that could be utilized for applying novel techniques to boost the performance of ECR ion sources.



## 1. Introduction

Electron cyclotron resonance ion sources (ECRISs) are used for a wide range of applications requiring highly charged heavy ion beams, both in research and industry (see e.g. [1] and the references therein). Numerous techniques have been developed to improve the performance of ECR ion sources. These include the use of a negatively biased disk at the injection end of the plasma chamber [2–4], the gas mixing technique in which lighter gas is introduced into the plasma to boost the production of the high charge states of the heavier element [5,6], the use of two (or multiple) microwave frequencies to produce additional resonance surfaces [7–10], the introduction of metal–dielectric (MD) surfaces with high secondary electron emission coefficients into the plasma chamber [11,12] and, more recently, the fine tuning of the heating microwave frequency [13–17].

In 2009 it was presented by Mironov [18] that using a so-called collar structure around the extraction aperture (see Fig. 1) could yield improved ECR ion source performance by shifting the charge state distribution of ions toward higher values. In addition to offering a possible performance improvement, such a structure at the extraction region of the ion source could be used to probe the dynamics of the extracted ions. Despite the promising initial results, systematic studies of the collar structure have not been published.

This paper presents the results of the collar studies conducted with the JYFL 14 GHz ECR ion source [19]. A detailed description of the collar structure and the experimental setup is given in the next section. This is followed by experimental results and discussion.

## 2. Experimental setup and procedure

The measurements have been performed with the AECR-U type JYFL 14 GHz ECR ion source. In order to enable installing the collar structure, a new plasma electrode with removable center piece was manufactured. The cylindrical collar structure with 10 mm inner and 14 mm outer diameters was implemented into the center piece around the 8 mm extraction aperture (see Fig. 1). Multiple center pieces with varying length and material were manufactured. The baseline measurements were performed with an aluminum center piece with 8 mm extraction aperture, recreating the original plasma electrode structure. The new plasma electrode with a 30 mm collar is presented in Fig. 1.

The length of the collar was varied from 5 to 60 mm. Since the influence of the plasma flux on the long collars was originally unknown, nonmagnetic stainless steel was chosen as the collar material for this study due to its favorable thermal properties, especially the high melting point. The results obtained with stainless steel were later compared to 20 mm collars manufactured from aluminum and aluminum oxide ($Al_2O_3$) in order to

* Corresponding author. Tel.: +358 408054068.
*E-mail address:* ville.toivanen@jyu.fi (V. Toivanen).

0168-9002/$ - see front matter © 2013 Elsevier B.V. All rights reserved.
http://dx.doi.org/10.1016/j.nima.2013.05.153

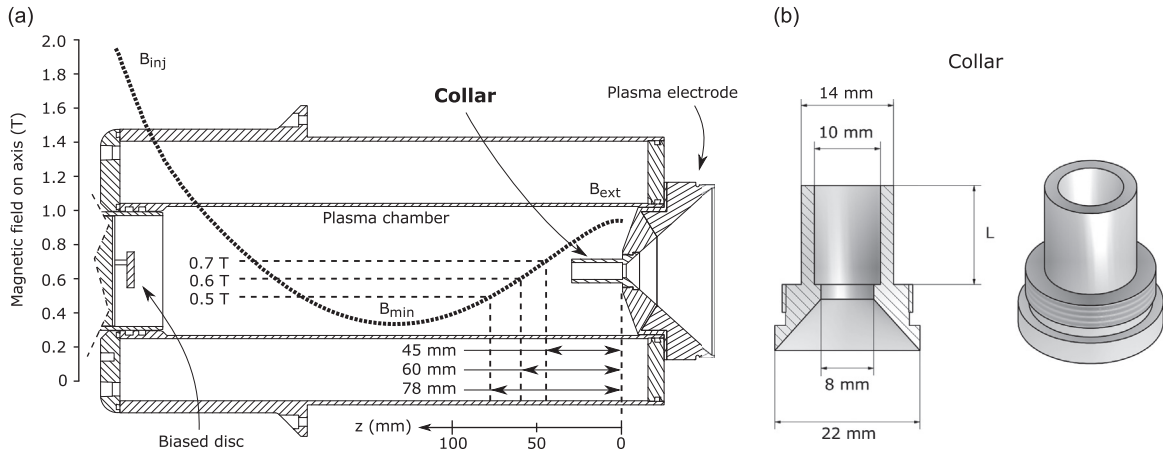


**Fig. 1.** A schematic presentation of the collar installed to the plasma electrode of the JYFL 14 GHz ECRIS (a) and the structure of a separate collar (b). The solenoidal magnetic field on axis is also presented with $B_{inj} = 1.95$ T, $B_{min} = 0.35$ T and $B_{ext} = 0.94$ T. The collar length $L$, defined in part (b) of the figure, was varied between 0 and 60 mm. In the figure $L = 30$ mm in the schematic plasma chamber assembly (a) and $L = 15$ mm for the presented separate collar (b).

study the possible material dependent behavior. Aluminum has higher secondary electron emission coefficient compared to stainless steel and is therefore the preferred material for ECRIS plasma chamber walls. $Al_2O_3$ was chosen to study if the performance was affected by a dielectric material.

Possible ion species dependent effects were studied using $^{14}N$, $^{16}O$, $^{20}Ne$, $^{40}Ar$ and $^{82}Kr$ plasmas and gas mixing with Ar+$O_2$. The ion source extraction voltage was varied between 10 and 14 kV, corresponding to the typical injection energies of the JYFL K-130 cyclotron [20].

Changing the collar between the measurements required venting the ion source. The ion source was subsequently conditioned for a few days to achieve good performance and deplete residual gas contaminations, e.g. water and oxygen. The same procedure was performed for the baseline measurements to ensure identical conditions. With the $Al_2O_3$ collar the conditioning period was extended until the level of residual oxygen detected in the extracted beam decayed to a normal level. The performance of the ion source was quantified by measurements of beam current, transverse emittance and profile of $m/q$ separated ion beams. The beam current was measured with a conventional Faraday cup, the transverse emittance with an Allison type emittance scanner [21] and the beam profiles were recorded using potassium bromide (KBr) coated scintillation screens. The transverse emittance values were calculated with 90% threshold value in the vertical plane, i.e. perpendicular to the bending plane of the analyzing magnet. The limitation of the Allison scanner is that it provides 2D emittance, compared to the 4D emittance achieved with a pepper pot emittance meter. However, the results obtained with the scanner have been correlated with the beam transmission efficiency at JYFL (see e.g. [22]) and it has been shown experimentally that Allison scanners and pepper pot emittance meters provide consistent results [23]. The first section of the low energy beam transport downstream from the JYFL 14 GHz ECRIS and the locations of the diagnostics is presented in Fig. 2.

The experiments were performed with the extracted beam currents $I_{ext} < 1.5$ mA because the extraction system of the JYFL 14 GHz ECRIS is known to degrade the properties of the extracted beams with high total extracted beam current. After the collar experiments the extraction has been replaced with a new system providing improved performance [22].

Because of the demanding beam time schedule of the JYFL accelerator laboratory, the collar experiments were distributed over a time period of roughly 2 years. As a consequence, the measurements included numerous baseline measurements, providing a good

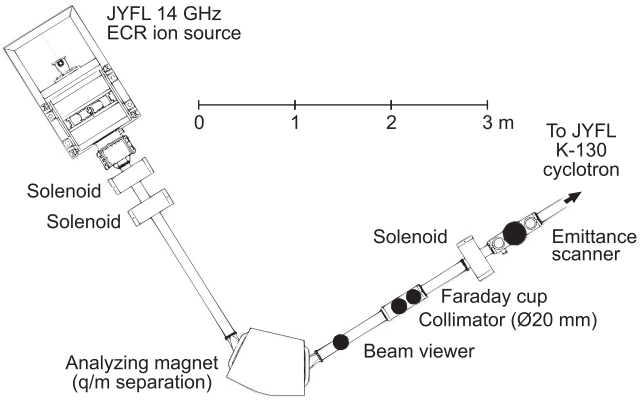


**Fig. 2.** A schematic presentation of the low energy beam transport downstream from the JYFL 14 GHz ECRIS.

assessment of the normal variation of the ion source performance. This information has been utilized for establishing error estimations for the collar measurements.

## 3. Experimental results

The experiments with varying collar lengths were performed with argon plasma. The ion source was optimized for the production of $^{40}Ar^{12+}$ with 10 kV extraction voltage and the extracted current and transverse emittance of charge states 5 + …16+ were measured. The $^{40}Ar^{12+}$ beam current and normalized rms emittance obtained with collar lengths between 0 and 60 mm are presented in Fig. 3, with $L = 0$ mm corresponding to the baseline measurements. With collar lengths between 5 and 30 mm $^{40}Ar^{12+}$ exhibits an average improvement of ~20% and ~30% in the beam current and the transverse emittance, respectively, compared to the baseline. The beam current and emittance of the other argon charge states exhibit more variation. This is probably due to slight variations in the ion source tunes, such as gas pressure and microwave power, yielding the optimum $^{40}Ar^{12+}$ performance. This underlines the sensitivity of the charge state distribution on the tuning parameters, especially for the high charge states. This is demonstrated in Table 1, which presents the beam currents and current improvements compared to baseline average for all measured argon charge states with varied collar lengths. The ion species for which the ion source is optimized exhibit moderate

performance improvement compared to the baseline ($^{40}Ar^{12+}$ in this case) consistently with all collar lengths. However, such a clear trend is not observed with the other charge states. Significant differences were not observed in the beam profiles with different collar lengths, including the baseline measurements, which imply that the collar does not interfere with the plasma flux toward the extraction.

With collar lengths $L > 30$ mm the ion source performance is substantially degraded, as the results with 40 and 60 mm collars in Fig. 3 show. The total extracted beam current and the current of all individual charge states decrease significantly (see Fig. 4). The decrease is most pronounced for the highest charge states, indicating that the long collars disturb the plasma. After the measurements it was observed that the 60 mm collar was damaged by the plasma bombardment up to a distance of 15 mm from the collar tip.

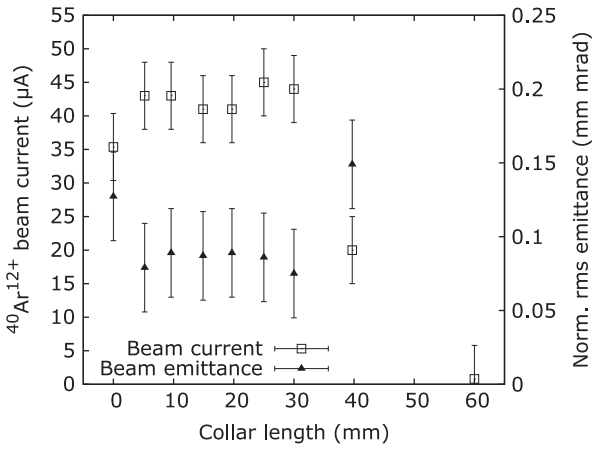


**Fig. 3.** Beam current and normalized rms emittance of $^{40}Ar^{12+}$ with varying collar lengths.

The measurements were performed with varying collar lengths at 10, 12 and 14 kV extraction voltages. The measured ion beams exhibited the behavior described above with all extraction voltages.

In addition to stainless steel, aluminum and $Al_2O_3$ were tested as the collar material with $L=20$ mm. No significant differences were observed in the ion source performance between the different collar materials. The stainless steel and aluminum collars exhibited very little evidence of interaction with the plasma particles, but the $Al_2O_3$ collar experienced significant damage after several days of operation.

The influence of the collar was further studied with $^{14}N$, $^{16}O$, $^{20}Ne$, $^{40}Ar$ and $^{82}Kr$ plasmas. The measurements were performed with 15 mm stainless steel collar. The results obtained with the ions species for which the ion source was optimized, i.e. $^{14}N^{6+}$, $^{16}O^{7+}$, $^{14}N^{6+}$, $^{40}Ar^{12+}$ and $^{82}Kr^{20+}$, seem to suggest a weak mass per charge dependence, as is presented in Fig. 5(a). However, when all extracted ion species, not just the optimized ones, are studied, this dependence is obscured by the performance variation of the ion source, as presented in Fig. 5(b).

The effect of mixing gas was studied with Ar+$O_2$ plasma. As expected, the mixing gas enhanced the production of high charge states with the collar effect remaining similar as with pure argon.

## 4. Discussion

The experiments show that surprisingly long (up to 30 mm with the JYFL 14 GHz ECRIS) collar structures can be implemented without degrading the ion source performance in terms of extracted beam current and transverse emittance. For some beams a moderate performance improvement was obtained with the collar.

The collar measurements provide experimental information regarding the dynamics of the extracted ions. The collars with lengths up to 30 mm exhibited very little evidence of interaction with the plasma particles. Also, different collar materials had no

**Table 1**
Beam currents $I$ of $^{40}Ar$ charge states $Q$ and current improvement $I_{impr}$ compared to baseline average $I^{BL}_{avg}$ with varying collar lengths $L$ (in mm). The standard error of the mean for $I^{BL}_{avg}$ and the range of baseline variation between measurements $I^{BL}_{var}$ are also presented. Ion source optimized for $^{40}Ar^{12+}$.

| $Q$ | $I^{BL}_{avg}$ (μA) | $I$ (μA) and $I_{impr}$ (%) with varying collar length $L$ | | | | | |
|---|---|---|---|---|---|---|---|
| | $I^{BL}_{var}$ (μA) | $L=5$ | $L=10$ | $L=15$ | $L=20$ | $L=25$ | $L=30$ |
| 5 | 23 ± 3 | 28 ± 2 | 24 ± 2 | 24 ± 2 | 26 ± 2 | 22 ± 2 | 27 ± 2 |
| | 17 …28 | 20 ± 17 | 3 ± 15 | 3 ± 15 | 11 ± 16 | −6 ± 14 | 16 ± 17 |
| 6 | 25 ± 1 | 29 ± 2 | 23 ± 2 | 20 ± 1 | 26 ± 2 | 25 ± 2 | 23 ± 2 |
| | 23 …27 | 17 ± 17 | −8 ± 13 | −21 ± 11 | 3 ± 15 | 0 ± 14 | −7 ± 13 |
| 7 | 31 ± 2 | 35 ± 2 | 30 ± 2 | 24 ± 2 | 31 ± 2 | 31 ± 2 | 30 ± 2 |
| | 27 …35 | 15 ± 17 | −3 ± 14 | −21 ± 11 | 2 ± 15 | 2 ± 15 | −1 ± 14 |
| 8 | 65 ± 7 | 85 ± 5 | 71 ± 4 | 58 ± 3 | 70 ± 4 | 72 ± 4 | 72 ± 4 |
| | 53 …81 | 30 ± 19 | 9 ± 16 | −11 ± 13 | 7 ± 15 | 10 ± 16 | 10 ± 16 |
| 9 | 75 ± 3 | 87 ± 5 | 78 ± 4 | 63 ± 4 | 92 ± 5 | 83 ± 5 | 86 ± 5 |
| | 68 …79 | 16 ± 17 | 4 ± 15 | −16 ± 12 | 22 ± 18 | 10 ± 16 | 14 ± 16 |
| 10 | 73 ± 4 | 77 ± 4 | 76 ± 4 | 64 ± 4 | 87 ± 5 | 81 ± 5 | 86 ± 5 |
| | 64 …82 | 6 ± 15 | 5 ± 15 | −12 ± 13 | 20 ± 17 | 11 ± 16 | 19 ± 17 |
| 11 | 57 ± 3 | 62 ± 4 | 61 ± 4 | 56 ± 3 | 67 ± 4 | 63 ± 4 | 68 ± 4 |
| | 51 …62 | 9 ± 16 | 7 ± 15 | −2 ± 14 | 17 ± 17 | 11 ± 16 | 19 ± 17 |
| 12 | 35 ± 2 | 43 ± 3 | 43 ± 3 | 41 ± 3 | 41 ± 3 | 45 ± 3 | 44 ± 3 |
| | 31 …39 | 22 ± 17 | 22 ± 17 | 16 ± 17 | 16 ± 17 | 27 ± 18 | 24 ± 18 |
| 13 | 17 ± 2 | 18.0 ± 0.9 | 17.5 ± 0.9 | 21 ± 2 | 14.5 ± 0.8 | 19 ± 1 | 20 ± 2 |
| | 13 …19.3 | 8 ± 16 | 5 ± 15 | 26 ± 18 | −13 ± 13 | 16 ± 17 | 21 ± 17 |
| 14 | 5.8 ± 0.8 | 6.0 ± 0.3 | 5.9 ± 0.3 | 8.6 ± 0.4 | 4.0 ± 0.2 | 6.6 ± 0.4 | 7.1 ± 0.4 |
| | 4.1 …7.2 | 4 ± 15 | 3 ± 15 | 50 ± 21 | −30 ± 10 | 15 ± 16 | 23 ± 18 |
| 15 | 1.4 ± 0.3 | 1.60 ± 0.01 | 1.40 ± 0.07 | 2.5 ± 0.2 | 0.90 ± 0.05 | 1.60 ± 0.08 | 2.5 ± 0.2 |
| | 0.94 …1.6 | 17 ± 17 | 20 ± 15 | 82 ± 26 | −34 ± 10 | 17 ± 17 | 82 ± 26 |
| 16 | 0.14 ± 0.07 | 0.18 ± 0.01 | 0.14 ± 0.01 | 0.40 ± 0.02 | 0.01 ± 0.01 | 0.17 ± 0.01 | 0.23 ± 0.01 |
| | 0.01 …0.29 | 26 ± 18 | −2 ± 14 | 180 ± 40 | −93 ± 8 | 19 ± 17 | 61 ± 23 |

observable effect on the ion source performance, indicating that particle interaction with the collar surface is not a significant contributor to the properties of the extracted beams. As the 30 mm collar structure with 10 mm inner diameter strongly limits the plasma flow in radial direction around the 8 mm extraction aperture, the results suggest that the extracted ions originate from a plasma volume further away in the axial direction. This is in good agreement with several computational models of the ion dynamics inside the plasma volume of an ECR ion source [24–28]. Despite different assumptions, these models are capable of reproducing many of the observed properties of ECRIS plasmas and ion beams. The simpler models, used for beam extraction studies, assume the ion dynamics to be dictated by the external magnetic field of the ion source. Consequently, the extracted ions are bound to the magnetic field lines which go through the extraction aperture. With the conventional ECRIS magnetic field structure, composed of solenoidal and hexapole magnetic fields, these field lines remain closely bunched and are nearly parallel for a considerable axial distance upstream from the extraction aperture.

The unperturbed ion motion in external magnetic field $B$ is dictated by the Lorentz force, resulting to ion gyromotion around the magnetic field lines with Larmor radius $r_L = mv_\perp/qB$ and gyrofrequency $f_{ci} = \omega/2\pi = qB/2\pi m$, where $m$, $q$ and $v_\perp$ are the ion mass, charge and perpendicular velocity, respectively, with respect to the magnetic field. However, ion–ion collisions in the plasma disturb this motion, randomizing the ion path. As a result, the ion motion is not directly dictated by the magnetic field, i.e. the ions are not magnetized, if on an average $f_{ii}/f_{ci} > 1$, where $f_{ii}$ is the ion–ion collision frequency. In ECRIS plasma the $f_{ii}$ can be estimated with the equation presented by Melin et al. [6] and Girard et al. [6,29], showing that $f_{ii} \propto Q^2 Q_{eff} n_e / T_i^{3/2}$, where $Q$ is the charge state of the ion, $Q_{eff}$ the effective (mean) charge state of the ion population in the plasma, $n_e$ the electron density and $T_i$ the ion temperature. Using reasonable assumptions, obtained from experiments with ECRIS plasmas [6,29], the collision frequencies of $^{40}$Ar charge states 1+ and 12+ are $4.3 \times 10^5$ and $6.2 \times 10^7$ s$^{-1}$, for example. The corresponding ion gyrofrequencies range from $1.9 \times 10^5$ to $3.8 \times 10^5$ s$^{-1}$ for 1+ and from $2.3 \times 10^6$ to $4.6 \times 10^6$ s$^{-1}$ for 12+, when the magnetic field varies between 0.5 and 1 T. With 0.5 T the collision frequency is more than an order of magnitude higher than the gyrofrequency with charge states $Q \geq 5+$. For 1 T this occurs with $Q \geq 9+$. Based on the given collision frequency examples $f_{ii}/f_{ci} > 1$ even for the low charge states. Altogether, this implies that the ions are not magnetized. It is noted that the situation can be different in the plasma sheath, where the plasma density can be considerably lower than in the core plasma.

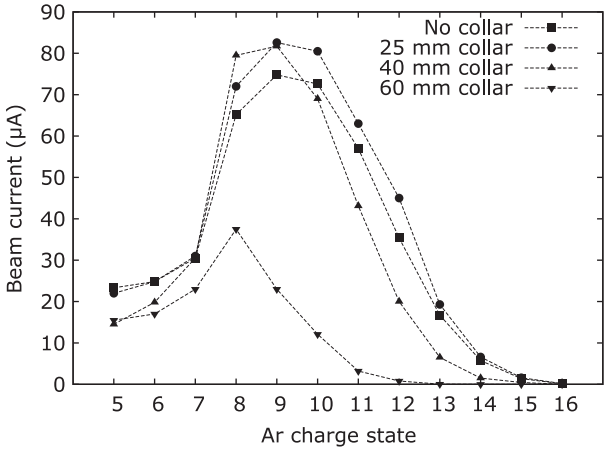


**Fig. 4.** Argon charge state distribution with varied collar lengths.

However, the ions are bound to the magnetic field lines indirectly through the dynamics of the magnetized electron population, as the experimental results reported in a recent study [30] indicate. In that study the ion and electron current density distributions were spatially resolved near the extraction region of an 11 GHz ECR ion source. It was shown that the strongly magnetized electrons follow the external magnetic field lines, and the ion distribution is localized around the electron distribution maintaining the plasma quasineutrality. This view is also in good agreement with simulations taking into account the ion–ion collisions (see e.g. [27]).

As the ion and electron dynamics can be considered strongly coupled, it can be argued that a rough estimation of the influence of the collar on the extracted ions can be made by studying how the collar structure limits the motion of the magnetized electrons. The electron trajectories were calculated in a static 3D representation of the magnetic field structure of the JYFL 14 GHz ECRIS, i.e. superposition of the solenoid and hexapole fields. The field structure can be described with the injection, extraction and minimum fields on axis, $B_{inj} = 1.95$ T, $B_{ext} = 0.94$ T and $B_{min} = 0.35$ T, and the radial field strength on the magnetic pole at the chamber wall, $B_{rad} = 1.06$ T. Collision processes and electric fields, i.e. electron heating, were not considered. Monoenergetic 10 keV electrons were used in the calculation. No significant difference was observed using a distribution of electron energies.

The electrons were launched from the plasma electrode aperture toward the chamber in order to identify the spatial volume from where the magnetized electrons, followed by the nonmagnetized ions, are transported into the extraction. In the

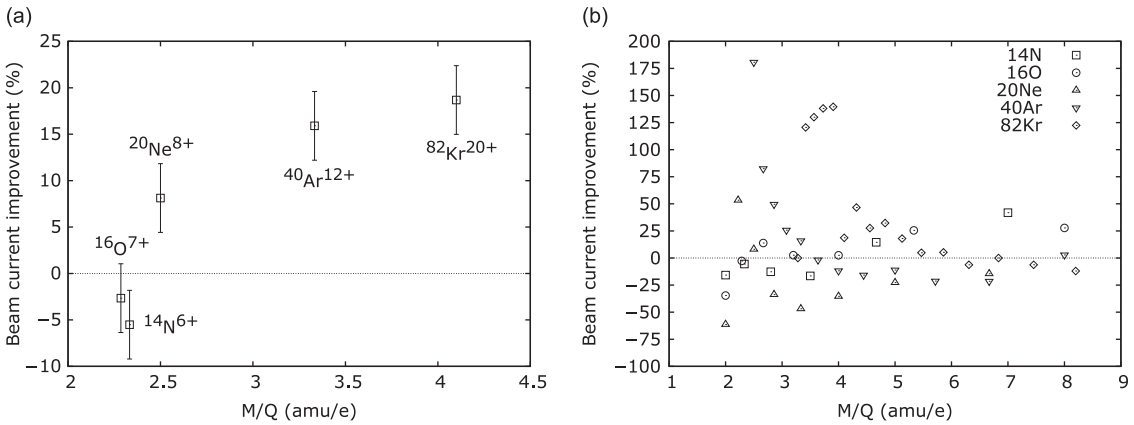


**Fig. 5.** Beam current improvement compared to baseline for (a) ion species for which the ion source is optimized and (b) all extracted ion species as a function of the ratio of the ion mass (in amu) and charge state.

calculations it was assumed that the initial electron population occupies the whole aperture area. This is supported by the plasma flux induced markings on the plasma electrode of the JYFL 14 GHz ECRIS, presented in Fig. 6. In addition a uniform distribution was assumed over the aperture. This can be considered as a worst case scenario for the fraction of electrons blocked by the collar structure.

The results of the electron calculations are presented in Fig. 7 showing the electron density distributions on the ($x$,$y$) planes at different axial distances $z$ from the plasma electrode. It is observed that the collar can be several tens of millimetres long until it starts to severely limit the flow of electrons (and thus, the ions) which would reach the extraction aperture without the collar. This rough estimate is in good agreement with the measured performance of the ion source with varied collar lengths. It is also noted that the distributions launched from the plasma electrode, reflecting the population that could pass through the circular extraction aperture, are rotated 60° compared to the distribution arriving from the plasma. The measured performance with the collars and the electron calculation results is also in good agreement with the fact that the collar can have a considerable length before it intercepts the magnetic field lines going through the extraction aperture. This is demonstrated in Fig. 8. The contribution of the hexapole is small close to the axis (radial direction) and the extraction aperture, and has been omitted from the schematic projection of the field lines in the collar region. The effect of the hexapole on the field lines intercepting with the extraction aperture is thoroughly discussed in Ref. [31] (see Fig. 2 therein).

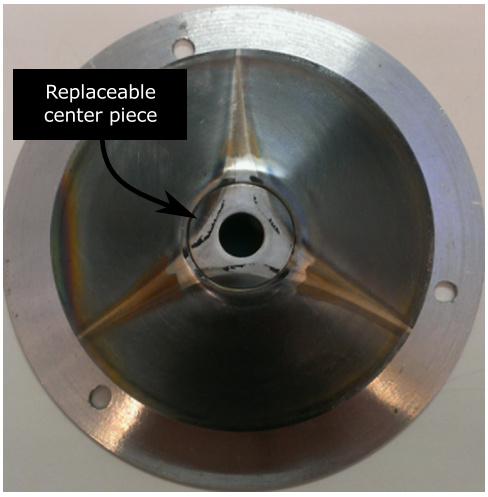


**Fig. 6.** A photo of the plasma electrode of the JYFL 14 GHz ECRIS with replaceable center piece for the collar measurements. The photo shows the baseline center piece (no collar) and the triangular markings induced by the plasma flux.

The plasma induced markings on the 60 mm collar indicate that the collar tip entered into a volume of plasma with substantial density. The axial location of the resonance field for the cold electrons ($B_{ECR} = 0.5$ T), where high plasma densities are expected, is 78 mm from the extraction aperture (see Fig. 1). The location of the damaged part of the collar corresponds to the distance of 45–60 mm. In this region the magnetic field on axis varies from 0.7 to 0.6 T, which is the resonance field for hot electrons with temperatures ranging from about 100 to 200 keV. The existence of electron population at such energies in the JYFL 14 GHz ECRIS has been confirmed experimentally with bremsstrahlung measurements (see e.g. [32,33]).

The fact that the performance of the ECR ion source is not significantly altered by the introduction of the collar structures indicates that the ECR plasma heating is rather insensitive to variations of the plasma chamber geometry, at least near the extraction. This is in good agreement with the microwave power absorption experiments performed with the JYFL 14 GHz ECRIS,

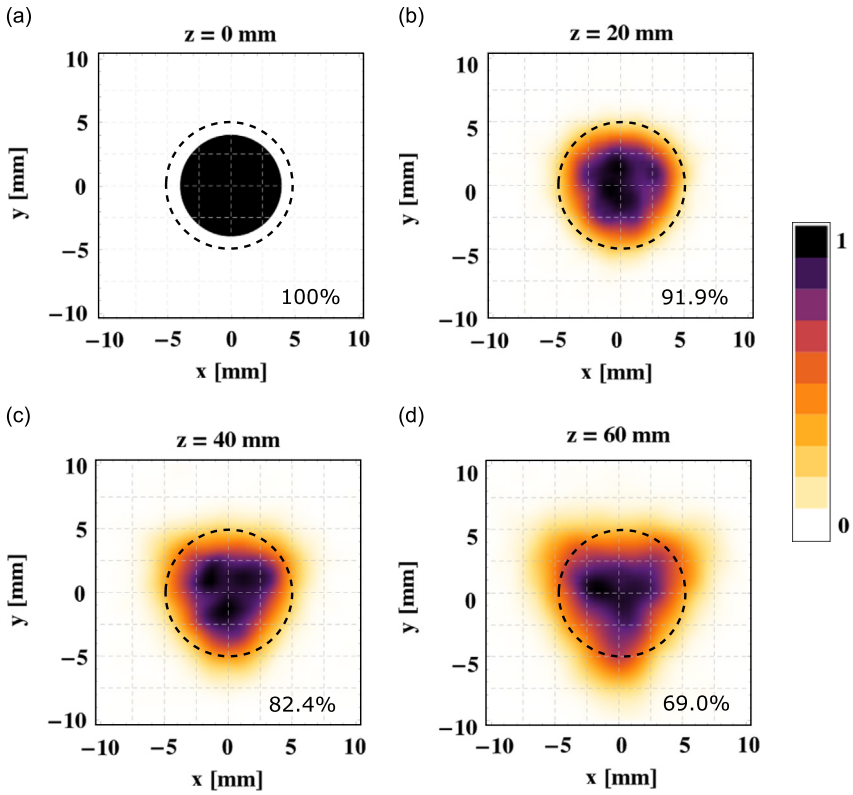


**Fig. 7.** Electron density distributions at different axial distances from the plasma electrode based on electron tracking from the extraction aperture (∅8 mm) toward the plasma in the magnetic field of the JYFL 14 GHz ECRIS. The fraction of electrons inside the ∅10 mm collar, indicated with dashed circles, is also presented.

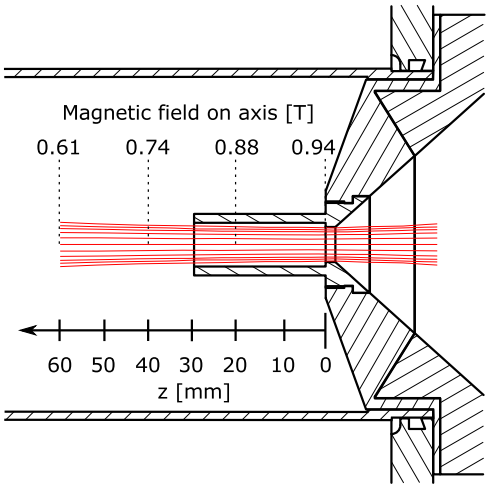


**Fig. 8.** Magnetic field lines of the solenoidal field going through the 8 mm extraction aperture superimposed with 30 mm collar structure in the extraction region of the JYFL 14 GHz ECRIS. The value of the magnetic field on axis is also indicated at selected points.

which have shown that with high microwave powers the mode structure of the AECR-U type ion source is strongly damped and the exact heating frequency ceases to play a critical role [34].

It is concluded that based on the results obtained with the JYFL 14 GHz ECRIS, the collar structure itself does not provide remarkable improvement to ECRIS performance. However, the experiments open up a discussion on possible new techniques to achieve this, because the results indicate that the volume around the collar could be utilized without compromising the ion source performance. This volume is demonstrated very clearly in Fig. 1 with 30 mm collar. Possibilities to enhance the ion source performance could include, for example, hexapole correction of extracted ion beams with compact magnetic design around the extraction aperture. This could offer a simpler passive alternative for the implementation of active correction downstream in the beamline, which is made challenging by the ion species dependent ion optics (see e.g. [35]). Another possibility could be the enhancement of ion extraction by local manipulation of the ECRIS solenoidal magnetic field with a small solenoid assembly around the extraction aperture. This could yield an improvement in the emittance which is dominated by the influence of the solenoidal magnetic field at the extraction. This might also provide a way to affect the charge state distribution of the extracted beams. Ideas such as these could be studied with relatively simple redesigns of the ion source plasma electrode.

## Acknowledgments

The authors thank D. Leitner for providing the $Al_2O_3$ collar. This work has been supported by the EU 7th framework programme "Integrating Activities—Transnational Access", Project number: 262010 (ENSAR) and by the Academy of Finland under the Finnish Centre of Excellence Programme 2012–2017 (Nuclear and Accelerator Based Physics Research at JYFL).

## References

[1] D. Hitz, Advances in Imaging and Electron Physics 144 (2006) 1.
[2] G. Melin, et al., in: Proceedings of the 10th International Workshop on ECR Ion Sources, November 1–2, 1990, Knoxville, USA.
[3] S. Gammino, J. Sijbring, A.G. Drentje, Review of Scientific Instruments 63 (1992) 2872.
[4] S. Runkel, O. Hohn, K.E. Stiebing, A. Schempp, H. Schmidt-Böcking, V. Mironov, G. Shirkov, Review of Scientific Instruments 71 (2000) 912.
[5] G.D. Shirkov, Plasma Sources Science and Technology 2 (1993) 250.
[6] G. Melin, A.G. Drentje, A. Girard, D. Hitz, Journal of Applied Physics 86 (1999) 4772.
[7] Z.Q. Xie, C.M. Lyneis, in: Proceedings of the 12th International Workshop on ECR Ion Sources, April 25–27, 1995, Riken, Japan.
[8] G.D. Alton, F.W. Meyer, Y. Liu, J.R. Beene, D. Tucker, Review of Scientific Instruments 69 (1998) 2305.
[9] R.C. Vondrasek, R.H. Scott, R.C. Pardo, in: Proceedings of the 15th International Workshop on ECR Ion Sources, June 12–14, 2002, Jyväskylä, Finland.
[10] R.C. Vondrasek, R. Scott, R.C. Pardo, Review of Scientific Instruments 77 (2006) 03A337.
[11] L. Schächter, K.E. Stiebing, S. Dobrescu, Al.I. Badescu-Singureanu, L. Schmidt, O. Hohn, S. Runkel, Review of Scientific Instruments 70 (1999) 1367.
[12] L. Schächter, S. Dobrescu, K.E. Stiebing, Review of Scientific Instruments 73 (2002) 4172.
[13] L. Celona, G. Ciavola, F. Consoli, S. Gammino, F. Maimone, D. Mascali, P. Spädtke, K. Tinschert, R. Lang, J. Mäder, J. Roßbach, S. Barbarino, R.S. Catalano, Review of Scientific Instruments 79 (2008) 023305.
[14] F. Consoli, L. Celona, G. Ciavola, S. Gammino, F. Maimone, S. Barbarino, R.S. Catalano, D. Mascali, Review of Scientific Instruments 79 (2008) 02A308.
[15] L. Celona, S. Gammino, G. Ciavola, F. Maimone, D. Mascali, Review of Scientific Instruments 81 (2010) 02A333.
[16] T. Lamy, J. Angot, M. Marie-Jeanne, J. Medard, P. Sortais, T. Thuillier, A. Galata, H. Koivisto, O. Tarvainen, in: Proceedings of the 19th International Workshop on ECR Ion Sources, August 23–26, 2010, Grenoble, France.
[17] F. Maimone, L. Celona, R. Lang, J. Mäder, J. Roßbach, P. Spädtke, K. Tinschert, Review of Scientific Instruments 82 (2011) 123302.
[18] V. Mironov, in: presentation at the 37th European Cyclotron Progress Meeting, October 28–31, 2009, Groningen, Netherlands and personal communication, 2009.
[19] H. Koivisto, P. Heikkinen, V. Hänninen, A. Lassila, H. Leinonen, V. Nieminen, J. Pakarinen, K. Ranttila, J. Ärje, E. Liukkonen, Nuclear Instruments and Methods in Physics Research Section B 174 (2001) 379.
[20] E. Liukkonen, in: Proceedings of the 13th International Conference on Cyclotrons and their Applications, July 6–10, 1992, Vancouver, Canada.
[21] P.W. Allison, J.D. Sherman, D.B. Holtkamp, IEEE Transactions on Nuclear Science NS-30 (4) (1983) 2204.
[22] V. Toivanen, T. Kalvas, H. Koivisto, J. Komppula O. Tarvainen, Journal of Instrumentation 8 (2013) P05003.
[23] H.R. Kremers, J.P.M. Beijers, S. Brandenburg, S. Saminathan, V. Mironov, T. Thuillier, in: Proceedings of the 18th International Workshop on ECR Ion Sources, September 15–18, 2008, Chicago, USA.
[24] P. Spädtke, K. Tinschert, R. Lang, J. Mäder, J. Roßbach, J.W. Stetson, L. Celona, Review of Scientific Instruments 79 (2008) 02B716.
[25] P. Spädtke, Review of Scientific Instruments 81 (2010) 02B725.
[26] D.S. Todd, D. Leitner, C.M. Lyneis, D.P. Grote, Review of Scientific Instruments 79 (2008) 02A316.
[27] V. Mironov, J.P.M. Beijers, Physical Review Special Topics—Accelerators and Beams 12 (2009) 073501.
[28] D. Mascali, S. Gammino, L. Celona, G. Ciavola, Review of Scientific Instruments 83 (2012) 02A336.
[29] A. Girard, D. Hitz, G. Melin, K. Serebrennikov, Review of Scientific Instruments 75 (2004) 1381.
[30] L. Panitzsch, T. Peleikis, S. Böttcher, M. Stalder, R.F. Wimmer-Schweingruber, Review of Scientific Instruments 84 (2013) 013303.
[31] P. Spädtke, R. Lang, J. Mäder, F. Maimone, J. Rosßbach, K. Tinschert, Review of Scientific Instruments 83 (2012) 02B720.
[32] T. Ropponen, O. Tarvainen, P. Jones, P. Peura, T. Kalvas, P. Suominen, H. Koivisto, J. Ärje, Nuclear Instruments and Methods in Physics Research Section A 600 (2009) 525.
[33] T. Ropponen, O. Tarvainen, I. Izotov, J. Noland, V. Toivanen, G. Machicoane, D. Leitner, H. Koivisto, T. Kalvas, P. Peura, P. Jones, V. Skalyga, V. Zorin, Plasma Sources Science and Technology 20 (2011) 055007. (14pp).
[34] V. Toivanen, O. Tarvainen, C. Lyneis, J. Kauppinen, J. Komppula, H. Koivisto, Review of Scientific Instruments 83 (2012) 02A306.
[35] P. Spädtke, R. Lang, J. Mäder, F. Maimone, J. Roßbach, K. Tinschert, in: Proceedings of the 19th International Workshop on ECR Ion Sources, August 23–26, 2010, Grenoble, France.

# APPENDIX A.VII

PUBLISHED BY IOP PUBLISHING FOR SISSA MEDIALAB

RECEIVED: *March 4, 2013*
ACCEPTED: *April 15, 2013*
PUBLISHED: *May 10, 2013*

# Double einzel lens extraction for the JYFL 14 GHz ECR ion source designed with IBSimu

**V. Toivanen,**[1] **T. Kalvas, H. Koivisto, J. Komppula and O. Tarvainen**

*Department of Physics (JYFL), University of Jyväskylä, 40500 Jyväskylä, Finland*

*E-mail:* ville.toivanen@jyu.fi

ABSTRACT: In order to improve the performance of the JYFL 14 GHz electron cyclotron resonance ion source (ECRIS) and initiate low energy beam transport (LEBT) upgrade at the University of Jyväskylä, Department of Physics (JYFL) accelerator laboratory, a new ion beam extraction system has been designed and installed. The development of the new extraction was performed with the ion optical code IBSimu, making it the first ECRIS extraction designed with the code. The measured performance of the new extraction is in good agreement with the simulations. Compared to the old extraction the new system provides improved beam quality, i.e. lower transverse emittance values and improved structure of beam profiles, and transmission efficiency of the LEBT and the JYFL K-130 cyclotron. For example, the transmission efficiencies of $^{40}Ar^{8+}$ and $^{84}Kr^{16+}$ beams have increased by 80 and 90%, respectively. The new extraction system is capable of handling higher beam currents than the old one, which has been demonstrated by extracting new $^{4}He^{+}$ and $^{4}He^{2+}$ record beam currents of 1.12 mA and 720 $\mu$A, exceeding the old records of the JYFL 14 GHz ECRIS by a factor of two.

KEYWORDS: Ion sources (positive ions, negative ions, electron cyclotron resonance (ECR), electron beam (EBIS)); Simulation methods and programs; Beam Optics

[1]Corresponding author.



doi:10.1088/1748-0221/8/05/P05003

2013 JINST 8 P05003

## Contents



2013 JINST 8 P05003

## 1 Introduction

The low energy beam transport of the JYFL K-130 cyclotron [1] at the University of Jyväskylä, Department of Physics (JYFL) accelerator laboratory is being upgraded to improve the ion beam transport efficiency from ion source to target. The upgrade is carried out in intermediate steps, starting from the JYFL 14 GHz electron cyclotron resonance ion source (ECRIS) [2]. A new extraction system has been designed and installed to improve the performance of the ion source and provide better tuning and operation flexibility in comparison to the old system. The new extraction enables controlling the properties of the extracted beam — such as beam diameter and divergence — in a wide range without compromising the beam quality. This is essential for further beamline upgrades.

The new extraction system of the JYFL 14 GHz ECR ion source has been designed with the ion optical code IBSimu, developed at the University of Jyväskylä [3]. In the past the code has been used successfully for the development of extraction systems for light ion sources [4, 5]. The extraction system presented in this paper is the first one developed with IBSimu for an ECR ion source. Successful operation of the extraction system acts as the first benchmarking result for the IBSimu code in ECRIS extraction design and development.

An overview of the simulation aspects and previous work specific for ECR ion source extraction is presented in the following section. An overview of the IBSimu code and the ECRIS specific

simulation parameters used in the presented work are given. This is followed by a description of the experimental methods which were used to compare the simulation results to measurements. A study of the old extraction system of the JYFL 14 GHz ECRIS is presented. This was performed to gain confidence in the use of the code for designing an ECRIS extraction and to find out the main problems of the old system. The design and simulation results for the new extraction system are presented and compared to the experimental results. Finally, the measured performance of the new extraction system is compared to the old one in terms of beam quality and transmission efficiency through the low energy transport and the JYFL K-130 cyclotron.

## 2 Simulation aspects

### 2.1 Simulating ECRIS extraction

Exact modeling of ECR ion source extraction is a challenging task. This is due to the complex plasma conditions determining the dynamics of the extracted ions. In ECR ion source the magnetized plasma is confined axially and radially with a combination of solenoid and hexapole fields. To achieve proper axial mirror ratio necessary for sufficient confinement necessary for production of highly charged ions, the axial magnetic field reaches a local maximum near or at the extraction aperture. This leads to extraction of ions from a strong magnetic field and subsequent beam formation in decaying fringe field. The highly charged ions are produced in the plasma via stepwise ionization driven by ECR heated electrons. The hot electrons are strongly confined and their movement is dictated by the magnetic field structure. In contrast, due to the selective heating of electrons, the ions remain cold and highly collisional, i.e. the ion collision frequency is significantly higher than the ion gyrofrequency around the magnetic field lines [6]. The ion dynamics is strongly influenced by the dynamics of the electrons, as the negative charge of the electron distribution bounds the ion population, resulting into quasineutrality. Direct experimental evidence supporting this view was provided by a recent study [7], in which the electron and the ion current densities were measured close to the extraction aperture of an ECR ion source. It was shown that the electron distribution was strongly localized into a triangular shape, dictated by the magnetic field, and surrounded by a spatially broader distribution of ions.

The computational efforts to model the ECR plasma and ion beam extraction from it can be roughly divided into two categories: (1) models of charged particle dynamics in the ECR plasma which include the entire plasma volume, and (2) models of ion extraction with simplified plasma models. Models of the first category are focused to the plasma processes such as electron heating, ionization, charged particle collisions and their connection to the particle dynamics. The TrapCAD code (see e.g. [8, 9]) and studies conducted by Heinen et al. (see e.g. [10, 11]) concentrate on the dynamics of magnetically confined electrons in the ECR plasma. The PIC-MCC (Particle In Cell Monte Carlo Collision) code developed by Mironov et al. [12] models the dynamics of ions, treating the electrons as neutralizing background. These models provide information on the ion distribution close to the extraction aperture, but are not self-consistently connected to the modeling of the following extraction systems. Consequently, the beam formation needs to be simulated separately (for an example, see e.g. [13]).

A few notable extraction case studies are very closely connected to the first category of computational tools. These approaches are based on the assumption of ion movement inside the plasma



2013 JINST 8 P05003

being directly dictated by the magnetic field, discarding the highly collisional nature of the ions. In the model presented by Spädtke [14, 15] the extracted ions originate from regions where the magnetic field exceeds the field at extraction, and are tracked along the magnetic field lines through the extraction aperture. As a result the extracted ions originate from the plasma volume close to the chamber walls. In the model presented by Todd [16] the initial ion population is defined from experimentally observed sputtering marks on the ion source biased disc, located at the injection end of the plasma chamber. The ion distribution at extraction aperture is obtained by tracking the ions through the plasma chamber along the magnetic field lines. The beam formation and extraction is modeled with this 3D distribution and precalculated cylindrically symmetric electrostatic potentials of the extraction system. Despite of the different initial conditions and ignoring the ion collisions both models are capable of reproducing many of the observed properties of ECRIS beams. These models have been applied to case studies of existing ion sources to link the observed beam properties to the ion dynamics inside plasma, but not for actual extraction system development.

Models of the second category decouple the entire plasma volume from the region of beam formation. The influence of the plasma is represented with simplified positive plasma models, usually based on the work of Self [17, 18]. The ions are produced inside a plasma volume close to the extraction aperture with predefined spatial and ion species distributions. Electrons are modeled as neutralizing background with Boltzmann distribution. The plasma sheath is resolved self-consistently by iterative calculation of potential, solved from Poisson's equation, taking into account the space charge of traced ions. Several codes exist with such plasma model capabilities, for example IGUN [19], PBGUNS [20], WARP [21], KOBRA3-INP [22], IONEX [23] and, most recently, IBSimu. Several studies focusing on different aspects of ECR ion source extraction have been performed with the given codes (see e.g. references [24–26]). However, comprehensive studies depicting complete ECRIS extraction system designs and directly comparing the simulated and measured performace in the literature are not known to the authors.

In the work presented here the extraction of the JYFL 14 GHz ECRIS has been simulated using the nonlinear positive plasma model of IBSimu. Features of ECR plasmas and ion beams are employed in the plasma model. The ions with known ECRIS charge state distribution and temperature are generated inside a predefined plasma volume, restricted to the region behind the extraction aperture, with neutralizing background electron density. The plasma has a predefined plasma potential, a well known parameter for the JYFL 14 GHz ECRIS. The magnetic field of the ion source, the most dominating feature of ECRIS extraction, is implemented based on the real magnetic field topology. The presented study is the first ECR ion source extraction which has been designed with IBSimu and subsequently benchmarked experimentally against the simulation results.

### 2.2 Overview of the simulation code IBSimu

IBSimu is a freely available[1] ion optical code developed at the University of Jyväskylä [3]. The code is modular in nature, distributed as a library package and accessed via C++ interface to maximize its versatility and flexibility. The main features of the code include geometry input using analytical definitions or CAD files, calculation of electrical potential distribution in the given ge-

[1] IBSimu and the related documentation is available at http://ibsimu.sourceforge.net.



2013 JINST 8 P05003

ometry, magnetic field importing, multispecies particle extraction from plasma volume (positive or negative) and trajectory tracking in electric and magnetic fields, space charge calculation and extensive diagnostics tools for particle and field data. Simulations can be performed in 2D (spatial coordinates $x$, $y$ and velocity coordinates $v_x$, $v_y$), in cylindrically symmetric 2.5D ($x$, $r$, $v_x$, $v_r$, $v_\theta$) or in 3D ($x$, $y$, $z$, $v_x$, $v_y$, $v_z$).

The simulation procedure is performed in steps, starting with the discretization of the simulated volume with rectangular mesh. The potential distribution is solved from Poisson's equation taking into account the defined geometry, electrode potentials and boundary conditions. The thermal background electrons of the plasma are included analytically in the Poisson's equation. Particle trajectories are traced integrating the equations of motion derived from the Lorentz equation. The space charge of the beam is distributed to mesh nodes and is taken into account when the electric potentials are solved iteratively. The above sequence is repeated until the solution converges to required precision.

More detailed presentation of the IBSimu code, its development and applications can be found in references [3–5, 27]. A description of the nonlinear positive plasma model can be found e.g. in reference [18].

### 2.3 Simulation parameters

The plasma model was defined using a plasma potential of 20 V, which matches the experimental values measured with the JYFL 14 GHz ECRIS [28, 29]. The temperature of the cold electron population in ECR ion sources is believed to be in the same order of magnitude with the plasma potential (in eV) [30], and was chosen to be 10 eV. The extracted ion beam was defined based on argon charge state distribution ranging from 5+ to 16+, measured with the old extraction system when the ion source was optimized for high charge state production, yielding highest beam currents to charge states 9+ and 10+. Contributions of charge states 1+ – 4+ were estimated based on the shape of the measured part of the spectrum, while charge states 17+ and 18+ were excluded due to their negligible currents. The simulated beam particles were generated inside the plasma volume 5 mm upstream from the extraction aperture with uniform radial distribution. The ions require some initial longitudinal energy to be extracted from the plasma volume (Bohm criterion, see e.g. [31]). To minimize the effect of this initial energy on the properties of the extracted beam, low values relative to the potentials present in the extraction are advisable. For the plasma parameters mentioned above, it was observed that initial particle energies on the order of 10 eV is needed for converging solution. Varying the value between 10 and 100 eV affects the properties of the extracted beam by a few percent. The ion temperature was chosen to be 1 eV, matching the generally accepted order of magnitude for ECR ion sources [6].

The simulations have been performed assuming entire space charge of the extracted ion beam outside the plasma volume. This assumption can be justified in the regions of the extraction where strong electric field exists. However, it is likely that in reality there are also regions where the density of electrons produced by the beam via residual gas ionization can yield substantial space charge compensation [32]. As the space charge defocuses the beam, the simulations with full space charge can be regarded as the worst case scenario. In practice this provides additional safety margin to the extraction design.



2013 JINST 8 P05003

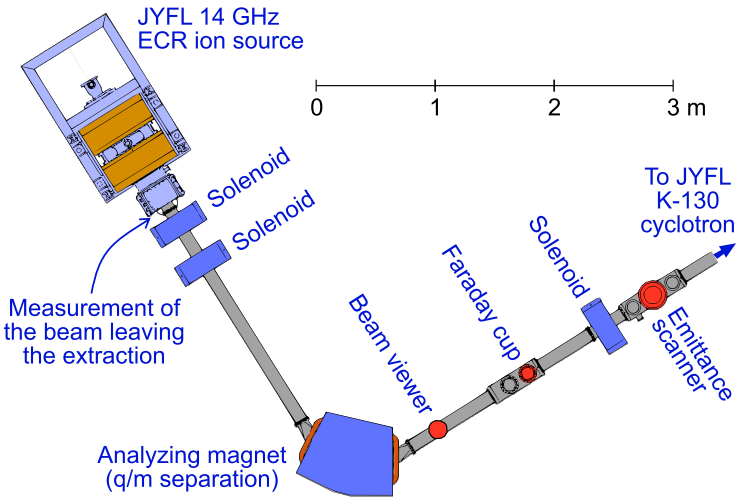


**Figure 1**. Schematic presentation of the first section of the low energy beam transport from the JYFL 14 GHz ECR ion source to the JYFL K-130 cyclotron.

The distance from the extraction aperture of the JYFL 14 GHz ECRIS to the end of the vacuum chamber housing the extraction electrodes is about 0.5 m. Consequently, the simulation volume becomes such that for 3D simulation the memory requirements to achieve reasonable accuracy exceed the memory capabilities of normal desktop computers. Furthermore, optimizing the extraction design requires a multitude of simulation runs to be performed when the effects of the design parameters are studied, which makes long simulation times impractical. As a result, the majority of the simulations were performed with cylindrically symmetric 2D geometry. The results were verified by running a few dedicated simulations in 3D with the final extraction design. The solenoidal magnetic fringe field of the ECR ion source, modeled with FEMM [33], was included in all simulations. The field correspond with the normal operating values of the JYFL 14 GHz ECRIS coils. The hexapole fringe field was omitted in the cylindrically symmetric simulations but a dedicated set of 3D simulations were performed to study its effect on the beam in the extraction region, as discussed later.

## 3 Experimental methods

The first section of the low energy beam transport (LEBT) from the JYFL 14 GHz ECR ion source to the JYFL K-130 cyclotron is presented in figure 1. The beam current measurements are conducted with a Faraday cup, located downstream from the analyzing magnet ($q/m$ separation). Measurements of beam transverse emittance, performed with an Allison type emittance scanner [34], are used to determine the quality of the extracted beams. Due to the fact that the emittance scanner is located at considerable distance from the extraction ($\sim 6$ m), the measured beam properties are somewhat affected by the intervening beamline ion optics and space charge effects. Profiles of $q/m$ separated beams are recorded after the analyzing magnet with a KBr coated scintillation screen.

The limited space available for measurements immediately after the extraction system restricts the possible diagnostics. A simple pepperpot-like (see e.g. [35]) system consisting of a multia-



2013 JINST 8 P05003

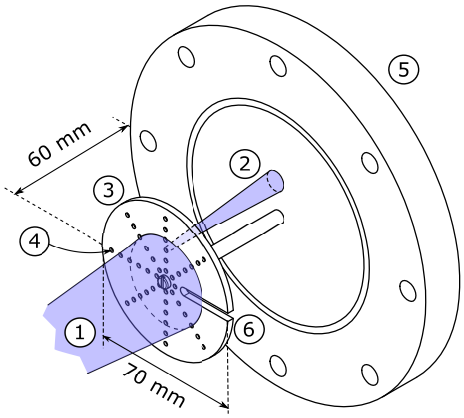


**Figure 2**. Schematic presentation of the pepperpot-like setup used to measure the beam diameter and divergence after the extraction. The incoming beam (1) is collimated into separate beamlets (2) by a pepperpot plate (3) (for clarity, only a single beamlet is shown). As the size of the apertures (4) on the pepperpot plate is known ($\varnothing$ 2 mm), the beam divergence can be determined from the beamlet induced markings on the flange (5). The slot (6) on the first plate is used to determine the beam radius.

perture plate and a flange (see figure 2) was installed after the extraction to determine the beam diameter and divergence from the induced markings on the aluminum flange. Water cooling was applied to the flange to ensure the heating caused by the ion bombardment would not distort the results.

## 4 Simulation and experimental results

### 4.1 Old extraction system

The old extraction system of the JYFL 14 GHz ECRIS was studied with IBSimu to gain confidence in the code for modeling ECR ion source extraction. The old extraction system consists of a plasma electrode, a puller electrode and an asymmetric accelerating einzel lens with a decelerating electrode acting as its first part. The system is presented in figure 3 with 1.1 mA of extracted argon beam. The on-axis magnetic field present in the extraction region is also indicated. The local minimum in the magnetic field around $x = 0.04$ m is caused by magnetic iron, which is used to shape and optimize the magnetic confinement of the plasma in the extraction end of the plasma chamber.

One of the main challenges of the JYFL 14 GHz ECRIS extraction is the low source potential, normally around 10 kV, dictated by the JYFL K-130 cyclotron injection. Hence, the extracted beam energies are relatively low, resulting in strong space charge effects. The old extraction design includes a decelerating electrode as the first part of the einzel lens. This further deceleration leads to increased emittance growth due to increased divergence and diameter of the beam inside the lens. However, the deceleration is inevitable as the increased beam diameter also results in stronger focusing by the weak einzel lens. Without this the beam is collimated at the end of the lens and the following beam pipe.

The case presented in figure 3 corresponds to the optimum simulated conditions for the extracted beam. The electrode potentials match well with the operational values. The beam is on



2013 JINST 8 P05003

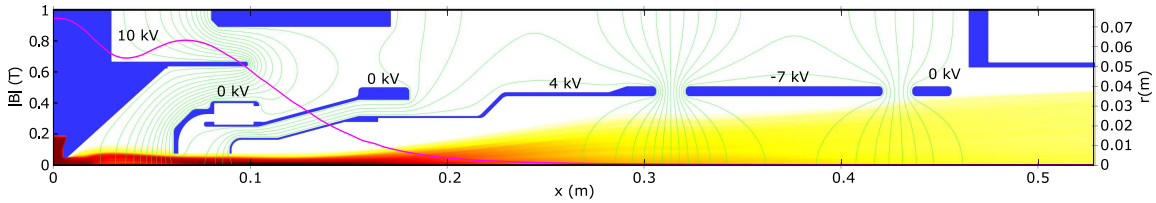


**Figure 3**. Simulation result (trajectory density) of the old extraction system for 1 mA argon beam. Extraction voltage 10 kV, puller at 0 kV, decel at 4 kV and einzel at −7 kV. Magnetic field on axis is indicated with the solid purple line.

the verge of being collimated at the puller face and at the last electrode of the einzel lens. If the puller voltage is increased or the acceleration gap length decreased to mitigate the collimation at the puller, the beam divergence increases further downstream, resulting to collimation inside the einzel lens. Increasing the focusing by applying higher voltage to the einzel lens would prevent this, but is prohibited by insufficient insulation.

The simulated beam diameter inside the extraction increases with the beam current due to space charge induced divergence and poor electric field structure in the acceleration gap between the plasma and puller electrodes. The strongly conical plasma electrode leads to increased acceleration gap length close the optical axis and subsequently reduces the electric field strength at the extraction aperture. As a result the extracted beams are strongly diverging. The modest electric field also decreases the local Child-Langmuir limit for the maximum space charge limited current [36, 37].

The transmission through the extraction drops substantially when the extracted beam current exceeds $\sim 1$ mA. At the same time the beam quality degrades because the large beam inside the einzel lens leads to strong aberrations. These effects have been confirmed experimentally [38].

The beam diameter and divergence were measured after the extraction and compared to simulations. Two measurements were performed with $\sim 1.1$ mA argon beam and two with $\sim 0.8$ mA argon beam, using the electrode potentials presented in figure 3. The measured beam diameters for the $\sim 1.1$ mA beam were $63 \pm 2$ mm and for the $\sim 0.8$ mA beam $51 \pm 2$ mm. The corresponding maximum half-axis beam divergences were $60 \pm 10$ mrad and $20 \pm 10$ mrad. For similar beam currents the simulations yield beam diameters of about 65 and 50 mm (surrounded by low intensity halos) and maximum half-axis beam divergences of 60 and 55 mrad.

The agreement between the simulated and measured behavior of the old extraction suggests that IBSimu has sufficient capabilities to be used for modeling the extraction of ECR ion sources.

### 4.2 New extraction system

A simulation of 1 mA argon beam is presented in figure 4. The extraction is composed of a modified plasma electrode, a puller electrode and two accelerating einzel lenses. Compared to the old extraction system (figure 3) the simulated beam transport through the extraction is clearly improved. The mechanical design is shown in figure 5.

Even though accelerating einzel lenses require higher operating voltages compared to decelerating ones, they were chosen for the design based on the advantages they offer for the quality of low energy ion beams. Decelerating lenses are prone to increased space charge effects, as the energies



2013 JINST 8 P05003

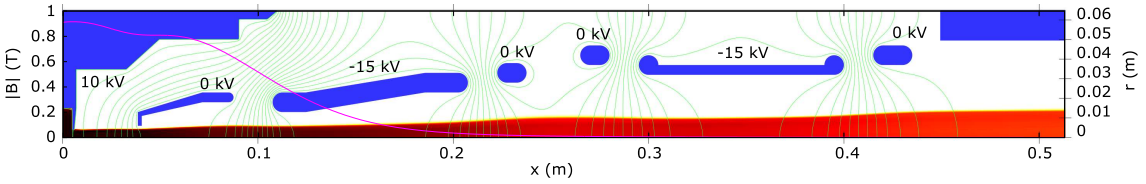


**Figure 4**. Simulation result (trajectory density) of the new extraction system for 1 mA argon beam. Extraction voltage 10 kV, puller at 0 kV and both einzel lenses at −15 kV. Magnetic field on axis is indicated with the solid purple line.

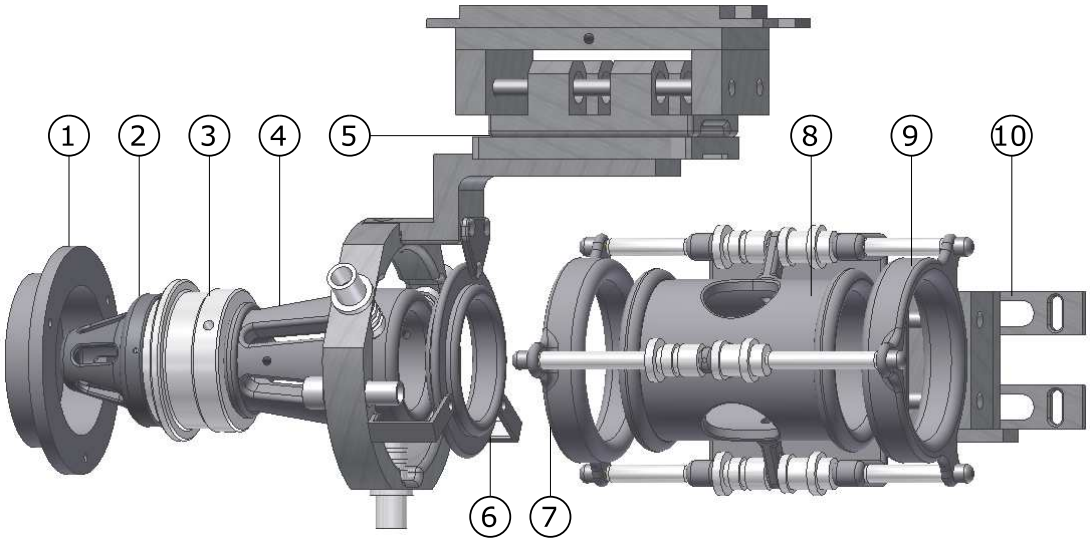


**Figure 5**. Mechanical design of the extraction system including the plasma (1), puller (2) and einzel electrodes (4 and 8). The puller electrode is separated from the first einzel electrode with MACOR insulator (3). The einzel lenses are completed with grounded electrodes (6, 7 and 9) and are independently movable on rails (5, 10). The electrodes have open structure for improved pumping.

of the ions passing through the lens are temporarily reduced. The positive lenses can also act as electron collectors decreasing the space charge compensation degree of the ion beam. Last but not least, accelerating einzel lenses induce less spherical and chromatic aberrations, as the beam size and energy spread remain smaller inside the lens [39].

### 4.2.1 Beam formation

In order to increase the electric field strength in the acceleration gap, the new design features almost planar plasma electrode. To facilitate this, the location of the extraction aperture is shifted 12 mm outwards from the plasma and the magnetic iron around the extraction is modified to match the axial magnetic field maximum to the new aperture location. The magnetic field on axis is presented in figure 4. The new extraction system has been simulated with extraction voltages ranging from 6 to 20 kV. No degradation of performance in terms of beam properties and transmission was observed. The beam transverse emittance decreases with increasing beam energy following the expected $1/\sqrt{V_{\text{ext}}}$ behavior.



2013 JINST 8 P05003

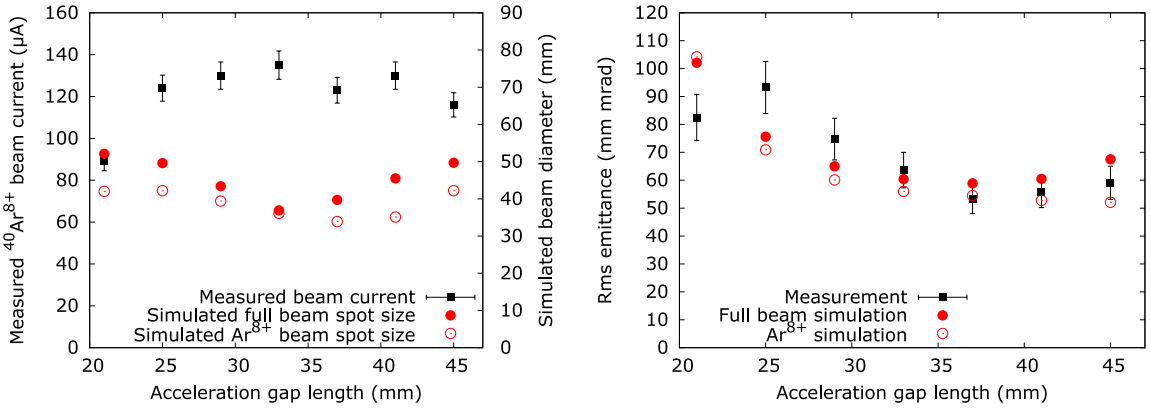


**Figure 6**. Comparison of measured $^{40}Ar^{8+}$ beam current and transverse emittance to simulated beam diameter and transverse emittance with varying acceleration gap length. 1 mA of total extracted current with $V_{acc} = 10\,kV$, $V_{puller} = -2\,kV$, $V_{E1} = -15\,kV$ and $V_{E2} = -11\,kV$. In the simulation the contribution of $^{40}Ar^{8+}$ in the total beam current is 140 $\mu$A.

Optimizing the performance of the extraction system for a wide range of beam energies and currents requires adjusting the acceleration gap length. As a consequence, in the new extraction design the puller electrode acts as the first part of the first einzel lens and both einzel lenses are designed to be independently movable along the optical axis, enabling a high degree of tuning flexibility.

As an example, the measured $^{40}Ar^{8+}$ beam current and transverse emittance with varying acceleration gap length is compared with simulated beam diameter and transverse emittance in figure 6. The simulated values are determined at $x = 0.513\,m$ (see figure 4) and the results are shown for 1 mA beam (all ion species) and separately for the $^{40}Ar^{8+}$ component of the beam with 140 $\mu$A current, which follows the trend exhibited by the total extracted beam. The measured total extracted beam current was about 1 mA, decreasing 10% with the increasing gap length over the presented range. The simulations show a very good match with the measured transverse emittance behavior. Also, the minima of the simulated beam diameter and maximum of measured beam current are closely matched, which is believed to reflect improved beamline transmission with improved beam properties. Both the simulations and measurements indicate optimum performance with 33–41 mm acceleration gap length for the given extraction settings.

### 4.2.2 Beam focusing and manipulation

In the following text the expressions *higher lens voltage* and *lower lens voltage* denote higher and lower *negative* voltages, i.e. higher lens voltage corresponds to increase in the applied negative voltage leading to stronger focusing.

The simulated effect of varying einzel lens voltages is presented in figures 7 and 8. Figure 7 shows the transverse emittance and beam diameter of 1.5 mA argon beam (all ion species) when voltages of both einzel lenses, E1 and E2, are varied independently. Figure 8 shows the behavior of individual ion species of the same beam. $^{40}Ar^{4+}$ ($\sim 30\,\mu A$), $^{40}Ar^{8+}$ ($\sim 210\,\mu A$) and $^{40}Ar^{12+}$ ($\sim 150\,\mu A$) are chosen, as they represent the charge over mass range of 0.1…0.3, including most of the ion species used in the experiments at JYFL. The behavior of the individual ion species



2013 JINST 8 P05003

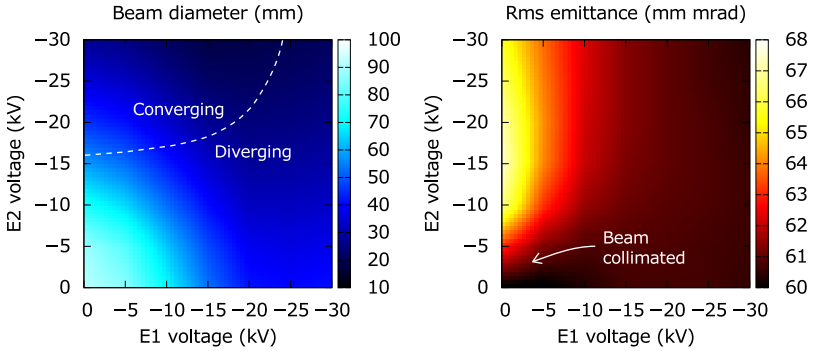


**Figure 7**. Beam diameter and transverse rms emittance (all ion species) of 1.5 mA argon beam with varying einzel lens (E1 and E2) voltages. The regions of converging and diverging beam are indicated. With low lens voltages (both lenses below −5 kV) the beam is collimated inside the extraction region.

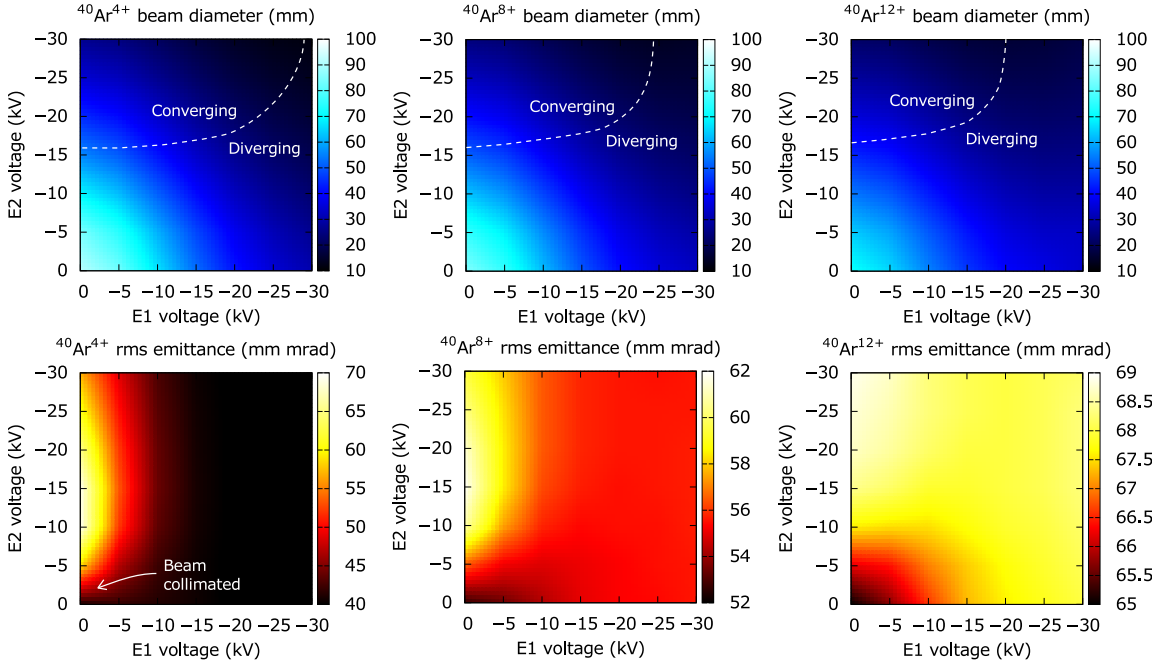


**Figure 8**. Beam diameter and transverse rms emittance of argon charge states 4+, 8+ and 12+ with beam currents $\sim 30\,\mu$A, $\sim 210\,\mu$A and $\sim 150\,\mu$A (part of the 1.5 mA argon beam) with varying einzel lens E1 and E2 voltages. The regions of converging and diverging beam are indicated.

follow the general behavior of the 1.5 mA beam. The beam diameter and transverse emittance variation decreases with increasing charge state. Focusing of the beam by increasing the voltages of the einzel lenses decreases the beam diameter as expected. If both lenses are operated with very low voltages (both below −5 kV), the low charge states are collimated inside the second einzel lens when the beam current exceeds 1.5 mA.

Converging beams are produced when the first einzel lens is operated with low and the second lens with high voltage. In this way the beam enters the second lens with large diameter, resulting to strong focusing. Figure 9 presents simulated beam transverse emittance and diameter with



2013 JINST 8 P05003

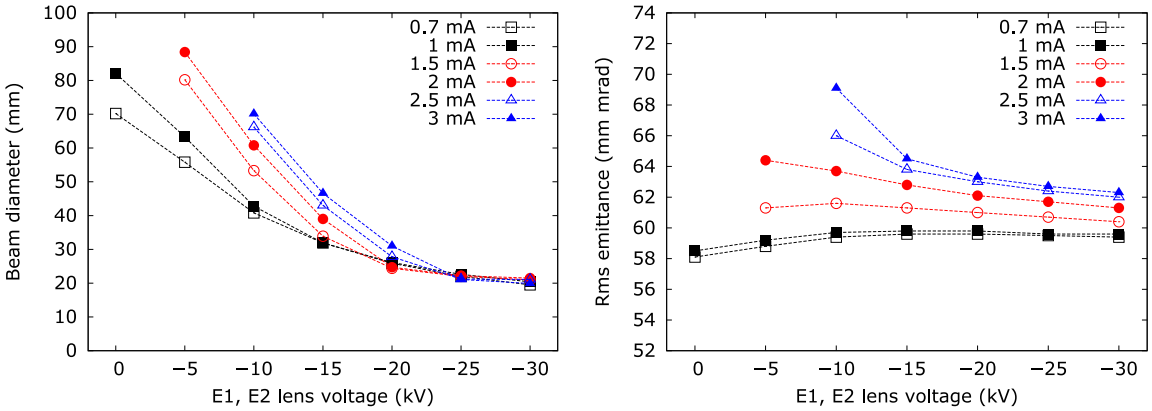


**Figure 9**. Transverse rms emittance and diameter (all ion species) of argon beams with varying einzel lens voltages. For extracted currents over 1 mA the data points with low absolute lens voltages have been omitted due to collimation inside the extraction.

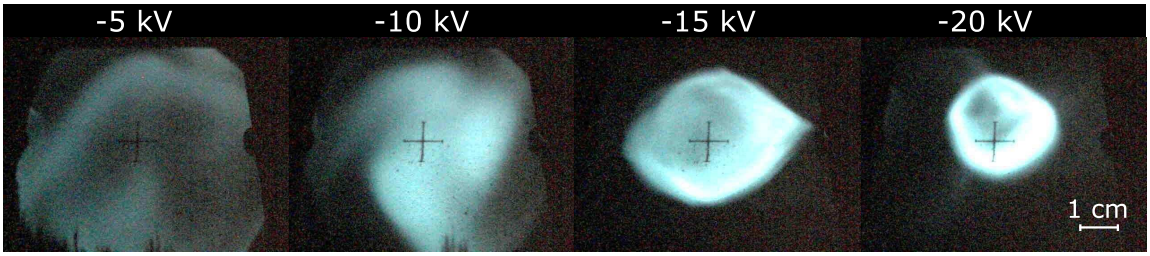


**Figure 10**. Measured $^{40}Ar^{8+}$ beam profiles when both einzel lens voltages are varied together. 1 mA of total extracted current. Profiles recorded after the $q/m$ separation. With the lowest lens voltages the beam spot becomes larger than the viewer plate.

different extracted beam currents in the case when both einzel lens voltages are varied together, corresponding to diagonal movement in figures 7 and 8. With low lens voltages the influence of varying beam current on the beam diameter and transverse emittance is clearly visible. With strong focusing good performance is achieved with all simulated beam currents up to 3 mA.

Figure 10 presents measured $^{40}Ar^{8+}$ beam viewer images with 1 mA of total extracted current. Despite the intervening beamline the focusing effect of the einzel lenses is evident which corresponds well with the predicted tendency. With low einzel lens voltages diameter of the beam entering the beamline solenoids is large, which results to strong aberrations. Higher lens voltages, and consequently smaller beam diameters, result to significantly improved structure of the beam profile.

The transverse beam emittance is mainly determined by the first einzel lens, which defines the diameter of the beam inside the second one. Large beam diameter inside einzel lenses leads to aberrations and subsequent emittance growth. The emittance variation is strongest with low charge states exhibiting the largest beam diameters. The minimum emittance is achieved when both lenses are switched off and only the space charge of the beam itself induces emittance growth. However, this leads to strongly diverging beams, which are collimated by the beam pipe right after the extraction. When both einzel lenses are operated with sufficiently high voltages, the emittance variation resulting from the varying lens voltages becomes insignificant (operation in the constant

2013 JINST 8 P05003

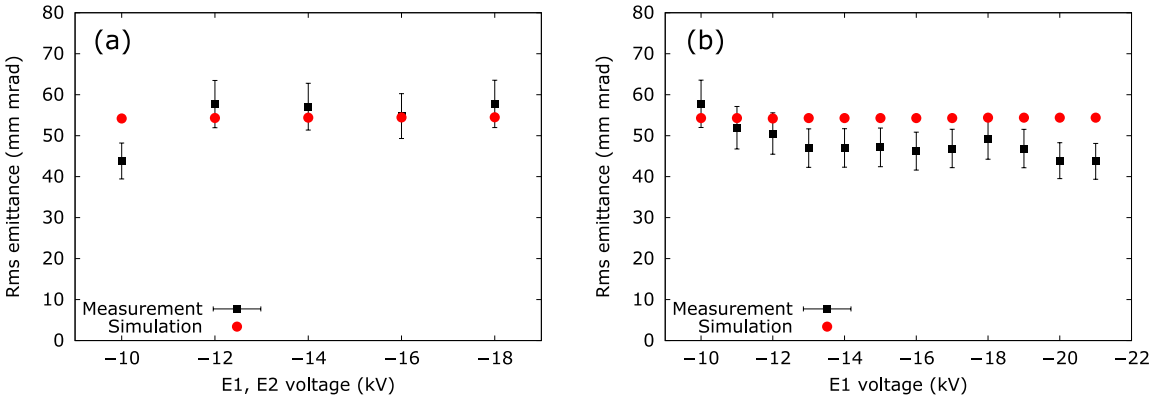


**Figure 11**. Comparison of measured and simulated transverse emittance behavior of $^{40}Ar^{8+}$ beam as a function of einzel lens voltages. (a) Both einzel lens voltages varied together. (b) First einzel lens varied, second lens at −11 kV.

emittance region in figures 7 and 8). The transverse emittance increases with increasing charge state, as shown in figure 8. This is caused by the ion source solenoidal magnetic field, which is discussed in more detail in the Discussion section.

The dependence of the beam emittance on the lens voltages has been studied experimentally. Figure 11 shows a comparison of simulated and measured $^{40}Ar^{8+}$ transverse emittance as a function of einzel lens voltages. The beamline optics limit the range of lens voltages that can be used without compromising the beam transport to the emittance scanner. The presented voltage ranges correspond to beam current variation of less than 10% at the Faraday cup in order to minimize the effect of beam collimation during transport on the results. In figure 11(a) both extraction einzel lens voltages are varied together between −10 and −18 kV. The total extracted current was 1.45 mA and the average $^{40}Ar^{8+}$ beam current 120 $\mu$A. In the given voltage range the simulated transverse emittance remains practically constant, which matches the measured emittance behavior. In figure 11(b) the second einzel lens is at constant −11 kV and the voltage of the first einzel lens is varied between −10 and −21 kV. The total extracted current was 1.55 mA and the average $^{40}Ar^{8+}$ beam current 150 $\mu$A. The measured transverse emittance values show a good match with the simulations. These results indicate that the extracted beam quality, in terms of transverse emittance, is not sensitive to the lens voltages, when operated with sufficiently high values. This allows flexible operation of the extraction system without compromising the beam quality.

Based on the simulations, it can be expected that the new extraction system is capable of handling considerably higher beam currents than the old system. The simulations have been performed up to 3 mA of total extracted current without observing degradation of beam properties. The capabilities of the new extraction system with high extracted beam currents have been tested experimentally by extracting 2.7 mA He beam. The ion source was tuned for the production of $^{4}He^{+}$ beam and yielded a new record beam current of 1.12 mA. The highest recorded $^{4}He^{+}$ beam current obtained with the old extraction system was 520 $\mu$A. The corresponding values for $^{4}He^{2+}$ are 720 $\mu$A (new system) and 325 $\mu$A (old record).

The beam spot diameters and divergences have been measured with the new extraction system using the setup presented in figure 2. The measurements were performed with 0.5, 1 and 1.5 mA



2013 JINST 8 P05003

**Table 1**. Measured beam spot diameters and maximum divergences of argon beams exiting the extraction region and the corresponding simulation results with two different extraction settings and varied extracted beam current $I_{ext}$. #1: $V_{ext} = 10\,\text{kV}$, $V_{puller} = -1\,\text{kV}$, $V_{E1} = -15\,\text{kV}$, $V_{E2} = -10\,\text{kV}$, 35 mm acceleration gap. #2: $V_{ext} = 10\,\text{kV}$, $V_{puller} = -1\,\text{kV}$, $V_{E1} = V_{E2} = -15\,\text{kV}$, 31 mm acceleration gap.

| Param. set | $I_{ext}$ (mA) | Beam diameter (mm) | | Max divergence (mrad) | |
|---|---|---|---|---|---|
| | | Measured | Simulated | Measured | Simulated |
| #1 | 0.5 | $31 \pm 1$ | 34 | $30 \pm 10$ | 25 |
| #1 | 1 | $43 \pm 1$ | 35 | $50 \pm 10$ | 36 |
| #2 | 1 | $26 \pm 1$ | 32 | $20 \pm 10$ | 20 |
| #2 | 1.5 | $47 \pm 1$ | 35 | $30 \pm 10$ | 26 |

argon beams with two extraction settings. The experimental results and the corresponding simulation results are presented in table 1. The measured beam diameters and maximum divergences agree relatively well with the values obtained from the simulations, although the measured beam diameter increases with the extracted current somewhat more than suggested by the simulations.

### 4.3 Transmission measurements

A series of transmission measurements has been performed with $^{40}Ar^{8+}$ and $^{84}Kr^{16+}$ beams to compare experimentally the performance of the old and the new extraction systems. The initial beam currents were measured after the $q/m$ separation and the final currents after the JYFL K-130 cyclotron. The total length of the LEBT from the ion source to the cyclotron is about 20 m. The results are presented in table 2. The total transmission efficiency of the $^{40}Ar^{8+}$ beam, averaged over the individual measurements presented in table 2, increased from 2.3% to 4.4% with the new extraction system, which translates to over 90% improvement compared to the old system. The transmission of the LEBT section increased from 23.0% to 35.2%, and the transmission through the cyclotron from 10.0% to 12.6%. The total transmission of the $^{84}Kr^{16+}$ beam increased from 4.9% to 9.0%, which translates to an increase of over 80% compared to the old extraction system.

The quality of the beams extracted with the old and the new extraction systems has been studied with transverse emittance measurements of $^{40}Ar^{8+}$ beams with varying beam currents. The results are presented in table 2, showing that the new extraction system yields lower emittance values, which indicates improved beam quality. This is supported by the beam profile measurements of $^{40}Ar^{8+}$ beams. Examples are presented in figure 12, showing improved current distribution with the new extraction system. These results demonstrate that the ion source extraction system can contribute significantly to the beam hollowness.

## 5 Discussion

The simulations conducted with IBSimu recreated well the observed behavior of the old extraction system of the JYFL 14 GHz ECR ion source. Thus the code was used to design a new extraction system that has demonstrated improved performance over the old one. The measured beam diameters and divergences agree reasonably well with the simulated values. The measured transverse



2013 JINST 8 P05003

**Table 2**. Transmission results with the old and the new extraction systems. $E_{ECR}$ and $E_{ACC}$ are the beam energies after the JYFL 14 GHz ECRIS and the JYFL K-130 cyclotron. $I_{ECR}$ and $I_{ACC}$ are the corresponding beam currents, $T$ the transmission efficiency and $\varepsilon_{rms,n}$ the normalized transverse 1-rms emittance.

| Ion beam | Extraction system | $E_{ECR}$ (keV) | $E_{ACC}$ (MeV) | $I_{ECR}$ ($\mu$A) | $I_{ACC}$ ($\mu$A) | $T$ (%) | $\varepsilon_{rms,n}$ (mm mrad) |
|---|---|---|---|---|---|---|---|
| $^{40}Ar^{8+}$ | Old | 82 | 200 | 90 | 2.3 | 2.6 | $0.13 \pm 0.02$ |
| $^{40}Ar^{8+}$ | Old | 82 | 200 | 138 | 3.1 | 2.3 | $0.13 \pm 0.02$ |
| $^{40}Ar^{8+}$ | Old | 82 | 200 | 170 | 3.6 | 2.1 | $0.10 \pm 0.01$ |
| $^{40}Ar^{8+}$ | New | 82 | 200 | 84 | 3.7 | 4.4 | $0.10 \pm 0.02$ |
| $^{40}Ar^{8+}$ | New | 82 | 200 | 102 | 4.1 | 4.0 | $0.10 \pm 0.01$ |
| $^{40}Ar^{8+}$ | New | 82 | 200 | 105 | 5.2 | 5.0 | – |
| $^{40}Ar^{8+}$ | New | 82 | 200 | 132 | 6.0 | 4.6 | $0.05 \pm 0.01$ |
| $^{40}Ar^{8+}$ | New | 82 | 200 | 187 | 7.4 | 4.0 | $0.07 \pm 0.01$ |
| $^{84}Kr^{16+}$ | Old | 156 | 383 | 31 | 1.6 | 5.0 | – |
| $^{84}Kr^{16+}$ | Old | 156 | 383 | 60 | 2.6 | 4.3 | – |
| $^{84}Kr^{16+}$ | Old | 156 | 383 | 30 | 1.6 | 5.3 | – |
| $^{84}Kr^{16+}$ | New | 156 | 383 | 40 | 3.1 | 7.8 | – |
| $^{84}Kr^{16+}$ | New | 156 | 383 | 30 | 3.1 | 10.3 | – |

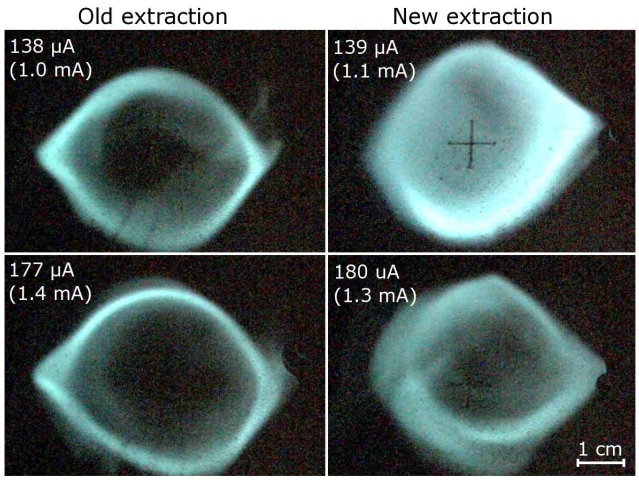


**Figure 12**. Profiles of $^{40}Ar^{8+}$ beams produced with the old and the new extraction systems with beam currents of about 140 and 180 $\mu$A.

emittance dependencies on the acceleration gap length and einzel lens voltages show very good correlation with the predictions obtained from the simulations.

The good results obtained with the new extraction system show that the double accelerating einzel lens approach is a viable option for a flexible, high performance ECRIS extraction, especially when the ion source potential is relatively low ($< 20$ kV). With increasing source potential the high voltage requirements of accelerating lenses can pose technical challenges in terms of HV insulation.



2013 JINST 8 P05003

As the increasing beam energy also mitigates the space charge effects, the use of decelerating lenses can become a more favorable option.

The strong magnetic solenoid field in the extraction region is one of the most significant factors defining the ECR ion source extraction. Variation of ±10% of the magnitude of the solenoid field around the normal operating point yields ±15% variation in the simulated beam diameter and ±10% variation in the simulated transverse emittance. This matches the linear magnetic field dependency of the theoretical emittance contribution due to the diverging solenoid field. For a beam of ions with charge $q$ and mass $m$, extracted from a solenoidal magnetic field $B_0$, the emittance contribution can be expressed as

$$\varepsilon_{\mathrm{rms}}^{\mathrm{mag}} = \frac{qB_0}{8mv_z} r_0^2 \,, \tag{5.1}$$

where $v_z$ is the longitudinal velocity of the ions and $r_0$ the radius of the extraction aperture. Due to some confusion in the exact form of the formula [40–42], it is derived in the appendix. The values of the simulated transverse emittance correlate closely with the values obtained from equation (5.1).

Due to the strong influence of the magnetic field on the beam properties, the simulations are sensitive to the discretization and structure of the imported magnetic field. As a result, it was observed that the simulated transverse emittance contribution of the solenoidal magnetic field can vary slightly around the theoretical value, leading in some cases to transverse beam emittance values which are a few percent below the theoretical prediction.

The ion source hexapole field is omitted from the cylindrically symmetric simulations. In order to study how the hexapole field in the extraction region affects the properties of the extracted beams with the assumption of uniform ion distribution from the plasma, a dedicated set of 3D simulations was performed. The beam profiles with and without the hexapole field are practically identical. The difference in the transverse emittance is on the order of 1%. The simulations were performed with 1.5 mA argon beam extracted with the new extraction system and the results apply both for the total extracted beam as well as individual charge states. The triangular beam shapes observed experimentally with ECR ion sources originate from the ion distribution inside the plasma and the hexapole fringe field present in the extraction region has an insignificant effect on the properties of the extracted beams. Even though the plasma effects resulting into triangular ion distribution have been neglected in the presented simulations, the good correlation between the simulation results and measurements indicate that this simplified approach is still rather suitable in modeling of ECRIS extraction.

After its installation the new extraction system has been in permanent use at the JYFL accelerator laboratory. It has proven to be both reliable and flexible to operate, providing improved performance of the ion source and the beam transport. As the presented transmission results (see table 2) show, the improvement of ion source beam formation can lead to substantial improvement in the performance of the whole accelerator laboratory. The next step of the JYFL LEBT upgrade is the removal of the beamline section between the JYFL 14 GHz ECRIS and the analyzing magnet (see figure 1). This is performed in order to mitigate the space charge effects which, combined with strong $q/m$ specific solenoid focusing, lead to beam quality degradation and hollow beam formation.



2013 JINST 8 P05003

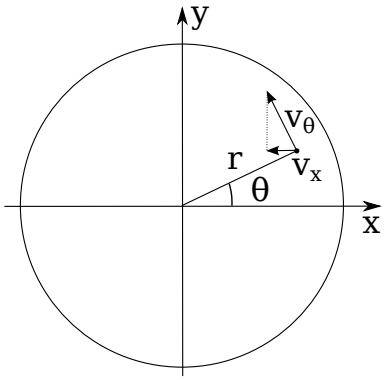


**Figure 13**. Azimuthal velocity thrust induced by the diverging solenoidal magnetic field.

## Acknowledgments

This work has been supported by the EU 7th framework programme "Integrating Activities — Transnational Access", project number: 262010 (ENSAR) and by the Academy of Finland under the Finnish Centre of Excellence Programme 2012–2017 (Nuclear and Accelerator Based Physics Research at JYFL).

## A Emittance from solenoidal magnetic field

An ion beam originating from a solenoidal magnetic field has an emittance contribution from the rotation induced by the magnetic field. The emittance contribution can be calculated by assuming a uniform, zero emittance (no plasma temperature) beam propagating from a round plasma electrode aperture with radius $r_0$ into the direction of decaying magnetic field with velocity $v_z$. According to Busch's theorem [43] the change of particle's angular velocity is coupled to the change of the axial magnetic field. In this case where the starting point angular velocity $\dot{\theta}_0$ is zero and the magnetic field is $B_0$, the angular velocity can be calculated at any point with $\dot{\theta} = q(B - B_0)/(2m)$. The azimuthal velocity of a particle in the zero field region is therefore

$$v_\theta = -\frac{qB_0 r}{2m}. \tag{A.1}$$

The simplest formulation for calculating the rms emittance can be achieved by assuming that the magnetic field drops abruptly from $B_0$ to zero giving the particles an azimuthal kick according to eq. (A.1). The resulting $\varepsilon_{\mathrm{rms}}$ is equivalent to the case where magnetic field decreases continuously, but the mathematical formulation is more simple. The beam divergence in $x$-direction is given by

$$x' = \frac{v_x}{v_z} = -\frac{yv_\theta}{rv_z} = -\frac{qB_0 y}{2mv_z} \tag{A.2}$$

as a function of location $y$ (see figure 13). The rms emittance can be calculated from $\varepsilon_{\mathrm{rms}} = \sqrt{\langle x'^2\rangle \langle x^2\rangle - \langle xx'\rangle^2}$ by integrating the expectation values $\langle x'^2\rangle$, $\langle x^2\rangle$ and $\langle xx'\rangle$ over the plasma electrode aperture. The normalized rms emittance ($\varepsilon_{\mathrm{rms,n}} = v_z/c \cdot \varepsilon_{\mathrm{rms}}$) is

$$\varepsilon_{\mathrm{rms,n}} = \frac{qB_0}{8mc} r_0^2 \approx 0.0402 \frac{Q\tilde{B}_0}{M} \tilde{r}_0^2, \quad \text{[mm mrad]} \tag{A.3}$$



2013 JINST 8 P05003

where in the approximate formula $Q$ is the charge state, $M$ is the ion mass in atomic mass units, $\tilde{B}_0$ is given in Teslas and $\tilde{r}_0$ in millimeters.

The obtained result agrees with the equation presented e.g. in reference [41]. However, in several publications (e.g. [24] and [40]) a somewhat different equation has been used for the rms emittance:

$$\varepsilon_{\mathrm{rms,n}} = \frac{qB_0}{10mc} r_0^2 \approx 0.032 \frac{Q\tilde{B}_0}{M} \tilde{r}_0^2 \quad \text{[mm mrad]} \tag{A.4}$$

This expression has been derived by calculating the normalized envelope emittance $\varepsilon_{100\%,\mathrm{n}} = qB_0 r_0^2/(2mc)$ and using a scaling of $\varepsilon_{100\%,\mathrm{n}} = 5\varepsilon_{\mathrm{rms,n}}$ which assumes that the beam follows a waterbag distribution in the zero field region. This is incorrect because the beam resulting from the uniform distribution at the plasma electrode has a KV-distribution outside the solenoidal magnetic field. For KV-distribution the envelope emittance scaling is $\varepsilon_{100\%,\mathrm{n}} = 4\varepsilon_{\mathrm{rms,n}}$ leading to the correct formula (A.3).

## References


[1] E. Liukkonen, *New K130 cyclotron at Jyväskylä*, in Proceedings of the *13th International Conference on Cyclotrons and their Applications*, Vancouver Canada, 6–10 Jul 1992.

[2] H. Koivisto et al., *The first results with the new JYFL 14 GHz ECR ion source*, *Nucl. Instrum. Meth.* **B 174** (2001) 379.

[3] T. Kalvas et al., *IBSIMU: a three-dimensional simulation software for charged particle optics*, *Rev. Sci. Instrum.* **81** (2010) 02B703.

[4] T. Kalvas, O. Tarvainen, H. Clark, J. Brinkley and J. Ärje, *Application of 3D code IBSimu for designing an $H^-/D^-$ extraction system for the Texas A&M facility upgrade*, in Proceedings of the *2nd International Symposium on Negative Ions, Beams and Sources*, Takayama Japan, 16–19 Nov 2010.

[5] T. Kalvas, R.F. Welton, O. Tarvainen, B.X. Han and M.P. Stockli, *Simulation of $H^-$ ion source extraction systems for the Spallation Neutron Source with Ion Beam Simulator*, *Rev. Sci. Instrum.* **83** (2012) 02A705.

[6] A. Girard, D. Hitz, G. Melin and K. Serebrennikov, *Electron cyclotron resonance plasmas and electron cyclotron resonance ion sources: physics and technology*, *Rev. Sci. Instrum.* **75** (2004) 1381.

[7] L. Panitzsch, T. Peleikis, S. Böttcher, M. Stalder and R.F. Wimmer-Schweingruber, *Current density distributions and sputter marks in electron cyclotron resonance ion sources*, *Rev. Sci. Instrum.* **84** (2013) 013303.

[8] J. Vámosi and S. Biri, *TrapCAD — a tool to design and study magnetic traps of ECR ion sources*, *Nucl. Instrum. Meth.* **B 94** (1994) 297.

[9] L. Maunoury, C. Pierret, S. Biri and J.Y. Pacquet, *Studies of the ECR plasma using the TrapCAD code*, *Plasma Sources Sci. Technol.* **18** (2009) 015019.

[10] A. Heinen et al., *Successful modeling, design and test of electron cyclotron resonance ion sources*, *Rev. Sci. Instrum.* **69** (1998) 729.

[11] A. Heinen, Ch. Vitt and H.J. Andrä, *Simulation of ECRIS*, in Proceedings of the *15th International Workshop on ECR ion sources*, Jyväskylä Finland, 12–14 Jun 2002.

[12] V. Mironov and J.P.M. Beijers, *Three-dimensional simulations of ion dynamics in the plasma of an electron cyclotron resonance ion source*, *Phys. Rev. ST Accel. Beams* **12** (2009) 073501.




2013 JINST 8 P05003

[13] S. Saminathan, V. Mironov, J.P.M. Beijers, R. Kremers and S. Brandenburg, *Study of ion beam extraction and transport from an electron cyclotron resonance ion source*, *Rev. Sci. Instrum.* **81** (2010) 02B706.

[14] P. Spädtke et al., *Prospects of ion beam extraction and transport simulations*, *Rev. Sci. Instrum.* **79** (2008) 02B716.

[15] P. Spädtke, *Model for the description of ion beam extraction from electron cyclotron resonance ion sources*, *Rev. Sci. Instrum.* **81** (2010) 02B725.

[16] D.S. Todd, D. Leitner, C.M. Lyneis and D.P. Grote, *Simulation and beamline experiments for the superconducting electron cyclotron resonance ion source VENUS*, *Rev. Sci. Instrum.* **79** (2008) 02A316.

[17] S.A. Self, *Exact solution of the collisionless plasma-sheath equation*, *Phys. Fluids* **6** (1963) 1762.

[18] J.H. Whealton, E.F. Jaeger and J.C. Whitson, *Optics of ion beams of arbitrary perveance extracted from a plasma*, *J. Comput. Phys.* **27** (1978) 32.

[19] R. Becker and W.B. Herrmannsfeldt, *IGUN — a program for the simulation of positive ion extraction including magnetic fields*, *Rev. Sci. Instrum.* **63** (1992) 2756.

[20] J.E. Boers, *PBGUNS: a digital computer program for the simulation of electron and ion beams on a PC*, in Proceedings of the *International Conference on Plasma Science*, Vancouver Canada, 7–9 Jun 1993.

[21] D.P. Grote, A. Friedman, J. Vay and I. Haber, *The WARP code: modeling high intensity ion beams*, in Proceedings of the *16th International Workshop on ECR ion sources*, Berkeley U.S.A., 26–30 Sep 2004.

[22] KOBRA3-INP simulation software, INP, Junkernstr. 99, 65205 Wiesbaden, Germany.

[23] S.A. Galkin, J.E. Grubert, B.P. Cluggish, N. Barov and J.S. Kim, *IONEX: a meshfree ion extraction code based on "particle in cloud of points" concept*, *Rev. Sci. Instrum.* **81** (2010) 02B705.

[24] M.A. Leitner, D.C. Wutte and C.M. Lyneis, *Design of the extraction system of the superconducting ECR ion source VENUS*, in Proceedings of the *2001 Particle Accelerator Conference*, Chicago U.S.A., 18–22 Jun 2001.

[25] H. Zaim and G.D. Alton, *Computational design studies for an ion extraction system for the Oak Ridge National Laboratory ECR ion source*, in Proceedings of the *2001 Particle Accelerator Conference*, Chicago U.S.A., 18–22 Jun 2001.

[26] B.P. Cluggish, S.A. Galkin and J.S. Kim, *Modeling ion extraction from an ECR ion source*, in Proceedings of the *2007 Particle Accelerator Conference*, Albuquerque U.S.A., 25–29 Jun 2007.

[27] T. Kalvas et al., *Fast slit-beam extraction and chopping for neutron generator*, *Rev. Sci. Instrum.* **77** (2006) 03B904.

[28] O. Tarvainen, P. Suominen, T. Ropponen and H. Koivisto, *Emittance and plasma potential measurements in double-frequency heating mode with the 14 GHz electron cyclotron resonance ion source at the university of Jyväskylä*, *Rev. Sci. Instrum.* **77** (2006) 03A309.

[29] O. Tarvainen et al., *Effect of gas mixing technique on the plasma potential and emittance of the JYFL 14 GHz electron cyclotron resonance ion source*, *Rev. Sci. Instrum.* **76** (2005) 093304.

[30] G. Douysset, H. Khodja, A. Girard and J.P. Briand, *Highly charged ion densities and ion confinement properties in an electron-cyclotron-resonance ion source*, *Phys. Rev.* **E 61** (2000) 3015.

[31] K.U. Riemann, *The Bohm criterion and sheath formation*, *J. Phys.* **D 24** (1991) 493.



2013 JINST 8 P05003

[32] V. Toivanen et al., *The effects of beam line pressure on the beam quality of an electron cyclotron resonance ion source*, *Nucl. Instrum. Meth.* **B 268** (2010) 1508.

[33] D.C. Meeker, *Finite Element Method Magnetics*, www.femm.info.

[34] P.W. Allison, J.D. Sherman and D.B. Holtkamp, *An emittance scanner for intense low-energy ion beams*, *IEEE Trans. Nucl. Sci.* **30** (1983) 2204.

[35] J.G. Wang, D.X. Wang and M. Reiser, *Beam emittance measurement by the pepper-pot method*, *Nucl. Instrum. Meth.* **A 307** (1991) 190.

[36] C.D. Child, *Discharge from hot CaO*, *Phys. Rev.* **32** (1911) 492.

[37] I. Langmuir, *The effect of space charge and residual gases on thermionic currents in high vacuum*, *Phys. Rev.* **2** (1913) 450.

[38] H. Koivisto et al., *Ion beam development for the needs of the JYFL nuclear physics programme*, *Rev. Sci. Instrum.* **79** (2008) 02A303.

[39] H. Liebl, *Applied charged particle optics*, Springer (2008) [ISBN 978-3-540-71924-3].

[40] D. Leitner, D. Winklehner and M. Strohmeier, *Ion beam properties for ECR ion source injector systems*, 2011 *JINST* **6** P07010.

[41] D.T. Palmer, X.J. Wang, I. Ben-Zvim, R.H. Miller and J. Skaritka, *Experimental results of a single emittance compensation solenoidal magnet*, in Proceedings of the *1997 Particle Accelerator Conference*, Vancouver Canada, 12–16 May 1997.

[42] Z.Q. Xie, *The effect of space charge force on beams extracted from ECR ion sources*, Ph.D. Thesis, Michigan State University, MSU CP-60 (1989), pg. 58.

[43] G.R. Brewer, *Focusing of high-density electron beams*, in *Focusing of charged particles. Volume II*, A. Septier ed., Academic Press, New York U.S.A. (1967), pp. 73–121.

2013 JINST 8 P05003